DEPARTMENT OF ELECTRONIC ENGINEERING

Design and fabrication of advanced fibre gratings and their applications to sensing instrumentations and telecommunications

Bashir Aliyu Labbo GWANDU

Doctor of Philosophy

ASTON UNIVERSITY

December 2003

ASTON UNIVERSITY

Design and fabrication of advanced fibre gratings and their applications to sensing instrumentations and telecommunications

Bashir Aliyu Labbo GWANDU
Doctor of Philosophy
2003

Abstract

This thesis describes a study of fibre grating devices, their fabrication and applications into systems that can be used in sensing and telecommunications. The study has focused mainly on three main types of grating: the fibre Bragg gratings (FBGs), the long period gratings (LPGs) and the sampled fibre Bragg gratings (SFBGs). A number of approaches to design the gratings through simulation and experiment have been pursued and the results are presented. Through simulation, LPG resonance curves were obtained for the first 53 cladding modes to enable interpretation of grating characteristics.

A number of grating structures have been designed and fabricated. For example, apodised gratings with 19dB strength in both transmission and reflection have been produced. Also, a compact-grating-array with high spatial resolution has been demonstrated for quasi-distributed and arbitrarily applied strain measurements. However, with the measurement of strain, there is a potential for temperature cross-sensitivity which needs to be compensated, thus, novel FBG strain sensors with the capability to compensate for temperature-induced wavelength shifts, are proposed and demonstrated.

Many specially designed LPG sensors are proposed: a standard LPG that can be interrogated using a single light source has been demonstrated to provide simultaneous measurement of strain and temperature. Also, an LPG produced in double-cladding fibre is demonstrated to be capable of simultaneously measuring refractive index and temperature. Furthermore, two special LPGs are demonstrated: one in a standard fibre, which allows for measuring several parameters along with temperature simultaneously; the other in B/Ge co-doped fibre which exhibit high responsivity.

For SFBG sensing, several novel configurations of multiple-parameter sensors are demonstrated. They include the use of a single SFBG to measure simultaneously the refractive index of the surrounding medium and the temperature or a combination of the strain, curvature and temperature. In addition, the largest curvature-induced mode splitting of 126nm is recorded and the capability of SFBG to measure curvature of $<0.4m^{-1}$ is demonstrated.

For telecommunications, the novel use of all the three main types of grating has been demonstrated: a technique for suppressing cladding-mode coupling loss is shown to achieve suppression down to ~0.2 dB in an FBG of 18dB strength. LPGs are demonstrated to provide tuneable loss filters in both 1500nm and 1300nm wavelength regions: the highest tuneability achieved is 2.75nm/°C. An important observation is that of two perturbation-independent loss peaks at 1245 and 1400nm wavelength regions, which can limit the tuning range of the loss filters. A method to eliminate or avoid these loss peaks is also presented

Two novel SSFBG-based microwave filters demonstrated include a transversal filter that achieved >45dB rejection and a bandpass filter that achieved a rejection level of ~30dB. Nevertheless, the use of SSFBGs have not been limited to microwave applications, but also to optical telecommunications, as a Dense Wavelength Division Multiplex (DWDM) filter with >22 flat-top channels was experimentally demonstrated.

Keywords: Bragg gratings; long period gratings; sampled gratings; Strain and temperature sensors; optical DWDM and microwave filters

Dedication

This work is dedicated to the memory of Alhaji Umar Bello Watse who was among those that advised me to leave an attractive NITEL job offer, to pursue this PhD, but tragically died in a road accident a year later. May his soul rest in peace. Ameen

Acknowledgement

I would like to acknowledge the continuous support accorded to me by my Supervisor and Advisor Dr Lin Zhang and Prof. Ian Bennion respectively. The encouragement given to me by Lin was no doubt what fuelled the rapid progress I recorded and led to a number of publications. Lin has also encouraged many of the post-doctoral fellows in the group to discuss a number of ideas and provided me with their professional guidance. Ian on the other hand considering his busy schedules has over the years a given me a huge slice of his precious time reading and correcting my work.

My thanks go to Kebbi State Scholarships Board, Nigeria, for the funding I received to support myself during this work. I must also thank Mr Bert Biggs who has been a fantastic Technician and Laboratory Manager. Bert has always provided material that facilitated my research on request and indeed promptly. I cannot thank him enough. I must also thank Dr Yu Liu, Dr Wei Zhang and Dr Xuewen Shu who I have worked with closely. They provided me academic guidance, and in the process became my very close personal friends. Yu gave me all the support I required particularly in respect of modification to grating fabrication software. Wei introduced me to Microwave photonics and was always ready to discuss experimental propositions. Wei's support was not limited to academic but also moral particularly during a very difficult period. Through my work with Xuewen I improved my understanding of long period gratings, and understood how to refine my research ideas and conduct my experiments more efficiently. Indeed as described in the Thesis, I used his simulation results to explain some of my experimental observations.

My thanks go to Profs. Ghafouri-Shiraz and Bajoga, who were behind my decision to come to Aston. I would also like to thank Dominico Gianonne, who taught me how to start making gratings, Karen and Kate who I have worked with intermittently during which I improved my FBG fabrication skills. I also enjoyed working with Tom and Mykhaylo from whom I have learned so much. One of the LPGs with 240 μm-period used was in fact fabricated by Tom. My working relationships with Steve, Paul, Rob, and Andy created a very good atmosphere for research; they are always happy to share equipment with me, sometimes at short notices.

I must also acknowledge the support given to me by Dr Dave Webb. Dave was always supportive and ready to discuss my work, and he offered me so much guidance, which helped

me to publish some of my results. My discussion with Dr John Williams helped me to refine my thoughts on microwave photonics; I must also thank him for correcting some of my work. The excellent research atmosphere was created not only by the grating guys but also the theoreticians. In particular, I would like to thank Sergei, Vladimir, Elena and Igor for being so friendly and the various academic discussions we had during this research.

The assistance provided to me by Mrs Helen Yard, Selena, Sarah and the remaining staffs and students are gratefully acknowledged. Sarki has helped to read this work and offered a number of useful suggestions to which I am grateful.

My special thanks goes to all members of my family, in both the UK and Nigeria, for their continuous support. In Particular, my wife Zainab and daughters Fatima and Aishat deserve thanks for tolerating and supporting me all through my studies. Indeed the support from Malam Bello Gwandu, Jibril, Umar, Bala, Abubakar, Haliru, Arabo, T.S Abdullahi, Mamman Dan-Masama, Suleman and Atiku are gratefully acknowledged. Finally, special thanks to my parents for all their support and encouragement.

Table of contents

Table of figures

List of table captions

Table of abbreviations

Abbreviations	Full words
AWG	Arrayed Waveguide Grating
B/Ge	Boron Germanium Co-doped
BBS	Broadband Light Source
CFBG	Chirped Fibre Bragg Grating
CMT	Couple Mode Theory
CW	Continuous-Wave
dB	Decibels
DFB	Distributed Feedback
DSC	Dual Shaped Core
DSF	Dispersion Shifted Fibre
DTP	Dispersion Turning Point
DWDM	Dense Wavelength Division Multiplex
EDFA	Erbium-Doped Fibre Amplifier
ESG	Electrical Strain Gauge
EMI	Electromagnetic Interference
FBG	Fibre Bragg Grating
FSR	Free Spectral Range
GeO_2	Germanium silicate
H_2	Hydrogen
HE	Hybrid-Electric
ISI	Inter-Symbol Interference
LCA	Lightwave Components Analyzer
LED	Light Emitting Diode
LOS	Line-of-Sight
LPG	Long Period Gratings
NA	Numerical Aperture
OH	Hydroxyl
OSA	Optical Spectrum Analyser
PM	Phase Mask
ROF	Radio On Fibre
Sinc-SFBG	Sinc-Sampled Fibre Bragg Grating
SFBG	Sampled Fibre Bragg Grating
SRI	Surrounding Refractive Index
SSFBG	SuperStructure Fibre Bragg Grating
T-Matrix	Transfer Matrix
TIR	Total Internal Reflection
TEM	Transmission Electron Microscopy
TTD	True Time Delays
UV	Ultra Violet
WDM	Wavelength Division Multiplex

1 Introduction

The development of low loss optical fibre has revolutionised telecommunications making it possible to provide high-capacity channel for transmission of high-quality data, images and voices across continents. Today, information is being transmitted reliably at speed of up to 80 Gbits/s, often across continents. The rapid development of video-conferencing and the Internet from 1992 to date meant that there is increasing demand for bandwidth. Fibre gratings are devices that are in-built within the core of a fibre and can be written at desired location -providing narrow-band wavelength selection. These gratings have many different applications in the areas of high-capacity telecom signal transmission and processing, as well as, optical sensing. The application areas include dispersion compensation, lasers, Dense Wavelength Division Multiplexing (DWDM), filters, structural health monitoring, as well as the measurement of chemical concentration, temperature, and many other parameters.

The gratings revolution started with Hill's end-writing technique [1] but the rapid progress commenced in 1989 after Meltz and co-workers introduced the technique of Fibre Bragg Grating (FBG) UV-inscription by side-writing through the cladding. Since then, many different types of gratings have been produced and several application areas have been identified. Currently, there is increasing drive towards research into ways of creating new types of gratings and to find new applications. Indeed with the recent "bursting of the telecom bubble" optical research activity has been increasingly focusing on niche areas such as fibre laser development, sensing in smart structures, civil, and aviation industries, temperature monitoring in oil and electricity industries, in-fibre radio signal distribution in tunnels and high-rise buildings, as well as instrumentations manufacture. The backbone of these niche activities is the development and progress recorded in fibre and grating technology. Research into ways of improving grating fabrication and applications is thus becoming increasingly important and this thesis presents a large number of contributions to the effort in producing new grating devices and the applications of such devices.

1.1 Arrangement of thesis

This thesis is concerned with the design, fabrication, and applications of fibre gratings in the areas of sensing and optical communications. There are seven chapters in the thesis. This chapter introduces the remaining parts of the thesis.

Chapter 2 focuses mainly on the overview of grating technology and its driving force. The history of fibre gratings is given and the techniques to side-write FBGs are described starting from 1989. The main inscription techniques considered are the transverse holographic and the phase mask types. A review of the other FBG-writing methods is also given followed by a general literature survey on the fabrication and application areas of different types of fibre grating device, including the Long Period Gratings (LPGs), and Sampled Fibre Bragg Gratings (SFBGs). Photosensitivity in optical fibres determines the strength of the grating that can be obtained. A number of methods to enhance photosensitivity have been proposed by researchers and some of these methods are reviewed.

In Chapter 3, the characteristics of uniform-period FBGs, including their reflectivity, transmitivity, sidelobe spectral positions, and line-width, are discussed. Coupled mode theory is used for the grating analysis. Subsection 3.2.1 focuses on contra-directional coupling which relates mainly to FBGs, and Subsection 3.2.2 focuses on co-directional coupling which relates to LPGs; the equations for spectral responses of both FBGs and LPGs are presented in the two respective subsections. The procedure for calculating the effective indices, starting from the Sellmier and eigen-value equations, is given in Subsection 3.2.1.1. Whilst Subsection 3.2.1.2 demonstrates a calculation of grating line-width, the modelling of FBGs based on the use of Matrix transform is presented in Subsection 3.2.1.3: the modelling technique employed is applicable to variety of Bragg gratings with the main distinguishing factor being the index modulation. Typical Bragg gratings that are investigated include uniform-period FBGs, apodised FBGs, chirped FBGs, and SFBGs.

Chapter 4 focuses on grating design and fabrication. First, the index modulations for various types of uniform period gratings are shown in Section 4.2 with their corresponding spectral responses. This is followed by a discussion on the spectral characteristics of such FBGs in Section 4.3, where the effects of changing the coupling coefficient of FBGs are highlighted. In Section 4.4, a discussion follows on the different experimental set-ups that can be used to fabricate the short and the long period, as well as, the sampled gratings. In Section 4.5, the discussion extends to the fabrication of specially designed FBGs, such as Apodised-, Chirped-, Chirp-Moiré-, Sampled-, and Sinc-sampled- FBGs. In particular, Subsection 4.5.1 focuses on apodisation of FBGs where both simulation and experimental results are presented. Subsections 4.5.2 and 4.5.3 discuss the fabrication of chirped, and chirped-moiré FBGs respectively. Finally, Subsection 4.5.4 discusses the design and fabrication of

specialised SFBGs, such as comb-filter and sinc-sampled types. The conclusion is drawn in Subsection 4.5.5.

In Chapter 5 the applications of FBGs, LPGs, and SFBGs as sensors are discussed in Sections 5.2, 5.3 and 5.4 respectively. Subsection 5.2.1 describes the design and use of FBG-arrays to measure arbitrarily distributed axial strain. The concept of high spatial resolution array is described and the use of such arrays to measure arbitrary distributed strain is discussed. The quasi-distributed strain sensor described in Subsection 5.2.1 does not have temperature compensation or discrimination. To this end, many novel solutions are proposed and demonstrated in Subsection 5.2.2, where different configurations of simultaneous temperature and strain FBG-sensors are described. The detailed measurement results of these sensors are presented in Subsection 5.2.2.2 and the effectiveness of these novel dual parameter FBG-sensors is demonstrated in Subsection 5.2.2.3.

In Section 5.3, the sensing applications of some special types of LPG fabricated in different types of fibre are discussed. The different sensitivities of LPG peaks to temperature are first described using LPG sensing equations; both positive and negative temperature slopes are identified and examined. Subsection 5.3.1 discusses the use of LPGs that display high diffraction order cladding modes to measure multiple parameters. One of the LPGs having both the fundamental- and second diffraction order -modes 50nm apart and demonstrating different temperature responses, are used to measure strain and temperature simultaneously and the result is described in Subsection 5.3.1.2. Further investigation in Subsection 5.3.1.3 focuses on LPGs with yet un-reported characteristics, which are demonstrated in both B/Ge co-doped and standard fibres. To identify, understand and explain the behaviour of some of these LPGs, a number of simulation exercises were carried out and some of the results obtained are also described in the subsection. The use of one such special LPGs to measure the combined effects of various parameters such as strain, curvature, refractive index and temperature is discussed in the subsection. In Subsection 5.3.1.4, simultaneous measurement of temperature and other parameters such as refractive index, bending curvature, and strain using one of the special LPGs produced in a standard telecom or Single Mode Fibre (SMF) is described.

In Subsection 5.3.2, the design, fabrication, and the use of LPGs fabricated in SMM900 3-layer fibre with a number of potentials for dual-parameter sensing and gain-flattening

applications are demonstrated. Subsection 5.3.2.1 provides the description of the fibre and the LPGs produced within the fibre with small ($<65\,\mu m$) and larger ($>90\,\mu m$) periods. The cladding modes obtained in the LPGs with period $>90\,\mu m$ are index-insensitive and are demonstrated to appear at the Erbium-Doped Fibre Amplifier (EDFA) wavelength region with potential for use in gain flattening. The LPGs with periods $<65\,\mu m$, however, are highly responsive to surrounding refractive index (SRI) and temperature. The use of a two cascaded LPGs, written side-by-side with both large and small periods to simultaneously measure refractive index and temperature in particular, is discussed in detail within Subsection 5.3.2.2.

In Section 5.4, the design and use of SFBG to simultaneously measure the combined effects of temperature and various other parameters are described. In particular, the results of the first demonstration of temperature and refractive index measurement using a single SFBG device are demonstrated in Subsection 5.4.1. In Subsection 5.4.2, the novel applications of SFBG to measure axial strain, temperature and curvature simultaneously are discussed. Within the same subsection, the capability of an SFBG to measure both very large and very small curvature values is also demonstrated. In Section 5.5, a conclusion is drawn from Chapter 5.

Chapter 6 focuses mainly on fibre grating filters that can be used in optical communications. The filters are grouped into FBG-based, LPG-based and SFBG-based filters and are discussed in Sections 6.2, 6.3, and 6.4 respectively. Under the FBG-based filtering section, the techniques to suppress the cladding mode coupling loss are presented. These techniques include changing the fibre-core refractive index through UV pre- and post-exposure as well as using fibres of different dimensions. Simulation and experimental results are presented to support the analysis.

In Subsection 6.3.1, LPG-based filters are considered. Tuneable loss filters that provide excellent temperature tuneability while operating in the 1500nm and 1300nm wavelength regions are discussed in Subsections 6.3.1.1 and 6.3.1.2 respectively. It should be pointed out that the tuning range of the loss filters presented can be limited by the appearance of perturbation-independent loss peaks at 1245 and 1400nm wavelength regions which are related to hydrogen and ultra-violet (UV)-induced hydroxyl (OH) ions respectively. These peaks can distort the spectral response of LPGs that possess cladding modes that are

spectrally located in either one or both regions. The peaks need to be eliminated or reduced for effective performance of the loss filter. Thus it is of vital importance to study their characteristics when written in both standard SMF and B/Ge fibres with a view to avoid or eliminate them. To this end the properties of both SMF and B/Ge co-doped fibres have been investigated and methods to eliminate or avoid these perturbation-independent peaks are discussed in Subsection 6.3.2.

In Section 6.4, the microwave sub-carrier related applications of SFBGs operating in both transmission and reflection are considered. Subsection 6.4.1 involves SFBGs operating in reflection to give a transversal filter, and in Subsection 6.4.2, a compact microwave sub-carrier bandpass filter that operates in transmission mode of the SFBG is discussed. Subsection 6.4.1.1 describes the transversal filter principle. Subsections 6.4.1.2 and 6.4.1.3 describe the experimental implementation of the filter and the novel results obtained. Subsection 6.4.1.4 provides a further analysis of the results by considering the distortion caused by the dispersive device used to create a delay line. For the bandpass filter, Subsections 6.4.2.1 and 6.4.2.2 present the design and experimental implementation respectively. Subsection 6.4.3 discusses the use of SFBG as DWDM filter. The SFBG has been demonstrated to achieve >22 channels for use in DWDM applications with potential use for multiple-channel dispersion compensation.

Chapter 7 focuses on conclusion and further work. It highlights the key results achieved in the areas of fabrication, sensing- and filtering-applications. Under fabrication, the sidelobe rejection level achieved in apodisation, the spatial resolution attained in grating arrays, and the different shapes of SFBG spectral response obtained are described. Under the sensing applications, attention is drawn to the numerous dual, and multiple-parameter sensors achieved based on FBGs, LPGs and SFBGs as well as the sensing performance. Finally, the applications to telecom systems and devices focus on the results of the suppression of coupling loss, tuneability of loss filters, microwave sub-carrier filter rejection-levels, and the prospects of DWDM using sinc-SFBGs.

1.2 Reference:

1. K.O. Hill, Y. Fujii, D.C. Johnson, and B.S. Kawasaki, "Photosensitivity in optical fibre waveguides: Application to reflection filter fabrication," *Appl. Phys. Lett.*, vol. 32, no. 10, pp. 647-649, 1978.

2 Overview of fibre grating technology

2.1 Historical overview of fibre gratings

Total Internal Reflection (TIR), on which the transmission of light in an optical fibre depends, has been known for decades. Despite this, the field of fibre optics did not expand until the 1950s when a cladding layer was incorporated into previously unclad glass fibre designs [2]. This revolutionised the field and led to the development of standard optical fibre.

The research into optical fibre as a telecommunications media was further strengthened by the need for economical media with large information carrying capacity. With the discovery of laser in the early 1960s its potential use as a coherent optical source was soon recognised where preliminary work on optical communications was reported [2]. The laser propagation through the atmosphere along with periodic focusing was suggested where experimental line-of-sight (LOS) systems were demonstrated [2]. The obvious lack of reliability and adverse weather conditions limited the use of the LOS-based technology.

In 1966, Kao and Hockham [3] proposed the use of optical fibre as a telecommunications media where they theoretically demonstrated that dielectric waveguide with a circular cross-section can support a family of H_{0m}, E_{0m} and hybrid HE_{nm} modes. In fact, the authors reported an example of fibre-surface corrugations that are similar to gratings.

In geometric optics however, the possibility of using optical fibre for telecommunications was illustrated by using the phenomena of TIR. At the time of Kao and Hockham's work optical fibre was still very lossy, typically ~600dB/km, which severely limited any practical application of both the fibre and the grating [3]. In 1970, the situation changed dramatically when Kapron et al [4], from Corning, managed to reduce this loss to ~20dB/km. The loss in silica fibre was then reduced to ~7dB/km in 1972 [5], and in 1973, Bell Laboratories, in the USA, achieved a loss reduction to ~2.5dB/km [6]. Researchers in the USA and Japan succeeded in reducing the fibre loss to ~2dB/km in 1975 and later in 1976, the loss was reduced to ~0.5dB/km in Japan [7]. By 1979 further advances in the fabrication technology resulted in the loss being reduced to ~0.2 dB/km in the 1550nm wavelength region [8]. The

availability of such a low loss fibre allowed the propagation of optical signals over large distances and the reduction of loss down to 20dB/km led to continuous activities in optical fibre communications and sensing.

Losses in optical fibre are wavelength dependent and the regions of major interest for optical communications are marked A, B and C in the spectrum of Fig. 2.1. Regions A, B, and C are located around 0.8μm, 1.3 μm and 1.55 μm wavelengths respectively. The 1.55 μm region have the best loss figure, followed by the 1.3 μm region. At 1.3 μm, the material and waveguide dispersions cancel out making the net dispersion zero. The 1.55 μm window has the least loss, but currently there is a dispersion of ~17ps/nm-km for any light propagating in a standard SMF at this wavelength. To minimise the effect of dispersion at 1550nm while maintaining the best loss figure of 0.2dB/km a Dispersion Shifted Fibre (DSF) may be employed [9]. The DSF is designed to shift the zero net-dispersion wavelengths to the 1500nm window. Also fibres that have large negative dispersion such as the Dispersion Compensation Fibre (DCF) can also be used to compensate for the effect of dispersion in the low loss 1500nm window.

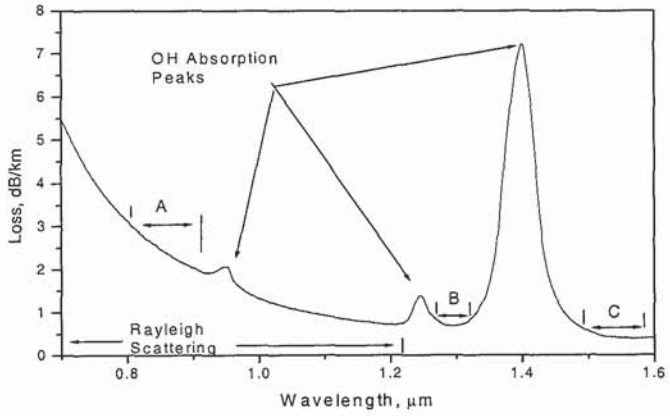

Fig. 2.1: Fibre loss as a function of wavelength showing high loss and low loss regions.

Another key advantage of 1.55 μm window is the discovery of the EDFA [10], which allows light signal to be amplified. This advantage further promotes the use of this window for long-haul optical transmission, because power losses incurred in the fibre can be compensated through amplification. In addition, the ability to compensate for the dispersion effect at 1.55 μm wavelength further increases the attractiveness of this window for optical communications and sensing.

Concurrent with the improvements in the loss characteristics of optical fibres in the three transmission windows A, B, and C was the first fabrication of permanent in-fibre gratings in germano-silicate fibre as periodic perturbations of the refractive index along the fibre length by Hill et al [11,12] in 1978. They reported that intense Argon-ion laser radiation, at a wavelength of 488nm or 514.5nm, was end-coupled into a germanium-doped fibre and after duration of several minutes an increase in the intensity of the reflected light was observed. With further Ultra-Violate (UV) light exposure the strength of the reflected beam grew until almost all the light was reflected back from the fibre. By strain and temperature tuning of the fibre, it was concluded that a narrowband Bragg grating had been produced along the 1m length of the fibre.

The grating was believed to be formed by standing-wave interference pattern formed between the counter propagating beams of laser light, with the backward travelling light occurring as a result of a small (~ 4%) reflection from the far end of the fibre. The gratings formed using this technique are called 'Hill gratings'. Unfortunately the applications for such gratings were restricted to those requiring gratings at the writing-source wavelength. The method of end-coupling of laser light into a fibre to produce Hill gratings, as well as the typical results that may be obtained are shown in Fig. 2.2. Fig. 2.2(a) shows the enlarged fibre and the standing wave pattern formed inside the fibre core, and Fig. 2.2(b) shows the typical spectral responses of a grating.

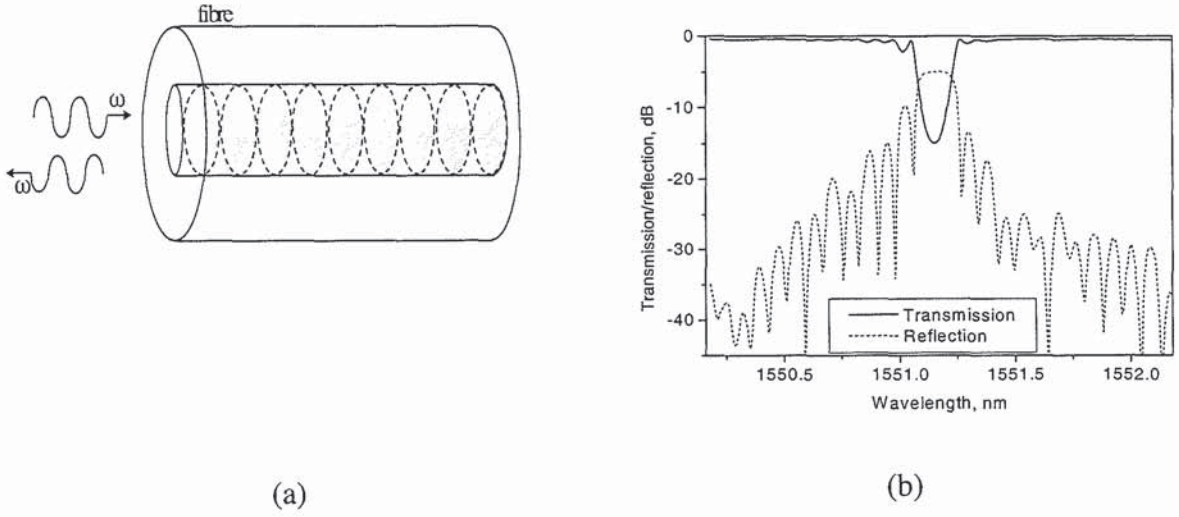

Fig. 2.2: The experimental method used by Hill and co-workers to produce a periodic modulation of the refractive index of the fibre, induced by a standing-wave of UV light in the fibre core, (b) the typical spectrum of light received at the two ends of fibre.

2.2 Side-writing techniques

Although the phenomena of writing Hill gratings generated much academic attention at the time, with the exception of small number of further studies, the subject was not extensively pursued until Meltz et al [13] rekindled the interest by reporting in 1989 that gratings could be written by two-beam holographic exposure through the *side of the fibre* using UV light radiation. The side-writing through a UV-transparent cladding is one of the most important developments in the area of fibre grating fabrication in the 1980s.

The experimental set-up for side-writing is depicted in Fig. 2.3. The enlarged part of the figure shows the fibre, intersecting UV beams, and the index fringes in the fibre. The work was followed on from that done by Lam and Garside in 1981 [14], who recognised that the underlying effect for the fabrication of in-fibre filters was based on a permanent UV-induced modification of the refractive index of the fibre core. Meltz and co-workers' side-writing method was found to be more efficient as a one-photon process rather than the two-photon process, which Hill had earlier observed in the end coupling method. Meltz et al's work [13] served to experimentally confirmed this when they demonstrated the grating fabrication by using two intersecting UV-beams of wavelength 244nm as shown in Figs. 2.3. Using this interferometric arrangement, gratings were formed at a wavelength, which was dependent on the period of the interference maxima, set by the angle between the two interfering beams, and the wavelength of the UV radiation, rather than by the visible radiation launched into the core of the fibre that allows the spectral responses to be recorded. The Bragg spectral wavelength of the grating is defined by

$$\lambda_B = \frac{\lambda_{UV}}{\sin\theta_1 + \sin\theta_2} \tag{2.1}$$

where λ_{UV} is the wavelength of the writing laser, and θ_1 and θ_2 are the UV interference angles as shown in Fig. 2.3 ($\theta_1 + \theta_2 = \theta$). This method of using interfering UV beams to write a grating through the side of the fibre is sometimes called the Transverse holographic FBG inscription technique.

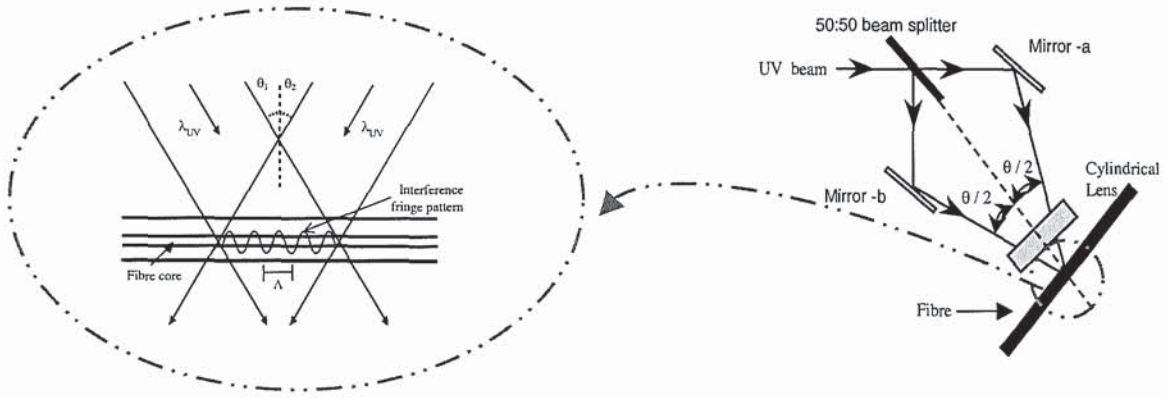

Fig. 2.3: The Meltz et al's transverse holographic grating writing arrangement: showing the set-up, and the enlarged section of fibre position relative to the interfering UV beams showing the periodic index modulation of the fibre core.

Transverse holographic technique of writing gratings demonstrated in Fig. 2.3 becomes possible because the fibre cladding is relatively transparent to UV light whereas the core is highly absorbing. The Meltz et al's fabrication arrangement proved to be flexible and is still in-use today, despite the fact that the grating writing techniques are now much more efficient.

This holographic fabrication technique was later extended by Kashyap *et al* [15] to allow the fabrication of gratings at wavelengths of ~1550nm, a region which as described earlier and shown in Fig. 2.1 is an important (low-loss) spectral region for optical communications and sensing. Despite the significant impact of the Hill's standing-wave- and Meltz's holographic-techniques of writing gratings, few prism-based interferometric methods have been proposed [16,17]. These prism-based methods offer the advantages of simplicity and stability, but sacrifice the control of flexibility that is offered by the holographic method.

Despite the capability of transverse holographic fabrication technique to produce high performance gratings with Bragg wavelength that is arbitrarily selectable with change of the angle between the interfering beams the popularity of this method and the other methods mentioned above diminished when Hill *et al* [18] in 1993 introduced the phase mask technique of fabricating Bragg gratings[1]. The phase mask technique generated a great deal of interest because it simplified the grating manufacturing process and had the capability to reproduce high performance devices unmatched by the other techniques of fabrication. It is

[1] Features of phase mask and its application will be described in the next chapter.

this phase mask technique that has attracted commercial interest around the world and stimulated the establishment of companies fabricating both gratings and phase masks. Today the fabrication of fibre gratings has been very much refined. The quality of gratings is now such that they are being employed in many real systems, and they compete with other photonics technologies.

For applications, FBGs have been proposed for measuring a variety of parameters and are used in many diverse applications, such as the measurement of strain [19], temperature [19], chemical concentration [20,21], wavelength [22], vibration [23,24], acceleration [25,26], ultrasonic field [27], pressure [28,29,30], electric current [31,32], human heart beat [33], and curvature, [34]. But the first Bragg grating sensors to be demonstrated were temperature and strain sensors [19].

Majority of the Bragg grating sensors functioned because the measurand induces a change in the Bragg wavelength. For example, in the case of strain sensors, a tensile strain results in a shift of the grating spectral peak to longer wavelengths and a compressive strain results in a shift to shorter wavelength.

The most common use of grating sensors is for point sensors, where an average value of the measurand along the short grating length is obtained. Gratings can be used to make quasi-distributed measurements, for example, by deploying an array of gratings of different wavelengths along the length of fibre [35,36]. Distributed sensing is now used commercially in many applications, a typical example is the measurement of strain in structures such as Aircraft wings, pipes, bridges, high-rise buildings, etc, where the gratings can be either embedded when the structure is made [37] or attached through secondary bonding.

One of the main issues concerning the use of Bragg gratings is that of isolating, the effect on the grating, of parameters which are not being measured. For example, it is difficult to distinguish between strain and temperature information when both are to be evaluated from a single wavelength shift. In majority of the sensing work reported in Chapter 4 different techniques have been adopted to address such a problem. In addition, many papers have been presented concerning the discrimination between strain and temperature effects measured by Bragg gratings [38,39,40,41]. Other areas where there is reasonable concern regarding the use of germano-silicate fibre grating sensors are in hazardous environments, such as, in the

presence of gamma rays. Gamma rays are known to introduce excess losses in GeO_2 fibre, hence Nitrogen doped fibre are used to address the problem [42]. Nitrogen-doped fibres have been shown to exhibit high resistance to gamma ray-induced losses. Areas of further concern include measurements at cryogenic temperatures where linearity of the gratings begins to deteriorate [43].

Bragg gratings are now routinely used in fibre lasers and have been demonstrated in many rare earth doped fibres, including Erbium fibres [44,45]. They are used for making fibre lasers. FBGs provide high wavelength selectivity and partially reflecting mirrors that are required in fibre lasers, and FBGs can be embedded easily [46]. FBGs are ideally suited for fibre lasers because, in many cases, the gratings can be fabricated directly in the active region of the fibre. Indeed, FBGs can also be positioned at the boundaries of the active region to serve as Bragg reflectors. If an FBG is produced in the active region, light signal passing through will suffer both forward and backward reflection at different points in the grating, these reflections occur at regular distances and take place continuously throughout the length of the grating, and these reflections add-up in phase ensuring high frequency selectivity leading to a distributed feedback (DFB) laser.

By compression tuning of the FBG fabricated within the active region of the Erbium-doped fibre a tuneable DFB laser can be achieved [47]. Grating-based DFB lasers are easy to produce, are fibre-inherent and thus do not suffer from compatibility problem, and produces high output power leading to high signal-to-noise ratio. An additional advantage of grating-based laser stems from their low thermal responsivity in comparison to their semiconductor counterpart. In optical communication systems there is requirement for narrow line-width of the grating. Therefore, longer FBG can be produced to meet this requirement. Other areas of optical communications where FBGs can be used include wavelength division multiplexing (WDM), add/drop filters, EDFA equalization and dispersion compensation.

Kashyap et al. [48] in 1993 was the first to report on the potentials of FBGs for gain equalization. Currently, Bragg grating-based gain equalizers have gained so much commercial interests. Indeed standard uniform period and slanted FBGs, and many long period gratings (LPGs) are currently used for EDFA gain equalization [10]. Bragg gratings can be used to flatten the gain of EDFA when arranged in both reflection [49,50] and transmission [50]. Because of their spectral width, Chirped Fibre Bragg Gratings (CFBGs)

are the most widely used types of FBG for gain equalization. However, gain equalizers based on CFBGs can exhibit group delay ripples, which can affect the transmission performances. Those ripples are due to reflections occurring at the edges of and along the gratings [51] and their characteristics have been analysed by Chotard et al. [52].

In WDM systems, add/drop filter nodes are required to select the individual channels or to insert or drop off a signal on a particular channel. There are many different FBG configurations used to achieve this, which include FBGs written in Mach-Zehnder interferometers [53] and in fused couplers [54]. Some of these FBG-based techniques have the advantage of offering low insertion losses for the added channels, and very high isolation for the dropped channels.

In standard SMF there are a number of mechanisms that causes group delay distortion to an optical pulse propagating within it. Two of the mechanisms that contribute to delay distortion are Material (chromatic) dispersion and Waveguide dispersion. Waveguide dispersion is negligible in a standard SMF, leaving the chromatic dispersion to be the dominant factor. For this SMF, the effects of the Material and Waveguide dispersion cancelled-out at ~1300nm [55].

CFBGs are dispersive devices that can be used for chromatic dispersion compensation, dispersion slope compensation [56], and broad bandwidth applications. The CFBG-based dispersion compensators were earlier proposed in [57] and the experimental demonstrations followed [58,59]. They operate on the basis of inducing differential reflective delay for different spectral components. To achieve a CFBG, either the period of the refractive index modulation or indeed the core-index may be varied with the grating length. The use of CFBG in both transmission [60] and reflection [61] as dispersion compensators has also been demonstrated.

The grating dispersion[2] can be represented by,

$$D = \frac{2n_{eff}L}{c\Delta\lambda} \tag{2.2}$$

[2] Grating dispersion will be further described in Section 4.5.2

Where n_{eff} is the effective index of the fibre core, L is the grating length, and $\Delta\lambda$ is the total grating bandwidth.

It has now become a common practice not only to produce CFBGs for dispersion compensation but also to design the gratings with minimal time-delay ripples [62]. Furthermore, because the chirp is a function of CFBG length, there is increasing drive towards the production of long length CFBGs for dispersion compensation. To this end, high quality dispersion compensators using gratings up to 1-metre in length have been demonstrated [63].

Radio On Fibre (ROF) system is another type of grating application that was first proposed and demonstrated by A.J. Cooper [64] with a view to addressing the weak RF signal within buildings, underground tunnels, shopping malls, etc. Today, ROF systems are increasingly gaining popularity and many companies have been formed to provide such services.

FBGs have been used to implement various types of microwave sub-carrier filters that are used to implement ROF systems. In addition, WDM filters based on FBGs are also shown to enhance distribution capacity of ROF systems [65, 66]. In Chapter 6, microwave sub-carrier filters for use in ROF systems are further discussed and novel implementations are investigated.

In addition to conventional in-core FBGs, two additional categories of in-core fibre gratings are studied during this research. These grating are the LPGs and the SFBGs. Whilst the LPG is produced with grating periods larger than that of FBGs, the SFBGs contains both long as well as short periods.

LPGs are currently being produced using continuous-wave (CW) frequency-doubled argon lasers at 244nm, and the pulsed lasers at 157nm or 193nm. However, LPGs fabricated using femtosecond laser pulses have been shown to be stable at temperatures up to 500°C [67], which is often not the case for the ones produced using CW argon lasers. Also, CO_2 pulsed laser has been shown to produce 480μm-period LPGs through periodic point-by-point exposure with the grating exhibiting high temperature stability [68]. Electric arc has been demonstrated for LPG fabrication and such LPGs have been shown to operate at temperatures

of up to 800°C [69]. Here, the electrodes of a fusion-splicer are used, exposing to the arc, a region of fibre with a length of the order of 100 μm, limiting the minimum period of LPG that may be fabricated. Chemical etching of the cladding has also been shown to produce LPG corrugations [70].

Whilst LPGs can be designed to have attenuation bands at specific spectral locations, the positioning is often imprecise. A number of methods to fine-tune the spectral positions of the bands exist and a type of post-fabrication tuning of LPG's transmission spectrum has been achieved by reducing the fibre diameter through etching of the cladding [71,72]. The effective indices of the cladding modes are dependent on the thickness, and the refractive index of the cladding layer. The reduction in cladding diameter thus alters the values of the effective indices of these cladding modes resulting in a shift of the modes to the longer wavelengths.

To produce LPGs with high temperature responsivity or to create LPG-based loss filters that are widely tuneable, a number of techniques have been reported, including the use of fibres of different core-composition [73] and multiple geometries layers [74], as well as the use of polymer coatings around the device [75]. Another technique for enhancing the temperature responsivity is based on surrounding the LPG with a material of large thermo-optic coefficient, resulting in the LPG responding to both the changes to temperature and the temperature-induced SRI change.

Furthermore, a tuneable loss filter has been demonstrated using LPGs coated initially with 15nm thick titanium, followed by a second-layer coating of 300nm thick copper [32] or platinum [76]. Passing controlled-electric current into a heat-dissipating resistive-coating led to the control of the tuneable loss wavelength of the grating. The deposition of the initial titanium layer serves to enhance adhesion, but was found to introduce a slight wavelength shift and also a reduction in cladding mode-coupling loss. The copper-coated LPG exhibited a 4nm wavelength shift for electrical power of 0.5W [32], while the platinum-coated LPG offered 11nm shift for 0.67W.

Whilst both LPG-based temperature-sensor and tuneable loss filters require cladding modes of highest responsivity, other applications such as gain flattening require the exact opposite, i.e., they require LPG modes to have the lowest possible temperature responsivity. The

responsivity can be very critical since a slight shift of the LPG modes can lead to a significant fluctuation in the flattened gain spectrum. To reduce LPG temperature responsivity, a number of approaches have been demonstrated including the recoating of the LPG with a material having a negative thermo-optic coefficient. A method involving the mounting of an LPG on a bend-inducing material been shown to permit the temperature responsivity to be reduced to 0.07nm/100°C [77]. The bending is normally induced through the expansion/compression of the material with temperature increase/decrease respectively. The bending-induced shift of the cladding mode is almost equal and opposite that induced by temperature.

Further solutions to the responsivity problem have been proposed, based on suitable fibre design or fibre composition, to reduce this temperature responsivity. Judkins et al. [78] proposed to tailor the fibre refractive index profile to carefully balance these responsivity effects. Wavelength temperature dependence of LPGs realized in such a fibre, was reported to be ~-4.5 pm/°C.

Further applications of LPG focused on the measurement of transverse load [79]. This applied transverse load induces linear birefringence in the optical fibre, with the result that each attenuation band is split into two, and the wavelength separation of the emerging bands has been shown to increase with applied load. Bending has also indicated similar band-splitting characteristics. In particular, the splitting of the LPG attenuation bands has been observed in B\Ge co-doped photosensitive fibre that is subjected to bending [34].

LPGs are not only responsive to strain and temperature [73] or bending [34] but also to the refractive index of the surrounding medium. This responsivity arises from the dependence of the effective refractive indices of the cladding modes on the index of the medium surrounding the cladding. The highest responsivity of LPG is shown by the higher resonance order cladding modes, and for index measurement the highest responsivity occurs at refractive indices approaching that of the cladding [80].

SFBG is another type of grating that is produced to offer the advantages of both FBGs and LPGs at the same time [81]. Applications of SFBG have been demonstrated in the areas of sensing [81] and telecommunications [82].

2.3 Photosensitivity

The fibre photosensitivity is a measure of the degree of change in the properties of fibre when induced with UV light. The photosensitivity generally manifests itself in the form of light-induced refractive index changes in the fibre core, hence producing an FBG. Photosensitivity of germano-silicate fibres was first reported in 1978 by Hill et al [11]. Using UV light from Argon ion laser with a wavelength of 488nm they observed that reflectivity of light coupled into the fibre under certain condition increased with time. Lam and Garside [14], after a detailed study, reported that it is more efficient to use UV light with half of the wavelength – that is, at 244nm to induce a grating.

Various means are now adopted to increase the level of fibre photosensitivity including the increased concentration of germanium in the core [83], post fibre-fabrication photosensitization, using processes such as loading with high pressure hydrogen (H_2) at both low [84] and high [85] temperatures, exposure to high-intensity ArF laser light [86], inducement of axial strain [87], and the co-doping using suitable elements [88]

The processes involved in refractive index change within fibre core are still not fully understood. Initially this photosensitive effect was thought to be limited to germano-silicate fibres. The phenomenon is not restricted to germanium-doped silica materials because several other dopants in silica fibre result in photosensitive effects. Materials such as As_2S_3, Ce^{3+}, Eu^{2+}:Al_2O_3, B/GeO_2, and AL_2O_3 doped with B_2O_3, have all demonstrated some degree of photosensitivity [89].

There is no agreed theory that models the process of photosensitivity in optical fibres. This subsequently led to the proposal of two main theories on the photosensitivity of optical fibres; the colour-centre model [90], and the glass densification model [91]. Both models were based on the photo-ionisation of GeO defects. In particular, Hand and Russell [90] connects the induced refractive index change to the photo-ionisation of GeO defect, which is associated with an absorption band at 242nm. They suggest that UV light incident on the glass photo-ionises some defects, this creates a GeE' centre ensuing the entrapment of released electron into the site. When a fibre is illuminated with UV light many such absorptions take place at different defect sites leading to changes in the refractive index as expressed by Kramers-Kronig relation [90,92,93].

Transmission Electron Microscopy (TEM)-based evidence of glass densification induced by the grating-inscription in germano-silicate fibre was reported by Cordier [94]. However, it was Bernardin and Lawandy [91] who suggested that the densification is due to the collapse of the high-order ring structure into the one that comprise 2-3 rings. Nevertheless, this mechanism has not been reported in photosensitive fibres.

The colour-centre model suggests that because electrons released from bleachable defects are free to move through the glass and can be re-trapped at other defects sites, they can lead to the formation of new defects which are more polarizable than the bleachable defects [90]. The refractive index change, which is associated with photosensitivity, is linked to the level of absorption in the processes. An argument in support of the colour-centre theory was presented by Atkins et al [95], who used thermal reversibility of the grating inscription process to make a case for the model.

2.4 Conclusion

A general overview of the fibre grating technology has been presented in this chapter. In the later chapters a more focused but brief review is presented prior to discussion on individual topics.

The review in this chapter started with the development of low loss fibre, followed by a discussion on the fabrication of the early gratings, the Hill gratings, the side-written Bragg gratings, the phase mask techniques, and alternatives.

Further discussion focused on the various types of FBGs, their fabrication, optimisation, photosensitivity, and gratings-application in the areas of sensing and telecommunications. Other types of gratings such as the LPGs and the SFBGs are discussed. The literature in the area has been briefly appraised in both production and applications. The literature surveyed is intended to bring about focus on the areas of both design and application. It should be pointed out that the literature survey is by no means exhaustive considering the fact that fabrication, optimisation, applications and interrogation of fibre gratings are vast areas and cannot be fully covered in a single thesis. It is hoped that the literature discussed will prepare the reader on what to expect in the later chapters of this thesis.

2.5 Reference:

2. S.E. Miller, and L.C. Tillotson, "Optical transmission research," *Appl. Opt.*, vol. 5, pp. 1538 -1549, Oct 1966.
3. K.C. Kao, and G.A. Hockam, "Dielectric-fibre surface waveguides for optical frequencies," *Proc. IEE*, vol. 113, no. 7, pp. 1151-1158, July 1966.
4. F.P. Kapron, D.B. Keck, and R.D. Maurer, "Radiation losses in glass optical waveguides," Appl. *Phys. Lett.*, vol. 17, no. 10, pp. 423-425, 1970.
5. D.B. Keck, P.C. Schultz, and F. Zimar, "Attenuation in glass optical waveguides," *Appl. Phys. Letts.*, vol. 21, pp. 215-217, Feb 1972.
6. D.B. Keck, R.D. Maurer, and P.C. Schultz, "On the ultimate lower limit of attenuation in glass optical waveguides," *Appl. Phys. Letts.*, vol. 22, no. 7, pp. 307-309, Apr 1973.
7. M. Horiguchi, "Spectral losses of low OH-content optical fibres," *Electron. Letts.*, vol. 12, pp. 310-312, June 1976.
8. T. Miya, Y. Terunuma, T. Hosaka, and T. Miyashita, "Ultimate low-loss single mode fibre at 1.55μm," *Electron. Lett.*, vol. 15, no. 4, pp. 106-108, 1979.
9. A. Ghatak, and K. Thyagarajan, "Introduction to fibre optics," Cambridge University Press, pp. 39-40, 1998.
10. R.J. Mears, L. Reekie, I.M. Jauncey, and D.N. Payne "Low-noise erbium-doped fibre amplifier operating at 1.54-mu-m," *Electron. Lett.*, vol. 23, no. 19, pp. 1026-1028, Sept 1987.
11. K.O. Hill, Y. Fujii, D.C. Johnson, and B.S. Kawasaki, "Photosensitivity in optical fibre waveguides: Application to reflection filter fabrication," *Appl. Phys. Lett.*, vol. 32, no. 10, pp. 647-649, 1978.
12. B.S. Kawasaki, K.O. Hill, D.C. Johnson, and Y. Fujii, "Narrow-band Bragg reflectors in optical fibres," *Opt. Lett.*, vol. 3, pp. 66-68, 1978.
13. G. Meltz, W.M. Morey, and W.H. Glenn, "Formation of Bragg gratings in optical fibres by a transverse holographic method," *Opt. Lett.*, vol. 14, no. 15, pp. 823-825, 1989.
14. D.K.W. Lam, and B.K. Garside, "Characterisation of single mode optical fibre filters," *Appl. Opt.*, vol. 20. no. 3, pp. 440-445, 1981.
15. R. Kashyap, J.R. Armitage, R. Wyatt, S.T. Davey, and D.L. Williams, "All-fibre narrowband reflection gratings at 1500nm,", *Electron. Lett.*, vol. 26, no. 11, pp. 730-732, 1990.
16. R. Kashyap, J.R. Armtiage, R.J. Campbell, D.L. Williams, G.D. Maxwell, B.J. Ainslie, and C.A. Millar, "Light-sensitive optical fibres and planar waveguides," *BT Technol. Jn.*, vol. 11, no. 2, pp.150-158, 1994.
17. Q. Zhang, D.A. Brown, L. Reinhart, and T.F. Morse, "Simple prism-based scheme for fabricating Bragg gratings in optical fibres," *Opt. Lett.*, vol. 19, no. 23, pp. 2030-2032, 1994.
18. K.O. Hill, F. Bilodeau, B. Malo, D.C. Johnson, and J. Albert, "Bragg gratings fabricated in monomode photosensitive optical fibre by UV exposure through a phase mask," *Appl. Phys. Lett.*, vol. 62, no. 10, pp. 1035-1037, 1993.
19. W.W. Morey , G. Meltz, and W.H. Glenn, "Bragg-grating temperature and strain sensors," *Springer Proc. Phys. (Optical Fibre Sensors)*, vol. 44, pp. 526-531, 1989.
20. J.D. Prohaska, and R.A. Lieberman, "A tuneable matched fibre gratings filter for chemical detection," Optical Fibre Sensors Conference, vol. 10, 1997, *OSA Technical Digest Series* (Optical Society of America, Washington, DC, 1997), PD1.

21. X. Shu, and D.X. Huang, "Highly sensitive chemical sensor based on the measurement of the separation of dual resonant peaks in a 100-mu m-period fibre grating," *Optics Comms*, vol. 171, no. 1-3, pp. 65-69, Nov 1999.
22. F. Zhao, K. Sayano, H.E. Miller, and N. Karvolac, "Subpicometer accuracy laser wavelength sensor using multiplexed Bragg gratings," *IEEE Photon. Technol. Lett.*, vol. 9, pp. 1493-1495, 1997.
23. A.M. Vengsarkar, J.A. Greene, B.R. Fogg, and K.A. Murphy, "Spatially weighted, grating-based, two-mode, elliptical-core optical fibre vibration sensors," *Opt. Lett.*, vol. 16, pp. 1707-1709, 1991.
24. W. Jin, Y. Zhou, P.K.C. Chan, and H.G. Xu, "A fibre-optic grating sensor for the study of flow-induced vibrations," *Sensors and Actuators A-Physical*, vol. 79, no.1, pp. 36-45, Jan 2000.
25. T.A. Berkoff, and A.D. Kersey, "Experimental demonstration of a fibre Bragg grating accelerometer," *IEEE Photon. Technol. Lett.*, vol. 8, pp. 1677-1679, 1996.
26. Y.J. Rao. "Recent progress in applications of in-fibre Bragg grating sensors," *Opt. Laser Eng.*, vol. 31, no. 4, pp. 297-324, Apr 1999.
27. N.E. Fisher, D.J. Webb, C.N. Pannell, D.A. Jackson, L.R. Gavrilov, J.W. Hand, L. Zhang, and I. Bennion, "Ultrasonic field and temperature sensor based on short in-fibre Bragg gratings," *Electron. Lett.*, vol. 34, pp. 1139-1140, 1998.
28. M.G. Xu, L. Reekie, Y.T. Chow, and J.P. Dakin, "Optical in-fibre grating high pressure sensor," *Electron. Lett.*, vol. 29, pp. 398-399, 1993.
29. J. Lim, Q.P. Yang, B.E. Jones, and P.R. Jackson, "DP flow sensor using optical fibre Bragg grating," *Sensors and Actuators A-Physical*, vol. 92, no. 1-3, pp. 102-108, Aug 2001.
30. Y.Q. Liu, Z.Y. Guo, Y. Zhang, K.S. Chiang, and X.Y. Dong, "Simultaneous pressure and temperature measurement with polymer-coated fibre Bragg grating," *Electron. Lett.*, vol. 36, no. 6, pp. 564-566, Mar 2000.
31. P.M. Cavaleiro, F.M. Araujo, and A.B. Lobo Ribeiro, "Metal-coated fibre Bragg grating sensor for electric current metering," *Electron. Lett.*, vol. 34, pp. 1133-1135, 1998.
32. O. Duhem, A. DaCosta, J.F. Henninot, and M. Douay, "Long period copper-coated grating as an electrically tuneable wavelength-selective filter," *Electron. Lett.*, vol. 35, no.12, pp. 1014-1016, Jun 1999.
33. Y.J. Rao, D.A. Jackson, D.J. Webb, L. Zhang, and I. Bennion, "In-fibre Bragg grating flow-directed thermodilution catheter for cardiac monitoring," *Optical Fibre Sensors Conference*, vol. 10, 1997, OSA Technical Digest Series (Optical Society of America, Washington, DC, 1997), pp. 354-357.
34. Y. Liu, L. Zhang, J.A.R. Williams, and I. Bennion, "Optical bend sensor based on measurements of resonance mode splitting, of long-period, fibre grating," *IEEE Photon. Technol. Letts*, vol. 12, no. 5, pp. 531-533, 2000.
35. L. Dong, J.L. Archambault, L. Reekie, P.S.J. Russell, and D.N. Payne, "Single-pulse bragg gratings written during fibre drawing," *Electron. Letts*, vol. 29, no.17, pp. 1577-1578, Aug 1993
36. C.G. Askins, M.A. Putnam, G.M. Williams, and E.J. Friebele, "Stepped-wavelength optical-fibre Bragg grating arrays fabricated in-line on a draw tower," *Opt. Letts.*, vol. 19, no. 2, pp. 147-149, Jan 1994.
37. E.J. Friebele, C.G. Askins, M.A. Putnam, A.A. Fosha, Jr., J. Florio, Jr., R.P. Donti, and R.G. Blosser, "Distributed strain sensing with fibre Bragg grating arrays embedded in CTRM composites," *Electron. Lett.*, vol. 30, pp. 1783-1785, 1994.

38. S.E. Kanellopoulos, V.A. Handerek, and A.J. Rogers, "Simultaneous strain and temperature sensing with photogenerated in-fibre gratings," *Opt. Lett.*, vol. 20, pp. 333-335, 1995.
39. M.G. Xu, J-L. Archambault, L. Reekie, and J.P. Dakin, "Discrimination between strain and temperature effects using dual-wavelength fibre grating sensors," *Electron. Lett.*, vol. 30, pp. 1085-1087, 1994.
40. F.M. Haran, J.K. Rew, and P.D. Foote, "A strain-isolated fibre Bragg grating sensor for temperature compensation of fibre Bragg grating strain sensors," *Meas. Sci. Technol.*, vol. 9, pp. 1163-1166, 1998.
41. M.G. Xu, L. Dong, L. Reekie, J.A. Tucknott, and J.L. Cruz, "Temperature-independent strain sensor using a chirped Bragg grating in a tapered optical fibre," *Electron. Lett.*, vol. 31, pp. 823-825, 1995.
42. E.M. Dianov, K.M. Golant, R.R. Khrapko, and A.L. Tomashuk, "Nitrogen doped silica core fibres: A new type of radiation-resistant fibre," *Electron. Lett.*, vol. 31, pp. 1490-1491, 1995.
43. S.W. James, R. Tatam, A. Twin, M. Morgan, and P. Noonan, "Operation of fibre gratings at cryogenic temperatures," *Photonex2001*, In-fibre FBGs and Special fibres, IOP, Conventry, UK, Oct 2001.
44. R. Kashyap, I.R. Armitage, R. Wyatt, S.T. Davey, and D. L.Williams, "All-fibre narrow-bandwidth relefection gratings at 1500nm," *Electron. Lett.*, vol. 26, pp. 730-732, 1990.
45. S.V. Chernikov, R. Kashyap, P.F. McKee, and J.R. Taylor, "Dual frequency all fibre grating laser source," *Electron. Lett.*, vol. 29, pp. 1089-1091, 1993.
46. J-L. Archambault, and S.G. Grubb, "Fibre gratings in lasers and amplifiers," *Jn. Lightwave. Technol.*, vol. 15, pp. 1378-1390, 1997.
47. S.Y. Set, M. Ibsen, C.S. Goh, and K. Kikuchi, "A simple broad-range tuning of DFB laser," *Proc. 27th Eur. Conf. On Opt. Comm.* (ECOC'01), Amsterdam, pp. 200-201, 2001.
48. R. Kashyap, R. Wyatt, and R.J. Campbell, "Wide-band gain flattened erbium fibre amplifier using a photosensitive fibre blazed grating," *Electron. Lett.*, vol. 29, no. 2, pp. 154-156, Jan 1993.
49. E. Delevaque, T. Georges, B. Landousies, and E. Taufflieb, "Multichannel equalised and stabilised gain amplifier for WDM transmissions," *Electron. Lett.*, vol. 31, no. 25, pp. 2149-2150, Dec 1995.
50. M. Rochette, M. Guy, S. LaRochelle, J. Lauzon, and F. Trepanier, "Gain equalization of EDFA's with Bragg gratings," *IEEE Photon. Technol. Lett*, vol. 11, no. 5, pp. 536-538, May 1999.
51. D. Garthe, G. Milner, and Y. Cai, "System performance of broadband dispersion compensating gratings," *Electron. Lett.*, vol. 34, no. 6, pp. 582-583, Mar 1998.
52. H. Chotard, Y. Painchaud, A. Mailloux, M. Morin, F. Trepanier, and M. Guy, "Group delay ripple of cascaded Bragg grating gain flattening filters," *IEEE Photon. Technol. Lett.*, vol. 14, no. 8, pp.1130-1132, Aug 2002.
53. T.J. Cullen, H.N. Rourke, C.P. Chew, S.R. Baker, T. Bricheno, K.C. Byron, and A. Fielding, "Compact all-fibre wavelength drop and insert filter," *Electron. Lett.*, vol. 31, pp. 2160-2162, 1994.
54. F. Bakhti, P. Sansonetti, C. Sinet, L. Gasca, L. Martineau, S. Lacroix, X. Daxhelet, and F. Gonthier, "Optical add/drop multiplexer based on UV-written Bragg grating in a fused 100% coupler," *Electron. Lett.*, vol. 33, pp. 803-804, 1997.

55. L.G. Cohen, and C. Lin, "Pulse delay measurements in the zero material dispersion wavelength region for optical fibres," *Appl. Opt.*, vol.16, pp. 3136-3139, Dec 1977.
56. J.A.R. Williams, L.A. Everall, I. Bennion, and N.J. Doran, "Chirped fibre Bragg gratings for dispersion slope compensation," *IEEE Photon. Technol. Lett.*, vol. 8, no. 9, pp. 1187-1189, 1996.
57. F. Ouelette, "All-fibre filter for efficient dispersion compensation," *Opt. Lett.*, vol. 16, pp. 303-305, 1991.
58. J.A.R. Williams, I. Bennion, K. Sugden, and N.J. Doran, "Fibre dispersion compensation using a chirped in-fibre Bragg grating," *Electron. Lett.*, vol. 30, pp. 985-986, 1994.
59. K.O. Hill, F. Bilodeau, B. Malo, T. Kitagawa, S. Theriault, D.C. Johnson, and J. Albert, "Chirped in-fibre Bragg gratings for compensation of optical fibre dispersion," *Opt. Lett.*, vol. 19, pp. 1314-1316, 1994.
60. B.J. Eggleton, T. Stephens, P.A. Krug, G. Dhosi, Z. Brodzeli, and F. Ouelette, "Dispersion compensation using a fibre grating in transmission," *Electron. Lett.*, vol. 32, pp. 1610-1611, 1996.
61. J.A.R. Williams, I. Bennion, and L. Zhang, "The compression of optical pulses using self-phase-modulation and linearly chirped Bragg gratings in fibres," *IEEE Photon. Technol. Lett.*, vol. 7, pp. 491-493, 1995.
62. D. Pastor, J. Capmany, D. Ortega, V. Tatay, and J. Marti, "Design of apodised linearly chirped fibre gratings for disperison compensation," *Jn. Lightwave. Technol.*, vol. 14, pp. 2581-2588, 1996.
63. M. Durkin, M. Ibsen, M.J. Cole, and R.I. Laming, "1m long continuously-written fibre Bragg gratings for combined second- and third-order dispersion compensation," *Electron. Lett.*, vol. 33, pp. 1891-1893, 1997.
64. A.J. Cooper, "Fibre-radio for the provision of cordless/mobile telephony services in the access network," *Electron. Lett.*, vol. 26, pp. 2054-2056, 1990.
65. C. Lim, A. Nirmalathas, D. Novak, R.S. Tucker, and R.B. Waterhouse, "Techniques for increasing optical spectral efficiency in millimetre-wave WDM fibre-radio," *Electron. Lett.*, vol. 37, pp. 1043-1045, Aug 2001.
66. D. Wake, "Trends and prospects for Radio on fibre picocells," paper W3-1, MWP2002 *The international topical meeting on microwave photonics*, Japan, pp. 21-21, Nov 2002.
67. Y. Kondo, K. Nouchi, T. Mitsuyu, M. Watanabe, P.G. Kazansky, and K. Hirao, "Fabrication of long-period fibre gratings by focused irradiation of infrared femtosecond laser pulses," *Opt. Lett.*, vol. 24, no. 10, pp 646-648, May 1999.
68. D.D. Davis, T.K. Gaylord, E.N. Glytsis, and S.C. Mettler, "CO_2 laser-induced long-period fibre gratings: spectral characteristics, cladding modes and polarisation independence," *Electron. Lett.*, vol. 34, no.14, pp. 1416-1417, 1998.
69. G. Humbert, and A. Malki, "Annealing time dependence at very high temperature of electric arc-induced long-period fibre gratings," *Electron. Lett.*, vol. 38, no.10, pp. 449-450, May 2002.
70. C.Y. Lin, G.W. Chern, and L.A. Wang, "Periodical corrugated structure for forming sampled fibre Bragg grating and long-period fibre grating with tuneable coupling strength," *Jn. Lightwave Technol.*, vol. 19, no. 8, pp. 1212-1220, Aug 2001.
71. S.A. Vasiliev, E.M. Dianov, D. Varelas, H.G. Limberger, and R.P. Salathe, "Postfabrication resonance peak positioning of long-period cladding-mode-coupled gratings," *Opt. Letts.*, vol. 21 no. 22, pp. 1830-1832, Nov 1996.

72. K.M. Zhou, H.T. Liu, and X.W. Hu, "Tuning the resonant wavelength of long period fibre gratings by etching the fibre's cladding," *Opt. Comms*, vol. 197 no. 4-6, pp. 295-299, Oct 2001.
73. X. Shu, L. Zhang, and I. Bennion, "Sensitivity characteristics of long-period fibre gratings," *Jn. Lightwave Technol.*, vol. 20, no. 2, pp. 255-266, 2002.
74. S. Yin, K-W. Chung, and X. Zhu, "A highly sensitive long period grating based tuneable filter using a unique double-cladding layer structure," *Opt. Comms.*, vol. 188, no. 5-6, pp. 301-305, 2001.
75. A.A. Abramov, A. Hale, R.S. Windeler, and T.A. Strasser, "Widely tuneable long-period fibre gratings," *Electron. Lett.*, vol. 35, no. 1, pp. 81-82, 1999.
76. D.M. Costantini, C.A.P. Muller, S.A. Vasiliev, H.G. Limberger, and R.P. Salathe, "Tuneable loss filter based on metal-coated long-period fibre grating," *IEEE Photon Technol. Letts*, vol. 11, no. 11, pp. 1458-1460, Nov 1999.
77. M.N. Ng, Z.H. Chen, and K.S. Chiang, "Temperature compensation of long-period fibre grating for refractive-index sensing with bending effect" *IEEE Photon. Technol. Lett.* vol. 14, no. 3, pp. 361-362, Mar 2002.
78. J.B. Judkins, J.R. Pedrazzani, D.J. DiGiovanni, and A. Vengsarkar, "Temperature-insensitive long-period gratings," *Proc. OFC'96*, Post-deadline paper PD1, 1996.
79. Y. Liu, L. Zhang, and I. Bennion, "Fibre optic load sensors with high transverse strain sensitivity based on long-period gratings in B/Ge co-doped fibre," *Electron. Lett.*, vol. 35, no. 8, pp. 661-663, Apr 1999.
80. H.J. Patrick, A.D. Kersey, and F. Bucholtz, "Analysis of the response of Long-period fibre gratings to the external index of refraction," *Jn. Lightwave Technol.*, vol. 16, no. 9, pp. 1606-1612, 1998.
81. B.O. Guan, H.W. Yaw, X. Tao, and X. Dong, "Simultaneous strain and temperature measurement using a superstructured fibre Bragg grating," *IEEE Photon. Technol. Lett.*, vol. 6, no. 12, pp. 675–677, Jun 2000.
82. P.C. Teh, P. Petropoulos, M. Ibsen, and D.J. Richardson, "A comparative study of the performance of seven- and 63-chip optical code-division multiple-access encoders and decoders based on superstructured fibre Bragg gratings," *Jn. Lightwave Technol.*, vol. 19, no. 9, pp. 1352-1365, Sept 2001.
83. D.L. Williams, B.J. Ainslie, J.R. Armitage, and R. Kashyap, "Enhanced photosensitivity in germanium-doped silica fibres for future optical networks," Proc. 14th *Eur. Conf. Opt. Comms.*, ECOC'92, Berlin, Germany, Paper, WeB9-5, 1992.
84. P.J. Lemaire, R.M. Atkins, V. Mizrahi, and W.A. Reed, "High pressure H_2 loading as a technique for achieving ultrahigh UV photosensitivity in GeO_2 doped optical fibres," *Electron. Letts.*, vol. 29, pp. 1191-1193, 1993.
85. B.A.L Gwandu, W. Zhang, X. Shu, L. Zhang, D.J. Webb, and I. Bennion, "Suppression of cladding mode coupling loss in Bragg grating using standard single-mode fibre," *Proc. IEEE/LEOS Conf. 2002*, Glasgow, Paper ThU3, pp. 815-816, Nov 2002.
86. J. Albert, B. Malo, K.O. Hill, F. Bilodeau, D.C. Johnson, and S. Theriaault, "Comparison of one-photon and two-photon effects in the photosensitivity of germanium-doped silica optical fibre exposed to intense ArF excimer laser pulses," *Appl. Phys. Letts.*, vol. 67, pp. 3529-3531, 1995.
87. E. Salik, D.S. Starodubov, and J. Feinberg, "Increase of photosensitivity in Ge-doped fibres under strain," *Opt. Lett.*, vol. 25, no.16, pp. 1147-1149, 2000.

88. L. Dong, J.L. Cruz, J.A. Tucknott, L. Reekie, and D.N. Payne, "Strong photosensitive gratings in tin-doped phosphosilicate optical fibres," *Opt. Lett.*, vol. 20, no. 19, pp. 1982-1984, Oct 1995.

89. M. Douay, W.X. Xie, T. Taunay, P. Berniage, P. Niay, P. Cordier, B. Poumellec, L. Dong, J.F. Bayon, H. Poignant, and E. Delevaque, "Densification involved in the UV-based photosensitivity of silica glasses and optical fibres," *Jn. Lightwave Technol.*, vol. 15, pp. 1329-1342, Aug 1997.

90. D.P. Hand, and P. Russell, "Photoinduced refractive-index changes in germanosilicate fibres," *Opt. Lett.*, vol. 15, pp. 102-104, 1990.

91. J.P. Bernardin, and N.M. Lawandy, "Dynamics of the formation of Bragg gratings in germanosilicate optical fibres," *Opt. Comms.*, vol. 79, pp. 194-199, 1990.

92. R.M. Atkins, and V. Mizrahi, "Observations of changes in UV absorption bands of singlemode germanosilicate core optical fibres on writing and thermally erasing refractive index gratings," *Electron. Lett.*, vol. 28, pp. 1743-1744, 1992.

93. V. Mizrahi, S. LaRochelle, G.I. Stegeman, and J.E. Sipe, "Physics of photosensitive-grating formation in optical fibres," *Phys. Rev. A.*, vol. 43, pp. 433-438, 1991.

94. P. Cordier, S. Dupont, M. Douay, G. Martinelli, P. Bernage, P. Niay, J. F. Bayon, and L. Dong, "Evidence by transmission electron microscopy of densification associated to Bragg grating photoimprinting in germanosilicate optical fibres," *Appl. Phys. Lett.*, vol. 70, pp. 1204-1206, 1997.

95. R.M. Atkins, V. Mizrahi, and T. Erdogan, "248 nm induced vacuum UV spectral changes in optical fibre perform cores: support for a color-centre model of photosensitivity," *Electron. Lett.*, vol. 29, pp. 385-387, 1993.

3 Fibre grating properties

3.1 Introduction

The characteristics of uniform-period FBGs such as their reflectivity, transmitivity, sidelobe spectral positions, and linewidth are discussed in Section 3.2.1 of this chapter. Coupled mode theory is used for the grating analysis. Modelling of Bragg gratings based on the use of Matrix transform is also presented. The modelling technique employed is applicable to a variety of Bragg gratings that are mainly distinguished by their index modulation. Typical Bragg gratings that are investigated include uniform-period FBGs, apodised FBGs, chirped FBGs and SFBGs. In Section 3.2.2 the coupling characteristics of LPGs are discussed.

The reader should note that the theoretical work presented in this thesis has been extracted from the published literature, and where necessary a reference to such literature is given. There is no claim to the originally in respect of any of the equations or theory used and the theory is only used to support the analysis presented in the thesis.

3.2 Coupled mode theory

When light is coupled into a standard optical fibre a single guided mode is transmitted from one end of the fibre to the other through the core. This condition remains unless the normalised frequency value for a single-mode condition is exceeded[3] or the fibre properties are changed. By inscribing a fibre grating within the core, light will be coupled from the guided mode to either a counter-propagating mode within the core (in the case of FBG), or to the co-directional modes within the cladding (in the case of LPG). Coupled mode theory (CMT) provides a description of the interaction between the guided light waves and the grating within the fibre. It is a widely used modelling tool for fibre gratings [96,97]. With the transform matrix [98] CMT can provide a technique for modelling the response of long and complex structure gratings. Other modelling techniques include the integration of the Ricatti differential equation [99] and inverse Fourier transform [100].

[3] To maintained single mode condition the normalized frequency cutoff 'V' in a single mode fibre should not exceed 2.405. Eqn. (3.12) defines the normalized frequency.

CMT assumed a distributed feedback structure [101,102]. Also, the contributions of longitudinal coupling are generally ignored by CMT because they are 1-2 orders of magnitude smaller than the transverse field components [103]. Furthermore CMT considers period sampling whilst ignoring the non-uniformity effects such as birefringence, phase shifts and chirps. The CMT assumed normal incidence at the input end and also ignores the effects of reflections at the boundaries [105]. All theses assumptions need to be taken into account when analysing the CMT-based simulation results of grating characteristics.

3.2.1 Coupled mode equations for contra-directional coupling: The FBG

A FBG couples a forward propagating core-mode to a backward propagating core-mode. It is a band-rejection filter, passing all wavelengths that are not in resonance with the grating and reflecting wavelengths that satisfies the Bragg condition. A typical uniform period FBG structure is shown in Fig. 3.1. The interactions of light with the index modulations of the grating and spectral response of the grating is shown with input, transmitted, and reflected components.

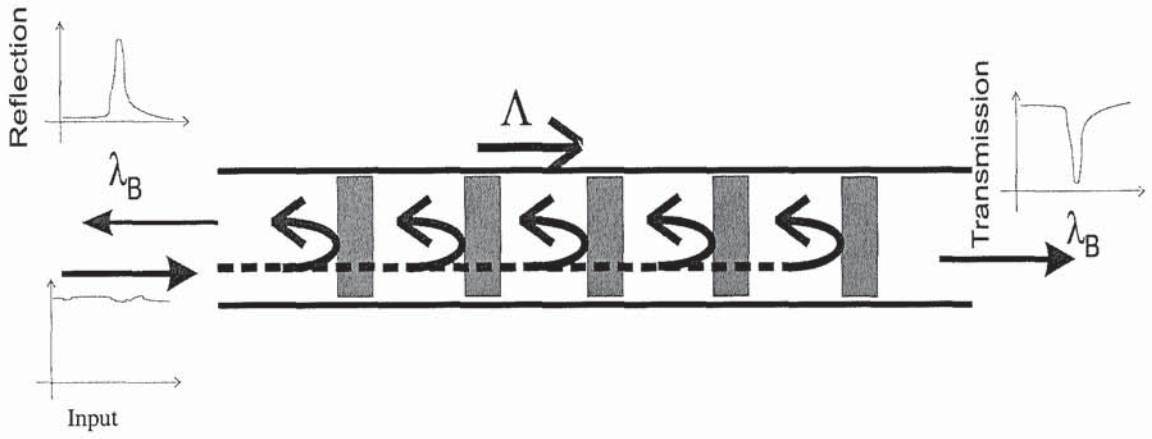

Fig. 3.1: Uniform period FBG and its responses, λ_B is the Bragg Wavelength

Coupling occurs in FBGs between counter-propagating modes and also between co-propagating modes (if the FBG is of very high reflectivity). Coupling between co-propagating modes leads to short wavelength loss in FBGs, as energy is coupled from the

core mode to the cladding modes, at wavelengths shorter than that of the main grating peak. Coupling between counter-propagating modes occurs between two core modes, and results in the reflection of light at the Bragg wavelength. The propagation of the two counter-propagating core modes in a perturbed fibre (say with FBG) can be represented by electromagnetic coupled mode equations given by

$$\begin{cases} \dfrac{dA_{01}^{co}(z)}{dz} = j\kappa_0 e^{-j2\delta_{01}z} B_{01}^{co}(z) \\ \dfrac{dB_{01}^{co}(z)}{dz} = -j\kappa_0 e^{j2\delta_{01}z} A_{01}^{co}(z) \end{cases} \tag{3.1}$$

where $A_{01}^{co}(z)$ and $B_{01}^{co}(z)$ represent the forward and the backward propagating core modes respectively. $\kappa_0(z)$ is the coupling coefficient, which is a slowly varying function with respect to variable z, expressed as

$$\kappa_0(z) = \frac{\pi \Delta n(z)}{\lambda} C_{01}^{co} \tag{3.2}$$

Where C_{01}^{co} represents the core mode overlap factor, $\delta_{01}(z)$ is local detuning from the Bragg resonance expressed as [104]

$$\delta_{01}(z) = \beta_{01}^{co} - \frac{\pi}{\Lambda(z)} = 2\pi n_{01}^{co}\left[\frac{1}{\lambda} - \frac{1}{\lambda_0(z)}\right] \approx -\frac{2\pi n_{01}^{co}}{\lambda_0^{\,2}} \Delta\lambda(z) \tag{3.3}$$

Where for weakly guiding fibre β_{01}^{co} is the propagation constant for the core mode LP_{01}^{co}, $\Delta\lambda$ is the wavelength detuning, $\Delta\lambda = \lambda - \lambda_0(z)$. $\lambda_0(z)$ is the Bragg resonance of sub-grating and expressed as [105, 106,107].

$$\lambda_0(z) = 2n_{eff}(z)\Lambda(z) \tag{3.4}$$

By expressing the electric field of the propagating light in the form

$$E(z) = \left[A^{+}(z)e^{-j\delta_{01}(z)z}\right]e^{j\beta_{01}^{co}z} + \left[A^{-}(z)e^{j\delta_{01}(z)z}\right]e^{-j\beta_{01}^{co}z} \tag{3.5}$$

Where, $A^{+}(z)$ and $A^{-}(z)$ are the amplitudes of the forward and the backward propagating core modes with relative phase, then

$$\begin{cases} A_{01}^{co}(z) = A^{+}(z)e^{-j\delta_{01}(z)z} \\ B_{01}^{co}(z) = A^{-}(z)e^{j\delta_{01}(z)z} \end{cases} \tag{3.6}$$

Substituting eqn. (3.6) into eqn. (3.1), followed by differentiation and re-arrangement, eqn. (3.1) has been shown in [105,108] to lead to

$$\begin{cases} \dfrac{d^2A^{+}(z)}{dz^2} = -\left[{\delta_{01}}^2(z) - {\kappa_0}^2(z)\right]A^{+}(z) \\ \dfrac{d^2A^{-}(z)}{dz^2} = -\left[{\delta_{01}}^2(z) - {\kappa_0}^2(z)\right]A^{-}(z) \end{cases} \tag{3.7}$$

Suppose the FBG is broken into sections and the index modulation period in each section (sub-grating) is assumed to be uniform (with δ_0 and κ_0 constant). Using boundary condition $A^{+}(-L/2)=1$ and $A^{-}(L/2)=0$, on eqn. (3.7) and solving eqn. (3.7) directly, the forward and backward propagation amplitudes along the sub-grating length is obtained as eqn. (3.7) [104,105,106,107].

$$\begin{cases} A^{+}(z) = \dfrac{S\cosh[S(z-L/2)] + \mathbf{j}\delta_0 \sinh[S(z-L/2)]}{S\cosh(SL) - \mathbf{j}\Delta\beta\sinh(SL)} e^{-\mathrm{j}\delta_0(z+L/2)} \\ A^{-}(z) = \dfrac{-\mathbf{j}\kappa_0 \sinh[S(z-L/2)]}{S\cosh(SL) - \mathbf{j}\delta_0\sinh(SL)} e^{j\delta_0(z+L/2)} \end{cases} \tag{3.8}$$

$$\begin{cases} t_i(\lambda) = \dfrac{S}{S\cosh(SL_i) - \mathbf{j}\delta_0\sinh(SL_i)} \\ r_i(\lambda) = \dfrac{\mathbf{j}\kappa_0\sinh(SL_i)}{S\cosh(SL_i) - \mathbf{j}\delta_0\sinh(SL_i)} \end{cases} \tag{3.8a}$$

The strength varying behaviour of the forward and backward amplitudes, $\left|A^{+}(z)\right|^2$ and $\left|A^{-}(z)\right|^2$ along the fibre axis is shown in Fig. 3.2.

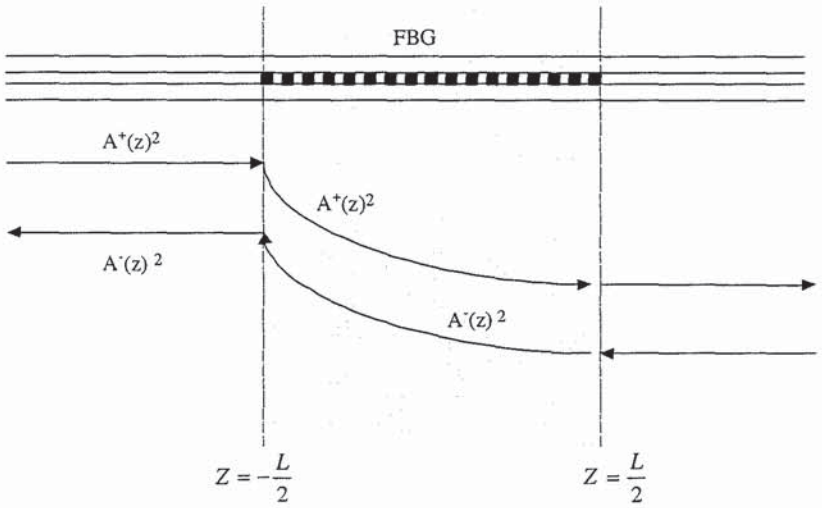

Fig. 3.2: The Index perturbation inside the fibre causes coupling between forward (A^+) and backward (A^-) propagating modes.

The variation in intensities of the modes during propagation through the fibre appears to be $\frac{d}{dz}\left[\left|A^+(z)\right|^2 - \left|A^-(z)\right|^2\right] \equiv 0$, which shows that the energy is conserved along the grating length. Both the Riccati analysis [109,110] and the analytical expression approaches have been shown to yield the FBG amplitude reflectance as [106,112]

$$\rho(-L/2) \equiv r(\lambda) = \frac{j\kappa_0 \tanh(SL)}{S - j\delta_0 \tanh(SL)} \tag{3.9}$$

Where, $r(\lambda)$ describes the amplitude reflectance of the entire grating. At Bragg resonance wavelength, $\delta_0 = 0$ and $S = \kappa_0 = \frac{\pi \Delta n}{\lambda_0} C_{01}^{co}$, eqn. (3.9) reduces to the power reflectance,

$$\left|r(\lambda_0)\right|^2 = \tanh^2\left(C_{01}^{co} \pi \Delta n L / \lambda_0\right) \tag{3.10}$$

Where, C_{01}^{co} is overlapping factor for the core mode LP_{01}^{co}, Δn is half of the index modulation depth, λ_0 is the grating resonance wavelength and L is the grating length.

Here, when mode fields interact coupling from one mode to the other modes results, and the extent of the overlap is determined by the mode field distribution. For a weakly guiding fibre, the eigen value equation governing this interaction for the guided core mode and cladding modes is given as [111].

$$\frac{J_l(u^i)}{u^i J_{l+1}(u^i)} - \frac{K_l(w^i)}{w^i K_{l+1}(w^i)} = 0 \tag{3.11}$$

Where, u^i and w^i (i=co, cl) are propagation parameters for core and cladding modes, respectively and $(u^i)^2 + (w^i)^2 = (V^i)^2$. $J_l(u^i)$, $K_l(w^i)$ are l-order Bessel functions and l-order modified Hankel function, V^i is normalized propagation frequency, defined as

$$\begin{cases} V^{co} = \dfrac{2\pi r_{co}}{\lambda}\sqrt{n_{co}^{\,2} - n_{cl_1}^{\,2}} \\ V^{cl_1} = \dfrac{2\pi r_{cl_1}}{\lambda}\sqrt{n_{cl_1}^{\,2} - n_{cl_2}^{\,2}} \\ V^{cl_2} = \dfrac{2\pi r_{cl_2}}{\lambda}\sqrt{n_{cl_2}^{\,2} - n_{surr}^{\,2}} \end{cases} \tag{3.12}$$

Where, n_{co}, n_{cl_1} n_{cl_2} and n_{surr} are the material indices of fibre core, inner cladding, outer cladding and the layer surrounding the outer cladding, respectively. V^{co} is the normalized frequency of the fibre core, also written as

$$V^{co} = \frac{2\pi r_{co}}{\lambda}\sqrt{n_{co}^{\,2} - n_{cl}^{\,2}} = \frac{2\pi r_{co}}{\lambda} \cdot NA \tag{3.13}$$

Where, r_{co} and r_{cl} are the respective core and cladding the radii of the fibre, V^{cl} is the normalized frequency of the fibre cladding and NA is the Numerical Aperture. The core mode overlap factor is given by [112]

$$C_{01}^{co} \approx 1 - \frac{1}{(V^{co})^2} \tag{3.14}$$

Clearly, the value of C_{01}^{co} (and hence the grating reflectivity $|r(\lambda_0)|$) can be changed by altering either the *core radius* or the *index difference* between the core and cladding materials. The eigen value equation (i.e. eqn. 3.11) assumed that modes are far from cut-off and the index difference between core and cladding is very small [113].

3.2.1.1 Material and effective mode index

For pure silica glass the material index n_i is approximated by the Sellmier equation [111]

$$n^i(\lambda) = \sqrt{1 + \sum_{j=1}^{3} \frac{A_j \lambda^2}{\lambda^2 - {\lambda_j}^2}} \tag{3.15}$$

where, λ_j is the resonance wavelength, A_j represent the amplitudes of the coefficient and (*i=co, cl*). This equation allows for evaluating material refractive index, by taking dispersion into account.

For the *l*-order mode, eqn. (3.11) has roots u_{lp}^i (p =1, 2, 3, ...), and every root corresponds to the mode LP_{lp}^i. But,

$$\left(u_{lp}^i\right)^2 + \left(w_{lp}^i\right)^2 = \left(V^i\right)^2 \tag{3.16}$$

In single mode fibre, eqn. (3.11) has only one root u_{01}^{co}, corresponding to the fundamental core mode LP_{01}^{co}.

The monomode fibres that are currently in use today can be approximated to have weakly guiding step-index profiles; the geometric-optics approximation to the eigen-value equation can then have the following form [111]

$$2\sqrt{\left(u_{lp}^i\right)^2 - l^2} - 2l\arccos\left(\frac{l}{u_{lp}^i}\right) - \left(p - \frac{3}{4}\right)2\pi = 2\arccos\left[\frac{\sqrt{\left(u_{lp}^i\right)^2 - l^2}}{V^i}\right] \tag{3.17}$$

where *i=co, cl* describes core mode and cladding modes. For LP_{01}^{co} core mode (*l*=0, *p*=1), eqn. (3.17) reduces to [104]

$$u_{01}^{co} = \arccos\left(\frac{u_{01}^{co}}{V^{co}}\right) + \left(\frac{1}{4}\right)\pi \tag{3.18}$$

Using the geometric optics approximation, the roots for the eigen-value equation u_{lp}^i (for *i=co, cl*) are derived from eigen-value eqn. (3.17) and the effective mode index , $n_{lp}^i(\lambda)$, for LP_{lp}^i modes is calculated using [111]

$$n_{lp}^i(\lambda) = [n^i(\lambda)]^2 - \left(\frac{\lambda u_{lp}^i}{2\pi r_i}\right)^2 \tag{3.19}$$

Where, $i = co, cl$ for the fibre core and cladding modes, respectively.

It should be stressed that eqn. (3.17) is very important in explaining the modal behaviour in optical fibres. The roots of this equation allows for the calculation of the effective refractive indices of the various modes. Once the effective refractive indices are calculated, various fibre modes can then be identified and the accuracy of such identification process is dependant of the approximations in the CMT. To identify a particular LPG cladding mode, dispersion curves are plotted and such curves do provide a well-reported and indeed generally accepted tool to guide users to identify modal position. It should be stressed that the curves provide only a guide, rather than accurate tool, for mode identification.

3.2.1.2 Grating sidelobes and linewidth

With the increase of the wavelength detuning $|\Delta\lambda|$, $\kappa_0^{\,2} - \delta_0^{\,2}$ decreases rapidly to zero and $\kappa_0^{\,2} - \delta_0^{\,2} < 0$, then effective detuning S goes to its imaginary region. In this case the new effective detuning W is define by

$$S = \mathbf{j}\sqrt{\delta_0^{\,2} - \kappa_0^{\,2}} = \mathbf{j}W \tag{3.20}$$

using identities sinh(**j**WL)=**j**sin(WL), cosh(**j**WL)=cos(WL), into eqn. (3.8a) leads to

$$\begin{cases} t_i(\lambda) = \dfrac{jW}{jW\cos(WL_i) + \delta_0 \sin(WL_i)} \\ r_i(\lambda) = \dfrac{-\kappa_0 \sin(WL_i)}{jW\cos(WL_i) + \delta_0 \sin(WL_i)} \end{cases} \tag{3.21}$$

Power reflectivity is therefore

$$|r_i(\lambda)|^2 = \begin{cases} \dfrac{\kappa_0^{\,2}\sinh^2(SL)}{S^2\cosh^2(SL) + \delta_0^{\,2}\sinh^2(SL)} & \left(\kappa_0^{\,2} - \delta_0^{\,2} \geq 0\right) \\ \dfrac{\kappa_0^{\,2}\sin^2(WL)}{W^2\cos^2(WL) + \delta_0^{\,2}\sin^2(WL)} & \left(\kappa_0^{\,2} - \delta_0^{\,2} < 0\right) \end{cases} \tag{3.22}$$

By plotting eqn. (3.22), the FBG reflection spectrum with clear sidelobes can be obtained. Fig. 4.2 in Section 4.3 will illustrate the typical spectral response that can be obtained.

The positions where $WL = N\pi$ (N = 1, 2, 3,...) indicate the spectral points of zero reflectivity on the longer wavelength side, and for (N = -1, -2,...) shows the zero reflectivity points on the shorter wavelength side of the Bragg peak.

The wavelength with of reflection is given as [106]

$$\lambda_N = \lambda_0 \pm \frac{\lambda_0^{\,2}}{2\pi n_{01}^{co} L}\sqrt{(\kappa L)^2 + (N\pi)^2} \tag{3.23}$$

The wavelength spacing between two symmetric zero points is obtained as

$$\Delta\lambda_{N,-N} = \frac{\lambda_0^{\,2}}{\pi n_{eff} L}\sqrt{(\kappa L)^2 + (N\pi)^2} \tag{3.24}$$

Where for convenience, n_{01}^{co} is normally used as an approximation of n_{eff}. n_{eff} is the effective index of the core.

For a strong grating, the spectral edges are steep slopes (i.e. vertically sharp) and the Full Width at Half Maximum (*FWHM*) is almost $\Delta\lambda_{1,-1}$, $FWHM \approx \frac{\lambda_0^{\,2}}{\pi n_{eff} L}\sqrt{(\kappa L)^2 + \pi^2}$. However, for a weaker grating, the spectral changes between the Bragg resonance and the first zero-reflection looks like a linear slope rather than steep vertical edge, thus $FWHM \approx \Delta\lambda_{1,-1}/2$. For the general case [114]

$$FWHM = \mu\frac{\lambda_0^{\,2}}{\pi n_{eff} L}\sqrt{(\kappa L)^2 + \pi^2} \tag{3.25}$$

Where, $0.5 < \mu < 1$ describes the grating strength. $\mu \approx 0.5$ for weaker grating while $\mu \approx 1$ for stronger gating. Clearly, longer grating length or weaker grating strength results into narrow linewidth.

3.2.1.3 Grating simulation using T-Matrix

T-matrix [115] is a well reported technique used to simulate fibre gratings, it is used, in this thesis, for simulation of Bragg gratings through which the grating characteristics can be analysed. Both the author built codes and Optiwave™ IFO that are used in this thesis employ CMT and T-matrix to evaluate grating characteristics. The Optiwave™ IFO is a black-box software that is said to rely on CMT and the T-matrix algorithm it therefore inherits all the limitations of both CMT and T-matrix [116].

The coupling coefficient $\kappa(z)$ can change with the grating length for non-uniform FBG structures [98]. For the purpose of simulation, the FBG can be viewed as a series of short length sections (called "finite elements" or sub-gratings). The length of each sub-grating is sufficiently short such that it can be viewed as a uniform structure. To calculate the spectral response of the whole grating structure with arbitrary boundary condition between the sub-gratings, the amplitudes of transmission, and reflection of the entire grating structure are obtained from eqn. (3.7) and written as [104,105]

$$\begin{bmatrix} A^{+}(z_i) \\ A^{-}(z_i) \end{bmatrix} = M_i \begin{bmatrix} A^{+}(z_0) \\ A^{-}(z_0) \end{bmatrix} \tag{3.26}$$

Where, $z_{i-1} \le z < z_i, z$ indicates the location of the centre of the sub-grating G_i within the overall grating structure $(i = 1,2,....N)$ and N is the number of sub-gratings or the sections of the grating. M_i is a matrix describing the sub-grating and expressed as [105,112]

$$M_i = \begin{bmatrix} 1/t_i^{*} & -(r_i/t_i)^{*} \\ -r_i/t_i & 1/t_i \end{bmatrix} \tag{3.27}$$

Where, the transmissivity (t_i) and reflectivity (r_i) are [106,112]

$$\begin{cases} t_i(\lambda) = \dfrac{S}{S\cosh(SL_i) - \mathbf{j}\delta_0 \sinh(SL_i)} \\ r_i(\lambda) = \dfrac{\mathbf{j}\kappa_0 \sinh(SL_i)}{S\cosh(SL_i) - \mathbf{j}\delta_0 \sinh(SL_i)} \end{cases} \tag{3.28}$$

If L is the length of the entire grating, $L_i = L/N$ is the length between the two sub-grating boundaries.

In general case of non-uniform grating, the average index, grating period, and the coupling strength are slowly varying along the grating axis. The Bragg resonance is therefore a function of the variable z_i the middle point of a finite sub-grating element that is short enough to be regarded as uniform structure. For a linearly chirped FBG, the Bragg wavelength of the *i-th* sub-grating G_i is

$$\lambda_i(z_i) = \lambda_0 + \frac{z_i}{L}\Delta\lambda \tag{3.29}$$

where $-L/2 \le z_i \le L/2$, λ_0 is the central wavelength of the chirped grating and $\Delta\lambda$ represent the chirp. The centre position of the grating G_i is given by

$$z_i = -\frac{L}{2} + \frac{L}{N}\left(i - \frac{1}{2}\right) \qquad (i = 1,2,3,...,N) \tag{3.30}$$

In this case, the simulation is based on solving eqn. (3.7) numerically. Alternatively, based on differentiation theory, any complex grating can be differentiated as a series of very short length uniform grating, expressed by eqn. (3.27). The entire grating structure is composed of all the differentiated gratings and the precision can be improved, as desired, by increasing the number (or reducing the size) of the finite elements used.

When a grating with $\Delta\lambda$ chirps and entire length L is segmented into N equal divisions, then, the grating length of every division is $L_i = L/N$ ($i = 1, 2, \ldots$), the matrix for the entire grating M can be obtained from repeated calculation of eqn. (3.26) for all sub-gratings and written as

$$M = \begin{bmatrix} M11 & M12 \\ M21 & M22 \end{bmatrix} = M_N M_{N-1} M_{N-1} \cdots M_1 \tag{3.31}$$

Considering the conventional boundaries condition as $A^+(-L_0/2) = 1$, $A^-(L_0/2) = 0$, t_i and r_i in eqn. (3.28) describe the amplitudes of transmittance (t) and reflectance (r) of the entire grating structure [117, 118].

$$\begin{cases} t = M11 - M12M21/M22 \\ r = -M21/M22 \end{cases} \tag{3.32}$$

In this point, the simulation of FBGs reduces to the calculation of the transform-matrix for entire grating structure.

The detuning and effective detuning of the sub-grating G_i are given as

$$\begin{cases} \delta_i(z_i) = 2\pi n_{eff}\left[\dfrac{1}{\lambda} - \dfrac{1}{\lambda_i(z_i)}\right] \\ S_i(z_i) = \sqrt{\kappa_0{}^2(z_i) - \delta_i{}^2(z_i)} \end{cases} \tag{3.33}$$

where $\kappa_0(z)$ is a slow varying function along the grating axis. The matrix M_i for every elementary grating is calculated by using eqns. (3.27) and (3.28). Substituting all M_i into eqn (3.31), the transmittance and reflectance for entire grating structure are in the form

$$r = -M21/M22$$

If there is no chirp in the grating period $\Delta\lambda = 0$, the chirped FBG becomes a grating of uniform period structure, as expressed in eqn. (3.29).

For case where there are no refractive index variations (i.e. no grating index fringes) in the fibre ($\kappa_0 = 0$), then, from eqn. (3.33) $S = j\delta_0$, substituting this into eqn. (3.28) leads to $r = 0$, $t = \exp(j\delta_0 L_i)$, and eqn. (3.27) reduces to

$$M_i = \begin{bmatrix} e^{j\delta_0 L_i} & 0 \\ 0 & e^{-j\delta_0 L_i} \end{bmatrix} \tag{3.34}$$

Matrix eqn. (3.34) describes the propagation of the light in fibre of length L_i without index perturbation where $2\delta_0 L_i$ is relative propagation phase. Compared to eqn. (3.34), the matrix for phase shift (ϕ) is given as

$$M_i = \begin{bmatrix} e^{j\phi/2} & 0 \\ 0 & e^{-j\phi/2} \end{bmatrix} \tag{3.35}$$

3.2.2 The LPG and its interactions with cladding and radiation modes:

Coupled mode equations for co-directional coupling[4] are used to explain the interaction between the LPG and its cladding as well as radiation modes. LPGs possess longer index modulation period which enable them to couple light from forward propagating core mode to the forward propagating cladding modes and to the radiation modes. As illustrated in Fig. 3.3 the light propagating can be coupled into the cladding and surrounding medium. Couple mode theory can be used to analyse the coupling characteristics of LPGs.

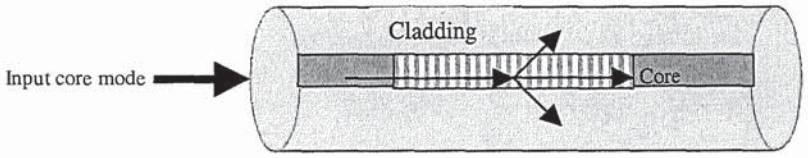

Fig. 3.3: LPG and its interaction with input light

Consider two electromagnetic modes propagating in a perturbed medium such as in long-period- or very strong Bragg -gratings, in the case of co-directional coupling, energy from the fundamental guided forward propagating mode is coupled to forward-propagating cladding modes. Taking $A_{01}^{co}(z)$ to be the amplitude of the LP_{01} guided mode and $B_m^{cl}(z)$ to be the amplitude of the m^{th} cladding mode, then the forward propagating guided mode can be described by

$$\frac{dA_{01}^{co}}{dz} = i\kappa_m \exp(-i\Delta\beta z)B_m^{cl} \tag{3.36}$$

and the forward propagating cladding modes can be described by

[4] Obtained from well reported literature

$$\frac{dB_m^{cl}}{dz} = i\kappa_m \exp(i\Delta\beta z) A_{01}^{co} \tag{3.37}$$

Where, κ_m is the coupling coefficient, given by $\kappa_m = \frac{\pi\Delta n}{\lambda} C_m$, for a refractive index change of Δn and C_m is the overlap coefficient between core mode and the cladding modes. The phase matching condition, $\Delta\beta$ is defined as [112]

$$\Delta\beta = \beta_{01} - \beta_m^{cl} = \frac{2\pi}{\Lambda} \tag{3.38}$$

Where, β_{01} is the propagation constant of the core (guided) mode, and $\beta_m{}^{cl}$ is the propagation constant of the m^{th} cladding mode. If the boundary condition at z=0 (all the light is in the guided mode and none has been coupled to the cladding modes) and δ is defined as $\delta = \sqrt{\kappa_m^2 - (i\,\Delta\beta/2)^2} = \sqrt{\kappa_m^2 + (\Delta\beta/2)^2} = S_m$, then eqns. (3.36) and (3.37) above will yield $A_{01}^{co}\big|_{z=0} = 1$ and $B_m^{cl}\big|_{z=0} = 0$. Taking this into account and solving (3.36) and (3.37) leads to

$$\left|A_m^{(cl)}(L)\right|^2 = \frac{\kappa_m^2}{S_m^2}\sin^2(S_m L) \tag{3.39}$$

Where, L = grating length. Substituting the value of S_m into eqn. (3.39) and dividing by $\kappa_m{}^2$ gives the final solution

$$\left|t_m(\lambda)\right|^2 = 1 - \frac{\sin^2\left[\kappa_m L\sqrt{1+\frac{(\Delta\beta/2)^2}{\kappa_m^2}}\right]}{1+\left(\frac{(\Delta\beta/2)}{\kappa_m}\right)^2} \tag{3.40}$$

Where, $\frac{P(L)^m}{P_{01}(0)} = \frac{\sin^2\left[\kappa_m L\sqrt{1+\frac{(\Delta\beta/2)^2}{\kappa_m^2}}\right]}{1+\left(\frac{(\Delta\beta/2)}{\kappa_m}\right)^2}$ is the ratio of the power (3.41)

coupled from the guided mode to the m^{th}-order cladding mode.

When the phase matching condition is satisfied, i.e., $\Delta\beta = \beta_{01} - \beta_m^{cl} = \frac{2\pi}{\Lambda} = 0$

Then $\left|t_m(\lambda)\right|^2 = 1 - \sin^2(\kappa_m L)$ (3.42)

From eqn. (3.40) the transmissivity of the LPG's m^{th} cladding mode can be plotted. It is also clear from eqns. (3.40) and (3.42) that the strength of each loss peaks of the LPG is determine by length of the grating and the coupling coefficient of the peak.

The effect of varying the length of the LPG can be seen in Fig. 3.4 in which the evolution of LPG from a length of 10mm to 61mm is shown. Each LPG spectrum is recorded after increasing the LPG length in step of 3mm. All parameters other than grating length are kept the same. The sinusoidal variation of the spectral responses is clearly evident on all the grating peaks with energy being transferred from one mode to the mode of the next resonance order.

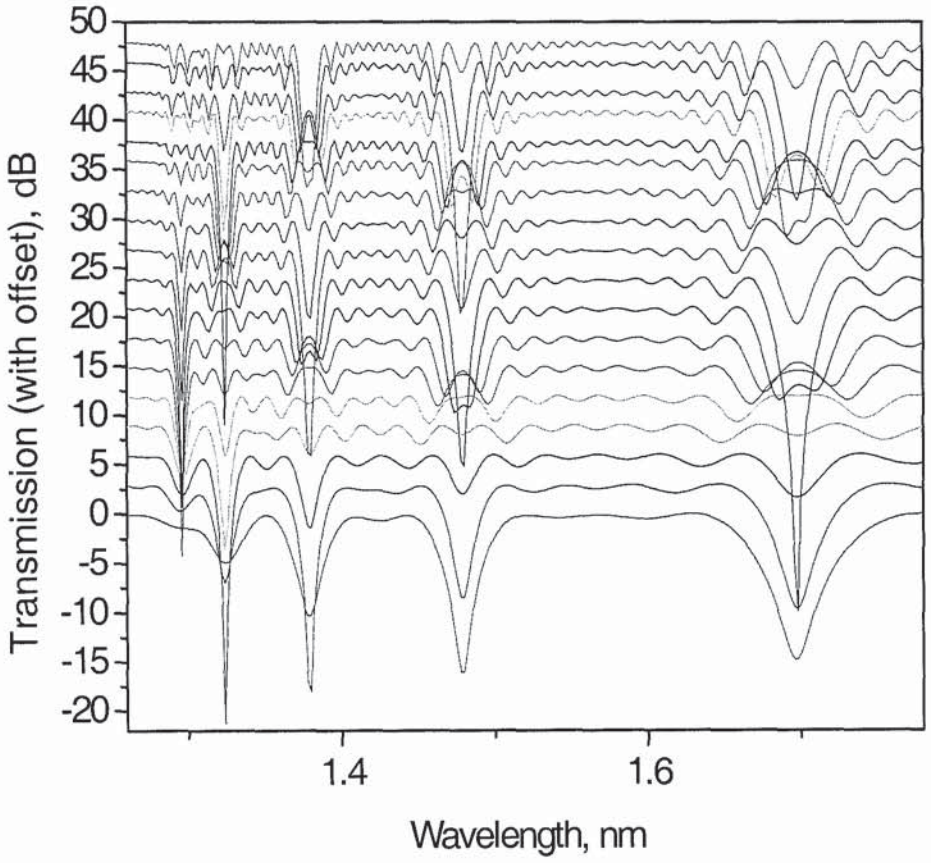

Fig. 3.4: Spectral evolution of LPG simulated for B/Ge fibre with length increased from 10mm to 61mm in steps of 3mm. Core and cladding radii and refractive indices of 4.15mm and 62.5mm, and 1.4492 and 1.4440 respectively

It can also be seen from Fig. 3.4 that the length of the grating can be used to obtain different spectral shapes for use in gain flattening.

3.3 Conclusion

In this chapter couple mode theory has been reviewed. The equations for calculating the spectral response of both FBGs and LPGs have been derived. For the FBGs, the spectral analysis has been successfully carried out whereby sidelobes properties and grating bandwidths were analysed. T-matrix for the modelling of fibre gratings has been examined and through such technique spectral responses of different types of Bragg gratings have been calculated. In addition, many of the equations presented herein have form the basis for the successful simulation of the spectral behaviour of fibre gratings

3.4 Reference:

96. H. Kogelnik, "Coupled wave theory for thick hologram gratings," *Bell. Syst. Techn. Jn.*, vol. 48, pp. 2909-2947, 1969.
97. H. Kogelnik, "Filter response of non-uniform almost-periodic structures," *Bell. Syst. Techn. Jn.*, vol. 55, pp. 109-126, 1976.
98. J.L. Cruz, L. Dong, S. Barcelos, and L. Reekie, "Fibre Bragg gratings with various chirp profiles made in etched tapers," *Appl. Opt.*, vol. 35, no. 34, pp. 6781-6787, 1996.
99. K.O. Hill, "Aperiodic distributed-parameter waveguides for integrated optics," *Appl. Opt.*, vol. 13, pp. 1853-1856, 1974.
100. S.M. Melle, A.T. Alavie, S. Karr, T. Coroy, K. Liu, and R.M. Measures, "Strain sensing using a fibre optic Bragg grating," *SPIE Fibre Optic Smart Structures and Skins IV*, vol. 1588, pp. 255-263, 1991.
101. G. Hall, "Coupled-mode theory for corrugated optical waveguides", *Opt. Lett.*, vol. 15 no.11, pp. 619-621, 1990.
102. Peng, T. Tamir, and H. L. Bertoni, "Theory of periodic dielectric waveguides", *IEEE Trans. Microwave Tech.*, vol. MTT-23, pp.123-133, 1975.
103. Yamamoto, T. Kamiya, and H. Y. Yanai, "Improved coupled mode analysis of corrugated waveguides and lasers", *IEEE J. Quantum Electron.*, QE-14, pp.245-258, 1978.
104. Y. Liu, "Advanced fibre gratings and their applications," *PhD Thesis*, Aston University, UK, April 2001.
105. A.Yariv, "Coupled-mode theory for guided-wave optics," *IEEE Jn. Quantum. Electron.*, vol. 9, pp. 919-933, 1973.
106. A. Yariv, "*Optical Electronics*," 3rd Ed., Holt-Sauders, vol. 503-514, pp. 405-455, 1985,
107. I. Bennion et al, "UV written In-fibre Bragg gratings," *Optical & Quantum Electron.*, vol. 28, pp. 93-135, 1996

108. D.G. Hall, "Vector-beam solutions of Maxwell's wave equation," *Opt. Lett.*, vol. 21, no. 1, pp. 9-11, 1996.

109. V. Mizrahi, and J.E. Sipe, "Optical properties of photosensitive fibre phase gratings," *Jn. Lightwave Technology*, vol. 11, no. 10, pp. 1513-1517, 1993.

110. E. Little, and H.A. Haus, "A variational coupled-mode theory for periodic waveguides," *IEEE Jn. Quantum Electron.*, vol. 31, pp. 2258-2264, 1995.

111. M.J. Adams, "An introduction to optical waveguide," John Wiley, pp. 223-233, 1981.

112. R. Kashyap, "*Fibre Bragg Gratings*," Academic Press," pp.130-189, 230-231, 1999.

113 . K. Mei, T. Weizhong, and Z. Wen, "Cladding mode resonances in long period fiber gratings," *Acta Photonica Sinica*, vol. 27, no. 5, May 1998.

114. J. Albert, K.O. Hill, B. Malo, S. Theriault, F. Bilodeau, D.C. Johnson, and L.E. Erickson, "Apodisation of the spectral response of fibre Bragg gratings using a phase mask with variable diffraction efficiency," *Electron. Lett.*, vol. 31, no. 3, pp.222-223, 1995.

115 . J. Hoge, W. Huang and Makion, "On the transfer-matrix method for distributed-feedback wave- guide devices", *J. Lightwave Technol.* vol. 10, no.12, pp.1860-1868, 1992.

116 . B. G. Kim and E. Garmire, "Comparison between the matrix-method and the coupled-wave method in the analysis of Bragg reflector structures", *J. Opt. Soc. Am.* vol. 9, no.1, pp.132-136, 1992.

117. H.G. Winful, "Pulse compression in optical fibre filters," *Appl. Phys. Lett.* vol. 46, no. 6, pp.527-529, 1985.

118. D.S. Peter, W. Hodel, and H.P. Weber, "Compression of pulses spectrally broadened by self-phase modulation using a fibre-grating: a theoretical study of the compression efficiency," *Opt. Commun.*, vol. 112, no. 1-2, pp.59-66, 1994.

4 Fabrication of fibre gratings

4.1 Introduction

In Chapter 2 holographic UV exposure technique, using a fixed beam, and the phase mask method, with scanned a UV-beam to side-write fibre gratings have been discussed. The scanning technique is the main method used during the research presented in this thesis. Few FBGs were produced using the holographic (fix-beam) technique. In this chapter, the fabrication of different types of fibre grating using UV scanning method is discussed.

First, the index modulations for various types of uniform period grating are shown, with their corresponding spectral responses. This is followed by a discussion on the spectral characteristics of such FBGs. Then a discussion follows on the different experimental set-ups that can be use to fabricate both the short and the long period gratings. The discussion was extended onto the specially designed FBGs such as Apodised, Chirped, Chirp-Moiré, Sampled, and Sinc-sampled FBGs. The chapter then highlighted, briefly, the general areas of fibre gratings applications and finally a conclusion is drawn.

4.2 Index modulation and spectral responses of standard fibre gratings

Figs. 4.1(a)-(c) illustrate the index modulations for each of the 3 main standard types of fibre gratings and Figs. 4.1(d)-(f) show the respective typical spectral responses. These grating types are FBGs, LPGs and SFBGs respectively. The index modulations for these gratings can be easily compared, for example, the standard FBG can be seen to have index modulation of high frequency as in Fig. 4.1(a), and the LPG on the other hand is produced using index modulation of low frequency as shown in Fig. 4.1(b). For the SFBG, being a hybrid, the index modulation has both high frequency as well as low frequency index modulations, as can be seen in Fig. 4.1(c). In all the three main types of gratings, the index modulations used are assumed to be square-shaped[5] with 50% duty cycle. In addition, it can be seen in Fig. 4.1(f)

[5]. Index modulation is assumed to be square-shaped, because, for example, simulation using Optiwave™ IFO does not suggest a significant difference between both sinusoidal and square shape modulations, 2. Amplitude mask is square shaped, and a square shape is easier handle graphically.

that for the SFBG the high frequency components of the index modulation lead to FBG resonance peaks, and the low frequency components produced LPG-type modes.

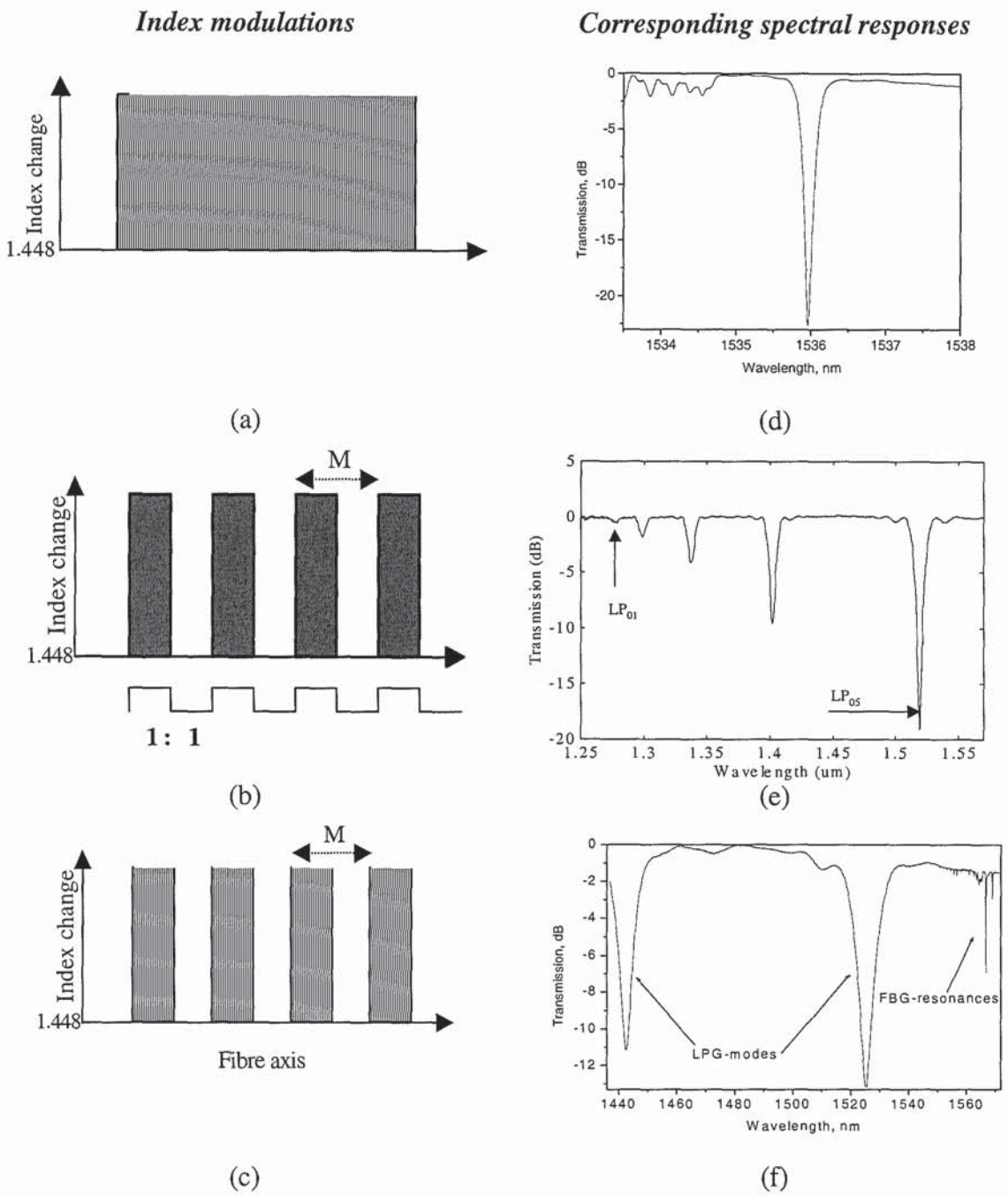

Fig. 4.1: Index modulation profiles (a) uniform high frequency index modulation imposed by phase mask to achieve FBG, (b) on-off low frequency index modulation imposed by shutter or amplitude mask to achieve LPG, (c) the SFBG index modulation obtained by combining index modulations of (a) and (b). Figs. (d), (e) and (f) respectively are the corresponding experimentally-obtained transmission-based spectral response for each index profile.

Note that in Fig. 4.1(f) only one LPG mode is shown. Other LPG modes are also observed but the spectrum analyser resolution (0.1nm) limits the ability to display both the FBG resonance

and more LPG modes. Thus, in this case only one LPG mode is displayed. It is also important to stress that all the LPG modes displayed in Fig. 4.1(e) are also present in the SFBG of Fig. 4.1(f).

4.3 Spectral characteristics of uniform un-apodised FBGs

Apodization is a technique used to suppress grating side-lobes through the control of the grating index modulation depth. To understand the effect of apodization in Bragg gratings, discussion will first focus on the standard un-apodized FBGs so that a comparison can be made with the apodized types. In the last section, Fig. 4.1(a) has shown the typical index modulation of a standard un-apodised FBG filter with a near constant coupling coefficient. For a standard un-apodised FBG the index modulation, as shown previously in Fig. 4.1(a), is clearly square-shaped and as will be described herein can exhibit pronounced sidelobes in the spectral response of the grating filter. The magnitude and wavelength of the sidelobes are dependent on the coupling coefficient 'κ', defined by eqn. (3.2), and the grating length. This relationship has been discussed in greater detail in Subsection 3.2.1.2 (see eqn. 3.24).

The reflection spectra, obtained by simulation of uniform period un-apodised gratings having different 'κ' are shown in Fig. 4.2: (a) shows the simulated spectral responses for 10mm grating with κ = 10, 20... 60 as labelled, and (b) shows the response for 50mm gratings with κ = 20, 40 and 60.

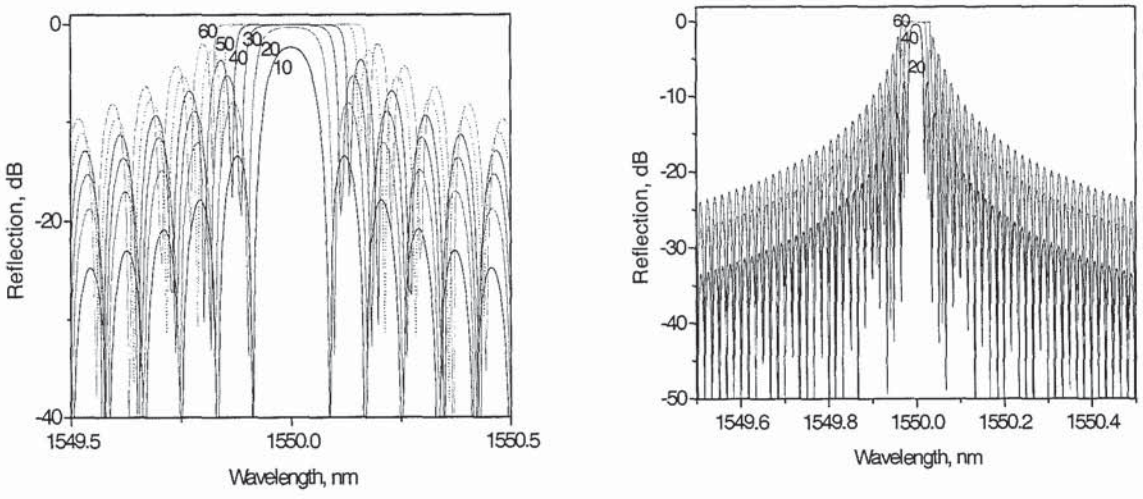

(a) (b)

Fig. 4.2: FBG simulated spectral responses (a) κ = 10-60, length l = 10mm, (b) κ = 20,40,60, l = 50mm

Typical experimentally obtained spectral responses of UV-inscribed un-apodised grating are shown in Fig. 4.3(a) and (b): (a) shows the transmission and reflection spectra for a 20mm long FBG written with a UV power of 70mW, and (b) had similar specification but written with a UV power of 105mW. The High UV power for FBG inscription leads to high value of 'κ'. Clearly, in uniform FBGs both simulation and experimental results suggest that the sidelobes are well pronounced. Furthermore, for FBGs simulated using a high value of 'κ'

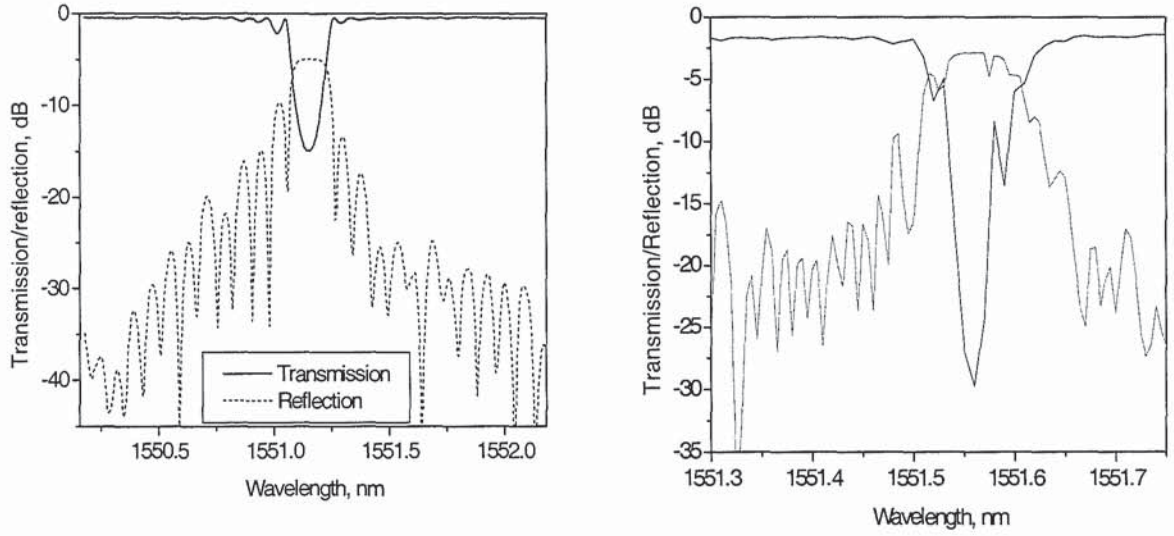

(a) (b)

Fig. 4.3: The spectral response of UV-inscribed un-apodised 20 mm long FBGs written with a UV power of (a) 70mW, and (b) 105mW.

the sidelobes are much more pronounced in comparison to those simulated using lower 'κ'. This simulation result is clearly supported by the experimental implementation of FBGs as shown in Fig. 4.3 (b), which indicates a very small rejection level because of the high UV power[6] of 105mW that has been used to produce the FBG. By comparing with the simulation results of Figs. 4.2(a) and (b), it can also be seen that longer gratings possess narrower spectral peaks.

[6] Remember that $\kappa = 60$ in Fig. 4.2 provides a very small rejection level in comparison to FBG of lower value of 'κ', e.g $\kappa = 20$.

4.4 Fabrication of standard fibre gratings

In this section the fabrication set-up for producing most of the gratings demonstrated in this thesis is described. The method principally involves the use of UV scanning rather than fixed beam. Scanning UV is achieved through a motorized translation stage, which scans the beam across a given length of fibre. Ways of achieving the various index modulations described earlier in Figs. 4.1(a)-(b), are discussed.

As a common rule for all UV-induced fibre grating fabrication, fibre to be used must be photosensitive, achieved either through doping or hydrogen loading or both. For hydrogen (H_2) loading, in Aston University we used two different systems: (a) Hydrogen tubes at room temperature, where a fibre can be loaded with H_2 for 1-4 weeks, and (b) Hydrogenation chamber where fibre can be loaded with H_2 at elevated temperature, typically 80°C, for 1-2 days, and for either case the pressure applied was ~130bars.

To produce gratings, if the fibre coating is not UV transparent, the coating must be removed by stripping to expose the cladding. To strip the fibre, a mechanical stripper may be used otherwise chemical stripping is another option. For some fibres, mechanical stripping is not the best option because the fibre may get broken during the process. From the author's experience, chemical stripping provides better control, and is less risky to the fibre. For the fibres used by the author, most of which were given to the University for free (without much details other than that of core dopants), chemical etching appear to be the preferred stripping technique.

After every UV-based grating-fabrication process, annealing follows. The annealing process involves placing the grating-containing fibre in an oven, on average for 1-3 days to remove the leftover hydrogen from the fibre. At all times, annealing is carried out at temperature that is at least 30°C higher than the maximum temperature under which the device would be used. Table 4.1 provides details of the UV laser power and the average time required to make individual gratings with a single UV scan.

Output power at laser (mW)	Laser power reaching the fibre core (W/cm^2)	
125	1029.13	
110	905.63	
100	823.30	
95	782.14	
90	740.97	
80	658.64	
70	576.31	
55	452.82	
Note: There were five mirrors in the UV-path. It is assumed that each mirror and lens contributes 5% loss, the paper-slit used, cuts out 30%, and the phase mask allows 80% (i.e. each order is 40%). Core diameter =10μm, slit size = 0.5mm		
Purpose of Scan	**Grating length (mm)**	**Average scan time (min.)**
To make FBG	10	2
	20	4
To make Apodized FBG/Chirped, FBG	10	20
	50	40
To make LPG and SFBG	50	10
To make SSFBG/Sinc-SSFBG	50	160

Table: 4.1: The fabrication parameters for reference

4.4.1 FBG fabrication

A set-up for the FBG fabrication using phase mask is shown in Fig. 4.4. As illustrated in Fig. 4.4 (b), which is a magnified part of Fig. 4.4 (a), the phase mask is simply a flat plate of silica, which is transparent to UV light, and has corrugations of spatial period Λ_{PM} etched upon it. UV light that is incident normal to the phase mask is diffracted by the periodic corrugations of the mask with minute or no light transmitted in the zero-order beam. In practice, most of the light is contained in the 0, +1 and -1 diffracted orders. Figs. 4.4(a) and (b) in general describe the experimental arrangement for the fabrication of not only the standard but also many other types of FBGs. The periodicity of the phase mask determines the type of grating produced. Thus, for a uniform period FBG, a phase mask with constant spacing between corrugations is used. But, to produce a chirped FBG, a phase mask with increasing or decreasing spacing is used instead.

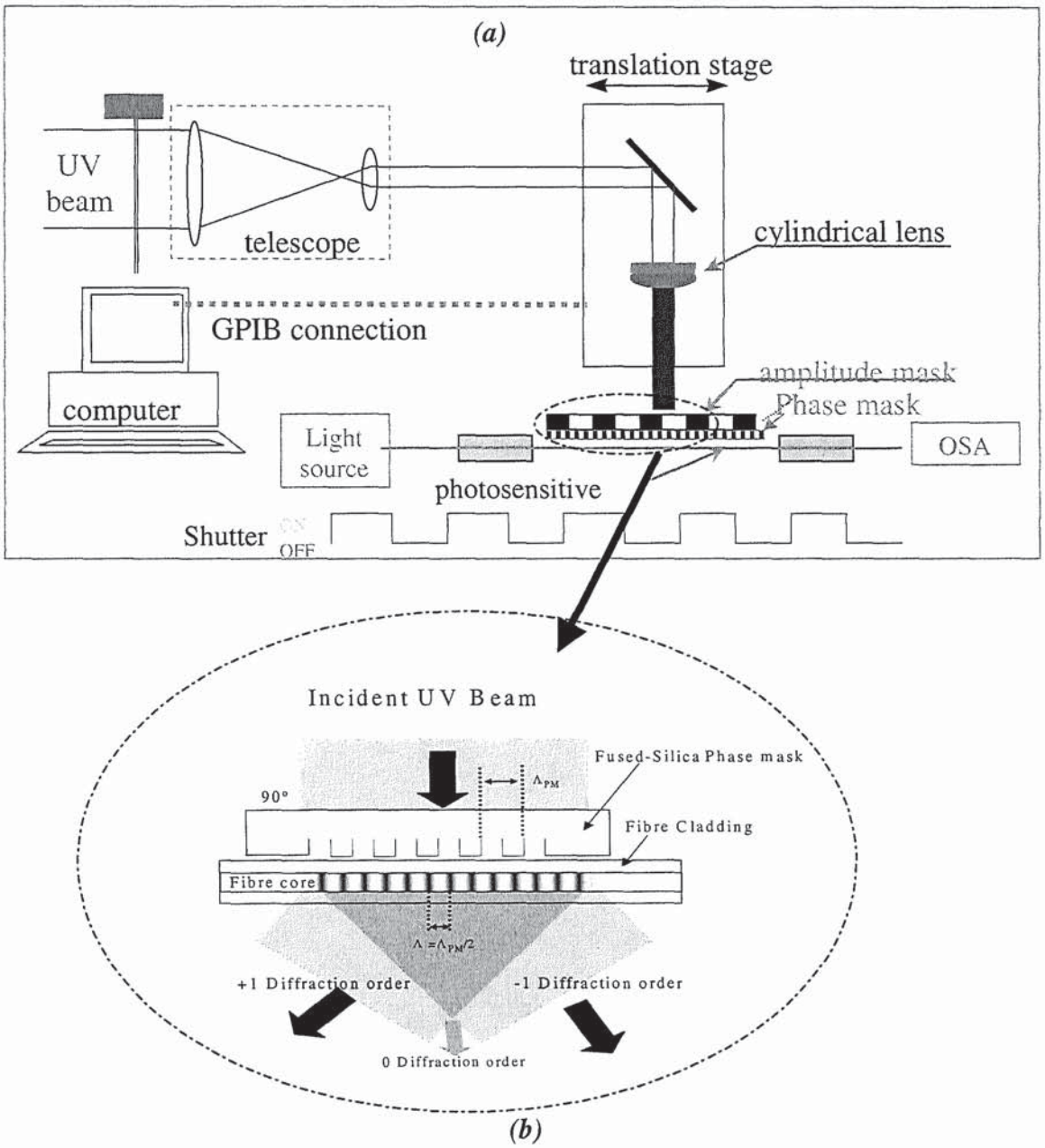

Fig. 4.4: The phase mask grating writing arrangement

The phase mask corrugations are designed so that the zero order is suppressed, to < 5%, with approximately 40% of the total incident light intensity in each of the +1 and -1 diffracted orders. The grating is written with a period $\Lambda = \Lambda_{PM}/2$ by the interference between the +1 and −1 diffracted orders of UV emanating from the phase mask. The period of the resulting grating is independent of the exposure source (laser) wavelength.

A disadvantage of the phase mask method stems from the need to have a separate phase mask for each Bragg wavelength required. It has been demonstrated however that a magnifying lens positioned right in-front of the phase mask permits variation of grating peak wavelength [119]. It has also become a common practice to vary the grating wavelength using the same phase mask by application of strain to the fibre [120]. A wavelength shift of up to 6nm has been achieved using this method as will be seen in Section 5.2.1. Another method used to alter the FBG wavelength is by using pre- or post-exposure of the fibre containing the grating with UV [121].

The phase mask fabricated Bragg gratings have received wide acceptance from both the telecom and sensing industries. This has encouraged further research into the fabrication of improved grating structures for a wider range of applications. Using the phase mask fabrication technique, it has been possible to write many new and interesting grating structures, including apodised, chirped, phase shifted, Moiré, sampled, and chirp-sampled gratings. Such gratings are non-uniform, either in period or in the amplitude of the induced refractive index change. The variety of in-fibre Bragg grating devices that can now be fabricated has led to their employment in a wide range of applications, many of which were not considered previously.

Recently, a method, which offers the advantages of both the transverse holographic and phase mask gratings fabrication, has been reported [122]. This method allows for using a phase mask to flexibly achieve FBGs of diverse wavelengths and with low levels of sidelobes.

Another method for producing FBGs that was reported recently, involves the use of polarization beam splitter to achieve FBGs with reduced sidelobes [123]; this method allows for producing FBGs of different profiles. In this beam scanning method movement of either the fibre or the phase mask is not required. The method involves control of coupling coefficient and phase-shifts by using UV polarisation beam-splitter: the polarisation of scanned beam is effectively tailored to give various profiles. Apodization is obtained with a single scan of the UV beam with a constant speed and UV intensity. Using the polarisation beam splitter method it has been shown that various apodization profiles can be achieved with up to 28dB sidelobe suppression in a grating with 8dB transmission dip [123]. Most methods used for FBG fabrication lead the production of re-producible gratings, but, generally,

methods that involve the use of phase mask, from author's experience, seemed to offer grater control and reproducibility.

4.4.2 LPG fabrication

Long period gratings, as the name suggests, are another set of fibre gratings whose period is much larger than that of FBGs. LPGs are easy to fabricated and have grating period in the order of 5 to 2800 μm [124] compared with FBGs whose periods are usually less than 1 μm . LPGs can be fabricated using the experimental set-up shown in Fig. 4.4 used for FBGs, but the phase mask should be substituted by amplitude mask. Larger periods enable the UV-inscription of LPGs using amplitude masks [125] in place of phase mask. In addition, the amplitude masks are much cheaper than phase masks and their large periods also permit greater tolerance of error.

Alternatively, point-by-point UV exposure can be used to produce LPGs [126]. The point-by-point writing method allows for the LPGs to be written without amplitude masks. In fact this method also allows FBGs to be written using a very short phase mask. Whilst both the amplitude mask and the point-by-point methods provide LPGs of high quality, the later technique offers the added advantage of arbitrary periods and profiles. To use point-by-point method, a UV light shutter is computer-programmed to switch on-off (i.e. open & close) with a 50% duty cycle during inscription process. The computer control has improved the flexibility of the LPG fabrication to the extent that the control of length and index modulation depth permits the design of different spectral profiles. Non-UV based LPG writing techniques have also been reported [127,128], some of which show that LPGs can be produced using a fusion splicer [129,130]. In all cases, the LPGs can be re-produced with more than 97% match but are extremely difficult to obtained 100% reproducibility as in other short-period devices.

4.4.3 SFBG fabrication

A Sampled Fibre Bragg Grating (SFBG) is a Bragg grating having a high-spatial-frequency refractive index modulation superimposed with a periodically-varying, low-frequency envelope of index modulation superimposed on it during UV inscription [22]. The slowly

varying envelope with a long period of Λ_{LPG} ($\Lambda_{LPG} \equiv$ M) leads to an LPG-like transmission attenuation response, characterised by several broad loss bands with resonance wavelength $\lambda_{LPG} = (n_{co}^{eff} - n_{cl,m}^{eff})\Lambda_{LPG}$, where n_{co}^{eff} and $n_{cl,m}^{eff}$ are the effective indices of the fundamental core mode LP_{01} and cladding mode LP_{0m} respectively. The LPG response is derived from the light coupling between the forward-propagating core and cladding modes.

From Figs. 4.1 (c) and (f) it can be seen that SFBG is a series of similar short length FBGs (sub-gratings) cascaded serially along a fibre. The rapidly varying index modulation in each sub-grating with a short period of Λ_{FBG} lead to an FBG-like reflection response characterised by multiple-harmonic narrow resonances with a central Bragg wavelength $\lambda_{FBG} = 2n_{co}^{eff}\Lambda_{FBG}$. The FBG response results from the light coupling between the counter-propagating LP_{01} core modes. According to coupled mode theory, every Fourier component contributes a reflectivity peak to the Bragg resonances of the SFBG. The wavelength spacing, $\Delta\lambda$, of the Bragg resonances of SFBG is given by

$$\Delta\lambda = \frac{\lambda^2}{2nM} \tag{4.1}$$

Where, λ is the Bragg wavelength, n is the effective refractive index of the fibre core, and M the period of the low frequency envelope of index modulation (i.e. the period of amplitude mask). Clearly, by changing the period, M, it is possible to change the spacing between FBG resonance peaks of the resulting grating. Longer period M can be altered by changing the duty cycle of the UV exposure. Thus, changing the duty cycle can also alter the resonance spacing, $\Delta\lambda$.

The arrangement of the phase- and amplitude- masks for SFBG fabrication is shown in Fig. 4.5. It can be seen in the arrangement that both the phase and amplitude masks are used. The UV first passes through the amplitude mask before subsequently getting diffracted by the phase mask to the usual orders (+1, 0, -1) as seen in Fig. 4.4 (b). Amplitude mask does not alter the direction of the UV significantly –the dark spots blocks the UV and the clear parts are transparent. This is similar to superimposing the index modulation of an LPG over that of

an FBG. Clearly, with this arrangement the amplitude mask can be removed if point-by-point[7] method is required. The point by-point is the main LPG and SFBG fabrication method adopted in the work reported in this thesis.

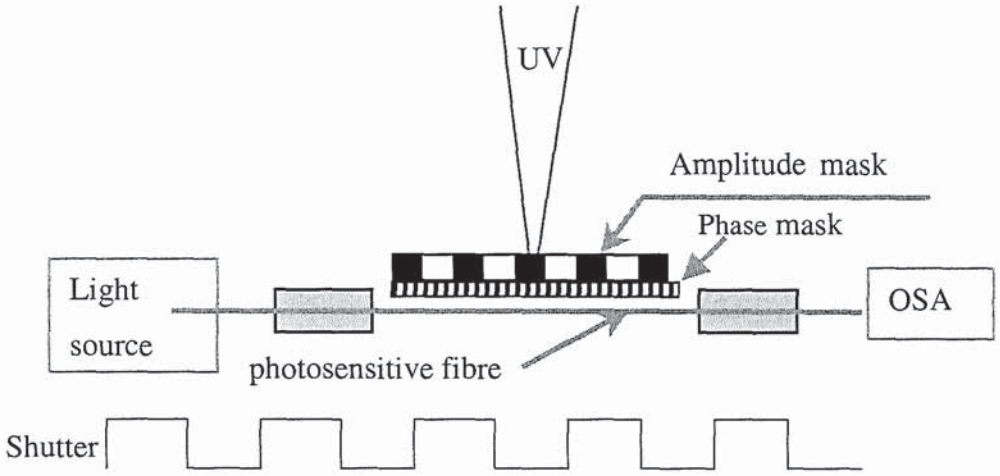

Fig. 4.5: Experimental set-up for the fabrication of SFBGs

SFBGs are produced with 50% scan duty-ratio just like LPGs, and just as for the LPGs the long period spectral response is thus difficult to replicate with 100% matched. However, the Bragg components of the spectral response are easily reproducible in view of the fix period phase mask used.

4.5 Specially designed fibre gratings

For the FBGs and SFBGs, other variants of the gratings can be obtained by changing the period, duty-cycle, or depth of the index modulation along the grating length. In FBGs, changing the intensity of the index modulation along the grating length can be used to obtain an apodised FBG. Furthermore, the period of index modulation can also be gradually increased or decreased to produce another type of grating called Chirped Fibre Bragg Grating (CFBG). Also, by overlapping two CFBGs another grating called Chirped-Moiré grating can be achieved [131]. In addition, the fabrication of two special types of SFBG is also discussed.

[7] Point-by-point method is simply the illumination of the fibre with shots of UV at different points along the fibre length. Often, the illuminated points have the same spacing between them.

4.5.1 Apodised in-fibre Bragg grating filters

Standard FBG reflection-profile exhibits a series of sidelobes on either side of the main Bragg peak. These sidelobes are inherent in un-apodized Bragg gratings and are highly undesirable for most grating applications. In DWDM systems, for example, these sidelobes could induce cross-talk between adjacent channels, and in dispersion compensating systems they introduce ripples in the dispersion characteristic of a chirped Bragg grating, degrading the system performance [132]. A typical FBG-based DWDM system requires gratings with flat dispersion characteristics, square-shaped reflection and sidelobes rejection level of up to 25 dB.

In Section 4.3, where the characteristics of uniform period fibre gratings has been discussed, it was demonstrated that the coupling coefficient 'κ' determines the level of sidelobes in the FBG reflection spectrum. In this subsection, it is demonstrated that the spatial variation of 'κ' can be tailored to obtain various reflection profiles in FBGs.

4.5.1.1 Apodisation principle

Suppression of the grating sidelobes can be achieved by spatially varying the κ from 0 to κ_{max} (κ_o) from grating ends to the centre with some degree of symmetry as shown in Fig. 4.6. The spatial variation of the grating coupling coefficient, with the highest value at the centre and lowest value at the grating ends, is called *apodisation*. As the edges of the grating have near-zero coupling coefficient after apodisation, the effective length of the grating becomes a fraction of the total exposure length. This means that an increment in the linewidth of the grating can result from apodisation. In addition, during fabrication, the coupling coefficient of an apodised grating must be higher than that of the standard un-apodised grating if the same transmission strength is to be achieved.

It is noteworthy that using the value of 'κ' to reduce grating sidelobes, otherwise known as apodisation, has generated considerable interest over the last few years. A large effort has been made in the theoretical design of apodised grating filters [133,134,135,136]. Also, there have been many demonstrations of different experimental techniques for the fabrication of apodised gratings including, the use of UV-pulse interferometry [122], a phase mask with variable diffraction efficiency [137], and methods for CFBGs [138,139]. These works have

highlighted the importance of apodisation for the majority of applications employing Bragg gratings, but has concentrated mainly on the design of the overall profile for a grating of unrestricted length.

A standard square-shaped index-modulation envelope of a un-apodised FBG similar to that seen in Fig. 4.1 (a) was superimposed with a Gaussian apodisation profile to achieve the apodisation envelope shown in Fig. 4.6. The resulting grating coupling coefficient in this case is defined by

$$\kappa(z) = \kappa_o \,.\, \text{funct}(z) \tag{4.2}$$

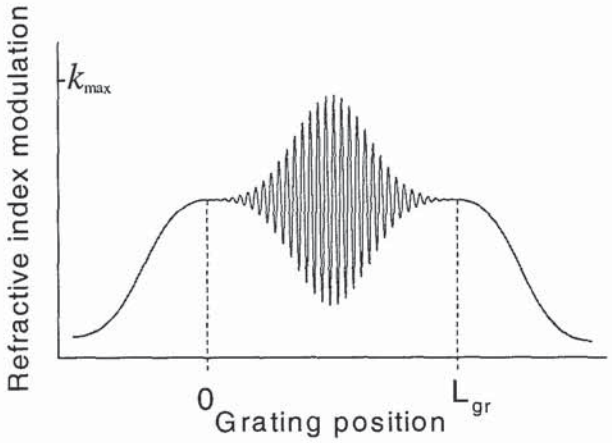

Fig. 4.6: Apodisation envelope of Index modulation imposed on a uniform period FBG

Where $\kappa_o = \kappa_{max}$ for the un-apodised index modulation, and funct (z) varies from 0 to 1 according to the apodisation function used.

4.5.1.2 Apodisation functions and simulation results

Several κ-varying functions have been suggested for apodisation of Bragg gratings, including Gaussian, Blackman, Cosine and Sinc [104]. Table 4.2 shows these functions used for different index modulation profiles.

Profile	κ-varying function	
Gaussian	$funct(z,m) = \exp\left(-m\left\|z/L/2\right\|^2\right)$	.....(4.3)
Blackman	$funct(z) = \frac{\left[1.19\cos\left(\frac{\pi z}{L/2}\right)+0.19\cos\left(\frac{2\pi z}{L/2}\right)\right]}{2.38}$	.....(4.4)
Cosine	$funct(z) = \cos\left(\frac{\pi z}{L}\right)$	.....(4.5)
Sinc	$func(z,N) = \frac{\sin(2N\pi / L)}{2N\pi / L}$	.....(4.6)
$-L/2 \le z \le L/2$, L is grating length.		

Table 4.2: The list of apodisation functions

A comparison of the calculated responses of gratings apodised with Gaussian and Blackman envelopes is shown in Fig. 4.7: (a) shows the responses for 10mm long grating whereas (b) shows the response for the 50mm long grating. It may be observed from the figures that the longer the grating the better the apodisation –with Blackman envelope leading to a better rejection level when compared with its Gaussian counterpart. As can be seen in Fig. 4.7(a), theoretically, up to 50dB can be achieved by using a standard Gaussian profile to apodised a 10mm FBG, and a 25 dB further improvement can be obtained for the same length of grating by using the modified-Gaussian or Blackman profiles.

For longer gratings higher rejection levels can be achieved, as seen in Fig. 4.7(b): typically, for a 50mm FBG that is apodised using standard Gaussian function 56dB rejection was recorded. However, Blackman or modified Gaussian functions offered a rejection level of 96dB as seen in Fig. 4.7 (b). Clearly for both profiles, improved rejection levels can be achieved in a longer FBG.

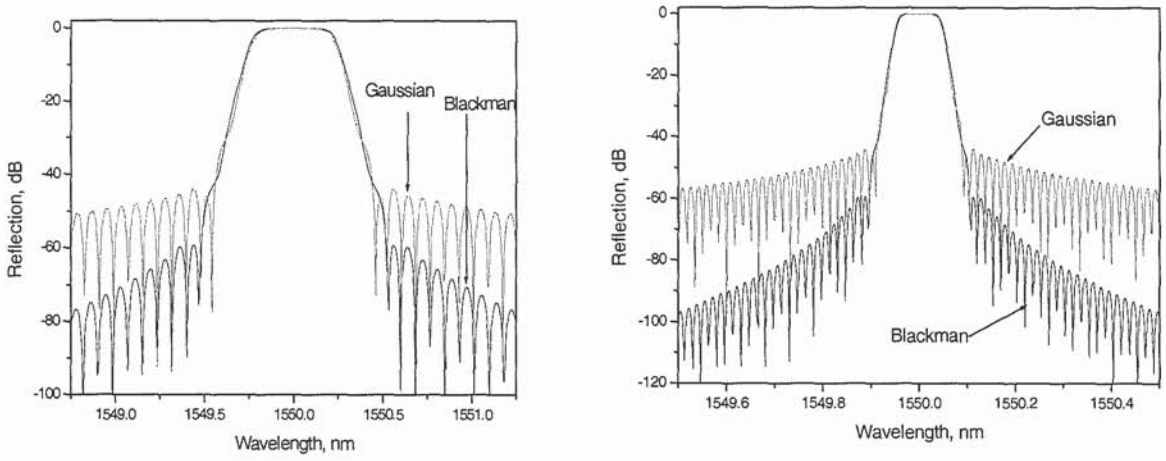

Fig. 4.7: Simulated apodised FBG responses (a) κ =85, l=10m (b) κ =85, l=50m

4.5.1.3 Apodisation of phase mask fabricated FBGs

Several methods have been suggested for the apodisation of phase mask fabricated Bragg gratings. One of the simplest techniques, reported by Hill *et al* [138], involves varying the rate of exposure along the length of the grating, which produces a corresponding variation in the average refractive index and coupling coefficient thereby apodising the grating profile. Unfortunately this technique, though effective for controlling sidelobes, generates an unwanted chirp along the length of the grating [10].

Other apodisation techniques include the longitudinal stretching of the fibre during grating fabrication which reduces the fringe visibility toward the grating ends while maintaining the visibility at the grating centre (e.g. cosine) [139]. Position weighting technique of apodisation has also been proposed, where a number of sub-gratings are made to overlap, thus controlling the local grating strength. Using this method, a 10cm-long grating was fabricated with a truncated sinc apodisation profile [140].

Apodisation can also be achieved by using a custom-made apodised phase mask [122,137]. Despite the cost and inflexibility of this method, it has gained so much popularity due to the inherent reproducibility of the resulting gratings. In this technique, apodisation can be achieved by varying the diffraction efficiency along the length of the mask. This efficiency can be varied by continuous changing of the ridge duty cycle with the length of the mask or

by maintaining a constant ridge duty cycle of ~50% while introducing numerous phase shifts, from π in the middle to zero at both ends of the mask. Apodised phase masks are now very common and their effectiveness in producing apodised gratings is well recognised.

Advanced apodisation profiles can also be achieved by either moving the fibre [138,141] or phase mask during UV scanning [142]. Despite the sensitivity to vibration and sometimes the need for interferometric control, these methods are quite flexible. Also, the fact that phase mask of any period can be used for the fabrication means that the cost is significantly reduced. A method whereby a phase mask is not only moved but also shaken during fabrication, generally known as the phase mask dithering technique, has also been investigated. Typical results obtained using this method are described in the next subsection.

4.5.1.4 Experimental apodisation by phase-mask dithering

The experimental apodisation technique used for the work reported in this thesis is based on the dithering of the phase mask during exposure. It provides all the advantages of Meltz's and Hill's holographic techniques described in Chapter 2, and has increased flexibility that enables a device of any desired profile to be fabricated.

Fig. 4.8 shows a schematic diagram of the experimental set-up used for the phase mask dithering technique for the fabrication of the apodised gratings. The UV beam's diameter was reduced to ~0.5mm after passing through the cylindrical lens. The beam was incident at right angle to the mask and the fibre. The mirror and cylindrical lens were mounted on a translation stage as illustrated in the figure, which allowed the beam to be scanned longitudinally along the length of the phase mask/fibre arrangement. The phase mask itself was mounted onto a single piezoelectric crystal, driven to dither the phase mask by using a profiled triangular waveform from a computer controlled function generator. The magnitude of the dither was varied as the beam scanned the length of the fibre through the phase mask: maximum dither occurred when the beam was at either ends of the grating, with the minimum or no dither occurring at the centre of the grating, to obtain a symmetric index profile similar to that shown in Fig. 4.6. Smaller UV beam sizes do follow apodization profile more accurately, thus, can lead to improved efficiency due to reduced overlap between the two interfering UV diffraction orders [143]. But, for a given distance between fibre core and the phase mask, as the beam get smaller diffraction order of the UV beam do diverge, and where this happens

(for example when beam sizes are tens of microns), then diffraction pattern will form away from the core. With no diffraction patterns forming in the fibre core there is effectively no grating. Care must therefore be taken to strike an optimal balance between the trade-offs.

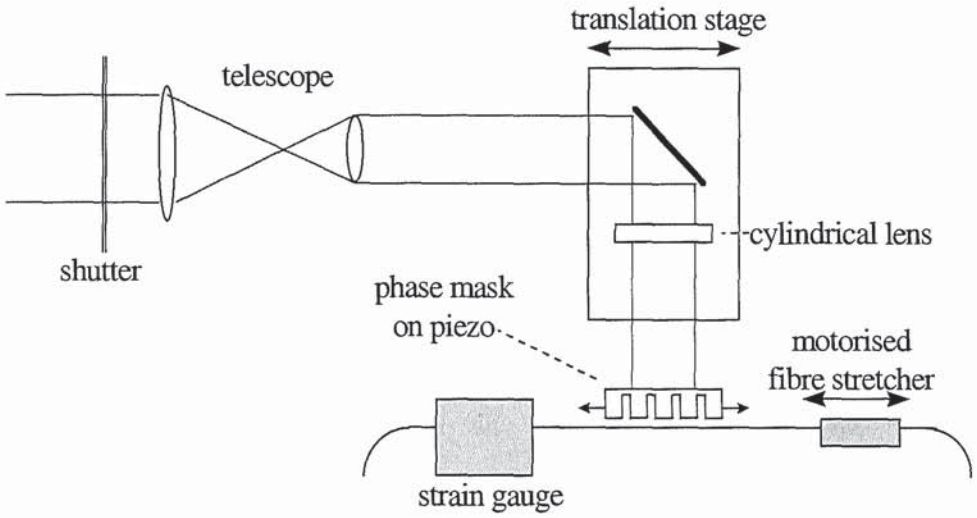

Fig. 4.8: The experimental set-up for the fabrication of apodised gratings using a phase mask dither technique.

The only constraint for a fully apodised grating was that the phase mask had to be moved by exactly half the mask period at both edges of the grating in order for the fringe visibility to be minimised to $\kappa = 0$. This means that for every phase mask, a voltage by which the dithering amplitude is exactly equal to half the mask period $\left(\frac{\Lambda_{Mask}}{2}\right)$ had to be established. This voltage is referred to as the optimal dithering voltage. The optimal voltage for dithering the mask was first identified through the writing of gratings using different voltages, applied to the piezoelectric crystal on which the phase mask sits, to obtain the dithering amplitude that matches the half phase-mask's period. The idea here is that with the maximum dither amplitude there is complete UV shading and no grating is written. With lowest or no dithering the maximum index modulation depth can be obtained because there is no shading.

By measuring the spectral response of the fibre, the accuracy of the identified optimal dithering voltage (giving an amplitude of half the mask period) was corroborated; no grating was discernible after scanning the whole length of grating with UV power of 110mW. Fig. 4.9 illustrates the relationship between the dithering voltage and the FBG transmissivity that was

realized during the tests. Clearly, the 'half-period' shaking voltage established for the particular phase mask used is ~0.898V. At this voltage the transmissivity of the FBG is zero.

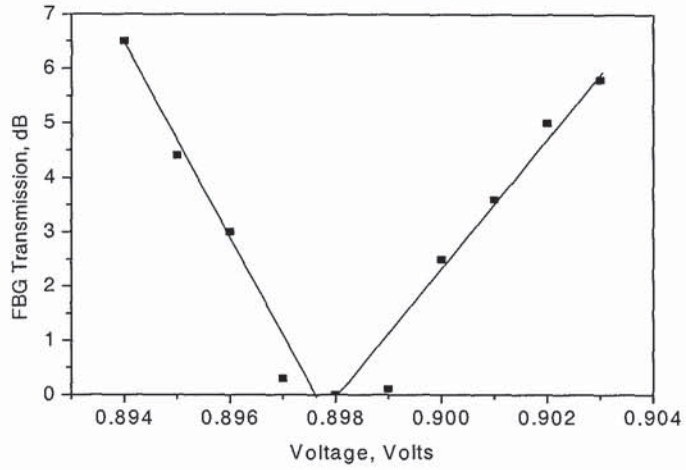

Fig. 4.9: The piezo shaking-voltage against the strength of FBG transmission dip

A uniform period phase mask was used to fabricate all the apodised gratings and for consistency, the same phase mask and the same type of fibre hydrogenated under the same condition were employed for each separate work. Standard SMF which is known to be mechanically strong, and compatible with most telecom systems, was used for all the work reported in this section. The phase mask used had a spatial period of 1071nm and the output power for the 244nm Fred-laser used to write the gratings for establishing the optimal dithering voltage was 110mW.

The Gaussian apodised gratings having the spectral response shown in Figs. 4.10(a) to (d) were fabricated using a frequency doubled Argon-ion laser with output power ranging from 70mW to 110mW. In particular, the FBGs shown in Figs. 4.10(a), (b), (c) and (d) were written with laser output powers of 80, 90, 110, and 100mW respectively. Clearly, the depth of the transmission dips of the FBGs indicate direct relationship[8] with the UV power used as suggested by Figs. 4.10(a), (b), (c), and (d) showing transmissivity of 6.6, 8, 44, and 22dB respectively. However, the gratings of stronger transmissivity are often spectrally broad and of low rejection level, as seen in Fig. 4.10 (c).

[8] As the UV power increases, the depth of the FBG transmission dip increases. This remains the case until saturation is reached.

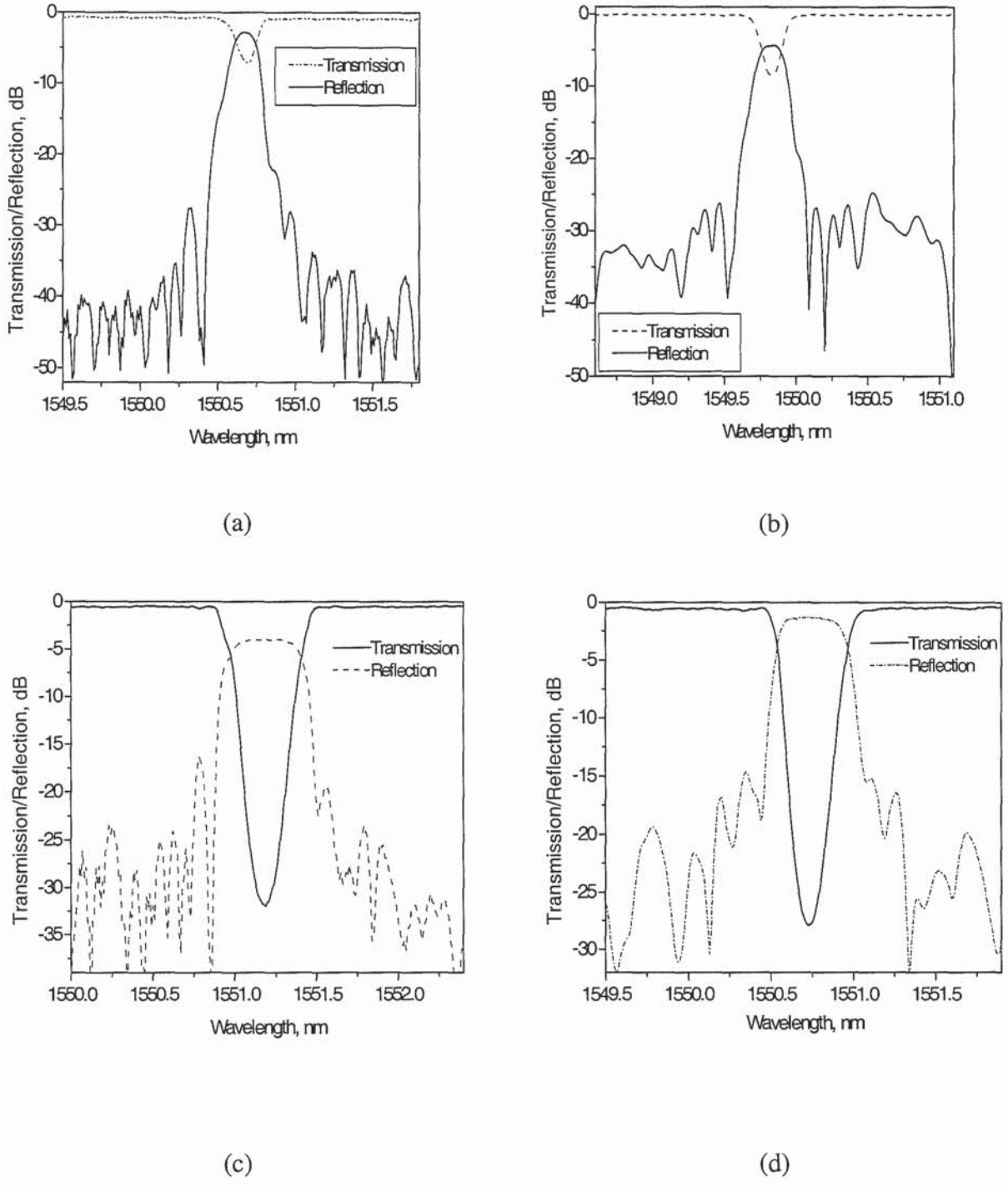

Fig. 4.10: Experimentally obtained apodised FBG transmission and reflective spectra, (a) UV power 80mW, (b) UV power 90mW, (c) UV power 110mW, (d) UV power 100mW

On the other hand there is, as expected, an indication that smaller transmissivity can lead to gratings of stronger reflectivity levels. This suggests, as expected, that there is a trade-off between reflectivity and transmissivity, therefore, an optimum level needs to be established whereby both the transmission and reflection spectra indicate a reasonably good sidelobe

rejection level. It is necessary to stress that a saturated grating often offers low sidelobe rejection. A typical example is shown in Fig. 4.10 (d), where both the transmissivity and reflectivity are about 19dB. It should be mentioned that greater FBG transmission and reflection strengths can be achieved with improved stability of the fabrication optics. For example, the number of mirrors to be used must be as minimal as practically possible, fibre and phase-mask must be firmly fixed during the scan, effect of undesired vibration on the mask and fibre must be eliminated, laser must be well aligned so that exactly the same UV intensity is applied through the whole grating length, phase-mask must be clean, and the fibre must not be touching the phase-mask during the scan.

In summary, Subsection 4.5.1 has described the technique to design and fabricate apodised FBGs. The apodised FBGs owing to their large rejection ratio (dynamic range) can offer superior optical filters, and provide sensing heads that are easier to interrogate than standard FBGs. Various apodisation functions have been described; Gaussian and Blackman profiles have been compared. Methods to implement apodisation experimentally were also considered. In addition, a number of FBG filters fabricated during this research have been demonstrated paving the way for further development of specialized FBGs.

4.5.2 Chirped fibre Bragg gratings (CFBGs)

The fabrication of CFBG involves the use of the same set-up as that used for FBGs (see Fig. 4.4) –the only difference is the phase mask. That is, instead of using uniform-period phase-mask, one with a linearly increasing spatial period is employed. Typical index modulation imposed in the fibre core by this type of phase mask is shown in Fig. 4.11 (a) and an example of CFBG spectral response is depicted in Fig. 4.11 (b). As can be seen in Fig. 4.11 (a), there is increasing spatial period of index modulation from left to right -matching the phase mask corrugations.

The width of the spectral response, $\Delta\lambda$, is large in comparison to that of standard FBGs because light components passing through the device are reflected at different points along the length of the CFBG. The spectral width thus indicates the maximum degree of chirp in the CFBG. For a grating with a given chirp rate, the longer it is the wider the bandwidth. But CFBGs with larger bandwidths are more likely to be affected by ripples.

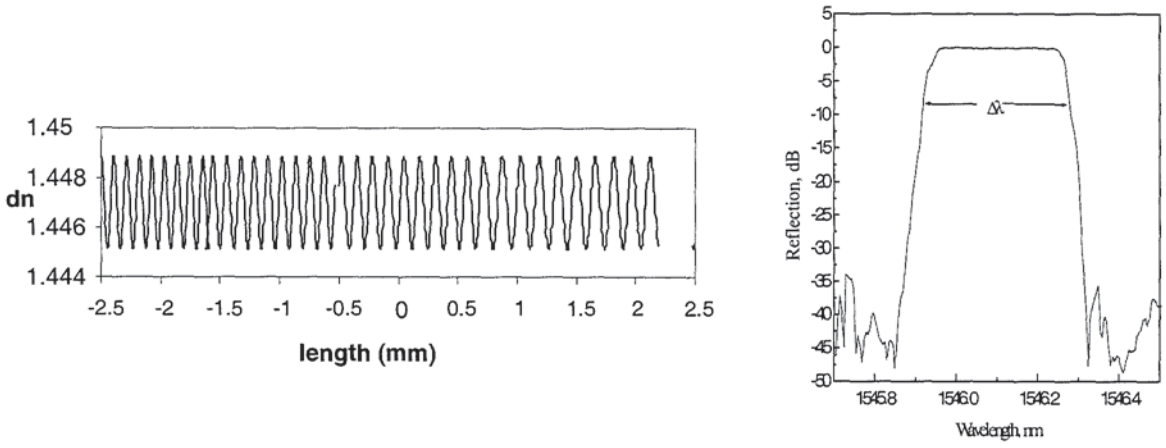

Fig. 4.11: A typical CFBG, (a) illustration of index modulation and (b) experimental spectral response

A CFBG can be used to compensate for fibre dispersion if used in the way described by Fig. 4.12. Here, the CFBG is used with the longer period side at the light input end, which cause reverse dispersion effect as well as reducing the effect of spectral distortion that may result from short wavelength loss.

The interaction between light components and the grating's index modulations can be seen in the enlarged CFBG section shown within the figure, where different wavelengths are reflected at different points along the grating. This implies that pulses that have been broadened by fibre-induced dispersion can be compressed back to their original size using a CFBG as demonstrated. It can be seen in the figure that at the fibre input there is a train of pulses that are distinctly separate, but after passing through the length of the fibre, say 200Km, the pulses that arrive at the receiver side are broadened and sometimes they overlapped. To reverse the effect, a CFBG with equal dispersion to that of the long-haul fibre is used in the reverse order, as shown in Fig. 4.12. Clearly, after passing through the CFBG, the broadened overlapped pulses are separated and compressed back to their original shaped.

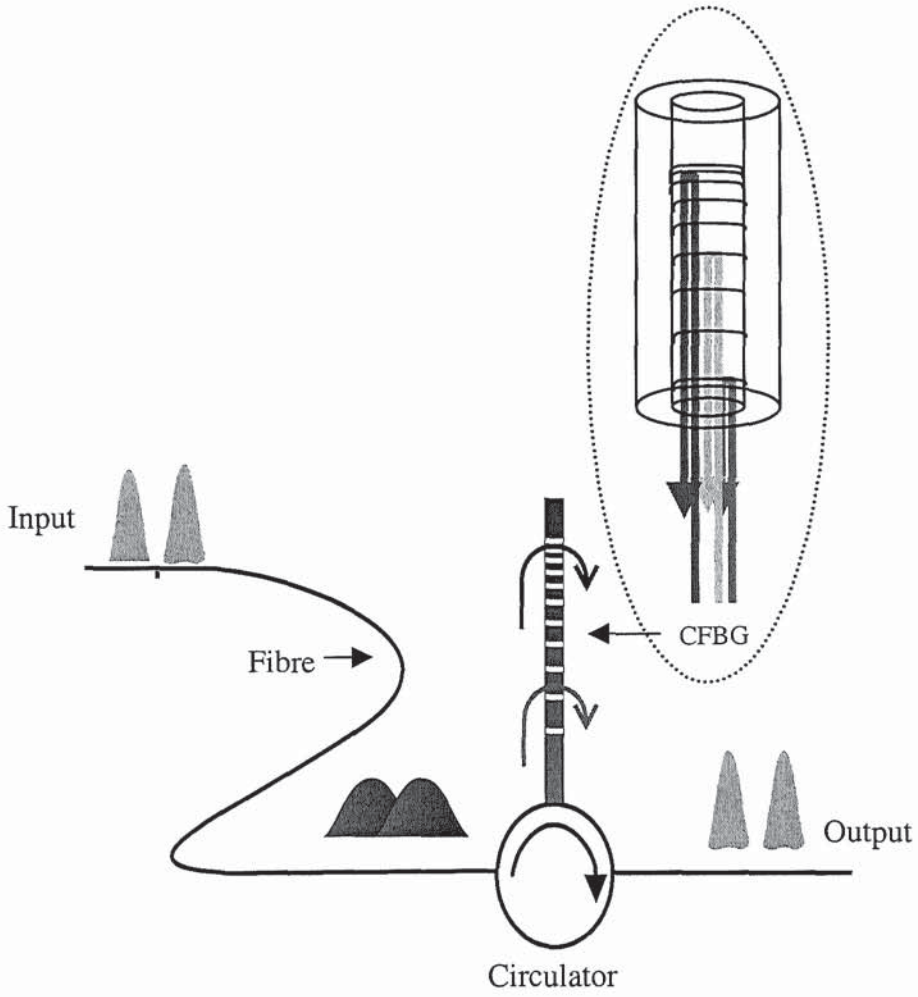

Fig. 4.12: A typical experimental arrangement for dispersion compensation showing CFBG reflecting light of different wavelengths at different points along the grating

A CFBG can be used to either compensate for or indeed to introduce dispersion when required. To introduce dispersion in a channel, instead of using the CFBG in the way described by Fig. 4.12, it is used with the shorter period side connected to the circulator. This is often the case when used in microwave sub-carrier related applications where CFBG acts as a delay line. This principle will be further discussed in Chapter 6, under transversal filters.

4.5.3 Chirped-Moiré FBG

Chirped-Moiré grating is obtained by the superimposition of two CFBGs of different periodicities in the same section of fibre core. It is fabricated mainly by dual exposure using chirped period phase mask. The initial CFBG is produced, and the second CFBG is then

superimposed on it with an offset. The length of the offset distance will determine the number of peaks within the chirp-grating stop band. Typical index modulation of this type of grating, obtained through simulation, and spectral transmission response, obtained experimentally, are respectively shown in Fig. 4.13 (a) and (b).

Chirp-Moiré grating can be used for quasi-distributed strain and temperature sensing applications [144]. For quasi-distributed sensing the individual peaks of the grating shifts differently depending on the physical position within the grating that is exposed to the external perturbation.

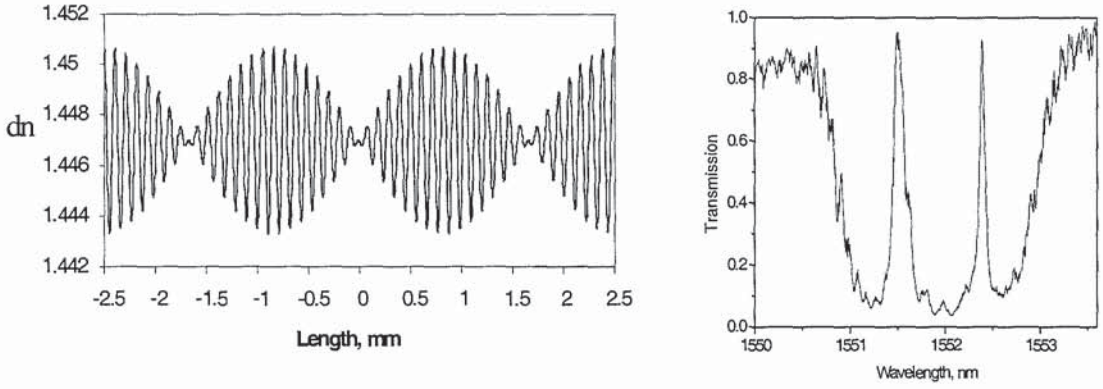

(a) (b)

Fig. 4.13: A typical 1cm long Moiré grating; (a) simulated index modulation and (b) experimentally obtained spectral response

4.5.4 Standard-superstructure and sinc-sampled FBG

For easy of discussion, from this point, two abbreviations will be used to represent sampled fibre Bragg gratings. SFBG will represent grating produced with 50% UV-scan duty ratio and it is mainly used in transmission only (i.e. showing both short- and long period components). However, when such type of grating is produced with <10% duty ratio and the use is made of only the short period (Bragg) components either in transmission or reflection, the grating will be referred to as the SuperStructured Fibre Bragg Grating and abbreviated as SSFBG.

Apart from the standard type SFBG described earlier and shown in Figs. 4.1 (c) and (f), two additional superstructured variants can also be achieved by first reducing significantly the

duty cycle of the low frequency index modulation from 50%, followed by either

(i) maintaining a square-shaped low frequency index modulation envelope as shown in Fig. 4.14 (a) or

(ii) imposing a sinc-shaped index modulation on the low frequency index modulation as demonstrated in Fig. 4.14 (c).

In the case of (i), the resulting spectral response of the SSFBG shows a Gaussian envelope containing N multiple channels, as exemplified in Fig. 4.14(b). This grating is sometimes called FBG comb-filter. For (ii), the spectral response depicts a set of flat-top channels, and the SSFBG is called Sinc-Superstructured Fibre Bragg Grating (Sinc-SSFBG) and its spectrum is shown in Fig. 4.14(d).

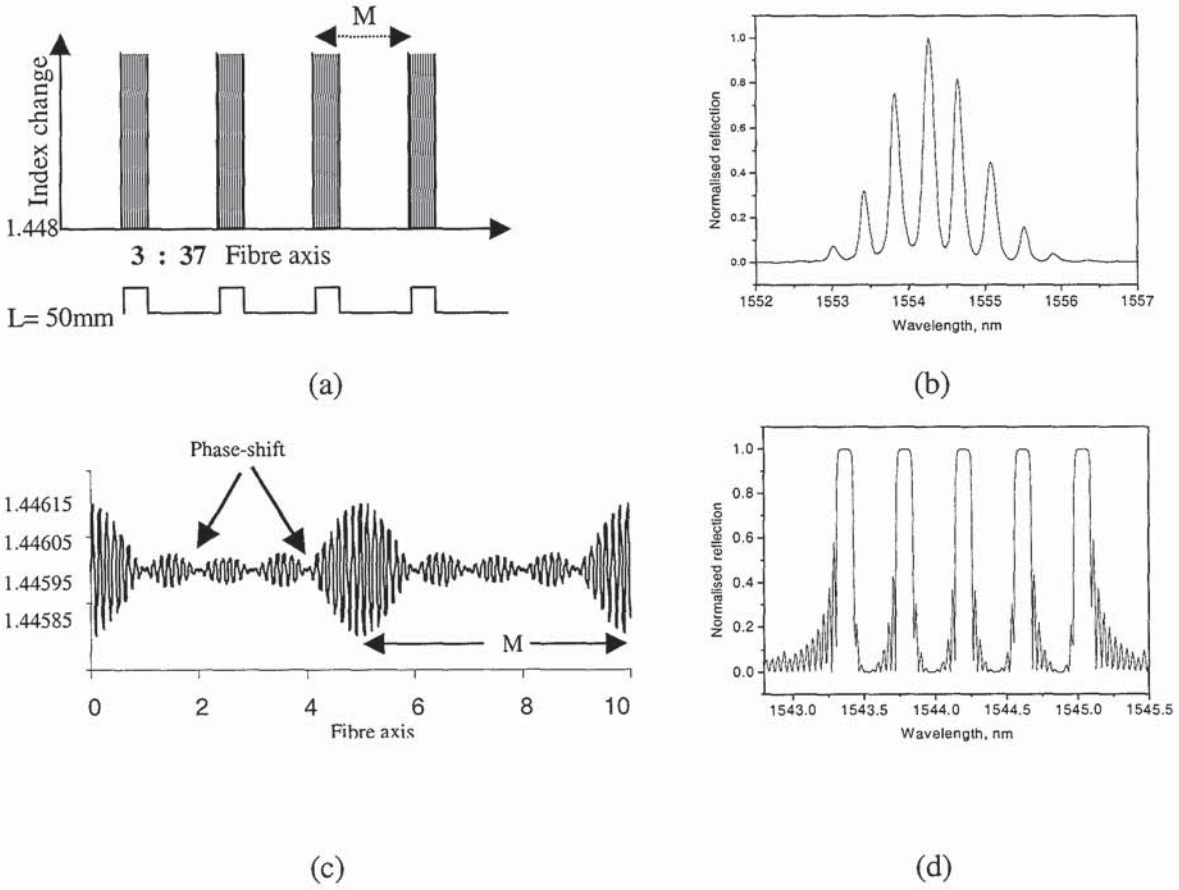

Fig. 4.14: Typical SSFBGs (a) square-shaped index modulation of a 5cm long SSFBG, (b) spectral response of a 5cm long experimentally obtained SSFBG with square-shaped index modulation (c) calculated sinc-shaped index modulation of a 1cm long SSFBG, (d) calculated spectral response of a 5cm long SSFBG with sinc-shaped index modulation.

The SSFBG consist of a cascade of very short similar FBGs, produced using the same uniform period phase-mask. The short-gratings are arranged serially at equal distances apart in a piece of fibre. Because most commercial amplitude masks are designed with 50% duty ratio, it is not possible from the authors experience to obtained dense –channel with the combine use of such amplitude mask and a phase mask. Instead, a point-by-point method of UV-shots (scans) must be used with the desired low (<10%) duty ratio in place of the amplitude mask (i.e. UV should be scanned along the length of the fibre, through the phase mask with <10% duty-ratio). SSFBG spectral responses can be designed and fabricated in practice, with precision, and indeed that has been done during this research.

However, for sinc-SSFBG each of the short similar FBGs is *individually-apodised.* The apodisation of each FBG is implemented using a sinc-profile. To produce the sinc-SSFBG, a phase-mask dithering technique of apodisation is used, and therefore the optimal dithering voltage must first be established. The voltage that is used to produce phase-shifts also needs to be identified. Whilst the dithering voltage shakes the phase mask, the phase-shift voltage normally causes a skip of the translation stage during the inscription. As soon as the two voltages are identified the remaining process is similar to producing apodised FBG. The only difference is that low frequency index modulation is introduced instead of the one large envelope, and each of the sub-gratings needs to be sinc-apodised.

Just like FBGs, these dense channel SSFBGs are highly reproducible. It is to be recommended that when producing, SSFBGs, spectral response should first be designed by simulation, before the actual implementation.

Table 4.3 provides the equations representing the index modulation for the Bragg gratings discussed. These equations defined the index modulation that was controlled by the computer to obtain the respective gratings. Where, N+1 is the number of channels, L is the entire grating length, M is the period of index maxima, m is an integer, and Δn_0 is the index modulation depth.

Standard FBG [145]	$n(z) = n_0\left[1 + \sigma(z) + h(z)\cos\left(\frac{2\pi}{\Lambda_0}z + \phi(z)\right)\right]$	.....(4.7)
Chirped FBG	$n = n_0 + \Delta n_0(z)\cos\left(\frac{2\pi}{\Lambda(z)}z + \varphi/2\right)$	.....(4.8)
Moire	$n = n_0 + \frac{\Delta n_0}{2}\cos\left[\frac{2\pi}{\Lambda_1(z)}z\right] + \frac{\Delta n_0}{2}\cos\left[\frac{2\pi}{\Lambda_2(z)}z + \varphi\right]$	.....(4.9)
Standard SFBG	$n(z) = n_0 + \Delta n_0\left[\frac{1}{2} + \sum_{m=0}^{\infty}\frac{2}{(2m+1)\pi}\sin\left(\frac{2(2m+1)\pi}{L/M}z\right)\right]\cos\left(\frac{2\pi}{\Lambda_0}z\right)$	....(4.10)
Sinc-SSFBG	$n(z) = n_0 + \Delta n_0\frac{1}{N+0.5}\left[\frac{1}{2} + \sum_{m=1}^{N}\cos\left(\frac{2mM\pi}{L}z\right)\right]\cos\left(\frac{2\pi}{\Lambda}z\right)$	....(4.11)

Table 4.3: Index modulations for Standard FBG, Chirped FBG, Chirped-Moiré FBG, Standard SFBG, and Sinc-Superstructured FBG

These modulations have been imposed on the fibre to achieve a desired grating using computer control.

4.6 Grating spectral measurements

To start measurement using Optical Spectrum Analyser (OSA) a piece of "test" fibre of similar material and length to that of grating-containing fibre should be (and has been) used for the light source spectral flattening (i.e. normalization). Once the spectral response of the "test" fibre is recorded, an OSA-generated flat signal is then placed at around 0dB level. The difference in amplitude of the flat signal (at 0dB) and that of the spectral response of the "test" fibre is then calculated and stored in the OSA. Such difference is then added to the spectral response of any fibre that is connected afterwards. If the connected fibre is of the same length with the "test" one used and has no grating within it, then the resultant signal will be flat spectrum, at 0dB amplitude. By flattening the OSA-displayed spectrum of the light source before grating measurement, and at the same time taking note of the signal amplitude, any changes away from the flat response (at 0dB), after replacing the "test" fibre with grating-containing fibre could easily be associated with the grating. Assuming insignificant connection loss at the input to the grating-containing fibre, all changes to the amplitude of the

signal, from what it was when the "test" fibre was connected (i.e. 0dB), will be an indication of the grating-induced loss and indeed all spectral-changes from flat-line will clearly reflect the grating characteristics. For the flattening to be useful and effective, both the "test" and the grating-containing fibres must be of the same length; also, the light source output needs to be stable. The reader should note that the author has not measured the losses associated with the gratings at the time these experiments were being conducted, but, in retrospect, such measure should have been carried out. Fig. 4.15 shows the set-up for grating spectral measurement (interrogation). Both reflection and transmission characteristics have been recorded by the author using this type of set-up.

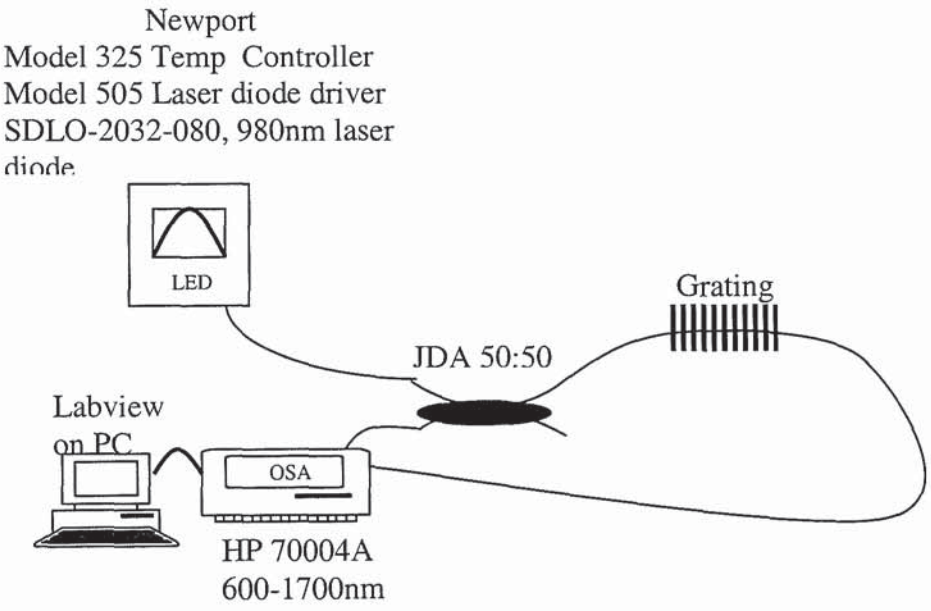

Fig. 4.15: The interrogation set-up for grating-based sensors used for both transmission and reflection measurement.

4.6.1 Strain measurement

To measure axial strain, the fibre containing the device was first positioned straight (with 0.0 m^{-1} curvature). One end of each device-containing fibre was fixed firmly, whilst the other end was attached to a micrometer-drive by which axial strain could be applied. The devices were subjected to strains ranging from 0 to 7.2 x 10^3 $\mu\varepsilon$ in incremental steps of either 400 $\mu\varepsilon$ or

500 $\mu\varepsilon$ and the spectral responses were recorded at each step. Strain measurement for each FBG-sensor was carried out within two minutes during which each grating was placed in a temperature-controlled environment.

4.6.2 Temperature measurement

For temperature measurement, heat was applied to the device, or devices in turn, using an in-house Peltier heat pump (of 1% resolution) controlled by a thermo-electric temperature controller. The device is normally placed inside a v-grove of about 150μm depth machined in the middle of the 1cm width of the 1cm x 7cm x 0.5cm heating-element along its 7cm horizontal length. The arrangement was enclosed in a 3cm x 9cm x 2.5cm plastic box so as to maintain a constant temperature across the length of the in-fibre device, and before the application of heat, each of the two fibre-ends protruding out from the middle of the Peltier-box was fixed to avoid changes in the axial strain during temperature measurements[9]. In most cases, temperature was varied, in the selected direction, in steps of ~5°C from an arbitrary starting value: the corresponding spectral responses were recorded at each step.

4.6.3 Surrounding refractive index (SRI) measurement

To measure the SRI, each of the in-fibre devices was initially fixed into a straight v-groove machined in an aluminium metal plate. The depth of the groove is at least 2 times the diameter of the fibre. The ends of the fibre that protrude outside the groove were fixed in order to avoid changes in strain on the device. The aluminium plate containing the groove was placed on a metallic heat-conducting platform (i.e. aluminium table) such that a stable temperature was maintained around the device. Oils of different refractive indices, ranging from 1.3 to 1.478, were applied in-turn around the device by filling the v-groove: the corresponding spectral responses were recorded using a computer and an OSA. After each measurement using an oil of a particular refractive index the device was cleaned using de-ionised water and methanol until the spectral response of the device completely matched the original spectrum that was recorded when the dried device was surrounded by air only.

[9]. The particular value of other parameters (such as strain) is not important as long as there is consistency in their value during measurements.

4.6.4 Recording grating wavelength shifts

As soon as grating response is recorded using OSA, it is possible to identify the peak wavelength of the grating. There are several ways to measure grating peak wavelength, including the selection of highest or the lowest point on the peak for reflection or transmission respectively. Also, by differentiating the spectrum, zero crossing points have often been identified and used. But, for broad spectral peaks it is possible that there might be a number of highest/lowest points that have the same value and thus it might be difficult to ascertain the most relevant point, even through differentiation. To this end, parabolic fits have been used to measure the centroid of most peaks, especially for the LPGs. Fitting a parabola provides more accurate indicator of the spectral position of grating peaks in comparison to highest/lowest point selection. The parabolic fit also takes into account any changes in the symmetry of the peaks

4.7 Conclusion

In this chapter the principle behind grating fabrication has been discussed starting from index modulation to its practical implementation. The focus was on the UV-scanning methods of fabrication that has been adopted for the research presented throughout this thesis. The fabrication of standard FBGs, LPGs and SFBGs was first considered and the discussion that followed focused on the inscription of specialised types of gratings (i.e. the derivatives). These special gratings include the Apodised FBGs, Chirped FBGs, Chirped-Moiré FBGs and Sinc-Sampled FBGs. All these gratings were successfully fabricated and their profiles demonstrated.

On apodised FBGs, both simulation and experimental results were provided and compared to support the analysis. In particular, different lengths of FBGs were apodised by using Gaussian and Blackman profiles –the results suggest that over 50dB rejection is theoretically achievable. Experimentally, however, over 19dB rejection has been demonstrated.

The poorer out of band rejection in the experimental results [i.e. ~19dB in 4.10(d)] as against the simulation results [i.e. ~40dB in Fig. 4.7(a)] is believed to be associated with a number of experimental sources of error, including (a) poor stability of the fabrication optics, (b) the five mirrors used, some of which were placed more than 1.5m apart, with each contributing to the

beam alignment error, (c) the effect of undesired vibration on the mask and fibre -emanating from laser cooling system and piped water, (d) the non-uniform laser-beam intensity applied across the grating length resulting from (i) poor alignment, and (ii) poor laser beam quality, (e) dirt or even phase/amplitude errors associated with the phase-mask, (f) resolution of the translation stage or (g) the rounding errors in the control software for translation stage electronics and (h) response error in the electronics etc.

4.8 Reference:

119. J.D. Prohaska, E. Snitzer, S. Rishton, and V. Boegli, "Magnification of mask fabricated fibre Bragg gratings," *Electron. Lett.*, vol. 29, no. 18, pp. 1614-1615, Sept 1993.

120. Q. Zhang, D.A. Brown, L. Reinhart, T.F. Morse, J.Q. Wang, and G. Xiao. "Tuning bragg wavelength by writing gratings on prestrained fibres," *IEEE Photon. Technol. Lett.*, vol. 6, no. 7, pp. 839-841, July 1994.

121. K.P. Chen, and P.R. Herman, "Enhancement and tuning of fibre Bragg grating reflection by 157 nm F-2-laser post exposure," *Electron. Lett.*, vol. 37, no. 13, pp. 822-823, Jun 2001.

122. P.-Y. Cortes, F. Ouellette, and S. LaRochelle, "Intrinsic apodisation of Bragg gratings written using UV-pulse interferometry," *Electron. Lett.*, vol. 34, no. 4, pp. 396-397, 1998.

123. P. Varming, J.B. Jensen, et al, "A new method for fabrication of advanced UV written Bragg gratings," *Bragg Grating meeting*, Stressa, Italy, paper BWA5, 2001.

124. X. Shu, B.A.L. Gwandu, L. Zhang, and, I. Bennion, "Ultra-long-period fibre gratings," Proc. 27th *Eur. Conf. Opt. Comm.* (ECOC'01), Amsterdam, Paper We.P.4, pp. 386-387, 2001.

125. H.J. Patrick, C.G. Askins, R.W. McElhanon, and E.J. Friebele, "Amplitude mask patterned on an excimer laser mirror for high intensity writing of long period fibre gratings," *Electron. Letts*, vol. 33, no. 13, pp. 1167-1168, Jun 1997.

126. B. Malo, K.O. Hill, F. Bilodeau, D.C. Johnson, and J. Albert, "Point-by-point fabrication of micro-bragg gratings in photosensitive fibre using single excimer pulse refractive-index modification techniques," *Electron. Lett.*, vol. 29, no. 18, pp. 1668-1669, 1993.

127. D.D. Davis, T.K. Gaylord, E.N. Glytsis, and S.C. Mettler, "CO_2 laser-induced long-period fibre gratings: spectral characteristics, cladding modes and polarisation independence," *Electron. Lett.*, vol. 34, no. 14 , pp. 1416-1417, 1998.

128. G. Rego, J.A.R. Fernandes, J.L. Santos, H.M. Salgado, and P.V.S. Marques, "New technique to mechanically induce long-period fibre gratings," *Opt. Comms*, vol. 220, no. 1-3, pp. 111-118, May 2003.

129. N. Godbout, X. Daxhelet, A. Maurier, and S. Lacroix, "Long-period fibre grating by electrical discharge," *Proc. of 24th European Conference on Optical Communication*, pp. 397, 1999.

130. G. Humbert, and A. Malki, "Electric-arc-induced gratings in non-hydrogenated fibres: fabrication and high-temperature characterizations," *Jn. Optics A-Pure and Appl. Opt.*, vol. 4, no. 2, pp. 194-198, Mar 2002.

131. M. Ibsen, M.K. Durkin, M.J. Cole, and R.I. Laming, "Chirped Moire fibre gratings operating on two wavelength channels for use as dual channel dispersion compensators," *IEEE Photon. Technol. Lett.*, vol. 10, no. 1, pp. 84-86, 1988.
132. W.H. Loh, R.I. Laming, A.D. Ellis, and D. Atkinson, "10Gbit/s transmission over 700km of standard single-mode fibre with a 10-cm chirped fibre grating compensator and doubinary transmitter," *IEEE Photon. Technol. Lett.*, vol. 8, no. 9, pp. 1258-1260, 1996.
133. M. Matsuhara, and K.O. Hill, "Optical-waveguide filters: design," *Appl. Opt.*, vol. 13, no. 12, pp. 2886-2888, 1974.
134. B.E. Little, and C. Wu, "Window functions for ideal response in distributed feedback reflection filters," *IEEE Photon. Technol. Lett.*, vol. 9, no. 1, pp. 76-78, 1997.
135. D. Pastor, J. Capmany, D. Ortega, V. Tatay, and J. Marti, "Design of apodised linearly chirped fibre gratings for dispersion compensation," Jn. Lightwave Technol, vol.14, no. 11, pp. 2581-2588, 1996.
136. M. Ibsen, M.K. Durkin, M.J. Cole, and R.I. Laming, "Optimised square passband fibre Bragg grating filter with in-band flat group delay response," *Electron. Lett.*, vol. 34, no. 8, pp. 800-802, 1998.
137. J. Albert, K.O. Hill, B. Malo, S. Theriault, F. Bilodeau, D.C. Johnson, and L.E. Erickson, "Apodisation of the spectral response of fibre Bragg gratings using a phase mask with variable diffraction efficiency," *Electron. Lett.*, vol. 31, pp. 222-223, 1999.
138. K.O. Hill, S. Theriault, B. Malo, F. Bilodeau, T. Kittigawa, D.C. Johnson, J. Albert, K. Takiguchi, and K. Hagimoto, "Chirped in-fibre Bragg grating dispersion compensators: Linearisation of dispersion characteristics and demonstration of dispersion compensation in 100km 10Gbit/s optical fibre link," *Electron. Lett.*, vol. 30, no. 21, pp. 1755-1756, Oct 1994.
139. R. Kashyap, A. Swanton, and D.J. Armes, "Simple technique for apodising chirped and unchirped fibre Bragg gratings," *Electron. Lett.*, vol. 32, no. 13, pp. 1226-1228, Jun 1996.
140. H. Storøy, H.E. Engan, B. Sahlgren, and R. Stubbe, "Position weighting of fibre gratings for bandpass filtering," *Opt. Lett.*, vol. 22, no. 11, pp. 784-786, 1997.
141. W.H. Loh, M.J. Cole, M.N. Zervas, and R.I. Laming, "Compensation of imperfect phase mask with moving fibre-scanning beam technique for production of fibre gratings," *Electron. Lett.*, vol. 31, no. 17, pp.1483-1485, Aug 1995.
142. M.J. Cole, W.H. Loh, R.I. Laming, M.N. Zervas, and S. Barcelos "Moving fibre/phase mask-scanning beam technique for enhanced flexibility in producing fibre gratings with a uniform phase mask," *Electron. Lett.*, vol. 31, no. 17, pp.1488-1490, 1995.
143. R. Feced, and M. Zervas, "Effects of random phase and amplitude errors in optical fibre Bragg gratings," *Jn. Lightwave Technology*," vol. 18, no. 1, pp. 90-101, 2000.
144. K.E. Chisholm et al., "Application of chirped Moire fibre Bragg gratings to quasi-distribuited monitoring of strains experienced by fibre during processing," paper THU6-2, *Proc. SPIE,* vol. 4185, Ofs2000, pp. 600-603, 2000.
145. V. Mizrahi and J.E. Sipe, "Optical properties of photosensitive fibre phase gratings," *Jn. Lightwave Technology*," vol. 11, no. 10, pp. 1513-1517, 1993.

5 Sensing applications of fibre gratings

5.1 Introduction

In this chapter the applications of Fibre Bragg Gratings (FBGs), Long Period Gratings (LPGs), and Sampled Fibre Bragg Gratings (SFBGs) to sensing are discussed in Sections 5.2, 5.3 and 5.4 respectively.

In Subsection 5.2.1, the design and use of advanced FBG-arrays to measure arbitrarily quasi-distributed axial strain is described. The designed array sensor achieved very high spatial and spectral resolutions. However, the quasi-distributed strain sensor has limitations, which stems from its susceptibility to temperature cross-sensitivity. A mechanism to factor out such effects thus became a necessity. To this end, many solutions are proposed and demonstrated in Subsection 5.2.2. Different techniques are adopted for the solution as described in Subsection 5.2.2.1 so as to produce FBG-sensors that can simultaneously measure strain and temperature. The detailed measurements are presented in Subsection 5.2.2.2 and the effectiveness of these dual parameter FBG-sensors is demonstrated in Subsection 5.2.2.3.

In Section 5.3, the sensing applications of some special types of LPGs fabricated in different types of fibre are discussed. In particular, discussion starts on the use of LPGs with harmonic cladding modes. Further investigation focused on LPGs with yet un-reported characteristics, which are demonstrated in both B/Ge co-doped and standard fibres. The use of one of such LPGs to measure the combine effects of various parameters such as strain, curvature, refractive index and temperature is discussed. To explain the behaviour of some of these LPGs a number of modelling exercises were carried out using Matlab and Optiwave^{TM} IFO: some of the results obtained are also described.

LPGs fabricated in double-cladding (3-layer) fibre with potentials for dual-parameter sensing and gain-flattening applications are demonstrated in Subsection 5.3.2. The use of such types of LPG to simultaneously measure refractive index and temperature in particular, are discussed in greater detail.

In Section 5.4, the design and use of SFBG to simultaneously measure the combined effects of temperature and various other parameters are described. In particular, the results of the first demonstration of temperature and index measurement using a single SFBG device are demonstrated in Subsection 5.4.1. In Subsection 5.4.2, the novel applications of SFBG to measure axial strain, temperature and curvature simultaneously are discussed. Within the same subsection, the capability of an SFBG to measure both very large and very small curvature values is successfully demonstrated.

5.2 Fibre Bragg grating (FBG) sensors

The ability to provide real-time information for structural health monitoring of civil, aerospace and maritime engineering structures is an important diagnostic process for preventative maintenance of these structures [146]. There is a growing need for incorporating monitoring instrumentations into structures formed from concrete or modern composite materials. Various types of sensor have been tested for this purpose over the years, the most common of which is the Electrical Strain Gauge (ESG) [146]. Unfortunately, ESGs are susceptible to electromagnetic interference (EMI). In addition, the bulky nature of ESGs makes them unsuitable to be embedded into structures for quasi-distributed strain sensing.

In the past few years, intensive research and development have been carried out on FBG sensing technologies for smart structure applications [147,148,149,150]. In comparison with conventional sensors such as ESGs, FBGs have many attractive features that make them well suited for a wide range of strain measurement applications [151]. They are light in weight, small in size and immune to EMI. Most significantly, FBGs can be fabricated in array forms and used to make an optical data-bus network, which can be wavelength-division-multiplexed. The combination of their multiplexing capability and inherent compatibility with fibre-reinforced composite materials permits in-fibre Bragg gratings to be embedded in a number of important structural materials for smart structure applications.

To date, the most highly research areas of fibre grating applications is the measurement of strain and temperature, separately, and simultaneously. The change in strain or temperature induced on a fibre can be easily determined from the shift in the Bragg wavelength of a

grating, $\Delta\lambda_B$, caused largely by stretching or thermal expansion of the fibre. The change in strain within the fibre is given by [152]

$$\Delta\varepsilon = \frac{\Delta l}{l} = \frac{\Delta\lambda_B}{\lambda_B \xi} \tag{5.1}$$

Where, Δl is the change in fibre length due to strain, l is the initial fibre length, $\Delta\lambda_B$ is the difference between the Bragg wavelengths of the strained and unstrained grating, and λ_B is the unstrained Bragg wavelength of the grating. ξ is the strain optic coefficient, which describes how the refractive index of the fibre changes with strain. ξ has a typical value of $0.78\times10^{-6}\ \mu\varepsilon^{-1}$.

Similarly, the change in temperature of the medium surrounding the fibre is [152]

$$\Delta T = \frac{\Delta\lambda_B}{\lambda_B \kappa} \tag{5.2}$$

Where, κ is the combined thermo-optic coefficient for the fibre which has a value of $6.67\times10^{-6}\mathrm{K}^{-1}$ for germanosilicate fibre.

From the above equations, it is quite easy to calculate the strain or temperature changes induced to the grating. It should be noted that ξ and κ vary with material composition of the fibre.

5.2.1 Compact FBG array sensor

FBG-sensor arrays [153] have been successfully used for a range of smart structure applications, performing quasi-distributed strain monitoring [154,155]. Most of the demonstrated FBG-sensor arrays are capable of spatial resolution of typical values ranging from few centimetres to several meters. However, there are some applications requiring distributed sensors capable of much higher spatial resolution with relative small sensing gauge, for instance, crack detection [156]. FBG based high spatial resolution distributed sensing have been reported by Volanthen et al [157] and LeBlanc et al [158,159]. However, the interrogation techniques that they used are cumbersome to use for real time measurement, limiting the practical implementation for applications particularly where there is cross-sensitivity effects to resolve.

In this section, an implementation of quasi-distributed sensors that employ compact-grating-array structure, offering advantages of arbitrary dynamic range, spectral sweeping range, high spatial resolution and simple interrogation by utilising established WDM technique is discussed. The sensors have been demonstrated for measuring linearly quasi-distributed strain with high spectral and spatial resolutions. Indeed, non-linearly quasi-distributed strain can also be measured using this type of FBG array [160]. This FBG-sensor array interrogation technique, therefore, offers an advantage of high practicability for real applications. The additional advantage is that the array can be designed with specific dynamic range, maximum measurand range, and spatial resolution.

5.2.1.1 Concept of compact FBG-array sensing

The concept of a compact-grating-array is illustrated in Fig. 5.1. The element gratings with different wavelengths are concatenated along a fibre without any physical gaps. The spatial resolution and sensing spectral sweeping-range for quasi-distributed sensing from such a structure are simply defined by the physical length of the element grating and the spectral spacing between the adjacent gratings respectively. The spatial resolution can be as high as 1mm since now it is possible to produce fibre gratings of such a short length but still with sufficiently high reflectivity. However, there are some difficulties in the realization of free-tailoring wavelength, high spectral resolution and incorporating large number of element gratings. The phase-mask grating fabrication techniques have been advanced to the point that gratings of versatile structures are possible. It has been demonstrated that by straining fibre technique, arbitrary wavelength is realizable even by using a wavelength-dedicated phase-mask [161]. A phase-mask grating fabrication system which is capable of arbitrary positioning and scanning UV beam on the fibre has been developed through co-operation with a colleague Dr Y. Liu. The utilization of fibre straining technique on such a system facilitates compact-grating-array fabrication, capable of generating a structure concatenating ten element gratings using a five-wavelength patterned phase-mask.

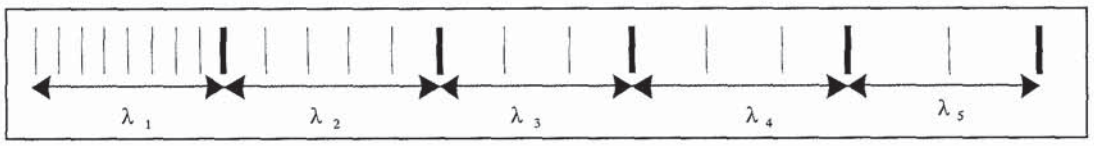

Fig. 5.1: The concept of a compact grating-array indicating period increase.

5.2.1.2 Features of the compact FBG-array

Two designs of compact-grating-array are proposed using the above described grating fabrication system. The phase-mask used in the fabrication is a non-commercial product and produced by the e-beam lithographic technique. The mask contains a group of five 5mm-long concatenated pitch-patterns of different periods denoted by Λ_i (i= 1,2...5), as shown in Fig. 5.2(a). A direct continuous UV beam scan across this phase-mask will allow for production of a compact-grating-array consisting of five gratings of Bragg wavelengths from 1548nm to 1562nm with a ~3nm spectral spacing. Fig. 5.2(b) shows a typical transmission spectrum of such a grating-array structure. It should be pointed out that the slightly large spectral spacing between the second and third peaks was due to the intrinsic larger period difference between the two corresponding neighbouring mask patterns. This fibre grating-array structure can be used for quasi-distributed sensing offering an intrinsic spatial resolution of 5mm and a total sensing gauge of 2.5cm.

(a)

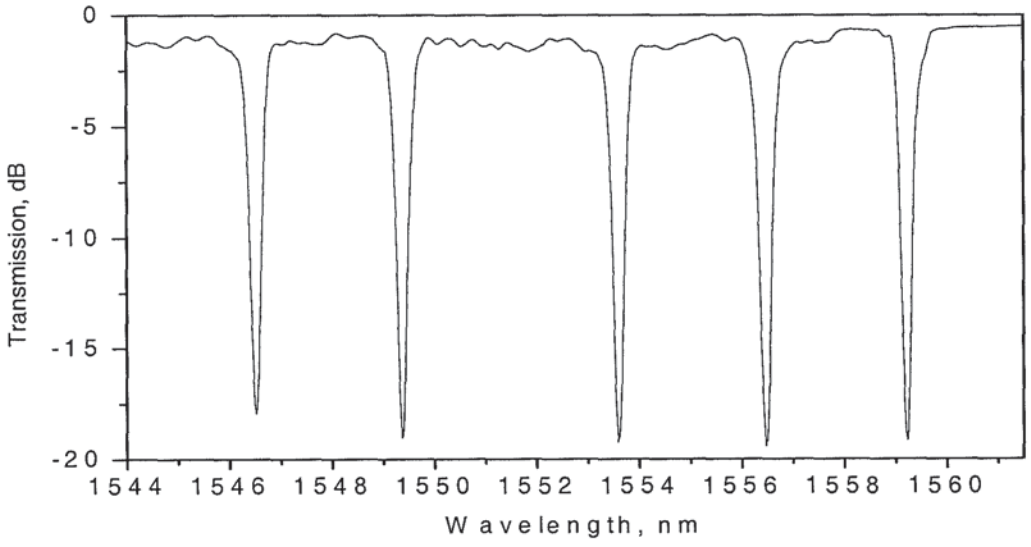

(b)

Fig. 5.2: Five 5mm concatenated pitch-patterns of phase-mask and the resulting spectra after continuous UV scan

In order to increase the spatial resolution, compact-grating-arrays comprising ten 2.5mm-long FBGs have been fabricated using the same phase-mask. This was achieved by a combination of straining fibre and dual-scanning of the UV beam along the mask. Prior to the UV exposure, a strain of 1265.8 $\mu\varepsilon$ was applied to the fibre, which caused a shift to the shorter wavelength of Bragg peak by ~1.5nm. Then, the UV beam scan procedure was programmed in an on-and-off fashion along the phase-mask with a 50% duty cycle as depicted in Fig. 5.3(a). As a result, five 2.5mm-long gratings with 2.5mm physical gap and ~3nm spectral spacing between them were produced along the fibre. The fibre was then released from the strain and the second UV beam scanning was performed using the same 50% duty cycle procedure but with the start-position offset by 2.5mm in order to write the first grating in the first gap. This second scan produced another five 2.5mm-long gratings situated exactly in the five gaps, resulting in a final compact-grating-array structure formed by ten 2.5mm-long gratings with ~1.5nm spectral spacing as shown in Fig. 5.3(b). In comparison with the five-grating-array structure, this sensor has improved the spatial resolution by a factor of two.

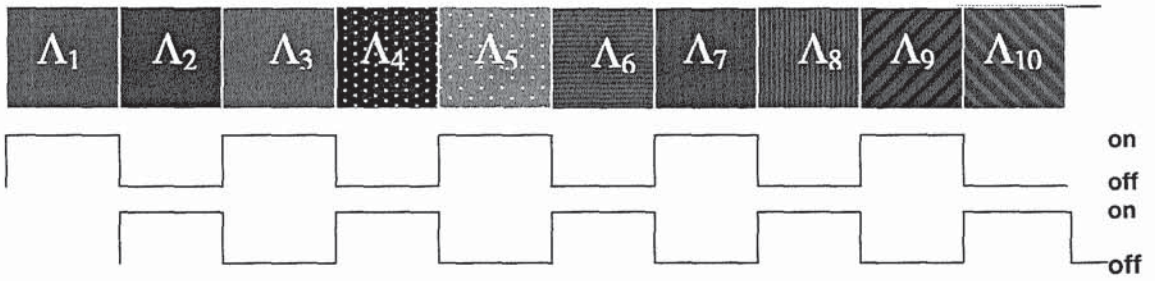

(a)

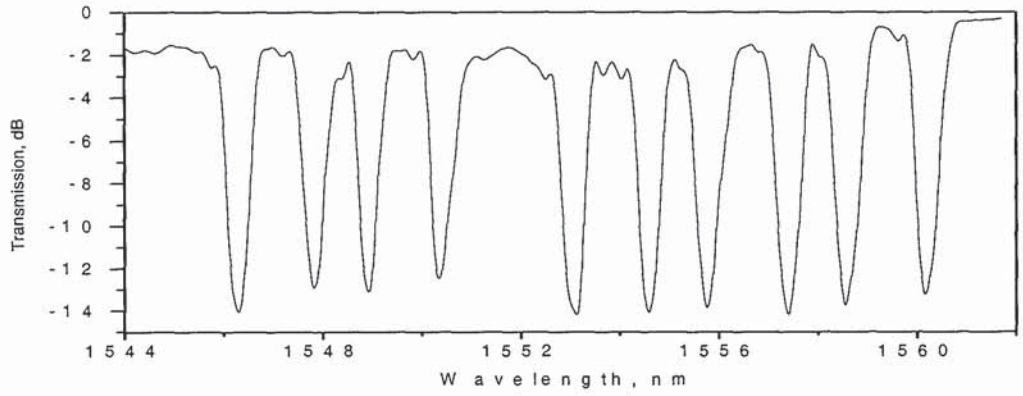

(b)

Fig. 5.3: A spectra of an array of ten 2.5mm gratings designed using on-off UV scan on 5 mask-patterns and the application of tension to the fibre by computer control

5.2.1.3 Quasi-distributed strain sensing using compact FBG array

The quasi-distributed strain sensing experiment was carried out by applying linearly distributed strain to the fabricated grating-arrays. A four-point bending jig was employed to create distributed strain. Fig. 5.4 shows the geometric configuration of this bending jig. The fibre containing 2.5cm-long compact-grating-array was attached to the one side of a 0.5mm thick, 20mm wide and 150mm long spring metal bar. In order to eliminate the slippage effect, the fibre was glued onto the spring metal bar. The glue used was a commercial Acrylite glue, which was applied and left to dry under ambient conditions for about 3 days. The bar was deflected by depressing its centre with a micrometer driver. The deflection distances, h, that were applied are 0, 2.7, 3.2 and 5.2mm for the five-element array, and for the ten-element array the 'h' values used are 0, 1.5, 2.7, and 3.5mm. According to the geometric configuration, the bend-induced strain distribution in the spring metal bar is approximately linear toward the ends of the bar but non-linear in the regions near the centre.

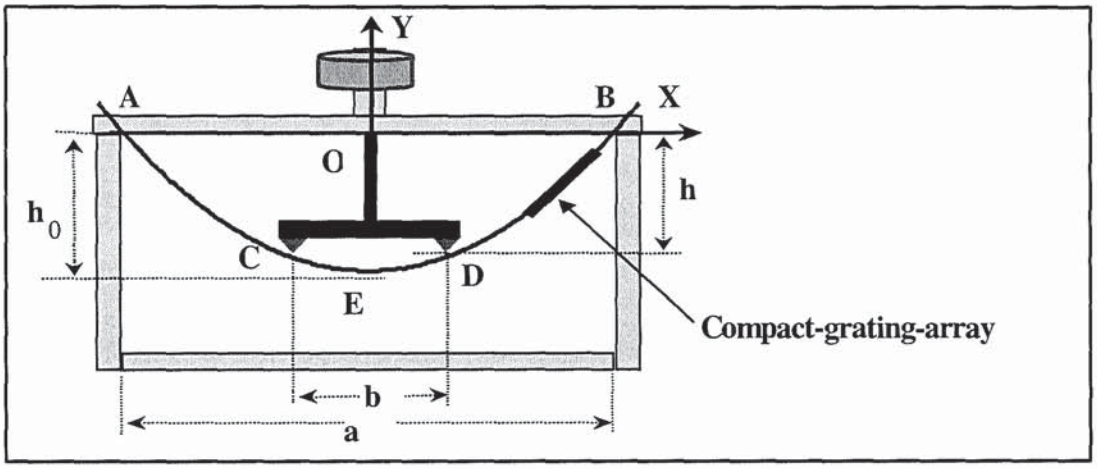

Fig. 5.4: Geometric configuration of a four-point bend jig used to generate distributed strain

When the grating-array was subjected to the distributed strain, the Bragg wavelength of each element grating shifts by an amount according to its physical position along the bent bar. The two compact-grating-arrays were tested for the linearly distributed strain. Figs. 5.5(a) and (c) show the transmission spectra of the five- and ten-element grating-arrays respectively, with (dashed line) and without (solid line) strain. It is clear from the figures that, when the arrays were under the strain, the central wavelength of each grating shifts and the spectral spacing between adjacent gratings changes as well. Figs. 5.5(b) and (d) plot the strain (converted from the wavelength shift) against the element grating number in the array for three deflected

positions of the spring metal bar, corresponding to three strain distributions. The plots show that the strain increases with the number of the grating (signifying position) in the array, clearly reflecting the linear distribution[10] of the strain in the spring metal bar. The gradient of the plot increases when the bar deflects more, demonstrating the effectiveness of such

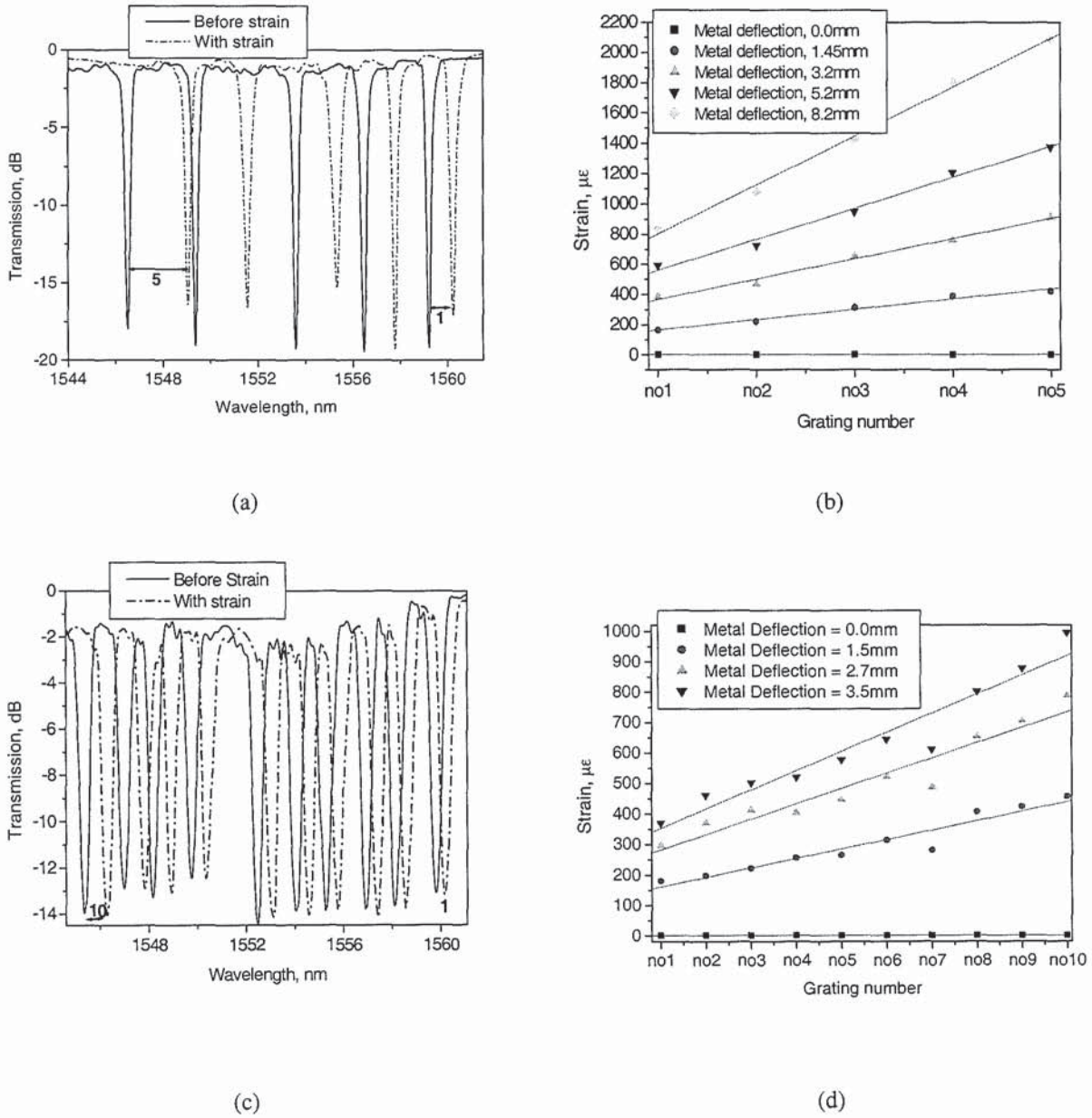

*Fig. 5.5: **(a) The transmission spectra of the 5 element grating-array (with and without linear strain) and (b) the corresponding linear strain plotted with respect to grating number (c) the transmission spectra of the 10 element grating-array (with and without linear strain) and (d) the corresponding linear strain plotted with respect to grating number for the 10 element grating***

[10] Linearly distributed strain in this case means a linear variation of strain with distance.

grating-arrays for quasi-distributed strain sensing. Fig. 5.5(d) also shows that the seventh grating in the ten-grating-array sensor does not fit with the linear plot (straight-line fits) for the high deflection position of the spring metal bar. This suggests that a slippage might have occurred on this grating at that time due to the loosen glue. This in a way demonstrates that it is possible to measure arbitrarily quasi-distributed strain using such a grating-array structure. In comparison with the previously reported FBG array quasi-distributed sensing technique [154], the compact-grating-array approach demonstrated here has achieved ten times higher spatial resolution.

Non-linearly quasi-distributed strain measurement can be performed by attaching the five-element grating-array to a position near the centre of the spring metal bar [160]. It should be pointed out that within its defined maximum measurand range, the element grating in the compact-grating-array is capable of monitoring arbitrary local strain having both positive (stretching) and negative (compression) signs, where these two cases will be reflected by shift of the Bragg peak to the longer or the shorter wavelength respectively. However, the practical maximum measurand range is limited by the spectral spacing between grating peaks. In the cases of the five- and ten-grating arrays demonstrated here, by taking the bandwidth of the gratings into consideration, the maximum measurand ranges of $\pm 4539\mu\varepsilon$ and $\pm 2182\mu\varepsilon$ have been estimated for the two structures respectively. Furthermore, although the spatial resolution can be improved by further shortening the element grating length, the short grating results in broadening its spectral response, thus reducing the spectral resolution. However, for applications where ~4-5mm spatial resolution is adequate, the grating apodisation technique can be employed to improve spectral resolution of the grating-arrays.

In summary, a compact-FBG-array structure, which allows for quasi-distributed strain sensing of high-spatial-resolution, and simple interrogation has been proposed and demonstrated. Two configurations involving five and ten gratings have been fabricated and successfully used to implement a high spatial resolution quasi-distributed strain sensing system. In comparison with other reported sensor structures and techniques such as that in ref. [157] which has been applied to measuring strain, within only a single grating, the compact-grating-array approach may offer a simple and practical solution for real applications as the WDM FBG sensing interrogation method can be directly applied. In addition, this structure permits independent design for spectral sweeping range and spatial

resolution. Further work needs to concentrate on (a) strain analysis in flat structures and correlating such analysis with the measured results from the FBG array, and (b) implementing the same scheme with reduced spacing between FBG centres to ≤ 1mm.

5.2.2 Sensitivity tailored FBGs for simultaneous measurement of strain and temperature.

FBGs are ideally suited for monitoring strain in concrete structures as described in Subsection 5.2.1 due to their small size, low cost, ability to be embedded internally, and multiplexing capabilities. Much research effort has been reported on the use of FBGs to evaluate strain in smart structures [162,163]. However, undesirable temperature responsivity of an FBG can introduce errors in the results of strain measurements. In particular, on a single measurement of Bragg wavelength shift, it is impossible to differentiate the effects due to strain and temperature. For example, in Section 5.2.1.3, the use of FBG array for quasi-distributed strain measurement assumed temperature stability.

In addressing the problem of temperature-induced wavelength shifts, significant efforts have been made in the use of FBGs for simultaneous sensing (or discrimination between the effects) of strain and temperature, ranging from splicing of two FBGs and an LPG to make up a sensor [164], combination of an FBG and a Fabry-Perot interferometric sensor [165], two superimposed dual-wavelength FBGs [166], two FBGs with each written on either side of a splice between two fibres of different diameter [167], use of sampled FBG [168], an FBG combined with EDFAs [169], FBG Fabry-Perot cavities [170], an FBG superimposed with polarization-rocking filters [171], to an FBG made on a splice between two fibres of different chemical compositions and refractive index [172].

Whilst most of these methods are based on the combination of either two FBGs or an FBG with another element, Guan et al's work [172] is based on the use of a single FBG written on a splice joint between corning-28 and ErYb fibre of the same diameter. The technique has significantly reduced cost of the sensing system by permitting the use of only one grating and a single light source. Unfortunately, in such work, two different pieces of fibres are required. In addition, the grating is inscribed on a splice joint which reduces the magnitude of strain that can be measured because of the inherent weakness of splice joints.

In the work presented in this section, a number of novel FBG-based sensors for simultaneous sensing of temperature and strain are presented. The FBGs that make-up the sensor was fabricated in the same piece of fibre that has two different but controlled numerical apertures[11] (NAs) at adjacent sections (0.117 & 0.226). The difference in NA (0.11) was achieved by multiple scan of one section of the FBG with UV light until a large increase in the effective refractive index (e.g. 0.0176) is realised before either extending the FBG length or writing another type of FBG at the adjacent section. The FBG possess two main Bragg reflection peaks that, as will be described herein, have the same strain but remarkably different (up to 4.5pm/°C differences) but controllable temperature-responses that permit the simultaneous measurement of the two parameters. These sensors have the added advantage that they can measure axial strain of large magnitude in comparison to competing devices.

5.2.2.1 Sensing principle and sensor configurations

To produce the sensing device, a number of methods have been adopted. In general the concept is to produce either one FBG with two parts that have different temperature coefficients or two types of FBG that are physically not-separated but spectrally distinguishable and showing two Bragg reflection peaks with different temperature coefficients.

Both parts of the device are fabricated within the same piece of fibre that has the same core-diameter, as demonstrated in the typical sensor configuration[12] shown in Fig. 5.6. Thus, the axial strain responses of the two peaks are expected to be similar [172]. The contribution to wavelength shifts from strain and temperature can then be calculated simultaneously using the well-known matrix equation

$$\begin{pmatrix} \Delta\lambda_{peak_L} \\ \Delta\lambda_{peak_R} \end{pmatrix} = \begin{pmatrix} K_{\varepsilon_{Peak_L}} & K_{T_{Peak_L}} \\ K_{\varepsilon_{Peak_R}} & K_{T_{Peak_R}} \end{pmatrix} \begin{pmatrix} \Delta\varepsilon \\ \Delta T \end{pmatrix} \quad \ldots\ldots\ldots \quad (5.3)$$

[11] NA = $\sqrt{n_{co}^2 - n_{cl}^2}$ where n_{co} and n_{cl} are the core and cladding refractive indices, respectively. The change in the refractive index of the fibre-core has not been measured experimentally, but is almost obvious that there is increase in the core refractive index in view of the well-known UV absorption effect. The wavelength shift recorded, however, suggest that the index increase in the core can be up to 0.0125 which suggests that there is a change in NA at the section of fibre which contains FBG.

[12] Note that there is no physical gap between the two parts of the sensing device.

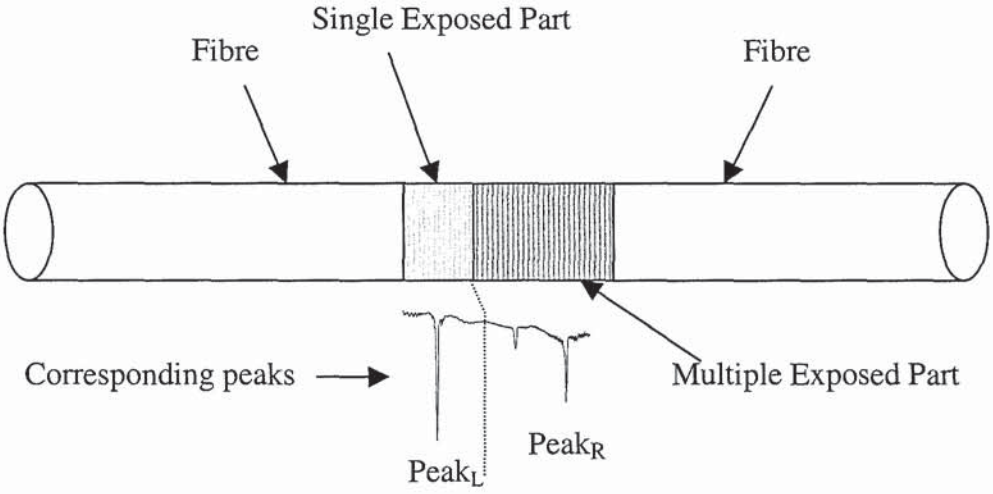

Fig. 5.6: The configuration of the strain and temperature sensor

Where, $K_{\varepsilon_{Peak_L}}$, $K_{\varepsilon_{Peak_R}}$ and $K_{T_{Peak_L}}$, $K_{T_{Peak_R}}$ are the respective strain and temperature coefficients of peak$_L$ and peak$_R$ (i.e. the main Bragg peaks on the left- and the right hand side, respectively). $\Delta\lambda_{Peak_L}$ and $\Delta\lambda_{Peak_R}$ are the respective wavelength shifts of peak$_L$ and peak$_R$, while $\Delta\varepsilon$ and ΔT are the applied strain and temperature changes. Clearly, if the strain coefficients are the same, then the temperature coefficients of the two peaks need to be different in order for the matrix to have a solution.

5.2.2.2 Inscription of sensors, and measurement of strain and temperature coefficients

Throughout Section 5.2 terms describing different types or grouping of Bragg gratings are used. Table 5.1 describes each of the types of grating that are likely to be mentioned in this sub-section. The name of each of the FBG-type is given in the left column and the corresponding details are provided in the right column.

Type	Details
Type I	These are the most commonly produced FBGs normally fabricated by a single or few UV scans using moderate laser intensity on a photosensitive, often hydrogen loaded, fibre.
Type I over-exposed	Over-exposed FBGs are produced in a hydrogen-loaded fibre with many more UV Scans in comparison to the Type I FBGs. During its fabrication, there is a continuous-shift towards the longer wavelength before the final shift to the shorter wavelength. Details of these will become clearer in Section 5.2.2.2 (Options D & F).
Type II	Type II gratings often called the damaged gratings and is produce using single pulse fluence of high energy (>0.5J/cm^2). The grating appears to be broad and has many spectral features or the grating profile. It has strong coupling into the cladding.
Type IIA	Type IIA FBGs are produced in a non-hydrogen-loaded fibre with many more UV Scans in comparison to the Type I FBGs. During its fabrication, there is usually a slight shift towards the longer wavelength at the onset, followed by a continuous shift to the shorter wavelength. Details of these will become clearer in Section 5.2.2.2 (Option C).

Table 5.1: Grating types and their description

The FBG-sensors used in this work were UV-written in both hydrogen (H_2)-loaded and non-H_2-loaded B/Ge and H_2-loaded standard SMFs using a uniform-period phase-mask and a CW frequency-doubled argon laser with an output power of 102mW. The inscription was implemented by scanning the UV beam on the fibre lengthwise through the phase-mask. Each of the gratings investigated is ~ 15mm in length. Several FBG-sensors were fabricated for the experiments. After the final inscription, the sensors were annealed at 110°C for 45 hours in an Oven.

For the experiments discussed in this subsection the FBG components that make up a single sensor are produced in the same piece, of the same type of fibre. In producing the FBGs that formed the sensors, six options were tried. These options are:

(A) Multiple UV scan without the phase-mask on H_2-loaded fibres (B/Ge co-doped and standard SMF) to produce an FBG followed by a final UV scan that overlap both the over-exposed and un-exposed parts of the fibre.

(B) Multiple UV scan without a phase-mask (post-processing) on a newly formed FBG fabricated in H_2-loaded B/Ge fibre.

(C) Multiple UV scan on a non-H_2-loaded B/Ge fibre through a phase-mask (to obtain Type IIA FBG [173]), followed by extension of FBG length during the final UV scan (to obtain a Type I FBG).

(D) Multiple UV scans on a H_2-loaded fibre through a phase-mask (to obtain an over-exposed FBG) followed by the extension of grating length during the final UV scan (to obtain a Type I FBG).

(E) Double multiple UV scan through the phase mask to produce two FBGs, in both cases, on the same piece of fibre with no gap between the FBGs, first when the fibre is H_2-loaded (leading to an overexposed FBG), and subsequently after the H_2 is removed by annealing (leading to a Type IIA FBG).

(F) Double multiple UV scan through the phase mask to produce two FBGs, in both cases, on the same piece of fibre with no gap between the FBGs, first before the fibre is loaded with H_2 (leading to a Type IIA FBG), and subsequently after the FBG-containing fibre is hydrogenated (leading to an overexposed FBG). This is essentially a reverse of Option-E.

Each of the options above was followed with a view to obtaining two FBG peaks that have different temperature coefficients. In all the fibres, the aim is to raise or reduce the effective index of the fibre core in the grating section through the use of prolonged UV exposure.

In all of the measurements discussed herein, the spectral responses of the FBG-sensors were measured using a broadband LED light source and a HP70004A Optical Spectrum Analyser (OSA) with a resolution of 0.1nm. Furthermore, in all the experiments carried out in this section to measure strain, the technique explained in Subsection 4.6.1 was followed. Similarly, the technique explained in Subsection 4.6.2 was followed for measuring temperature of range 22°C to 102°C.

Option A: *Multiple UV scan without the phase-mask on H_2-loaded fibres (B/Ge and standard SMF) to produce an FBG followed by a final UV scan that overlap both the over-exposed and un-exposed parts of the fibre.*

To produce FBG-sensors using this option, a short length of fibre was pre-exposed to UV for a over 2 hours without phase-mask (~10mm), followed by writing an FBG to overlap both the non-pre-exposed (~5mm) and the pre-exposed parts of the fibre. As long as a high index change of the section is achieved, the responsivity of the grating written on such section will change accordingly[13]. The two sides of the same grating have two different refractive indices leading to the grating having two Bragg peaks: $peak_{Left}$ ($peak_L$) and $peak_{Right}$ ($peak_R$) which are used for the measurements. Figs. 5.7(a) and (b) show the spectral responses of the FBG-sensor obtained in B/Ge and standard SMF fibres respectively. As expected, positive index change was induced by the pre-exposure. In particular, the separations between $peak_L$ and $peak_R$ of the FBG-sensor were observed to be ~6.44- and ~6.9nm for H_2-loaded B/Ge- and standard telecom-fibres that were pre-exposed for 80 and 185 minutes respectively.

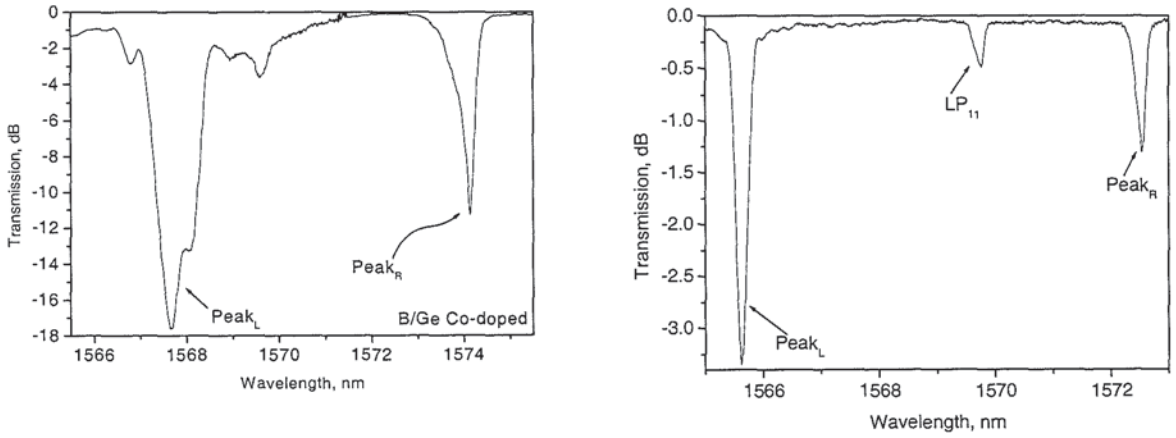

(a) Sensor1 (b) Sensor2

Fig. 5.7: The spectral responses of Sensor1 and Sensor2 produced in H2-load fibre using optionA. (a) in B/Ge fibre, (b) in standard SMF

Figs. 5.8(a) and (c) on the on the one hand, and Figs. 5.8(b) and (d) on the other plot the strain and temperature responses of the FBG-sensors 1 and 2 fabricated in B/Ge co-doped and standard SMF respectively. Each of the dual FBG peaks shifted towards longer wavelengths with increasing strain yielding similar sensitivities of ~9 x 10^{-4} $nm/\mu\varepsilon$ for the dual FBG peaks

[13] responsivity will reduce with index increase, but the relationship is non-linear

in H_2-loaded B/Ge (Sensor1), and ~8 x 10^{-4} $nm/\mu\varepsilon$ in respect of dual FBG peaks obtained in the standard SMF (Sensor2). It can be seen from the parallel nature of the linear-fits that, for each fibre, similar strain responsivity was recorded clearly due to the fact that the diameter of the fibre is the same and in fact the strain applied is exactly the same for both parts of the overlapping grating [172]. The rise in the value of the core refractive index was not sufficient enough to change the strain-optic coefficient of the fibre.

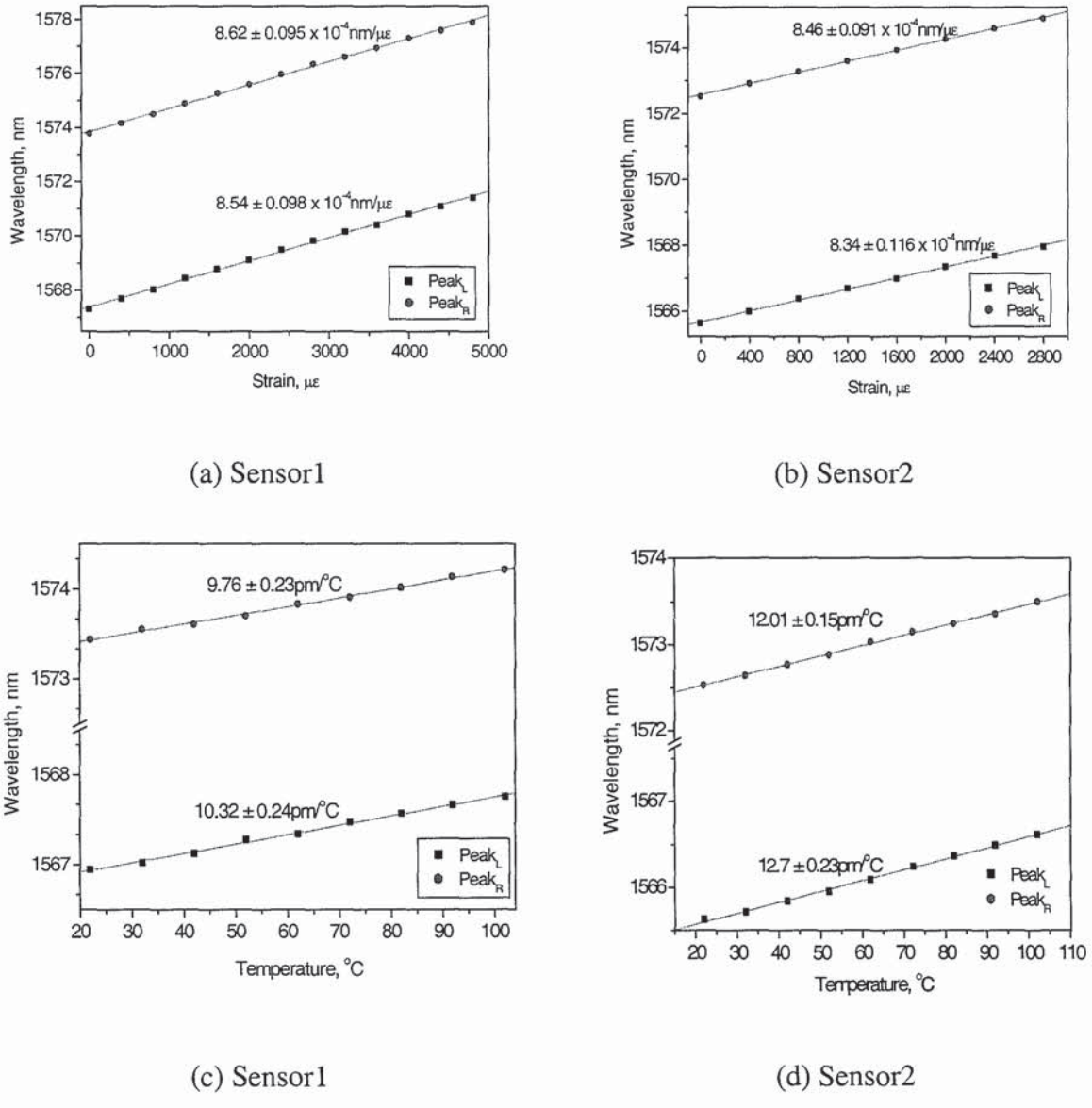

Fig. 5.8: Wavelength shift plotted against strain, and temperature for Sensor1 and Sensor2; (a) and (b) for strain measurements, (c) and (d) for temperature measurements

It is also clear from the Figs. 5.8(c) and (d) that the temperature responses are linear, and the wavelength shifts with respect to temperature for the dual peaks of each FBG-sensor are also

similar, as indicated by the linear fits. The matrix of coefficients therefore will clearly not be well-conditioned for the case of the sensors produced using OptionA in either type of fibre.

***OptionB**: Multiple UV scan without a phase-mask (post-processing) on a newly formed FBG fabricated in H_2-loaded B/Ge fibre*

In this arrangement which is aimed to raise the refractive index of the fibre core, the FBG was first fabricated in a hydrogen-loaded B/Ge fibre followed by immediate multiple UV exposure of the grating without phase mask. The multiple exposures led to, first, a shift to the longer wavelength of the grating peak and subsequently followed by the complete erasure of the FBG-sensor as shown in Fig. 5.9. With the grating erased, increased number of UV scans did not yield to any visible change in the grating spectra. Obviously this grating cannot be used for any sensing application in its erased form. A similar behaviour can be obtained in the standard SMF-based FBGs owing to the fact that the UV light scanned on the fibre serve to reduce the modulation depth of the grating.

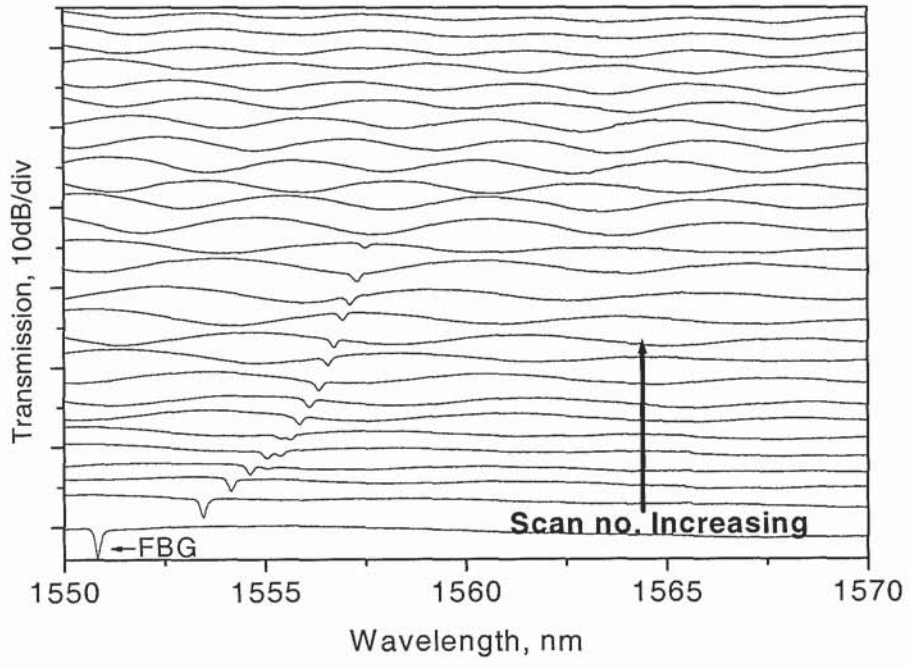

Sensor3

Fig. 5.9: The spectral evolution showing the effect of multiple scan (without a phase mask) over the newly formed Bragg grating in a hydrogen-loaded B/Ge co-doped fibre

***Option C**: Multiple UV scan on a non-H_2-loaded B/Ge fibre through a phase-mask (to obtain Type IIA FBG), followed by extension of FBG length during the final UV scan (to obtain a Type I FBG)*

For this fabrication option, a non H_2-loaded B/Ge fibre was used to produce an FBG-sensor via the process of multiple UV scan on the fibre through the phase mask. During the multiple exposure, the FBG shows no shift of the Bragg peak to longer wavelength despite prolonged multiple UV scans, instead, a small shift to the shorter wavelength of the FBG peak (by ~0.4nm) was observed after the multiple-scans for ~180 minutes, as shown in the evolution spectra featured in Fig. 5.10 (each spectrum was recorded at a time interval of 250sec during UV scanning). This wavelength shift indicates a very small index change, suggesting a Type IIA FBG. Further extension of the FBG length from 10mm to 15mm during the final UV scan did not lead to appreciable wavelength separation between the expected, and the existing Type IIA FBG peak. Therefore this sensor cannot on its own be used for dual parameter sensing purposes.

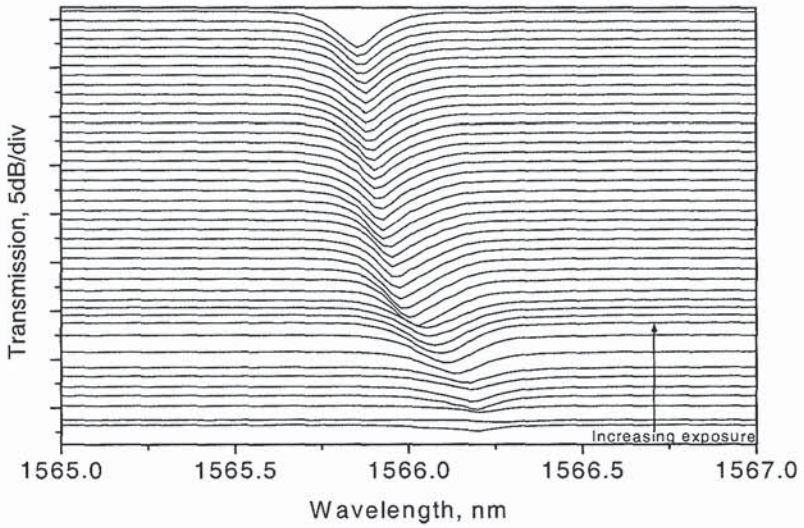

Sensor4

Fig. 5.10: The spectral evolution of Sensor4: a Type IIA FBG in B/Ge fibre produced using Option C (250sec per spectrum, totalling 180 minutes)

In a separate experiment the temperature response of a Type IIA grating was measured; the results indicate a temperature coefficient of ~12.24pm/°C which is slightly higher than that of Type I FBG produced in a H_2-loaded B/Ge co-doped fibre (~11pm/°C).

Option D: *Multiple UV scan on a H_2-loaded fibre through a phase-mask (to obtain an over-exposed FBG) followed by the extension of grating length during the final UV scan (to obtain a Type I FBG)*

This option involves the writing of a 10mm long FBG with a phase-mask followed by repeated UV scanning exposure under the same condition until an FBG is obtained and the Bragg peak shifts remarkably to the longer wavelengths, followed by an increase in the length of the FBG to ~15mm during the final UV scan.

It may be observed in Fig 5.11(a), which shows FBG evolution, that for H_2-loaded B/Ge fibre, the peak wavelength of the FBG obtained shifts to the longer wavelengths with increasing number of repeated UV exposures -indicating the inducement of positive index change. As exposure continues, the grating reached its reflectivity saturation level (>20dB) with relatively large line-width. The FBG peak then starts reducing in strength and line-width while ghost mode[14], LP_{11} [174] starts to form at ~ 2.9nm less than the wavelength of the main Bragg peak and exhibiting some trend characteristics similar to that of the main FBG peak.

As the repeated UV exposure continues both peaks of the FBG reduced to (~0.2dB) reflectivity level, and attained a maximum shift to the longer wavelength. After the reduction in reflectivity, both peaks re-grow again with a shift, but this time, to shorter wavelengths indicating a negatively induced index change. With more UV scanning exposure, the reflectivity of this over-exposed grating saturates and stopped shifting. After obtaining such a peak, the length of the FBG is then extended to 15 mm during the final UV scan using a rather lower UV light intensity (~55mW) which leads to the formation of another grating peak, $peak_L$, at wavelength ~13nm less than that of the main peak ($peak_R$). The low UV intensity used is meant to avoid generating a grating with >8dB reflectivity in view of the high photosensitivity of the fibre. $Peak_L$ corresponds to an ordinary Type I FBG obtainable using a single UV-exposure with a phase-mask.

[14] This peak did not appear in the reflection spectrum when measured

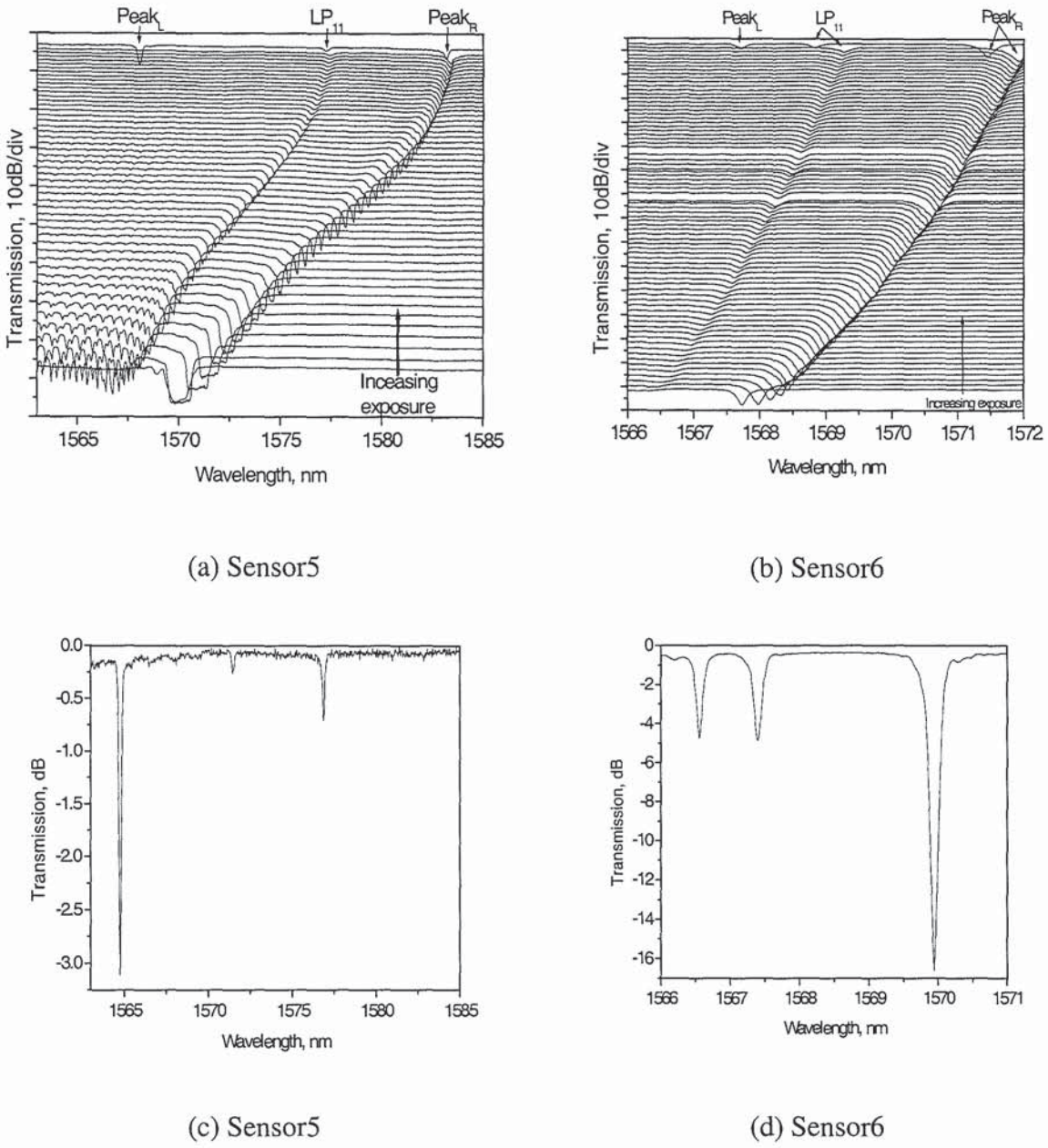

(a) Sensor5

(b) Sensor6

(c) Sensor5

(d) Sensor6

Fig. 5.11: The spectral evolution of FBGs obtained in hydrogen-loaded fibres by multiple scan over the fibre through a phase mask; (a) evolution of over-exposed FBG in B/Ge co-doped, (b) evolution of over-exposed FBG in standard SMF, (c) the spectral response of the FBG in B/Ge fibre after annealing, (d) the spectral response of the FBG in standard SMF after annealing. Each of the offset spectra in (a) and (b) were recorded after 167-, and 250-seconds of UV exposure for the two fibres leading to a total of 142-, and 180-minutes of scanning exposure respectively.

In H_2-loaded standard SMF, a positive index change was also observed as shown in Fig 5.11(b). However, in this fibre, although it was exposed to UV for 83 minutes longer[15] than

[15] Sensor6 (in SMF) was produce by 250 minutes of UV exposure while Sensor5 (in B/Ge) was produced by 167 minutes.

B/Ge type the final shift of the FBG peak that indicates the formation of over-exposed grating was not observed, but as usual a shift was noticed after the scanning has stopped. For this fibre, the maximum separation between $peak_L$ and $peak_R$ obtained was only ~ 3.7nm, which is clearly much less than that observed on the H_2-loaded B/Ge fibre (~14nm) as shown in the spectral response displayed in Fig. 5.11(c) and Fig. 5.11(d): Fig. 5.11(c) and 5.11(d) were the resulting spectral responses after the two FBGs produced in B/Ge and standard SMF respectively were annealed. It can be deduced, from the UV-induced wavelength shifts, that with the H_2-loaded standard SMF, only ~0.00356 index change has been induced. This is more than three times smaller as compared with the ~0.0125 index change induced in the H_2-loaded B/Ge fibre.

During the strain measurements, the positions of $Peak_L$ and $Peak_R$ were extracted from each recorded spectrum and are plotted against the applied strain as shown in Figs. 5.12(a) and (b). Figs. 5.12(a) and (b) provide plots of the wavelength shifts against applied axial strain for Sensor5 and Sensor6 in B/Ge and standard fibres respectively.

Similarly, during temperature measurements, the positions of $Peak_L$ and $Peak_R$ are extracted from each of the spectral responses and are plotted against temperature, as shown in Figs. 5.12(c) and (d): Figs. 5.12(c) and (d) provide plots of the wavelength shifts against temperature for the Sensor5 and Sensor6 in B/Ge and standard fibres respectively: the two fitted lines in each case indicates the best linear fit to the data points. The inset to Fig. 5.12(c) is the re-plot of the same figure where the origins of the linear fits are brought close to each other. The inset to Fig. 5.12(b) and (d) in each case shows the spectral responses from which the plotted data was extracted. It is clear from the figures that for each FBG all the peaks shifted towards longer wavelengths with increasing temperature or strain.

Whilst $Peak_L$ and $Peak_R$ belonging to each of the gratings of Sensor5 in B/Ge fibre posses significantly different temperature sensitivities (7.5pm/°C & 10.8pm/°C), there is almost insignificant responsivity difference for similar peaks of the Sensor6 obtained with H_2-loaded standard SMF (12.55pm/°C down to 12.33pm/°C). Therefore Sensor5 as against Sensor6 can provide a dual parameter sensing capability.

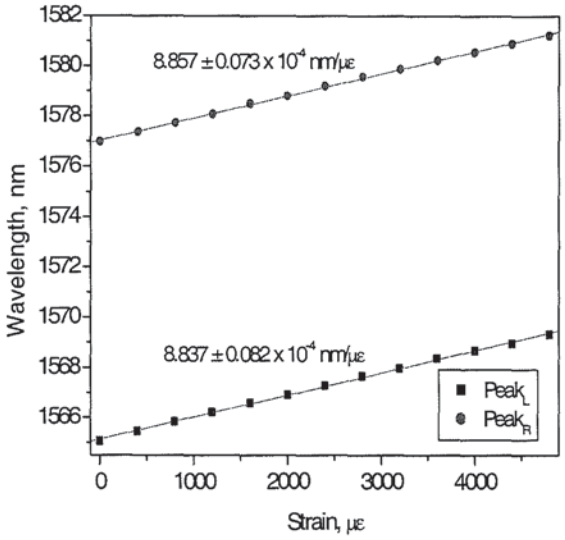

(a) Sensor5

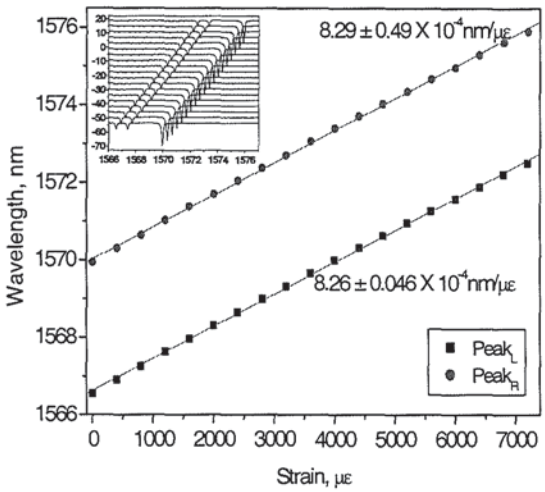

(b) Sensor6

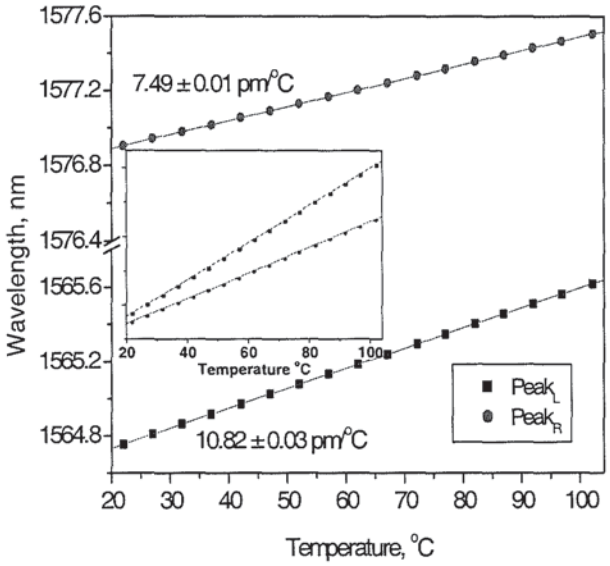

(c) Sensor5

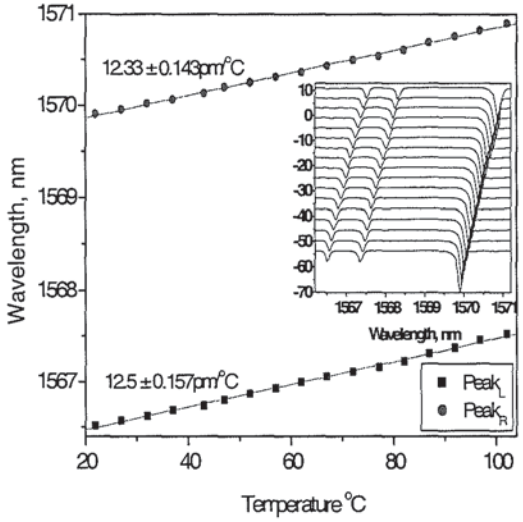

(d) Sensor6

Fig. 5.12: Wavelength shift plotted against strain, and temperature for Sensor5 and Sensor6. (a) and (b) for strain measurements, (c) and (d) for temperature measurement. The inset to (c) is a re-plot of the same figure but with origins of the linear fits brought closer, the inset to Fig. 5.12(b) and (d) in each case shows the spectral responses from which the plotted data was extracted

To show that the temperature responsivity of the FBGs can be tailored, another FBG-sensor (Sensor7) containing a Type I and an over-exposed FBG was produced in the H_2-loaded B/Ge

fibre with exposure durations of 102 minutes[16]. The spectral response for this FBG-sensor after annealing for 45 hours at 110°C is shown in Figs. 5.13 (a) and (b). The separation between $peak_L$ and $peak_R$ observed, though slightly less (i.e. ~12nm), in view of the shorter exposure time, and the FBG responsivity go along to confirm the repeatability of the inscription process. The ability to re-produce FBGs with low temperature responsivity clearly demonstrates the repeatability of the fabrication process. In addition, it also shows the flexibility of the method because the amount of UV exposure can determine the reduction in temperature responsivity of the FBG.

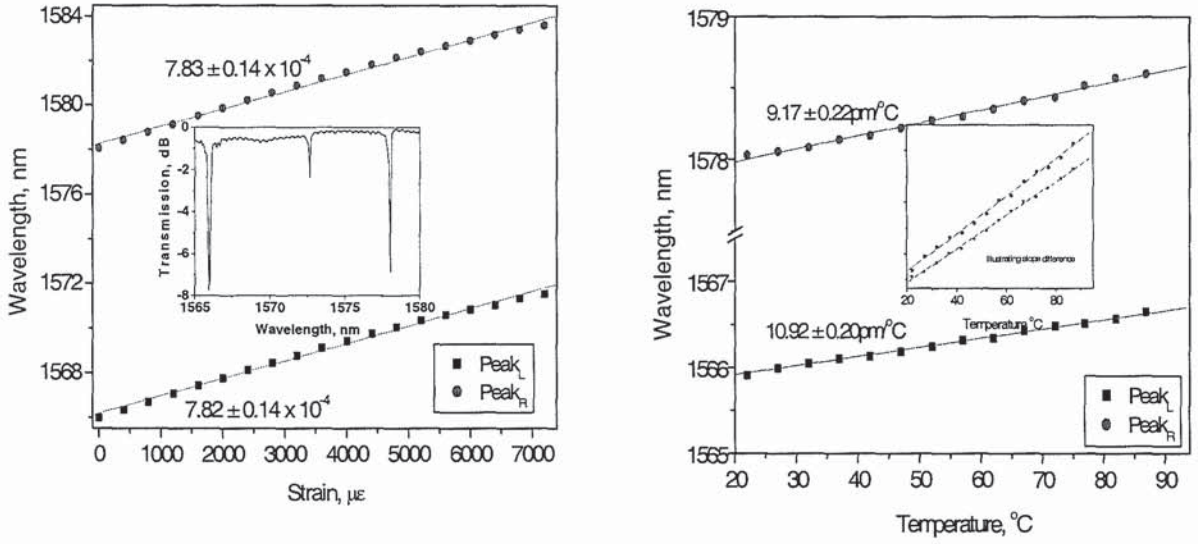

(a) Sensor7 (b)

Fig. 5.13: Wavelength shift plotted against strain and temperature for Sensor7 produced in B/Ge. (a) for strain measurements; the inset is the spectral response of the sensor at 0 $\mu\varepsilon$, (b) for temperature measurement; the inset is a re-plot of the same figure but with origins of the linear fits brought closer

The strain and temperature response of this FBG-sensor are plotted in Figs. 5.13(a) and (b) respectively. The inset to Fig. 5.13(a) is the spectral response of the sensor at 0 $\mu\varepsilon$. The inset to Fig. 5.13(b) is a re-plot of the same figure but with origins of the linear fits brought closer. It clearly indicates the difference in temperature coefficients of the FBGs used for the sensor –enabling the strain and temperature effects to be discriminated.

[16] Sensor7 is basically similar to Sensor5 but made using less UV exposure duration.

Option E: *Double multiple UV scan through the phase mask to produce two FBGs, in both cases, on the same piece of fibre with no gap between the FBGs, first when the fibre is H_2-loaded (leading to an overexposed FBG), and subsequently after the H_2 is removed by annealing (leading to a Type IIA FBG)*

Following the post-processing without a phase mask, another over-exposed grating of the type shown in Fig. 5.11(a) was produced using multiple scanning of the hydrogen-loaded B/Ge fibre through the phase mask. The grating was then annealed for 45 hours at 110°C to remove un-reacted hydrogen. After annealing for about 45 hours a second grating was subsequently produced within the same piece of fibre without re-hydrogenating the fibre, i.e. a Type IIA FBG. This was produced using a phase mask pattern that allows for producing an FBG that is located spectrally near to the first FBG. This grating was produced through multiple UV scan, and the evolution during the second set of UV exposures is shown in Fig. 5.14. It can be seen in the figure that due to the residual hydrogen (that remained in the fibre after annealing of the first over-exposed grating) the Type IIA grating gradually shifted to the longer wavelength before finally shifting back to its original wavelength in line with its usual characteristics. Here it can be seen that because the shift of the Type IIA FBG is so small, when there is an overlap, it can prove difficult to separate the two peaks by way of further UV exposure.

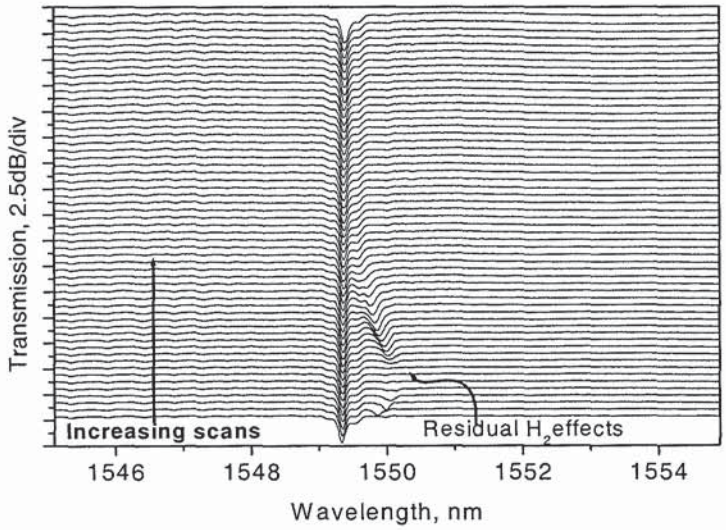

Sensor8

Fig. 5.14: The spectral evolution of a Type IIA FBG written physically- and spectrally- adjacent to the over-exposed FBG earlier formed in a hydrogen-loaded B/Ge co-doped fibre through multiple UV scans over the fibre through a phase mask

In view of the lower temperature responsivity of the over-exposed (~7.5pm/°C) FBG in comparison to Type IIA (~12pm/°C), it can be inferred that this sensor is capable of measuring strain and temperature simultaneously.

Option F: Double multiple UV scan through the phase mask to produce two FBGs, in both cases, on the same piece of fibre with no gap between the FBGs, first before the fibre is loaded with H_2 (leading to a Type IIA FBG), and subsequently after the FBG-containing fibre is hydrogenated (leading to an overexposed FBG). This is essentially a reverse of OptionE.

In Fig. 5.15 the spectral evolution of two FBGs written side by side physically is shown (Sensor9). The idea is to have the gratings both physically and spectrally close to each other. The procedure used is simply the reverse of that used in producing the Sensor8, shown in Fig. 5.14. A type IIA FBG was initially produced in the non-hydrogen-loaded B/Ge fibre at 1567nm wavelength. This Type IIA grating was produced using several UV scans on the fibre through the phase mask[17]. The fibre containing the Type IIA FBG was subsequently hydrogen-loaded. The second grating was then fabricated physically adjacent to the first

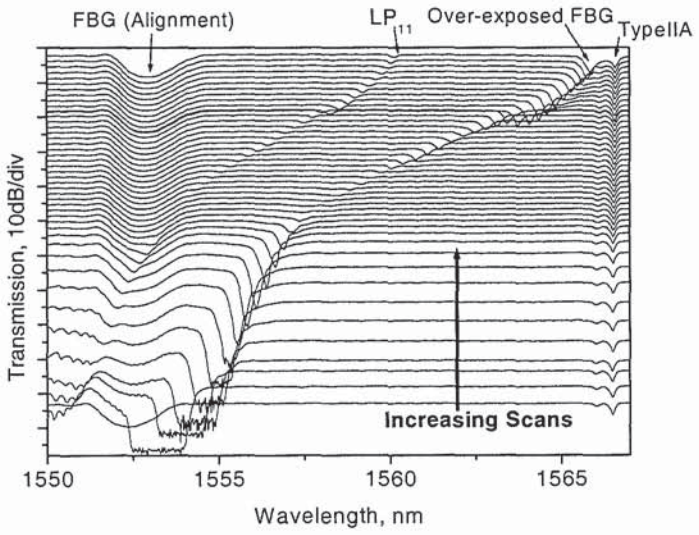

Sensor9

Fig. 5.15: The spectral evolution of Sensor9 showing the formation of over-exposed FBG after the inscription of a Type IIA FBG in B/Ge co-doped fibre by multiple UV scans over the fibre through a phase mask.

[17] Similar to that shown in Fig. 4.10

grating (with no gap) using a phase mask pattern that initially produced a grating at 1552nm wavelength, but following the repeated exposure the new grating shifted to the longer wavelength up to 1566nm as seen in the figure, and then with further exposure, there was a slight final shift to the shorter wavelength. This (second) FBG is similar to that shown for the over-exposed FBG in Fig. 5.11(a).

It can be seen in Fig. 5.15 that the LP_{11} mode appears at wavelength less than that of the Bragg peak of the over-exposed FBG. In addition the broad loss peak at 1552 nm (labelled as FBG alignment) is related to a very short grating (obtained in error) for which there was no multiple exposure (<1mm). This peak is the result of the initial UV light scanning beyond the desired length of the grating. Clearly the devices i.e. Sensor9 shown in Fig. 5.15, and Sensor8 in shown in Fig. 5.14, are similar, but contain FBGs that are produced in reverse order.

The results of strain and temperature measurements using Sensor9 are shown in Figs. 5.16 (a) and (b) respectively. The inset in each case shows the spectral responses that were plotted in the main figures.

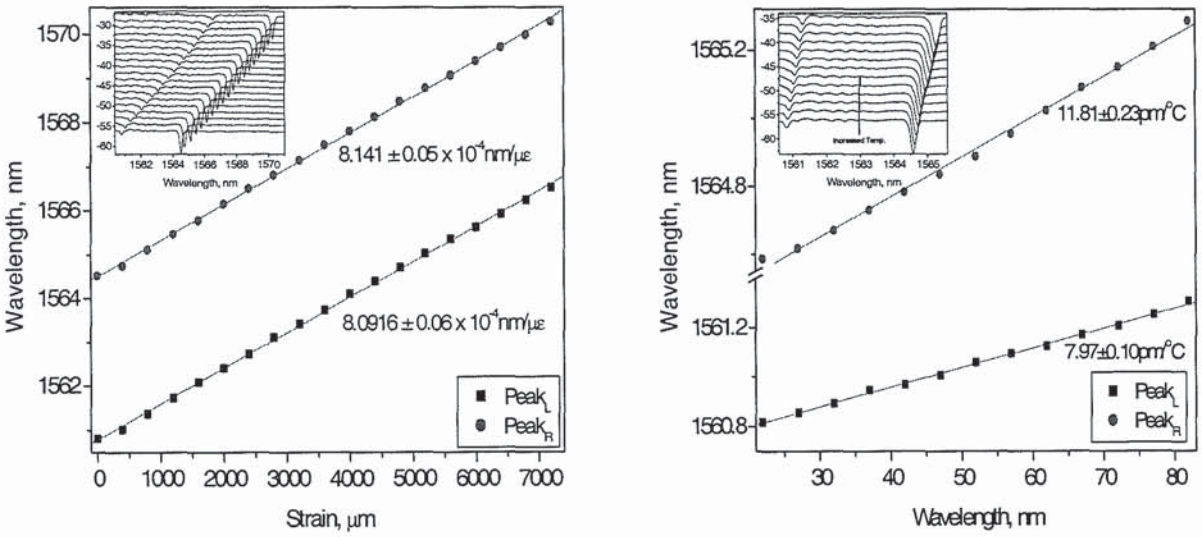

Fig. 5.16: Wavelength shifts for Sensor9 produced in B/Ge fibre plotted against (a) strain, and (b) temperature; the inset in each figure show the spectral response of the sensor from which the plotted data was extracted

The difference in the temperature coefficients (11.81-7.97pm/°C) coupled with the similarity of the strain coefficients (~0.00081 $nm/\mu\varepsilon$) of the main Bragg peaks of Sensor9 clearly

suggest that strain and temperature contributions to the wavelength shift can be easily calculated using matrix equation (eqn. 5.3).

Table 5.2 provides summarised list of the sensors used, the fabrication methods adopted and the figures in which the spectral responses of these sensors are displayed.

FBG Name	Type of Fibre Used	Writing Option	Fabrication Evolution	Annealed Spectrum
SENSOR1	H_2-loaded B/Ge	OptionA	-	Fig. 5.7 (a)
SENSOR2	H_2-loaded standard SMF	OptionA	-	Fig. 5.7(b)
SENSOR3	H_2-loaded B/Ge	OptionB	Fig. 5.9	-
SENSOR4	Non-H_2-loaded B/Ge	OptionC	Fig. 5.10	-
SENSOR5	H_2-loaded B/Ge	OptionD	Fig. 5.11(a)	Fig. 5.11(c)
SENSOR6	H_2-loaded standard SMF	OptionD	Fig. 5.11(b)	Fig. 5.11(d)
SENSOR7	H_2-loaded B/Ge	OptionD	-	Fig. 5.13(a)
SENSOR8	H_2-loaded B/Ge	OptionE	Fig. 5.14	-
SENSOR9	H_2-loaded B/Ge	OptionF	Fig. 5.15	Fig. 5.16(a) & (b)

Table 5.2: List of FBG-sensors, fibre used, and the fabrication method adopted

5.2.2.3 Performance as dual parameter sensor

In Table 5.3 the temperature and strain coefficients for some of the sensors are listed. It is necessary to stress that for those sensors where $K_{\varepsilon_{Peak_L}} = K_{\varepsilon_{Peak_R}}$ and $K_{T_{Peak_L}} \neq K_{T_{Peak_R}}$, the determinant of the matrix of coefficients is not zero ($|\boldsymbol{K}| \neq 0$). In other words, the inverse of the matrix $\boldsymbol{K}$ is defined. Solving eqn. (5.3) can clearly yield values for strain and temperature simultaneously.

It can be observed that Sensor5 offer the best performance: its condition number is the nearest to 1 (one). This highest performance stems from showing the largest difference in the temperature coefficients of the sensor peaks. The performance of Sensor9 almost matches that of Sensor5 even though the temperature coefficient of the over-exposed FBG has not been reduced to the same value as that of a similar peak ($Peak_R$) in Sensor5. By comparing these two sensors, it can be deduced that since the Type IIA FBG provides the highest temperature coefficient in comparison to Type I (as seen on Sensor4), and the overexposed

FBG used for Sensor5 can provide the temperature coefficient as low as 7.5 pm/°C, then the combinations used for either Sensor8 or Sensor9 are more likely to offer a better sensor.

Sensor	Parameter	$Peak_L$	$Peak_R$	Condition no[18]. of K	Relevant Fig.
Sensor1	Strain, K_ε	8.62 x 10^{-4} $nm/\mu\varepsilon$	8.54 x 10^{-4} $nm/\mu\varepsilon$	362.40	Fig. 5.8(a)
	Temperature K_T	9.76pm/°C	10.32pm/°C		Fig. 5.8(c)
Sensor2	Strain K_ε	8.46 x 10^{-4} $nm/\mu\varepsilon$	8.34 x 10^{-4} $nm/\mu\varepsilon$	421.70	Fig. 5.8(b)
	Temperature K_T	12.01pm/°C	12.7pm/°C		Fig. 5.8(d)
Sensor4	Strain K_ε	8 x 10^{-4} $nm/\mu\varepsilon$	-	-	-
	Temperature K_T	12.24pm/°C	-		-
Sensor5	Strain, K_ε	8.84 x 10^{-4} $nm/\mu\varepsilon$	8.86 x 10^{-4} $nm/\mu\varepsilon$	60.10	Fig. 5.12(a)
	Temperature K_T	7.5pm/°C	10.82pm/°C		Fig. 5.12(c)
Sensor6	Strain, K_ε	8.26 x 10^{-4} $nm/\mu\varepsilon$	8.29 x 10^{-4} $nm/\mu\varepsilon$	1740.4	Fig. 5.12(b)
	Temperature K_T	12.5pm/°C	12.33pm/°C		Fig. 5.12(d)
Sensor7	Strain K_ε	7.82 x 10^{-4} $nm/\mu\varepsilon$	7.83 x 10^{-4} $nm/\mu\varepsilon$	150.48	Fig. 5.13(a)
	Temperature K_T	9.17pm/°C	10.92pm/°C		Fig. 5.13(b)
Sensor9	Strain K_ε	8.09 x 10^{-4} $nm/\mu\varepsilon$	8.14 x 10^{-4} $nm/\mu\varepsilon$	66.60	Fig. 5.16(a)
	Temperature K_T	7.97pm/°C	11.81pm/°C		Fig. 5.16(b)

Table 5.3: Temperature and strain coefficients for Bragg peaks left and right

Since FBGs of different temperature sensitivities can be fabricated in the B/Ge fibre through these processes and it has been demonstrated that FBG peaks in this fibre can have sensitivities ranging from 12.24 down to 7.5 pm/°C depending on (a) the H_2 content of the fibre and (b) the level of UV exposure used, then this clearly suggests that the FBG responsivity can indeed be tailored to suit certain requirement[19].

In summary, this subsection has successfully demonstrated the design and applications of novel FBG-sensors for simultaneous measurement of strain and temperature. The dual-parameter sensing functionality of the sensors originates from their unique configuration of having two Bragg reflection peaks that exhibit the same strain- but different temperature-responses. Temperature sensitivities ranging from 7.5 to 12.24pm/°C were achieved for the sensors written in B/Ge fibre with different UV exposure time. This clearly indicates that the

18. Condition number provides a measure of responsivity of the sensor to data errors. It gives an indication of the accuracy of the sensor. Value near 1 indicates a well-conditioned matrix.

responsivity of the grating peaks can be tailored. The advantages of simple fabrication, tolerance of large strain effects and more importantly, the use of a single light source for interrogation offers the prospects of the development of practical temperature independent strain sensing system.

It is however necessary to note that there are potential problem areas when dealing with Bragg grating sensors. These problem areas have been described in ref. [175] as:

a) Spectral overlap –where two adjacent spectra over-shadow each other (i.e. cross talk) particularly when multiplex over a single piece of fibre. Here, there is likely to be both signal addition and some signal may pass through twice or more in the gratings because of reflection back and forth.

b) Side-band over-lap with grating peak –here, if the side-lobes of a grating are strong and the over-lap the next central Bragg peak, or if the light-source has side-bands whose spectra over-lap that of another grating peak, then measurement errors could result.

c) Effect of spatially varying field –In an arrangement where the grating spectral peaks are considered for interrogation, then should there be a non-uniform field of say, strain within the different points in a single grating, this may lead to the broadening or spectral distortion of the symmetry of the narrow reflective peak. Error could then emerge. However, centroid measurement should minimised errors from this effect.

d) Variation with the wavelength of the optical sources or components –here, for example, if the light source output is not flat, because what is observed on the display is the combined effect of the interaction between grating and the source, then a broad grating peak might appear narrower, or the slope of the transmission depth might appear different from reality.

e) Polarization effect: if the gratings are birefringent, then two peaks will result with each corresponding to one polarization mode. It is also known that birefringence in grating can result from many sources such as those from side illumination, oval

19. Tailoring responsivity is important because both sensing and telecommunications applications require

shapes in the core or cladding, and the applied transverse perturbations etc. But, where the detector measure only the intensity changes, the grating-based polarization will not lead to errors. However polarization from other components could well lead to errors.

In the next section, discussion will focus on the use of grating whose period is far larger than that of Bragg grating (i.e. LPG). This type of grating possesses much higher responsivity to a number of parameters such as bending, temperature and refractive index, in comparison to FBG.

5.3 Long Period Grating (LPG) sensors

Long-Period fibre Gratings (LPGs) have the intrinsic property that allow them to couple light between the core and cladding modes of an optical fibre. LPGs have gained increasing popularity for applications in the sensing area [73]. Their various properties have been exploited for use in gain equalization/flattening of Er-Doped Fibre Amplifiers (EDFAs) [176], temperature/strain/refractive-index sensing [177,178], thermally [179] or electrically [180] controlled tuneable filters. In addition, Bhatia et al [181] has reported on the use of an LPG cladding mode of high resonance order along with another cladding mode of lower resonance order for simultaneous measurement of strain and temperature. In comparison with FBGs, LPGs offer a number of additional advantages, including easy fabrication, low levels of back-reflection and high temperature responsivity, which render them more desirable for some special applications.

This section describes work on the fabrication and sensing application of LPGs inscribed in three different types of fibre. The LPGs are shown to be capable of various sensing applications such as simultaneous measurement of strain and temperature using a fundamental mode of lower resonance order ($^1LP_{02}$) and a higher resonance order, second diffraction order mode ($^2LP_{07}$) of a single LPG in B/Ge co-doped fibre. Analysis of the simultaneous measurement of strain and temperature is followed by a brief discussion on a unique and yet unreported, experimentally observed, responsivity characteristics of LPG in B/Ge fibre. Here, focus was made on a highly responsive cladding mode that is located

varying degree of FBG temperature-sensitivity.

within the set of fundamental modes. This mode exhibits a wavelength shift in the opposite (i.e positive temperature coefficient) direction to that of the fundamental mode $^1LP_{06}$ (i.e negative temperature coefficient) of the same LPG that is located close to it.

Further discussion focused on the use of yet another experimentally un-observed fundamental mode of LPG, this time in standard SMF. This special fundamental cladding mode is demonstrated to be capable of simultaneous measurement of temperature and other physical parameters. In this section the special cladding mode is used with a second order cladding mode of high resonance order to simultaneously measure temperature with strain, curvature or SRI. Finally, a discussion on the use of LPGs in 3-layer fibre to simultaneously measure SRI and temperature is addressed.

It is well known that the resonance wavelength, $\lambda_{res,}$ of an LPG with a period Λ is determined by the phase-matching condition [176]

$$\lambda_{res} = (n_{co}^{eff} - n_{cl,m}^{eff})\Lambda / N \tag{5.4}$$

Where, n_{co}^{eff} and $n_{cl,m}^{eff}$ are effective indices of the fundamental core mode and the m^{th} cladding mode, respectively, and N is the harmonic diffraction order. The number N determines whether or not the mode considered is fundamental or a harmonic. The temperature, axial strain and SRI responsivity of the resonance wavelengths of the LPG can be expressed, respectively, as [73]

$$\frac{d\lambda_{res}}{dT} = \lambda_{res} \cdot \gamma \cdot (\alpha + \frac{\xi_{co} n_{co}^{eff} - \xi_{cl} n_{cl,m}^{eff}}{n_{co}^{eff} - n_{cl,m}^{eff}}) \tag{5.5}$$

$$\frac{d\lambda_{res}}{d\varepsilon} = \lambda_{res} \cdot \gamma \cdot (1 + \frac{\eta_{co} n_{co}^{eff} - \eta_{cl} {}^{eff}_{cl,m}}{n_{co}^{eff} - n_{cl,m}^{eff}}) \tag{5.6}$$

$$\frac{d\lambda_{res}}{dn_{SRI}} = \lambda_{res} \cdot \gamma \cdot \frac{u_m^2 \lambda_{res}^3 n_{SRI}}{8\pi r_{cl}^3 n_{cl} (n_{co}^{eff} - n_{cl,m}^{eff})(n_{cl}^2 - n_{SRI}^2)^{3/2}} \tag{5.7}$$

Where, ξ_{co}, ξ_{cl} and η_{co}, η_{cl} are the thermo-optic and elasto-optic coefficients of the core and cladding materials, respectively, u_m is the m^{th} root of the zero-order Bessel function of the first kind, r_{cl} and n_{cl} are the radius and the refractive index of the fibre cladding, respectively.

α is the thermal expansion coefficient of the fibre, γ describes the waveguide dispersion and is defined as [73,182]

$$\gamma = \frac{\frac{d\lambda_{res}}{d\Lambda}}{n_{co}^{eff} - n_{cl,m}^{eff}} \tag{5.8}$$

γ is the 'general sensing factor' that mainly determines the responsivity of cladding modes of the LPG. It is also used to identify the cladding modes that shift either to the longer or the shorter wavelength with changes in external perturbations to the LPG [73,182].

Eqn. (5.5)[20] can be written as.

$$\frac{d\lambda_{res}}{dT} = \lambda_{res} \cdot \gamma \cdot (\alpha + \Gamma) \tag{5.9}$$

Where,

$$\Gamma = \frac{\xi_{co} n_{co}^{eff} - \xi_{cl} n_{cl,m}^{eff}}{n_{co}^{eff} - n_{cl,m}^{eff}} \tag{5.10}$$

In general, α is << Γ for silica-based fibres. Thus, from eqn. (5.9) it can be deduced that the temperature response of an LPG is largely dependent on the term of the product $\gamma \cdot \Gamma$. If the product is negative, the wavelength shift is to shorter wavelength otherwise it is to the longer.

Dr X. Shu helped to generate the raw data for the values of γ and Γ, using eqns. 5.8 and 5.10 and his own program, for two different types of fibre: the standard SMF and B/Ge co-doped fibres. The computer generated data for the values[21] of γ and Γ for the first 30 cladding

[20] This equation was obtained by the author's colleague, X. Shu following the earlier work of T.W. MacDougall et al [182].

[21] Equations based on weakly guiding approximation, were used for the calculations. The fibre specifications used are; the standard SMF with the core doped by 4.1m%GeO_2, having ξ_{co}=7.97×10^{-6}/°C and core radius r_{co}=4.2μm. The other is the B/Ge co-doped fibre with the core doped by 9.7m%B_2O_3 and 4.03m%GeO_2, having ξ_{co}=7.3×10^{-6}/°C and r_{co}=3.8μm. Both fibres were assumed to have a pure silica cladding with ξ_{cl}=7.8×10^{-6}/°C [215], radius r_{cl}=62.5μm, and an average UV induced core index change of 4×10^{-4}.

modes have been plotted by the author against the mode order in Fig. 5.17: the figure shows the values for γ and Γ for B/Ge co-doped fibre, and for the standard SMF. γ values are indicated by the left vertical axis, and Γ indicated by the right vertical axis. For both fibres the parameter γ exhibits a similar trend pattern, which is characterised by a flip-flop feature, emerging at regions of different mode order. γ changes the sign from positive to negative in this region, suggesting that high responsivity may be achieved for LPGs by choosing the modes with the orders close to this region.

Also shown in the figure, Γ-value increases for B/Ge co-doped fibre and on the other hand, decreases for standard SMF as mode order increases. Nevertheless, even for the same mode order, the values of $|\Gamma|$ for the B/Ge co-doped fibre is much larger than that of the standard SMF.

As described above using eqn. (5.9) the temperature responsivity of a resonant mode is predominantly determined by the $\gamma \cdot \Gamma$. Hence, an overall higher thermal responsivity can be expected from the LPGs produced in the B/Ge fibre in view of the larger values of $|\Gamma|$. Note that for the two fibres thermo-optic coefficients of their core are significantly different ($\xi_{co}=7.97\times10^{-6}$/°C for standard telecom fibre, and $\xi_{co}=7.3\times10^{-6}$/°C for the B/Ge co-doped fibre). Since, the thermo-optic coefficient for cladding is $\xi_{cl}=7.8\times10^{-6}$/°C for both cases, then Γ is negative for B/Ge fibre and positive for standard telecom fibre. At the Flip-Flop region, the product $\gamma \cdot \Gamma$ attains much higher values, thus, the responsivity is highest around this region. Further explanation to high responsivity of LPG in this region can be given by considering the slope of dispersion curves. This will be further explained in Sub-section 5.3.1.3 (B) where slopes of associated dispersion curves are considered.

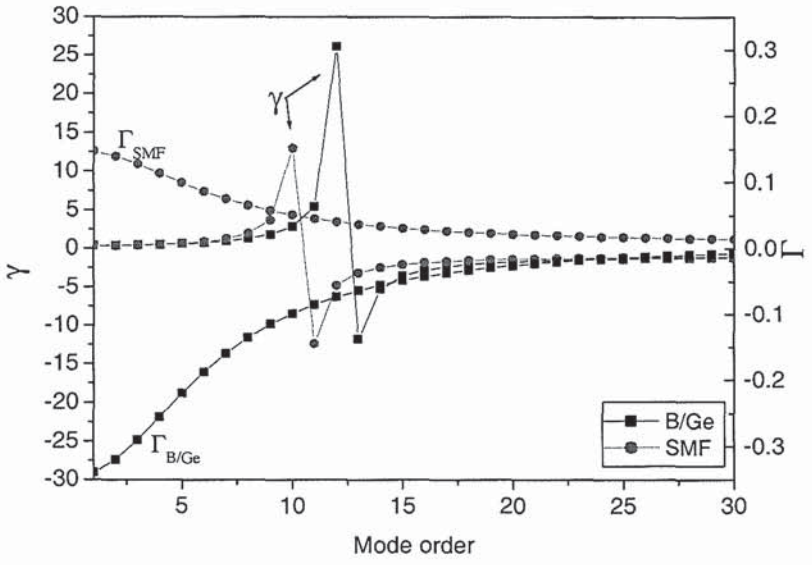

Fig. 5.17: Calculated variation of γ and Γ with mode order (a) for B/Ge co-doped optical fibre, and (b) for the standard SMF.

5.3.1 LPGs with harmonic-order cladding modes for sensing applications

In addition to the theoretical responsivity characteristics of LPGs discussed using Fig. 5.17 the fabrication of LPGs have been discussed in Chapter 2 where the main focus was on LPGs showing only the fundamental cladding modes. If the induced index corrugations in the fibre core are square-shaped this gives rise to harmonic cladding modes [183]. Grubsky et al [183] has described the process through which such harmonic coupling can be either reduced or completely eliminated by using various UV exposure envelop. If the grating is designed for specific applications that require only the fundamental modes to appear, then, Grubsky's technique can be employed to suppress the harmonics, otherwise, as demonstrated in this subsection, such harmonics can be put to an advantageous use for simultaneous measurement of strain and temperature.

5.3.1.1 The identification of harmonic LPG cladding modes

One of the LPGs used to demonstrate the appearance of harmonics was UV-written in hydrogenated B/Ge co-doped fibre using a 244nm Fred laser with an output power of

105mW. The inscription was implemented by scanning the UV beam on the fibre lengthwise in a point-by-point manner with a 50% duty-cycle using a computer-controlled UV-light shutter. An LPG of length 2.9cm was fabricated using 69 UV exposure samples leading to a period 421 μm. After inscription, the piece of fibre containing the grating was annealed at 115°C for ~64 hours in an oven.

The spectral response of the LPG obtained is shown in Fig. 5.18 where two sets of cladding modes can be seen: for ease of identification, a vertical dotted line separates the two sets. The resonance wavelengths of both sets of cladding modes $^{N}LP_{0i}$ (i = 2,...7, N=1,2) is governed by the phase matching condition of eqn. (5.4), with N= 1 for the fundamental cladding modes (located on the right-hand side of the dotted line) and N = 2 for the second order harmonic modes (located on the left-hand side of the dotted line). It is noted that because the effective indices of the core and cladding are dependent on the dispersion properties of the fibre, the second order harmonic modes will not always appear at half the resonance wavelength of the fundamental modes [22].

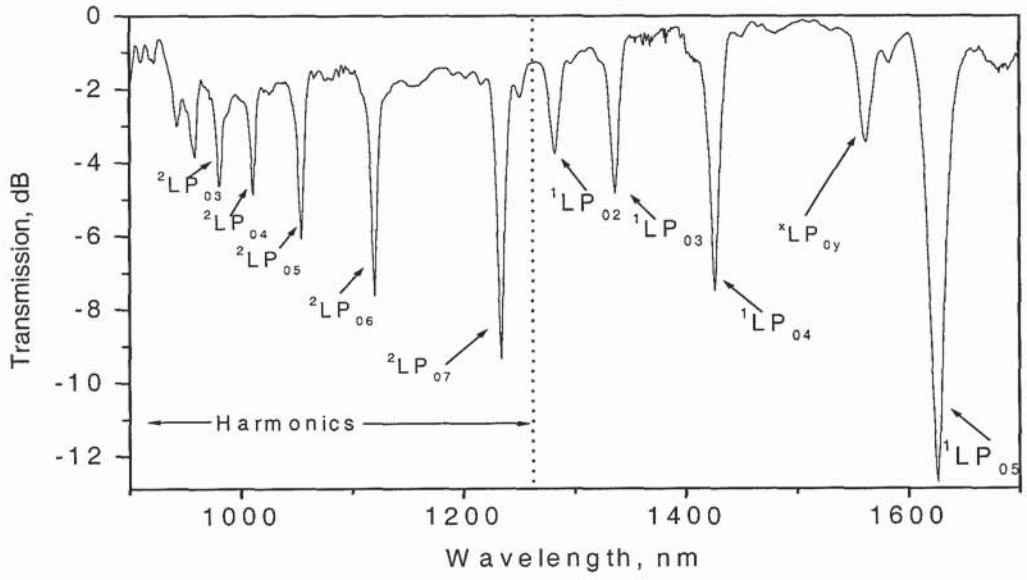

Fig. 5.18: Spectral responses of LPG of 421 μm-pitch in B/Ge co-doped fibre showing the fundamental and harmonic cladding modes of second diffraction order.

[22] See ref. no.18 on the author's publication list in Appendix 1 for further details

The study of the LPGs displaying dual diffraction order mode was not limited to those fabricated in B/Ge co-doped fibre but also extend to the type obtainable in standard SMF. Indeed, the LPGs in standard SMF are shown herein to exhibit both fundamental and second diffraction-order cladding modes within the spectral range of the OSA.

Table 5.4 provides the fabrication details relating to each of the LPGs produced in the standard SMF for this investigation. In all the four LPGs, the second diffraction order modes were observed. As an example, the spectral responses of LPG1 and LPG3 are shown in Figs. 5.19 and 5.20 respectively. In each spectrum, two sets of cladding modes can be seen: again,

LPG designation	Fibre type	Period (μm)	No. of samples	Approx. length (mm)	UV scan speed (mm/s)	Presence of harmonics	Presence of $^{1}LP_{02L}$
LPG1	Standard SMF	390	77	30.04	0.080	Yes	Yes
LPG2	Standard SMF	470	65	30.55	0.050	Yes	Yes
LPG3	Standard SMF	480	63	30.24	0.065	Yes	Yes
LPG4	Standard SMF	490	62	30.38	0.070	Yes	Yes
Note: All these LPGs were written in hydrogenated standard SMF using a laser via a point-by-point method with a 50% duty-cycle and gratings were annealed at 115 ℃ for ~64 hours.							

Table 5.4: LPGs in standard SMF and their fabrication details

for ease of identification, in each of the figures a vertical doted line separates the two sets. The cladding modes $^{N}LP_{0i}$ (i = 2,...7, N=1,2) of fundamental order (N= 1) are seen on the right-hand side of the dotted line and of harmonic order (N = 2) are located on the left-hand side of the dotted line).

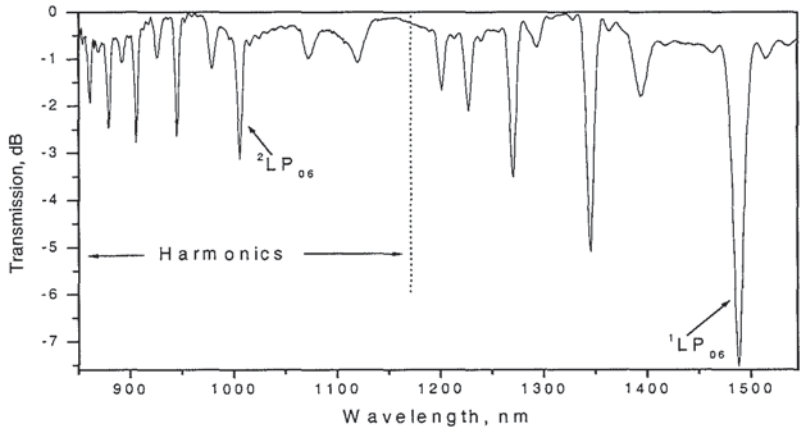

Fig. 5.19: Spectral responses of LPG1 of 390 μm -pitch in standard fibre showing fundamental modes and the harmonic cladding modes of second diffraction order with a broad weak cladding mode believed to be $^{1}LP0_{2L}$ located between the sets.

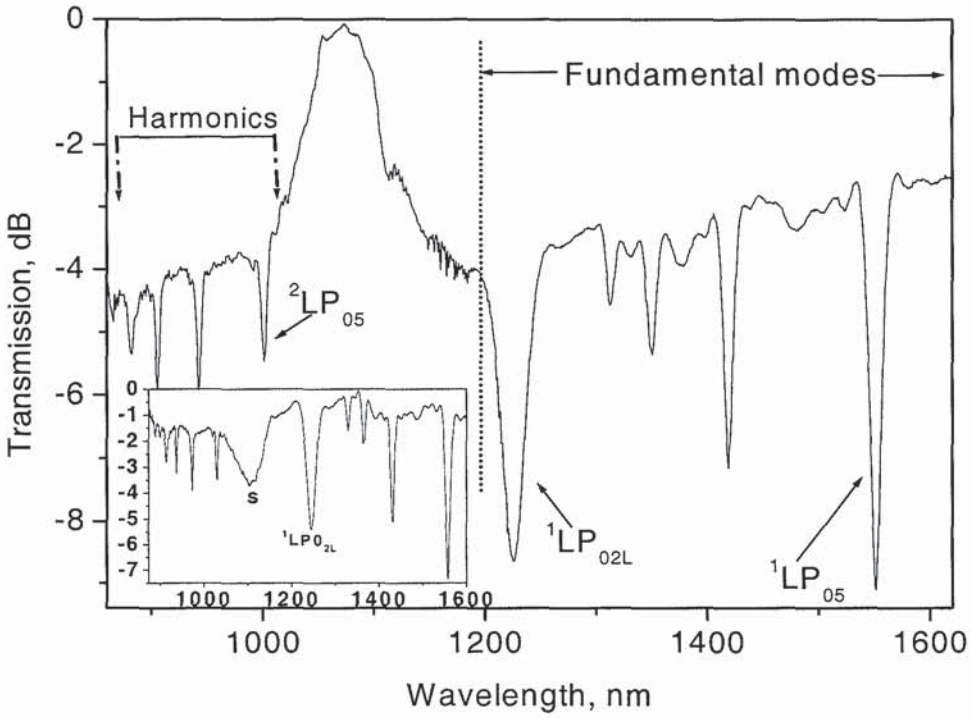

Fig. 5.20: Spectral responses of LPG3 of 480 μm -pitch in standard fibre showing fundamental modes and the harmonic cladding modes of second diffraction order with a broad $^1LP_{02L}$ peak located between the sets. The inset shows the spectral response of the same LPG recorded at different time indicating the unstable nature of the feature labelled 's'.

Although both LPG1 and LPG3 were fabricated in standard SMF the spectrum of LPG3, shown in Fig. 5.20, depicts more clearly some rather unusual but interesting features in the region 1050 to 1300nm: whilst the feature labelled 's' is associated with the light source used[23], the broad loss peak located at ~1244nm is an LPG peak, labelled $^1LP_{02L}$. The inset shows another spectral response for the same grating portraying the unstable nature of 's'. The peak $^1LP_{02L}$ appears in LPGs written with a certain range of periods in the standard SMF used. Interestingly, the broad peak $^1LP_{02L}$ did not appear in the LPG of 421 μm pitch fabricated in B/Ge co-coped fibre. Further details relating to $^1LP_{02L}$ are discussed in Subsection 5.3.1.3.

Fig. 5.21 shows the spectrum of LPG1 re-produced for the purpose of explaining further spectral details: the inset shows the spectral responses of second diffraction order mode $^2LP_{06}$

of the LPG to temperature in the wavelength range 960 to 1030nm for temperature changes from 22 to 57°C. The small peaks labelled a_4 and a_5 as well as b_2-b_6 are related to either asymmetric or high diffraction order modes in the fibre cladding. The temperature coefficient of the second diffraction order mode $^2LP_{06}$ of LPG1 is evaluated to be 65.64 ± 0.04pm/°C and for the fundamental mode $^1LP_{06}$ the value is 66.1 ± 0.73pm/°C. Given the temperature responses of the two peaks shown in the inset it can be concluded that the small peaks belong to resonance order lower than that of the modes at Dispersion Turning Point (DTP).

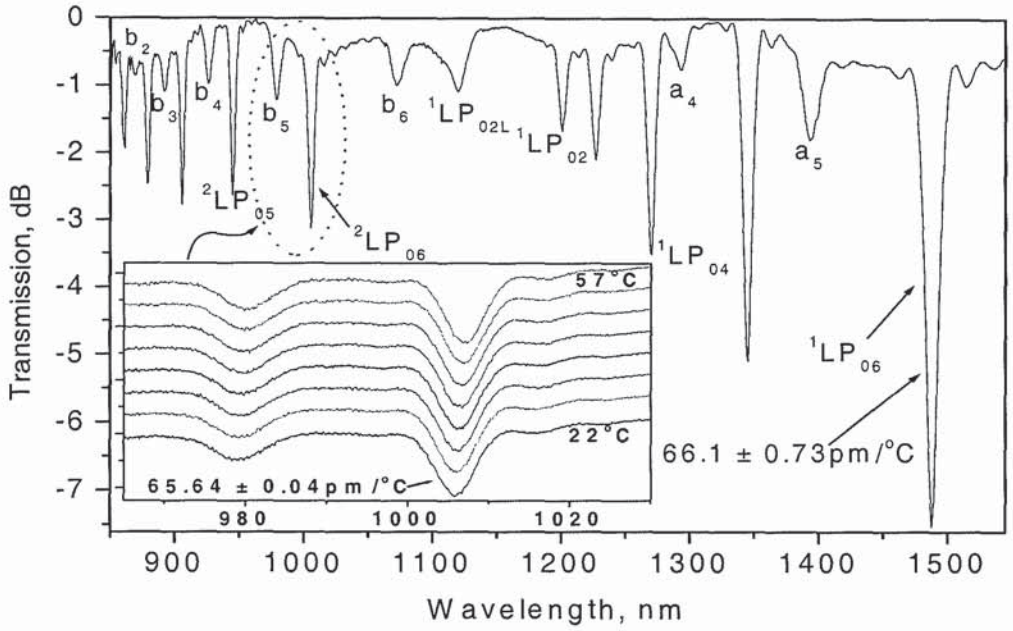

Fig. 5.21: Spectral response of LPG1: the inset shows the spectral responses of two second diffraction order modes of the LPG to temperature changes in the wavelength region 960 to 1030nm.

5.3.1.2 Using the fundamental and harmonic modes to measure strain and temperature

The LPG shown in Fig. 5.18 has highlighted a number of interesting LPG properties: a high resonance order harmonic mode ($^2LP_{07}$) is located very close to the fundamental cladding mode $^1LP_{02}$ such that the two neighbouring peaks offer the potential for interrogation using a single light source. For this reason such peaks have been selected to demonstrate the simultaneous strain and temperature measurement.

23. This was verified by the disappearance and unstable characteristics of the feature as exemplified in the inset to the figure.

Fig. 5.22 (a) shows the temperature responses of two modes $^2LP_{07}$ and $^1LP_{02}$ of the LPG. It can be seen in the figure that the two modes are located ~50nm apart in the wavelength region 1200 to 1310nm and they exhibit a large difference in temperature coefficients. This property can be exploited so that the peaks can be used for the simultaneous measurement of temperature and axial strain. Fig. 5.22(b) shows the plot of the wavelength for the two modes against temperature: the coefficients obtained from the linear fits to the data points are – 269.13 ± 5.4pm/°C and –146.24 ± 3.3 pm/°C for the cladding modes $^2LP_{07}$ and $^1LP_{02}$, respectively.

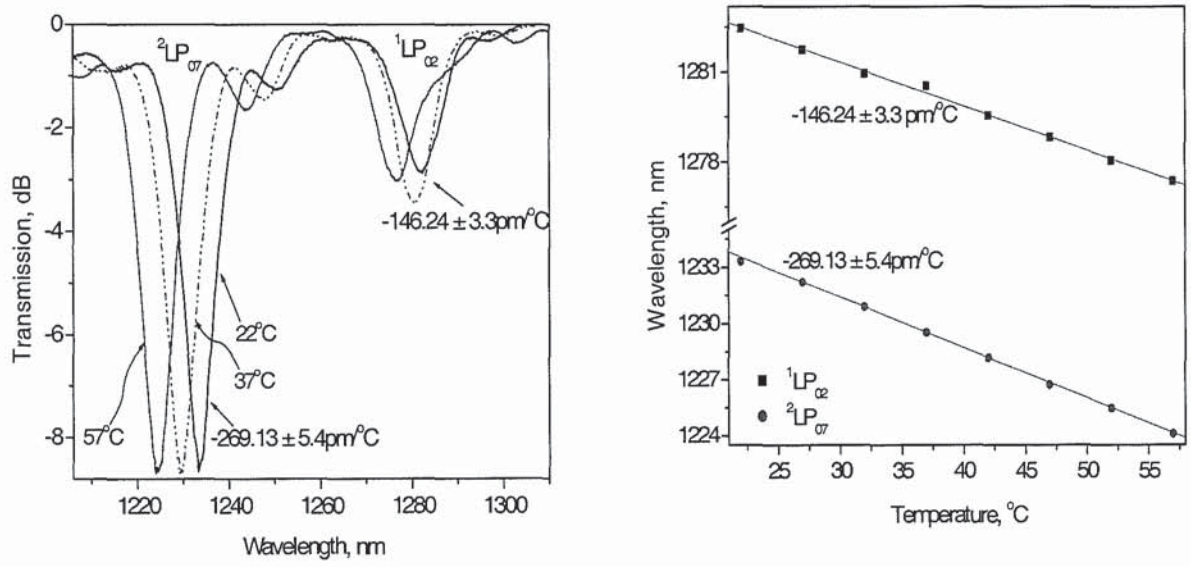

(a) (b)

Fig. 5.22: Spectral responses of an LPG in B/Ge fibre with respect to temperature in the wavelength region 1200 to 1310nm showing (a) modes $^2LP_{07}$ and $^1LP_{02}$ at three temperature values (b) the spectral positions of the modes $^2LP_{07}$ and $^1LP_{02}$ plotted against temperature.

Similarly, the strain response of these peaks have been investigated and the results are shown in Fig. 5.23: Fig. 5.23(a) shows the response with respect to axial strain values 0, 2000 and 4800 $\mu\varepsilon$, and Fig. 5.23(b) shows the plots of the shifts of the peak wavelength of the two modes against applied strain. As can be seen on Fig. 5.23(b), the axial strain responses are 1.29 ± 0.02pm/ $\mu\varepsilon$ and 0.58 ± 0.015pm/ $\mu\varepsilon$ for modes $^2LP_{07}$ and $^1LP_{02}$ respectively.

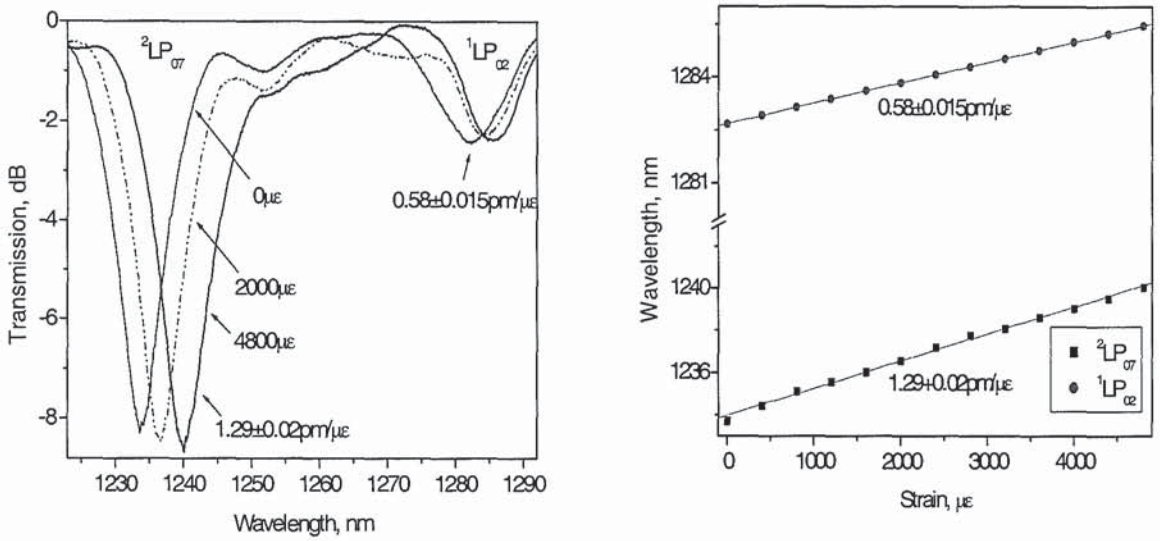

Fig. 5.23: ***Spectral responses of an LPG in B/Ge fibre with respect to axial strain in the wavelength region 1223 to 1292nm showing (a) modes $^2LP_{07}$ and $^1LP_{02}$ at axial strain values 0, 2000 and 4800 $\mu\varepsilon$ (b) the spectral positions of the modes $^2LP_{07}$ and $^1LP_{02}$ plotted against axial strain.***

Table 5.5 shows the list of the strain and temperature coefficients (K_ε and K_T) for the modes $^2LP_{07}$ and $^1LP_{02}$ of the LPG. The values for axial strain and temperature can be evaluated by solving eqn. 5.11 which contains the matrix of the coefficients

Grating	Parameter	$^2LP_{07}$	$^1LP_{02}$
LPG in B/Ge fibre	Strain, K_ε	1.29 ± 0.02pm/ $\mu\varepsilon$	0.58± 0.015 pm/ $\mu\varepsilon$
	Temperature K_T	-269.13 ± 0.54pm/°C	−146.24 ± 3.3pm/°C

Table 5.5: List of parameters used for simulations

$$\begin{pmatrix}\Delta\lambda_{2LP07}\\ \Delta\lambda_{1LP02}\end{pmatrix}=\begin{pmatrix}K_{\varepsilon_{2LP07}} & K_{T_{2LP07}}\\ K_{\varepsilon_{1LP02}} & K_{T_{1LP02}}\end{pmatrix}\begin{pmatrix}\Delta\varepsilon\\ \Delta T\end{pmatrix} \quad \ldots\ldots\ldots \quad (5.11)$$

Clearly, by using the coefficients listed in Table 5.5 as

$$\begin{pmatrix}\Delta\lambda_{2LP07}\\ \Delta\lambda_{1LP02}\end{pmatrix}=\begin{pmatrix}1.29 & -269.13\\ 0.58 & -0.58\end{pmatrix}\begin{pmatrix}\Delta\varepsilon\\ \Delta T\end{pmatrix} \quad \ldots\ldots\ldots \quad (5.12)$$

The inverse of matrix of eqn. (5.12) can be used to calculate the separate values for axial strain and temperature changes leading to a condition number 2881.9. It is noted that 208.63 $\mu\varepsilon$ =1°C for peak $^2LP_{07}$ and 253.14 $\mu\varepsilon$ =1°C for peak $^1LP_{02}$.

Similarly, LPGs in standard SMF can be used to achieve a simultaneous strain and temperature sensor. This can be accomplished by selecting any two cladding modes, one from fundamental set, and the other from the second diffraction order set. The measurement can easily be carried out using the two light sources. In comparison to the B/Ge fibre-based experiment, it can be seen in Fig. 5.21 that a high resonance order harmonic mode ($^2LP_{06}$) is located very far from the fundamental cladding mode $^1LP_{02}$ (>200 nm) such that the two peaks offer less potential for interrogation using a single light source. For this reason such peaks have not been selected to demonstrate the simultaneous strain and temperature sensing potentials of the LPG in standard SMF. In Subsection 5.3.1.3 (B), a newly observed fundamental mode (see $^1LP_{02L}$ in Figs. 19 and 20), which is located spectrally closer to the harmonic modes in comparison to the $^1LP_{02}$ cladding-mode, is demonstrated to be useful for the simultaneous strain and temperature measurement.

5.3.1.3 Additional sensing properties of LPGs with harmonics

In this subsection additional properties of the LPGs with harmonics are investigated. In both B/Ge co-doped and standard SMF, additional cladding modes showing previously unreported characteristics are described.

(A) The sensing characteristics of LPG harmonic mode of high resonance order in B/Ge fibre

The observation of a unique and yet unreported experimentally observed responsivity characteristics of an LPG in B/Ge co-doped fibre is discussed. Here, an LPG cladding mode (labelled $^xLP_{0y}$ in Fig. 5.18) that is highly responsive to temperature and SRI is seen within the set of fundamental modes (in the wavelength region 1500 to 1700nm). This cladding mode ($^xLP_{0y}$) exhibits reverse characteristics when compared with that of the observed fundamental as well as second diffraction order cladding modes: Whilst both of the observed

fundamental and harmonic modes shift to the shorter wavelength as the temperature or the SRI increased[24], this peak does exactly the opposite (i.e., it shifts to the longer wavelength).

Indeed, at the dispersion turning point region [73] grating peaks are known to separate further with increases in temperature (or the SRI), for this grating, the peaks at ~1560nm and ~1625nm are seen to converge with increase in temperature from 22 to 57°C, as shown in the inset to Fig. 5.24. The inset depicts the spectral responses of the device with respect to temperature in the wavelength ranges 1525 to 1680 nm. The narrow peak at ~1560nm has a temperature coefficient of 241.13pm/°C while the other at ~1625nm exhibit a coefficient of -335.6pm/°C.

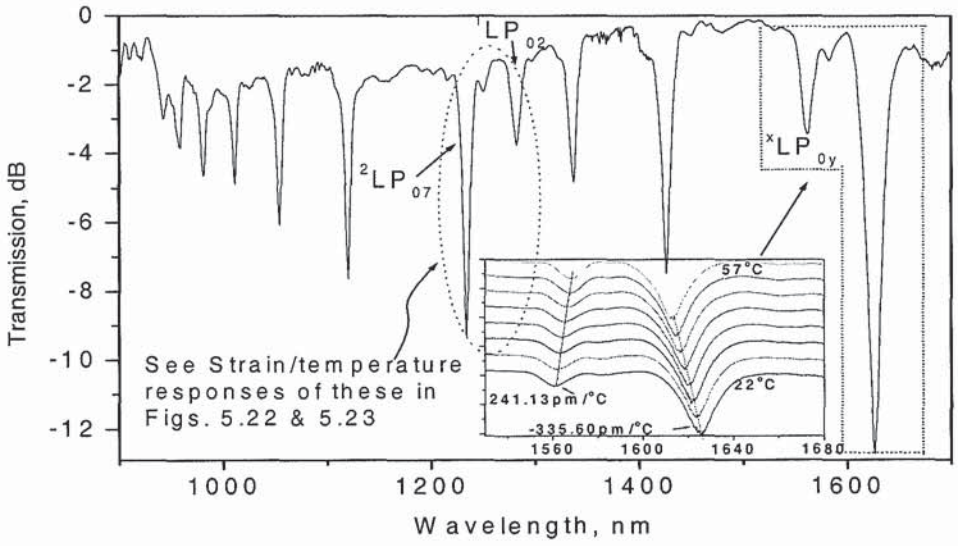

Fig. 5.24: Spectral response of an LPG in B/Ge co-doped fibre: the inset depicts the spectral responses of the device with respect to temperature in the wavelength range 1525 to 1680nm.

When the same LPG was exposed to oils of different refractive indices, the same peaks are observed to fully converge (at SRI=1.40) but with further increase in the SRI the peaks eventually cross over each other, as shown in Fig. 5.25.

The behaviour of these two closely located high order peaks need to be further investigated[25]. To the author's knowledge, the LPG peak at ~1560nm represent the first demonstration of a

[24] SRI increased not beyond the index of the cladding.

single narrow and highly responsive longer wavelength shifting[26] mode located in between all shorter wavelength shifting fundamental modes of the same LPG inscribed in B/Ge co-doped fibre. It is however believed that the narrow peak that shifted to the longer wavelength belongs to a set of cladding-modes that are of higher diffraction order and its resonance order is also higher than that of the peak that shifted to the shorter wavelength. The peak labelled 'k' is believed to be the short wavelength shifting branch of the usually broad LPG fundamental cladding mode located near to the dispersion turning point. The practical limitations of the HP70004A OSA clearly limit the ability to verify this assertion.

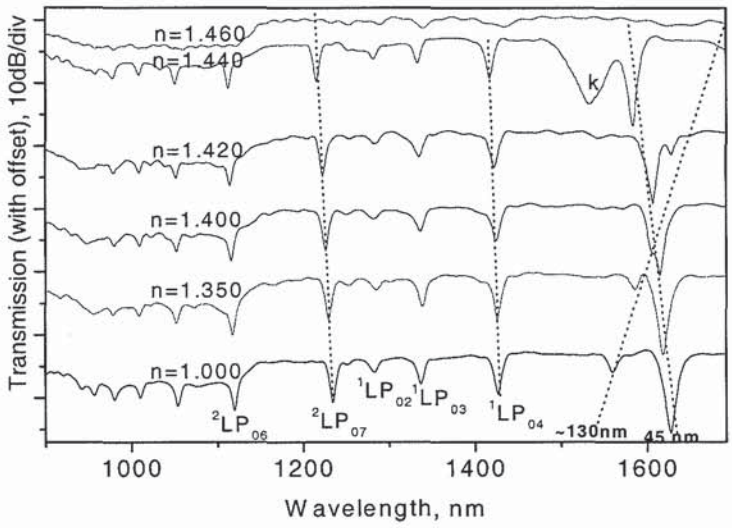

Fig. 5.25: Spectral responses an LPG in B/Ge co-doped fibre with respect to changing SRI showing one mode at 1560nm shifting to the longer wavelength by 130nm and the mode at 1625nm shifting to the shorter wavelength by 45nm for SRI increased from 1.00 to 1.46. Peak 'k' is believed to be the short-wavelength shifting branch of the mode located near the dispersion turning point.

(B) Fundamental cladding mode $^1LP0_{2L}$ in standard SMF and its use for sensing:

In applications such as gain flattening, the responsivity of a fibre grating device to external perturbations such as bending, temperature, strain and the SRI is not particularly desirable because, for example, the recoating of an LPG with a material of high index of refraction can shift the wavelength and also reduce the depth of the transmission loss bands thereby limiting the device's capability for use in sensing and gain equalization. Index insensitive LPGs that

[25] If the strain coefficients of the two peaks are equal then the change in spacing between the peaks should provide a direct measure of temperature, thus, leading to an LPG index or temperature sensor with intrinsic strain compensation.

are capable of addressing such a problem have been demonstrated in [184] and another solution is proposed in Subsection 5.3.2: in both works, a special fibre had to be used. Whilst in Subsection 5.3.2 a series of cladding modes of an LPG fabricated in a double-cladding fibre are demonstrated to be index-insensitive, in [184] a Dual Shaped Core (DSC) Dispersion Shifted Fibre (DSF) was used to inscribe an LPG that exhibits a 'strong first peak' that has no responsivity to SRI. To the author's knowledge, the origin of this index-insensitive LPG peak obtained in DSC-DSF has not been identified. In this work, it is demonstrated that a similar feature can be obtained in a standard SMF (see, for example, Fig. 5.20). Fig. 5.20 has revealed, more clearly, LPG features in the region 1050 to 1300nm: again, the broad loss peak located at ~1244nm is an LPG cladding mode labelled $^1LP_{02L}$. The peak $^1LP_{02L}$ appears in LPGs written with a certain range of periods in the standard SMF used. Typically such a peak appear broadly and clearly in LPG with period from 470 to 490 μm as shown in Fig. 5.26

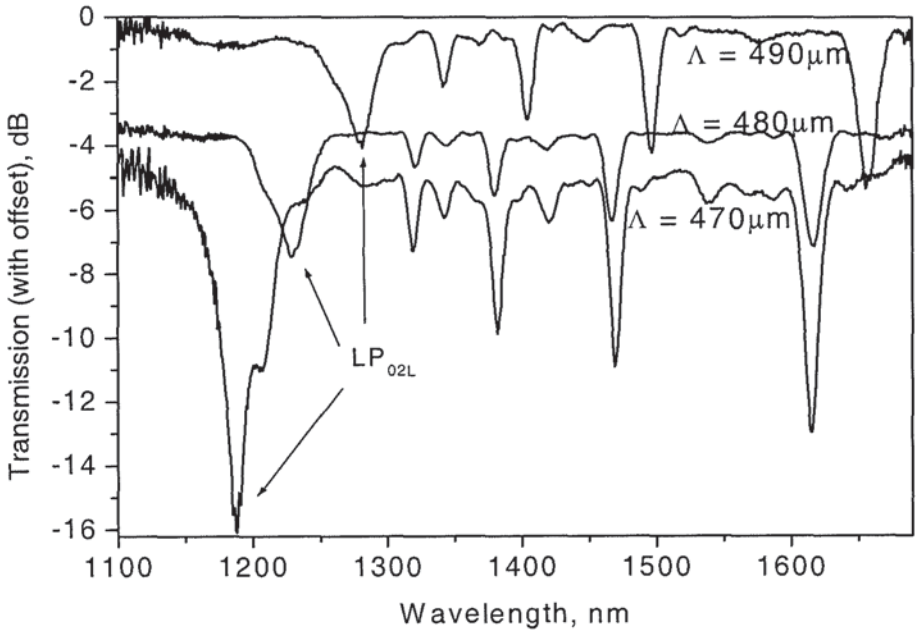

Fig. 5.26: Spectral responses of LPG2, LPG3 LPG4 in standard SMF showing the fundamental mode $^1LP_{02L}$ appearing at different wavelength for LPGs of different periods

Interestingly, the broad peak $^1LP_{02L}$ does not appear in any of the LPGs fabricated in B/Ge co-doped fibre under similar fabrication conditions. In particular, it did not appear in any of the LPGs having details listed in Table 5.6. Furthermore, it has been seen in Fig. 5.18 that the

[26] Shift to the longer wavelength w.r.t. increase in SRI

spectral response of LPG6 showed no cladding mode $^1LP_{02L}$. An additional example of LPG in this B/Ge fibre is depicted in Fig. 5.27, where the LPG of 490μm does not show $^1LP_{02L}$ mode.

LPG designation	Fibre type	Period (μm)	No. of samples	Approx. length (mm)	UV scan speed (mm/s)	Presence of harmonics	Presence of $^1LP_{02L}$
LPG5	B/Ge co-doped	421	69	29.05	2.400	Yes	No
LPG6	B/Ge co-doped	480	63	30.24	2.000	Yes	No
LPG7	B/Ge co-doped	490	62	30.38	2.000	Yes	No

Table 5.6: LPGs in B/Ge co-doped fibre and their fabrication details

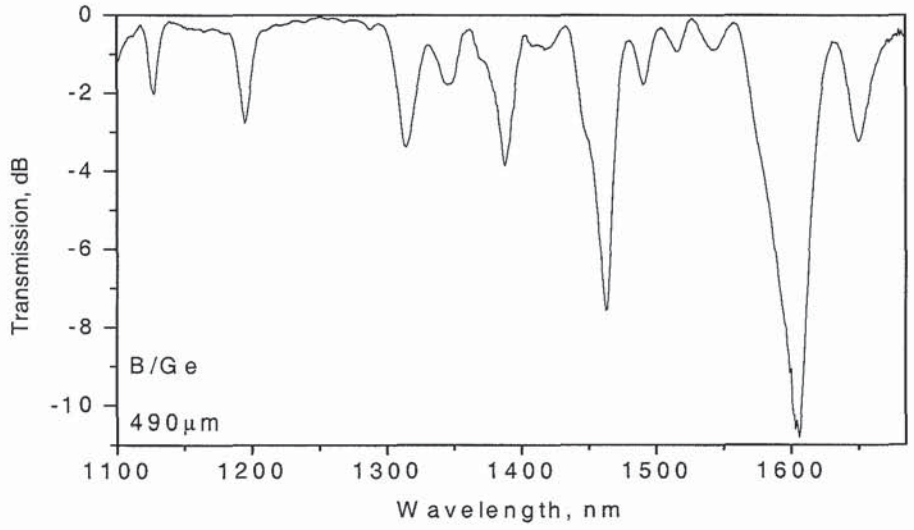

Fig. 5.27: The spectral responses of LPG6 of 490 μm -pitch in B/Ge co-doped fibre showing the fundamental cladding modes.

However, in view of the fact that an LPG fabricated in B/Ge co-doped fibre is much more responsive to external perturbations in comparison to that obtained in standard telecom[27] type, it is unlikely that the peak $^1LP_{02L}$, if obtained in B/Ge co-doped fibre, could be as insensitive as that obtained in a standard SMF.

Simulation results obtained using Optiwave™ IFO software suggest that this peak obtained in the standard SMF is a component of a fundamental cladding mode $^1LP_{02,}$ and for ease of discussion it is referred to as $^1LP_{02L}$ in the remaining parts of this thesis. Analysis described

27. Equations (5.4) – (5.8) and Fig. 5.17 provide a good insight into reason for difference in sensitivities of LPGs in SMF and B/Ge co-doped fibres.

herein suggests that the peak results from coupling of light from a second core mode to the fundamental cladding mode $^1LP_{02}$.

An analysis to identify the origin of $^1LP_{02L}$ has been carried out. The temperature coefficient of the mode $^1LP_{02L}$ has been measured. It is noted that though its temperature responsivity is seven times higher than that of a conventional FBG, this will not impede its use for gain equalization owing to the advantage of its SRI-insensitivity, which permits its coupling strength to be reasonably maintained whilst the LPG is embedded in a material that can protect it from small temperature fluctuations. For sensing applications, however, it is shown herein that the temperature responsivity of the mode $^1LP_{02L}$ can be put to a number of good uses.

For this analysis, having seen the appearance of $^1LP_{02L}$ only in standard SMF, further identification process for the origin of the cladding mode $^1LP_{02L}$ is discussed. In particular, the results of various experimental tests and analytical simulations, carried out to identify the origin of the cladding mode $^1LP_{02L}$, are analysed. Subsection 5.3.1.4 then discusses the capability of the mode $^1LP_{02L}$ for use in sensing applications.

The advantages of the lack of responsivity of the mode to bending and SRI have been exploited to demonstrate its use in conjunction with the nearby harmonic modes of the LPG for various simultaneous dual-parameter measurement applications such as strain and temperature, SRI and temperature, as well as, bending and temperature measurements. The nearby second diffraction order modes of high resonance order are selected and used together with the $^1LP_{02L}$ for the simultaneous measurement of the physical parameters in view of their high responsivity and the potential advantage of using a single light source for interrogating both spectral features. The results obtained from the measurements are detailed.

Origin of the broad peak $^1LP_{02L}$

Having seen the dual diffraction order LPGs with and without peak $^1LP_{02L}$ the origin of peak $^1LP_{02L}$ was examined. The study of the origin of the broad-loss peak $^1LP_{02L}$ was started by experimental measurement of its responsivity to external perturbations, such as temperature and the SRI. As shown in Fig. 5.28, the fundamental modes of LPG3, including $^1LP_{02L}$, are

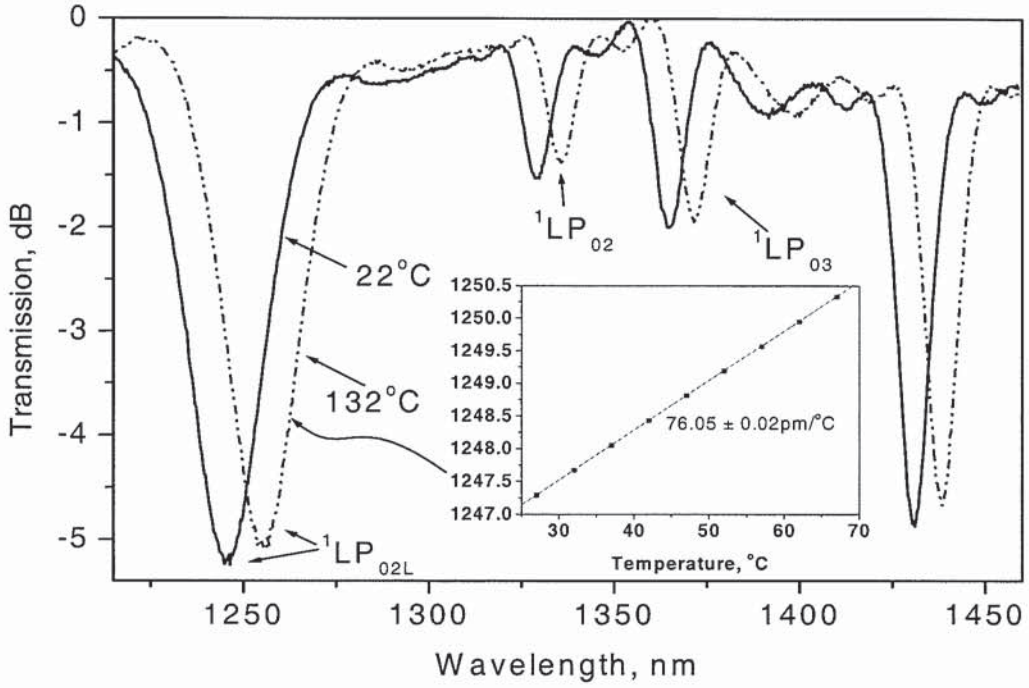

Fig. 5.28: Spectral responses of LPG3 showing the response of some of its fundamental cladding modes to temperature: the inset shows the wavelength shift of $^1LP_{02L}$ plotted against temperature.

responsive to temperature: the inset shows the temperature response of the peak $^1LP_{02L}$ for the temperature range 22 to 67°C, the temperature coefficient recorded from the linear fit to the data points in the inset is 76.05pm/°C which is about seven times more than a conventional FBG.

Also, when the reflection spectrum was measured, no peak was observed, as can be seen in the experimental results of Fig. 5.29: the shallow transmission dips seen on the reflection spectrum relates to the coupling of light that is reflected from the fibre end, into the cladding. In fact, it is possible that some of the light is coupled back into the core, which explains the reason for the appearance of weaker dips at the spectral locations of the stronger modes.

It may also be reasonable to suggest that the components of light at the wavelength of the deeper loss peaks have already been mostly lost before reaching the fibre end, as such, there is not a lot of light, at such wavelengths, reaching the fibre end to be reflected back and get coupled to the cladding during the return trip. This might also explain the reason for negative correlation of the reflection and transmission spectra where the reflection spectrum suffer

more loss at the lower wavelength, consistent with Fig. 2.1 which shows that fibre-loss is higher at low wavelength. In this case, the reflected spectrum suffered from such loss during both trips (i.e. to and fro), which explains its appearance. Clearly, since LPG peaks are intrinsically more responsive to temperature and posses no reflection peak, the response of the broad peak $^1LP_{02L}$ suggests that it is indeed an LPG mode.

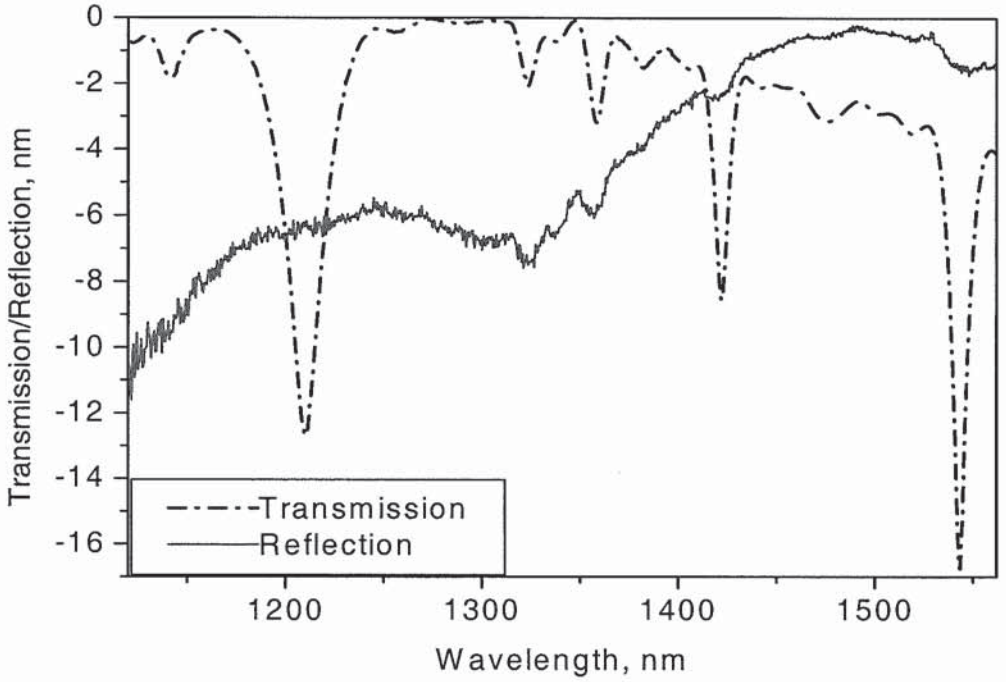

Fig. 5.29: Spectral responses of fundamental modes of LPG3 in transmission and reflection.

Fig. 5.30 shows the response of LPG3 with respect to SRI in the 1200 to 1600nm wavelength region. It can be seen from the figure that the modes $^1LP_{03}$, $^1LP_{04}$, and $^1LP_{05}$ display different amounts of wavelength shifts with respect to changes in SRI, but the modes $^1LP_{02}$ and $^1LP_{02L}$ show no measurable wavelength shift. The inset is the enlarged 1210 to 1280nm spectral region showing a slight decrease in transmission depth of $^1LP_{02L}$ with SRI increase. The $^1LP_{05}$ appear to shift to the longer wavelength when the SRI was 1.460 and 1.478, which are values higher than cladding index. Clearly, as the SRI becomes slightly higher than cladding index there is apparent increase in the cladding width which has the effect of causing a shift to the longer wavelength in standard-fibre based LPG cladding modes of lower order [185,186].

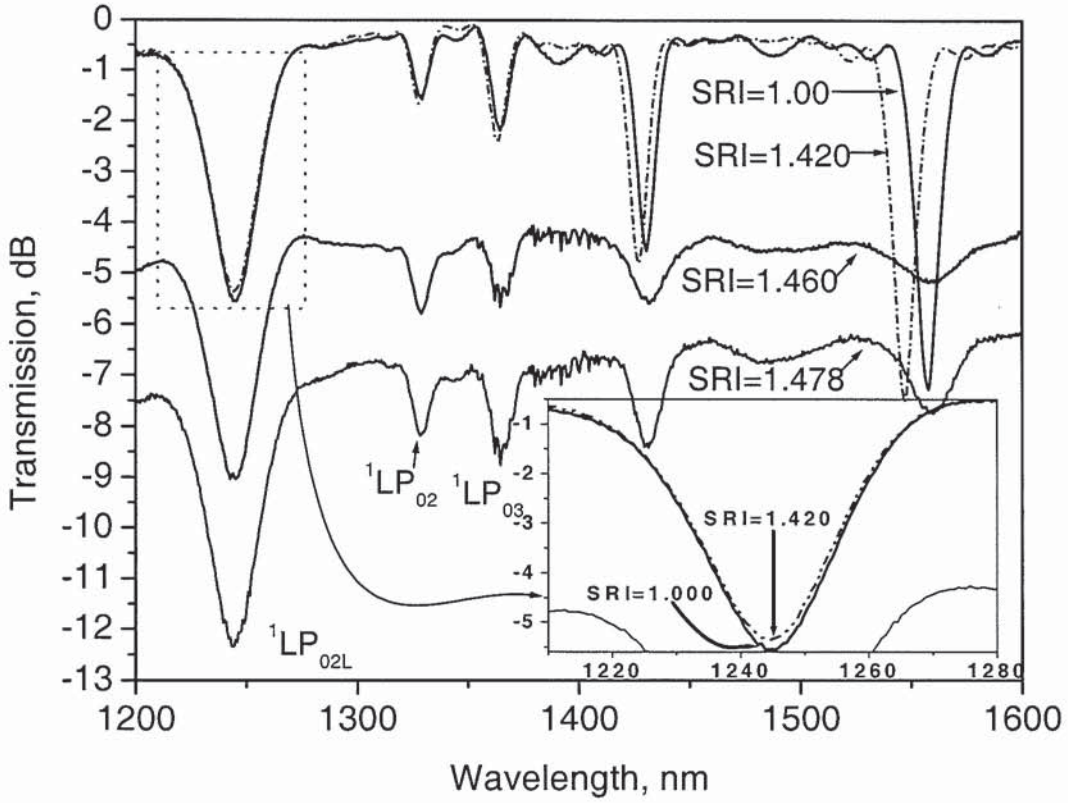

Fig. 5.30: The experimental spectral responses of LPG3 showing the response of some fundamental modes of LPG3 to SRI, with the peak $^1LP_{02L}$ showing no measurable wavelength shift: the inset shows the slight change in transmission depth of $^1LP_{02L}$ with SRI increase.

In addition to these experimental investigations, simulation was carried out to see whether or not an LPG with such characteristics could be obtained. An LPG displaying similar behaviour was generated by simulation using Optiwave™ IFO software with the input parameters listed in Table 5.7 and the spectral responses obtained are shown in Figs. 5.31 and 5.32. In Fig. 5.31 the simulated LPG was subjected to SRI ranging from 1.000 to 1.442: whilst the upper inset indicates that cladding modes $^1LP_{02}$ to $^1LP_{05}$ are SRI sensitive, it is quite obvious from the lower inset to the figure that the mode $^1LP_{02L}$ does not shift with changes in SRI, but slightly decreases in transmission strength as the SRI is increased, in agreement with the experimental results shown in Fig. 5.30. It is noted that the mode $^1LP_{06}$ shown in the spectral region 2.0 to 3.6μm in Fig. 5.31 is highly responsive (its bifurcated component shifted to the shorter wavelength by 690nm for the SRI change from 1.00 to 1.442) in view of its location, which is very close to the dispersion turning point [73].

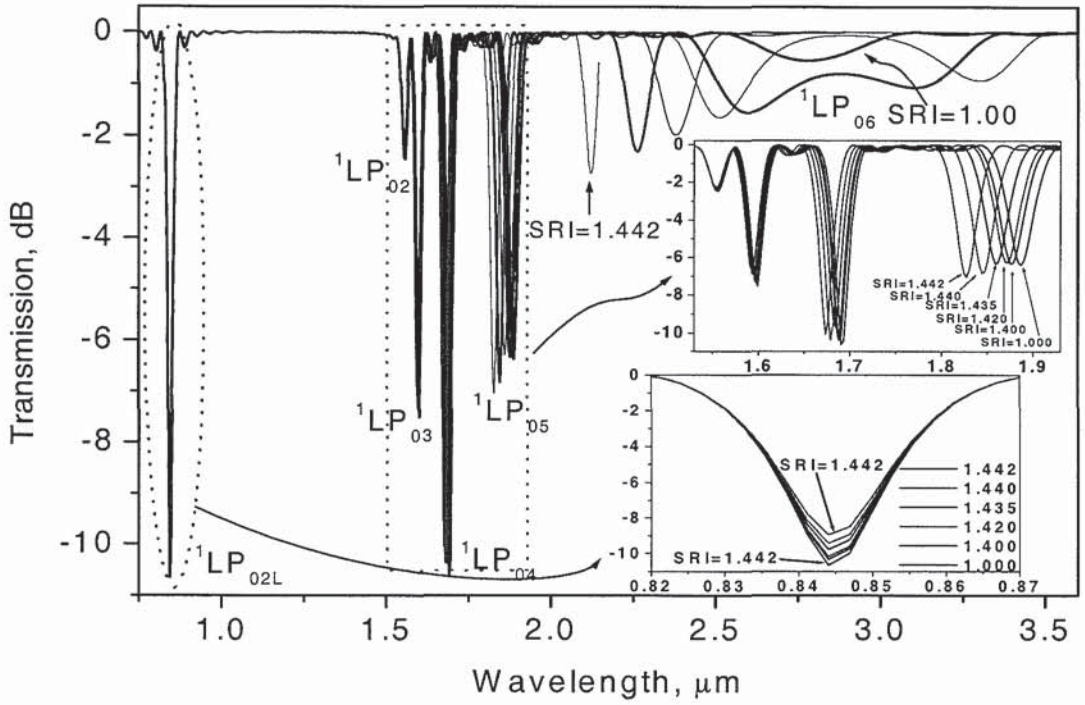

Fig. 5.31: Spectral responses of the calculated 480 μm -pitch LPG to SRI showing no measurable wavelength shift of the peak $^1LP_{02L}$ but showing slight decrease in the transmission depth of the peak.

Sellmier coefficients	Figure	Cladding index, n_{cl}	Core index, n_{co}	Cladding radius, r_{cl}	Period, Λ	SRI	UV-induced average index change	Spectral span	Grating Length
A_1=0.07028554 A_2=0.41463070 A_3=0.89745400 λ_1=0.07200000	Fig. 5.31	1.444	1.4488	62.05μm	480μm	Vary	$3x10^{-4}$	0.75-3.6μm	20.24mm
λ_2=0.11400000 λ_3=9.84100000	Fig. 5.32	1.444	Vary	62.05μm	480μm	1.00	$3x10^{-4}$	0.75-3.6μm	20.24mm

Table 5.7: List of parameters used for simulations

A further analysis that was carried out using the Optiwave™ IFO software suggests that the first two peaks of the LPG, shown in Fig. 5.31, belong to an $^1LP_{02}$ cladding mode. The analysis was supported by a selective display of individual modes of the calculated LPG spectral response permitted using the Optiwave™ IFO software which helped to re-confirm that the first two peaks belong to the fundamental mode $^1LP_{02}$. In a further analysis only the refractive index of the fibre core was changed from 1.44706 to 1.44835 as a result of which the spectral responses shown in Fig. 5.32 were recorded. The separation of the first two

modes with core index change resembles the type of separation obtained on a mode positioned on dispersion turning point ($^1LP_{06}$)

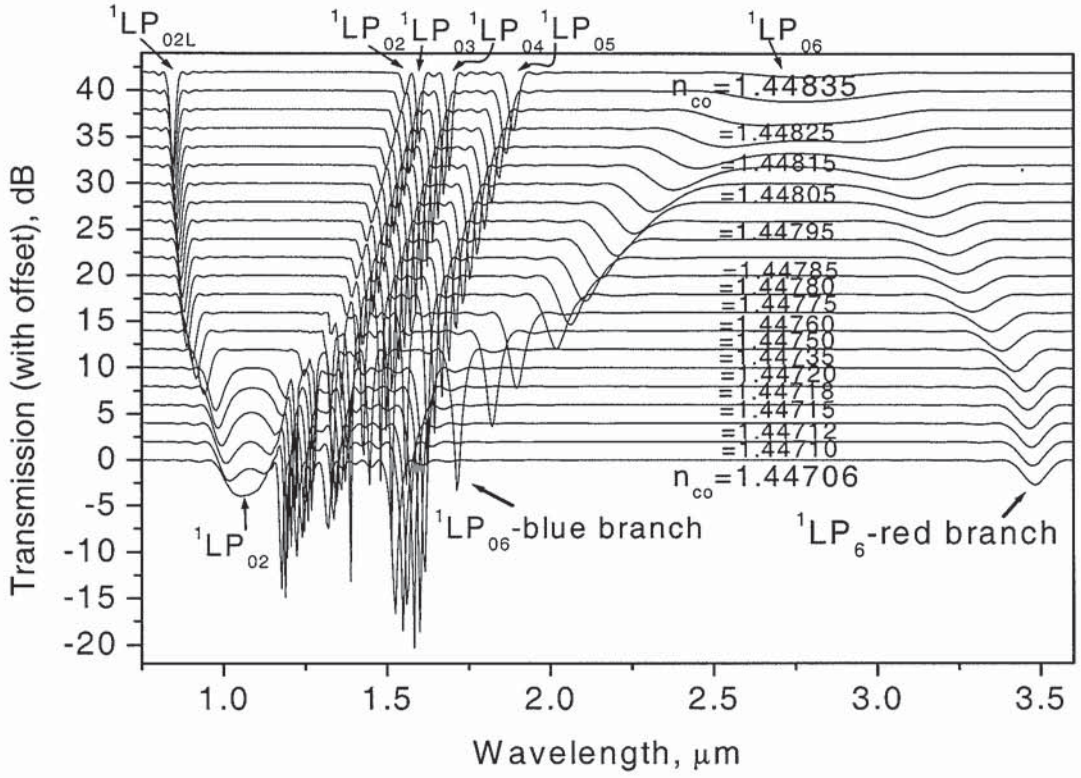

Fig. 5.32: Spectral responses of the calculated 480 μm -pitch LPG showing its evolution with respect of changes in the refractive index of the fibre core.

-when external perturbation is induced to the grating, but only that the separation is in reverse order, as seen in the figure. The lack of responsivity of the mode $^1LP_{02L}$ to SRI is attributed to the fact that it is the farthest cladding mode from the dispersion turning point on the shorter wavelength side and the value of the general sensing factor, γ [73,182], described by eqn. (5.8) is almost zero at such a position.

It might be necessary to note that, the main differences observed between the two peaks associated with $^1LP_{02}$ mode and the dual-resonance of the high order modes such as the $^1LP_{06}$ (at DTP) are that, whilst the dual-resonance of high resonance order modes of LPG are the most responsive and separate further with increase in temperature, the two peaks of $^1LP_{02}$ are the least responsive and both peaks shift in the same direction with temperature increase as seen earlier in Fig. 5.28.

Further analysis to verify whether or not there is a second dispersion turning point for the lower order cladding modes led to the calculation of phase relationships[28] for the first 53 fundamental cladding modes as shown in Fig. 5.33 (a)-(d). The curves were plotted to cover most of practically usable wavelength region, –no second dispersion turning point was observed for any of the modes as seen clearly in the figures.

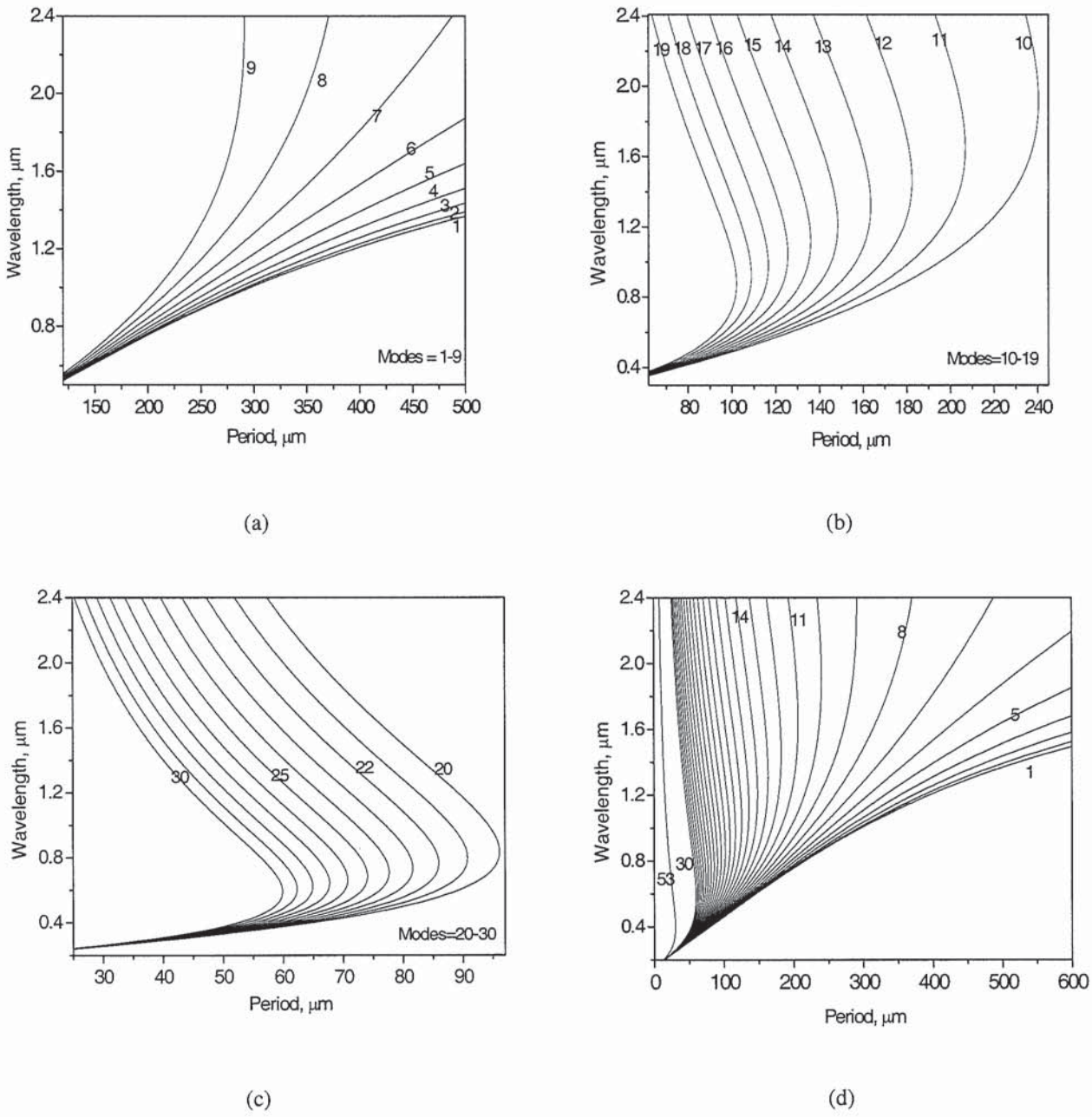

Fig. 5.33: The calculated relationships between resonant wavelengths and LPG periods for the first 53 cladding modes in standard SMF; (a) cladding modes 1-9, (b) cladding modes 10-19, (c) cladding modes 20-30, (d) cladding modes 1-30 and 53.

28. Phase relationship was calculated using Matlab software and the full program in shown in Appendix2

If the LPG period is known, which often the case, then using dispersion curves of Figs. 5.33 (a)-(d) as a guide, it is possible to have an idea regarding the wavelength at which to expect individual cladding modes. This process has facilitated the identification of LPG modes in Fig 5.18. Reference [124] has given more details of this identification method. It can be seen also in the figures that the direction of the slope ($\frac{d\lambda_{res}}{d\Lambda}$) of the phase curves changes, initially increasing, then reaching an infinite level (at the dispersion turning point) and then changed again to negative values[29]. The slope at the points nearest to the dispersion turning point are the steepest, therefore the cladding modes located at this position are the most responsive to any perturbation that may cause changes in either the grating period or the mode index. The parameters used for the simulations were obtained from Adam's book [187] and are matched those used for the Optiwave™ IFO simulations.

Further analysis of this rather unusual behaviour of the $^1LP_{02L}$ mode focused on the core modes. Using Optiwave™ IFO for the study, it was realized that any significant increase in either the core-index or increase in core radius (which matches what happens during UV exposure) [188] will lead to the emergence of the second core mode, and where there is a tilt angle the ghost mode LP_{11} will also become stronger as illustrated in the simulation results of Fig. 5.34. This analysis clearly supports the argument that the peak $^1LP_{02L}$ results from coupling from second core mode to the cladding mode $^1LP_{02L}$ as suggested by the Optiwave™ IFO software.

In the subsequent experiments described in Subsection 5.3.1.4 it is shown that the peak $^1LP_{02L}$ can be used in conjunction with a second diffraction order cladding mode of high resonance order to achieve a sensing device that has the capability for simultaneous measurement of various physical parameters.

[29] . This change from positive to negative is one reason for having modes, of the same LPG, in the same fibre, moving in opposite directions, with changes in external perturbations.

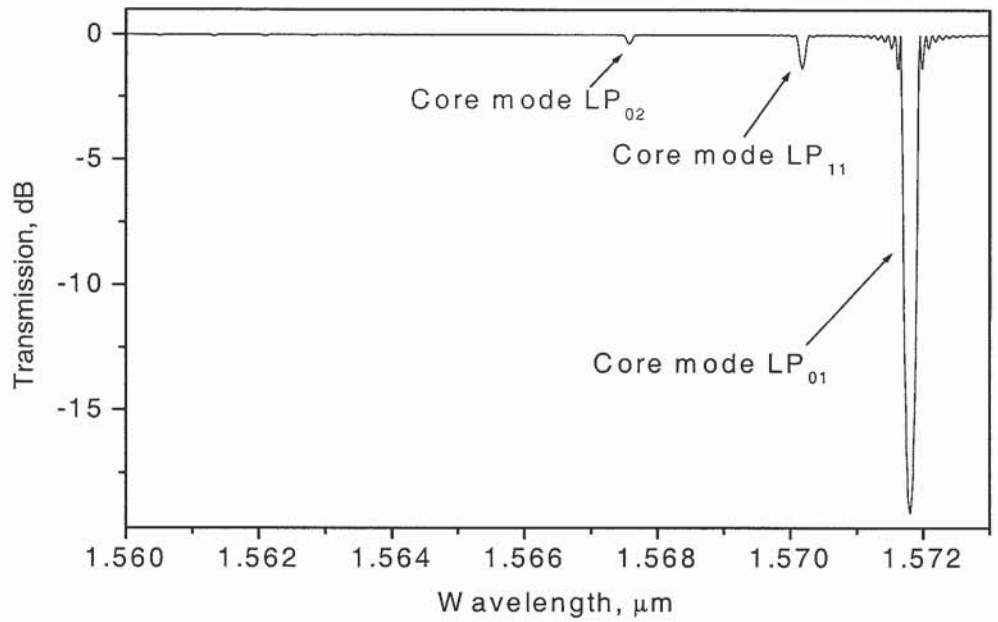

Fig. 5.34: Spectral response of a Bragg grating simulated for standard SMF showing using a tilt angle of 0.4° and a core index increase of 0.007676.

5.3.1.4 Using $^1LP_{02L}$ mode for measurement of temperature with other parameters

In general, fibre sensors have many attractive features that make them well suited for a wide range of strain, or curvature measurement applications in smart structures. They are light in weight, small in size and immune to electromagnetic interference. Unfortunately, the intrinsic temperature responsivity of in-fibre gratings can affect their use for the measurement of these parameters. It is therefore of vital importance to develop a device that can discriminate against, or simultaneously measure and compensate for the temperature-induced effects in order to improve the accuracy of the measured values of axial strain or curvature.

Similarly, in the area of chemical sensing although fibre gratings have been extensively used to measure the refractive index of chemicals, the precise determination of the concentration level of the chemicals equally needs temperature calibration since the refractive index of a chemical is a function of temperature. Thus, it is essential that the temperature be simultaneously measured with the SRI in these applications. Clearly, in both smart structures

and chemical sensing, simultaneous measurement of temperature with the relevant parameters such as strain, curvature, temperature and SRI is essential.

(A) Measurement of temperature

The technique explained in Subsection 4.6.2 was followed for measuring temperature around the LPG device which ranged from 22°C up to 132°C with an incremental step of 5°C and the corresponding spectral changes were recorded using the HP70004A OSA that has a resolution of ~0.1 nm.

It has been demonstrated in Fig. 5.28 that peak $^1LP_{02L}$ and the other fundamental modes of LPG3 are responsive to temperature, with $^1LP_{02L}$ having a temperature coefficient of 76.05 ± 0.02pm/°C. In Fig. 5.35, it can be seen that the harmonic modes of second diffraction order are also responsive to changes in temperature: the temperature coefficient of, for example, mode $^2LP_{05}$ was evaluated to be 42.16 ± 2.4 pm/°C.

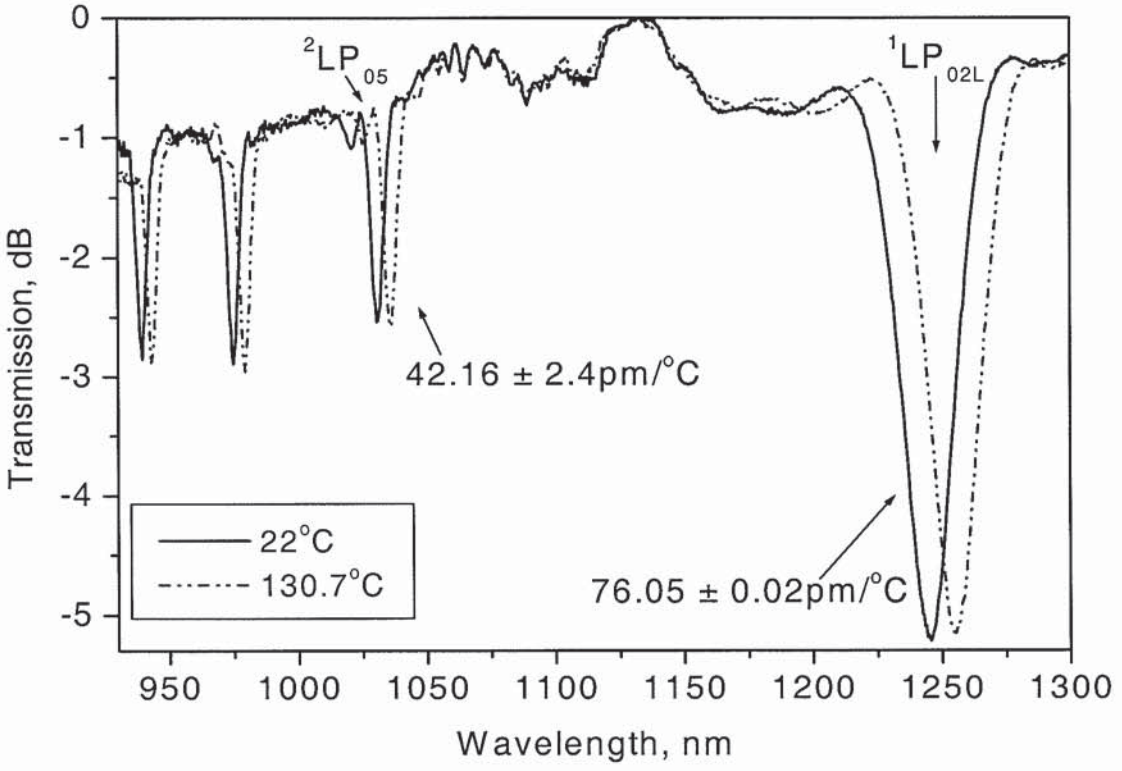

Fig. 5.35: Spectral responses of LPG3 at zero axial strain but different values of temperature showing cladding modes of second diffraction order and the peak $^1LP_{02L}$.

(B) Measurement of refractive index

To measure the SRI, using the in-fibre LPG devices the method earlier discussed in Subsection 4.6.3 was followed. But, earlier investigations have shown that whilst peak $^1LP_{02L}$ is insensitive to SRI, the fundamental cladding modes of high resonance order are clearly responsive to it, as demonstrated in Figs. 5.30 and 5.31. Unfortunately, the spectrally close fundamental modes (for example $^1LP_{03,}$) have shown a rather small SRI responsivity, which impede their effectiveness for use in simultaneous measurements of SRI and temperature. Although fundamental modes of high resonance order (for example $^1LP_{05,}$) exhibit high SRI responsivity, they are some distance away from the peak $^1LP_{02L,}$ (for example >250nm for LPG2) thus, to use such fundamental modes of high resonance order for simultaneous measurement of temperature and SRI, two light sources may be required.

To improve the possibility of using a single light source, the responsivity of a second diffraction order mode $^2LP_{05}$ that is located close to $^1LP_{02L}$ was investigated, and as expected[30], its responsivity to SRI was higher than that of the fundamental modes neighbouring the peak $^1LP_{02L}$.

Fig. 5.36 shows the spectral response of LPG3 with respect to SRI in the wavelength range 930 to 1280nm: the inset is the enlarged 965 to 1037nm region. The second order harmonic modes of this LPG clearly indicate a significant SRI responsivity with $^2LP_{05}$ showing higher responsivity in comparison to the lower resonance order second diffraction order modes shown in the figure.

[30]. Before, the DTP (i.e the Flip-Flop region shown in Fig. 5.17), the responsivity of lower resonance order modes is smaller than that of higher resonance order modes. For every diffraction order considered the case is the same. A higher resonance order harmonic mode has similar responsivity to that of similar order fundamental mode, thus, higher resonance order harmonic mode, by association, will have higher responsivity in comparison to lower resonance order fundamental modes.

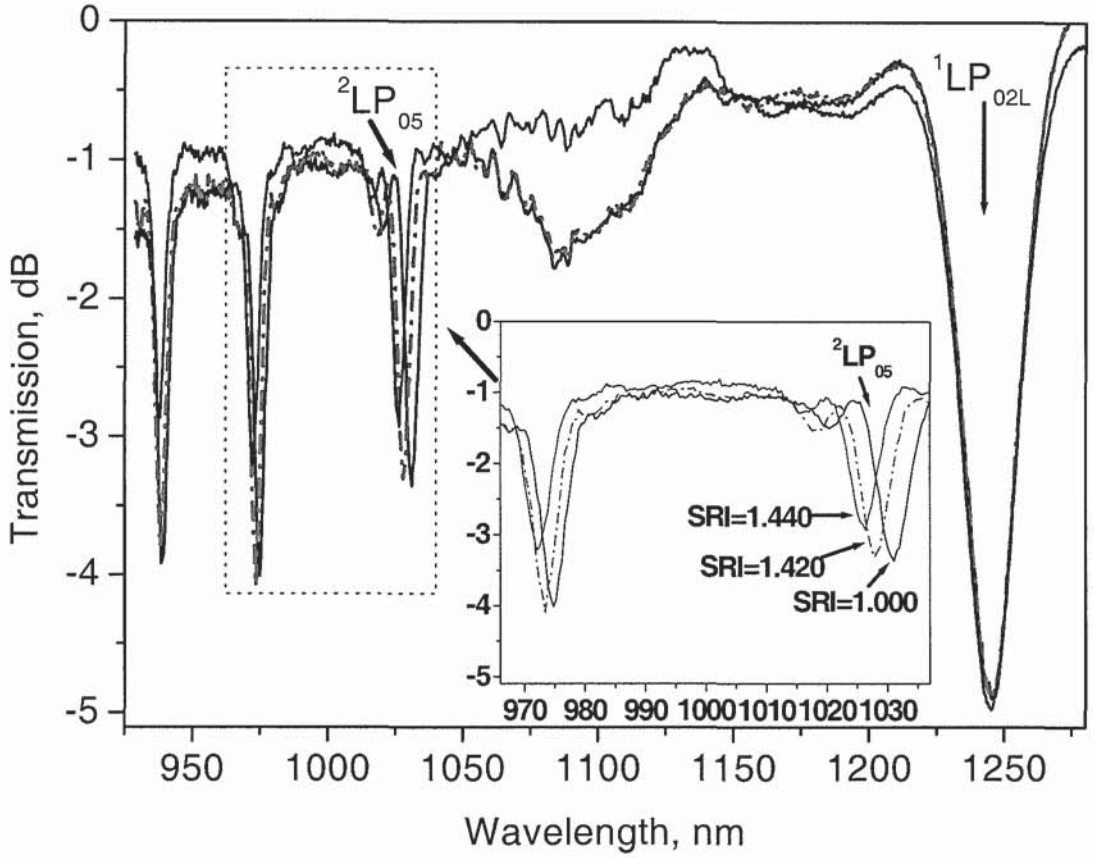

Fig. 5.36: Spectral responses of LPG3 at zero axial strain and constant temperature, but different values of SRI showing cladding modes of second diffraction order and the peak $^1LP_{02L}$: the inset is the enlarged 965 to 1037nm region.

Since the peak $^1LP_{02L}$ is responsive to only one of the two parameters (i.e. temperature), and the second diffraction order mode $^2LP_{05}$ is responsive to both, it implies that these two modes of the single device (LPG3) can be used for simultaneous measurements of SRI and temperature: indeed since the temperature coefficients of both peaks are known, the temperature-induced wavelength shifts can be compensated.

The use of this device for the simultaneous measurement of SRI and temperature assumes that the device will be maintained at constant strain. In a situation whereby strain is varying however, an SFBG (see Subsection 5.4.2) can be fabricated with the same long-period specifications, but a phase mask that allows for an FBG component to appear within the required wavelength region must be used. The strain variation on the FBG peaks can then be used for compensating the strain-induced wavelength shifts.

(C) Measurement of curvature

The 4-point bending jig shown earlier in Fig. 5.4 of Subsection 5.2.1.3 and in Fig. 5.37(a) was employed to induce different curvatures to LPG3. For the bending measurement, the fibre containing LPG3 was attached to a 0.5mm thick spring metal bar of 20mm width and 150mm length. One end of an 8cm central section of the LPG-containing fibre was fixed firmly to the metal bar, whilst the other end was held loosely so as to maintain a constant axial strain on the fibre. The application of curvature was achieved by depressing the central section of the spring metal bar with a micrometer-drive, and the resulting displacement of the bar was converted to curvature as follows:

Measuring curvature using the deflection distance of the spring-metal bar: Scheme I

In this Sub-section an analysis carried out by the author's colleague Dr Yu Liu is used to describe the bending Jig used for applying curvature. Fig. 5.37(a) shows the jig and (b) describes the result of curvature calculations using both the approximate and the exact representations. According to the geometric configuration, the curvature (1/R) applied to the fibre can be calculated from the following equations

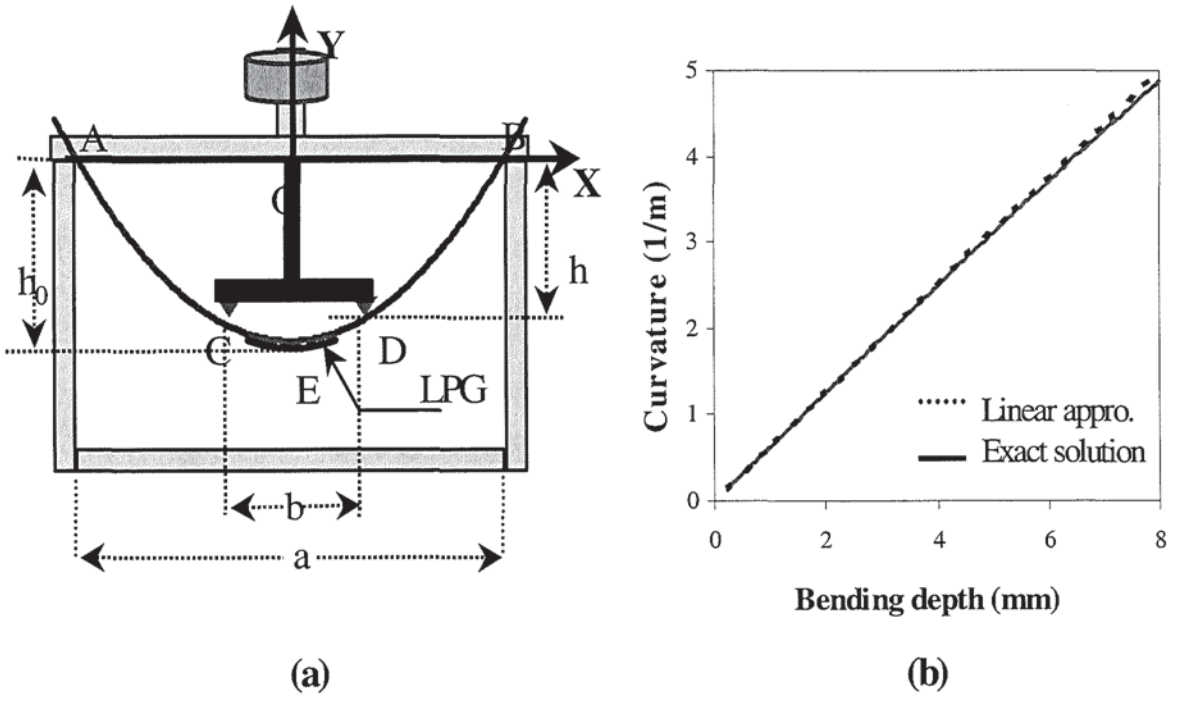

Fig. 5.37: (a) The geometric configuration of the four-point bending Jig. (a)=120 mm, b=20 mm, bending depth h=0~8 mm, (b) Plots of bending curvature against bending depth calculated from equations eqn. 5.14 and eqn. 5.15.

$$\begin{cases} R^2 = (R-h_0)^2 + (a/2)^2 \\ (b/2)^2 + [-h-(R-h_0)]^2 = R^2 \end{cases} \tag{5.13}$$

where the R is radius of the bent spring-metal bar, h is the bending depth which can be read from the micrometer, a and b are the spacing of the points where the force is exerted, as indicated in Fig. 5.37.

$$(a/2)^2 - 2R\left[R+h-\sqrt{R^2-(b/2)^2}\right] + \left[R+h-\sqrt{R^2-(b/2)^2}\right]^2 = 0 \tag{5.14}$$

If $R>>a$, b and h and also $a>>b$ and h, eqn. 5.16 can be approximated to

$$\frac{1}{R} = \frac{8h}{a^2-b^2} \tag{5.15}$$

Fig. 5.37 (b) plots the bending curvature ($1/R$) against the bending depth (h) in line with both equations (5.14) and (5.15). The two curves nearly coincide; suggesting that eqn. 5.15 is a good approximation to be used to calculate the curvature in experiments. Thus, eqn. 5.15 has been used to calculate the curvature applied using the jig.

The curvature response of the LPG3 was investigated, using the above analysis, with zero axial strain applied. Curvature-induced mode splitting [34] was observed for each of the second order harmonic cladding modes ($^2LP_{03}$ to $^2LP_{05}$) in the spectral range 910 to 1250nm. Fig. 5.38 shows the spectral evolution with changing values of curvature for LPG3 with curvature magnitude increased from zero to $3.125m^{-1}$: the inset to Fig. 5.38 is the enlarged spectral region 910 to 1244nm showing the spectra of the second diffraction order modes of LPG3 with an offset introduced for clarity.

It can be seen from Fig. 5.38 that, prior to bending, the harmonic modes of LPG3 are clearly defined by the deeper single loss-bands. As the LPG was subjected to curvature, however, each of the loss bands bifurcates with one sub-band shifting to longer wavelengths and the

other to shorter wavelengths with increase in curvature magnitude. In addition, some asymmetric cladding modes are also observed to appear with increasing curvature.

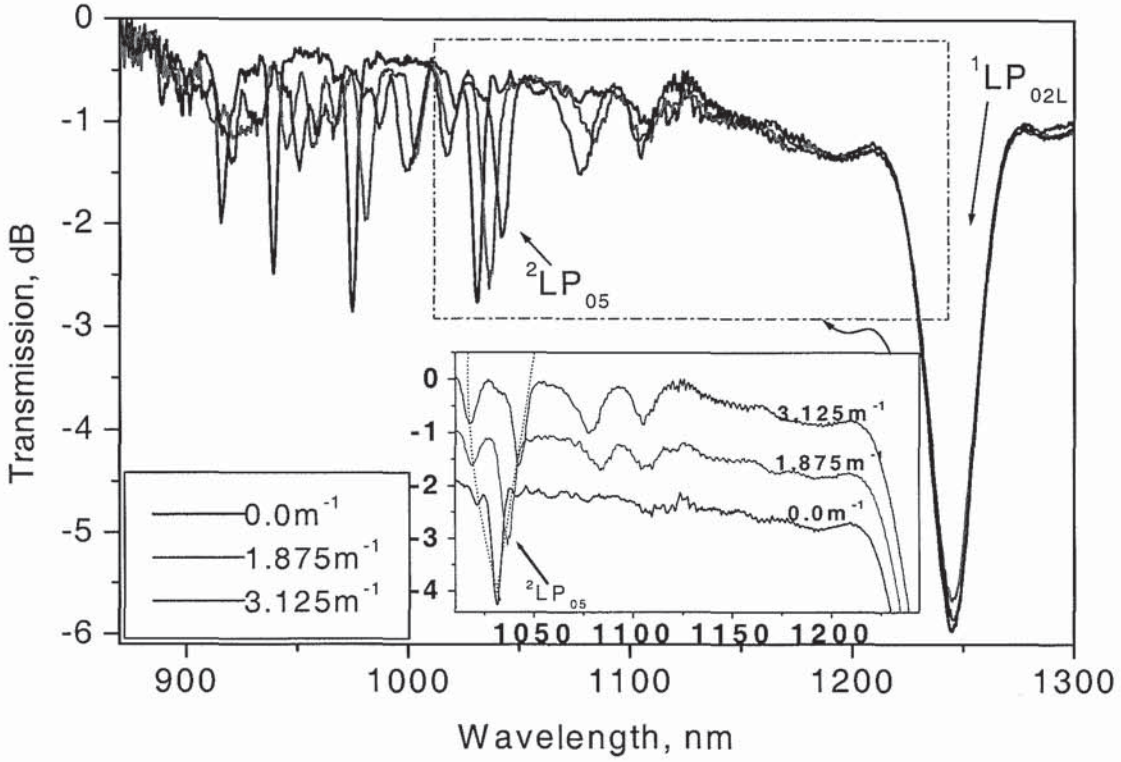

Fig. 5.38: Spectral responses of LPG3 at different values of curvature showing cladding modes of second diffraction order and the peak $^1LP_{02L}$: the inset is the enlarged 910 to 1244nm region with a spectral offset.

For simultaneous measurement of curvature and temperature, it is obvious that since the second order harmonics are bend-sensitive and the peak $^1LP_{02L}$ is not, the curvature values can be extracted from the mode splitting of, for example $^2LP_{05}$, whilst the strain- and temperature–induced wavelength shifts can be compensated by forming a matrix of coefficients of peak $^1LP_{02L}$ and midpoint between the splitting of mode $^2LP_{05}$ using the methods to be discussed in Subsection 5.4.2 (E).

(D) Measurement of axial strain

Following the bending experiment, the spectral response of the LPG3 to axial-strain was investigated. The LPG3 was used in the way described in Subsection 4.6.1 to measure axial strains ranging from 0 to 4.8 x 10^3 $\mu\varepsilon$.

The spectra obtained are shown in Fig. 5.39 and have been analysed to yield axial strain sensitivities of 0.3335 and –0.3894pm/ $\mu\varepsilon$ for the $^1LP_{02L}$ and $^2LP_{05}$ modes of LPG3,

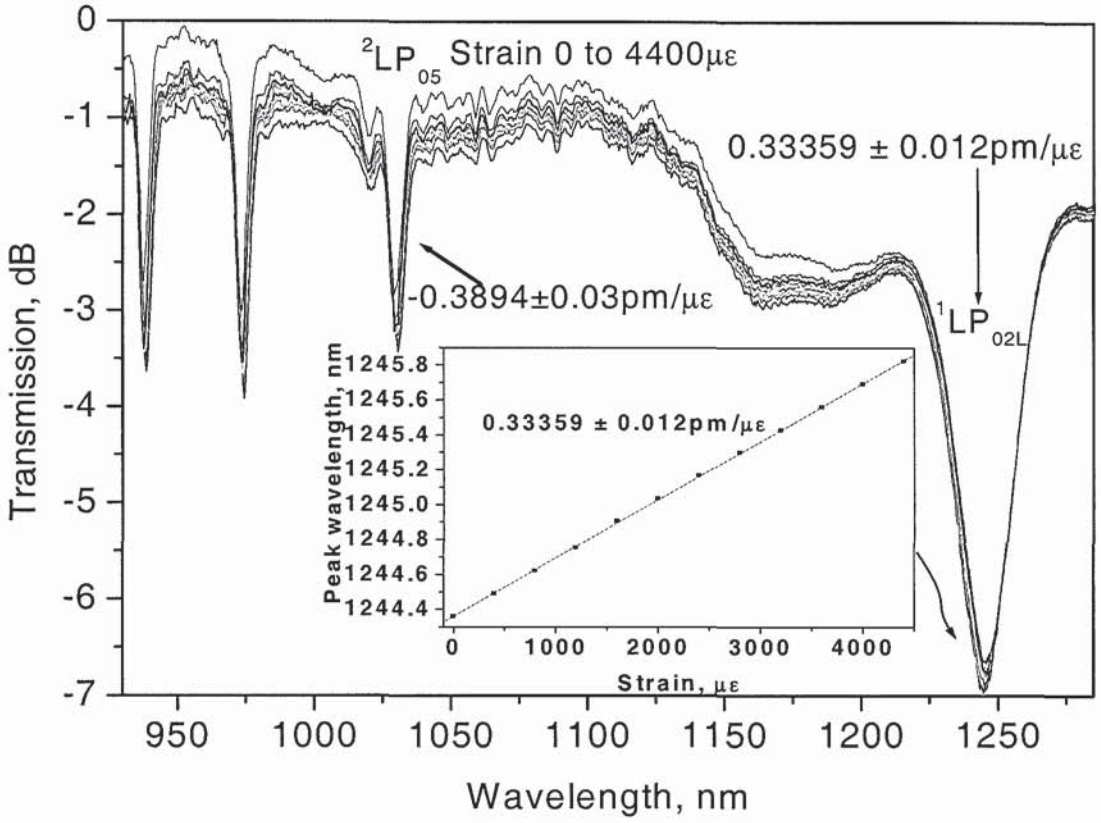

Fig. 5.39: Spectral responses of LPG3 at constant temperature but different values of axial strain showing cladding modes of second diffraction order and the peak $^1LP_{02L}$: the inset is a plot of the spectral positions of the peak $^1LP_{02L}$ against the applied axial strain.

respectively: the inset shows the wavelength shift of peak $^1LP_{02L}$ plotted against the applied axial strain. Table 5.8 shows the temperature and the strain coefficients of the two modes of LPG3 as specified in Figs. 5.35 and 5.39.

Grating	Parameter	$^2LP_{05}$	$^1LP_{02L}$
LPG3	Strain, K_ε	–0.3889 ± 0.02pm/με	0.3334 ± 0.02 pm/με
	Temperature K_T	42.16 ± 2.4pm/ °C	76.05 ± 0.02pm/ °C

Table 5.8: A typical comparison of the temperature coefficients for loss peak $^2LP_{05}$ and $^1LP_{02L}$ of LPG3 inscribed in a standard SMF.

The contribution to wavelength shifts from axial strain and temperature can be calculated simultaneously using the coefficients in Table 5.8 and the matrix equation

$$\begin{pmatrix} \Delta\lambda_{2LP05} \\ \Delta\lambda_{1LP02L} \end{pmatrix} = \begin{pmatrix} K_{\varepsilon_{2LP05}} & K_{T_{2LP05}} \\ K_{\varepsilon_{1LP02L}} & K_{T_{1LP02L}} \end{pmatrix} \begin{pmatrix} \Delta\varepsilon \\ \Delta T \end{pmatrix} \quad \ldots\ldots\ldots \quad (5.16)$$

Where $K_{\varepsilon_{2LP05}}$, $K_{\varepsilon_{1LP02L}}$ and $K_{T_{2LP05}}$, $K_{T_{1LP02L}}$ are the respective strain and temperature coefficients of $^2LP_{05}$ and $^1LP_{02L}$, $\Delta\lambda_{2LP05}$ and $\Delta\lambda_{1LP02L}$ are the respective wavelength shifts of $^2LP_{05}$ and $^1LP_{02L}$, while $\Delta\varepsilon$ and ΔT are the applied strain and temperature changes.

Substituting the coefficients of $^2LP_{05}$ and $^1LP_{02L}$ listed in Table 5.8 into eqn. (5.16) and inverting to solve for values for axial strain and temperature leads to

$$\begin{pmatrix} \Delta\lambda_{2LP05} \\ \Delta\lambda_{1LP02L} \end{pmatrix} = \begin{pmatrix} -0.3889 & 42.16 \\ 0.3334 & 76.05 \end{pmatrix} \begin{pmatrix} \Delta\varepsilon \\ \Delta T \end{pmatrix} \quad \ldots\ldots\ldots \quad (5.17)$$

The coefficients of strain and temperature are obtained from the linear fits to the data points. The sources of error in this work include the limitations of the equipment used (such as the resolution of the HP70004A OSA and thermoelectric-cooler), the mechanisms of heat transfer from the heating element, and the mechanism for inducing strain, to the device. In the overall, the matrix of coefficients is reasonably well conditioned providing a condition number of 173.29.

In summary, the discussion in Subsections 5.3.1 focused on investigation into the responsivity characteristics of LPGs in conventional B/Ge co-doped and standard SMFs. The LPGs fabricated in both fibres exhibit a set of harmonic cladding modes at shorter wavelength than those of the fundamental modes, while those gratings fabricated in standard SMF exhibited an additional 'broad-peak' ($^1LP_{02L}$) located between the two sets of cladding modes. The second diffraction order cladding modes of LPGs in B/Ge fibre are shown to be capable of being used with a fundamental mode of lower resonance order to measure the values of strain and temperature simultaneously. Here the spectral proximity of the two

cladding modes is such that the advantages of using a single light source for sensing interrogation can be realized.

For the LPGs in the standard SMF, a rigorous identification process for the mode $^1LP_{02L}$ has been pursued, and the sensing properties of the mode have been studied whilst the peak has been utilized in conjunction with the harmonic modes to demonstrate the capability of an LPG device for simultaneous measurement of temperature and other parameters, such as curvature, axial strain and SRI. The promising potential of the mode $^1LP_{02L}$ for gain flattening applications has also been highlighted and this could form the basis for further research in this area.

The advantages of simple fabrication, easy and cost-effective interrogation and, more importantly, inherent temperature referencing of the LPG structures offer the prospect of the development of practical sensors for temperature compensated sensing applications.

5.3.2 LPG sensor in 3-layer fibre

Having studied the LPGs in step index fibres in Section 5.3.1, in this section focus is placed on the use LPG sensor inscribed in a 3-layer fibre. Yin el al [189] demonstrated an LPG having very high responsivity to SRI fabricated in a double-cladding fibre. A pair of identical LPGs placed at a precise distance apart has also been demonstrated for SRI measurements [190]. The precise distance between the grating pair allows for obtaining very fine interference fringe pattern that are relatively narrow as compared with a loss peak of a single LPG. The use of the narrow bands for measuring SRI provides improved resolution of the device for sensing applications. However, because LPGs in general, are inherently responsive to temperature, there is a potential temperature cross-sensitivity problem when they are used in refractive index sensing. Furthermore, although LPGs may be used to measure the concentrations of chemicals [191, 192], precise determination of the concentration level needs temperature calibration since the refractive index of a chemical is a function of temperature. Thus, it is essential that the temperature be simultaneously measured with the SRI in these applications. The analysis of the distribution of energy in a cylindrical waveguide using Bessel functions [9, 113, 215] suggest that (a) such distribution is a function of radius, (b) the fundamental mode propagates in the fibre core, (c) lower order cladding modes propagates in the inner part of the cladding, and (d) the higher resonance order

cladding modes propagates closer to the cladding exterior boundary. Furthermore, the phase matching condition eqn. 5.4 and the normalised propagation frequency, V, (eqn. 3.12) obviously suggest that if there is a second cladding layer, then the modes supported by the inner cladding layer are not affected by change in index of the 4^{th} layer.

In this subsection, a simple compact scheme for simultaneous temperature and SRI measurement using two LPGs inscribed side-by-side in a single piece of SMM900 double-cladding fibre, manufactured by Fibrecore in Southampton, is presented. LPG modes with different SRI responsivity has been identified, with the higher order modes that propagate in the outer-cladding showing responsivity to SRI and the lower order modes that propagate in the inner-cladding exhibiting no measurable responsivity to the SRI. One of the LPGs in the cascaded device, used in this work, is only responsive to temperature while the other is responsive to both the temperature and the SRI. Here, the benefits of the high temperature responsivity of the index-insensitive LPG are exploited and utilized to build a compact sensor with the capability of dual parameter measurements.

5.3.2.1 Properties of a 3-layer fibre and the LPG sensor fabrication

The SMM900 fibre has a core radius of 2.6μm, radial cross-section[31] of the inner-cladding of 42.6μm and a radial cross-section of an outer cladding of 17.3μm. The material refractive index of the outer-cladding is less than that of the inner-cladding, which is also less than that of the core material. The inner cladding being the thicker layer supports the propagation of many cladding modes that are SRI-insensitive. The reason for the SRI insensitivity of the modes in this cladding stems from the fact that their effective mode indices depend only on the index of the core, inner-, and outer-cladding materials.

LPGs used in this work were UV-written in a hydrogenated double-cladding Fibrecore™ SMM900 fibre using a CW frequency-doubled argon laser with an output power of 125mW. The inscription was implemented by scanning the UV beam along the length of the fibre in a point-by-point manner with a 50% on-off duty-cycle using a computer-controlled UV-light shutter. An LPG of 18.9mm length containing 189 samples with $100\,\mu m$ pitch (referred to as

[31] . Radial cross-section here means, distance outward along the radius

LPG100) was first fabricated, and the second LPG (referred to as LPG62) having a length of 21.7mm containing 350 samples with 62 μm pitch was inscribed 10mm away from LPG100. After the side-by-side inscription, the fibre containing the cascaded LPGs was annealed at 105°C for 36 hours in an oven. A typical spectral response of the cascaded LPG device is shown in Fig. 5.40: the loss peaks 'a-f' belong to LPG100 and the peak 'g' belongs to LPG62.

Peaks a-f were identified as belonging to LPG100 at the time of fabrication, -the spectrum of the LPG100 was recorded immediately after inscription, and when the LPG62 was inscribed at the adjacent section, peak 'g' was observed to emerge. In addition, two sets of LPGs 'A' and 'B' were fabricated with periods ranging from 59 to 63 μm , and 96 to 110 μm respectively.

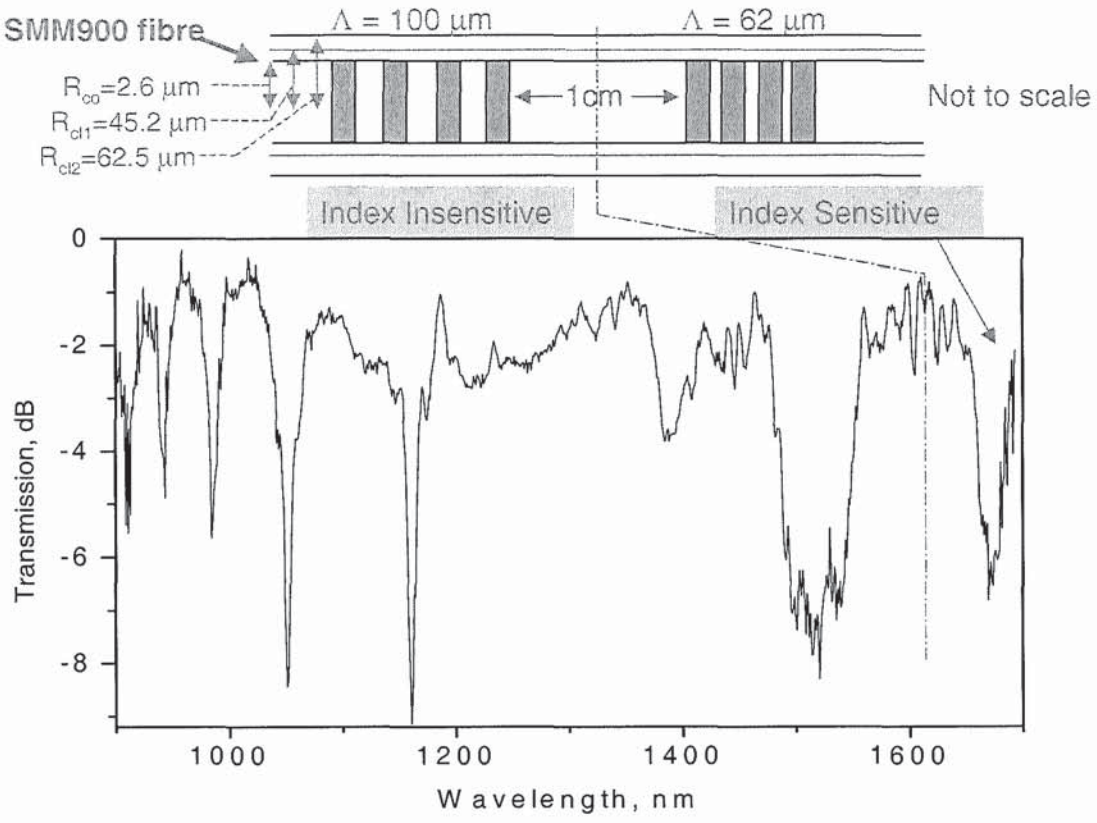

Fig. 5.40: The geometric configuration and spectral response of the cascaded LPG device showing two components with different responsivity regimes, separated by a doted line.

The appearance of one or more LPG peaks that are responsive to both temperature and the SRI, at wavelengths ~ 1660nm, was consistent in the gratings of set 'A'. For example, the

spectral response of an LPG of 60 μm pitch is shown in Fig. 5.41 (a). As can be seen in the figure, one of the LPG peaks is located at ~1663nm and another at ~1671nm. In Fig. 5.41 (b) the spectral responses of this LPG to temperature is indicated.

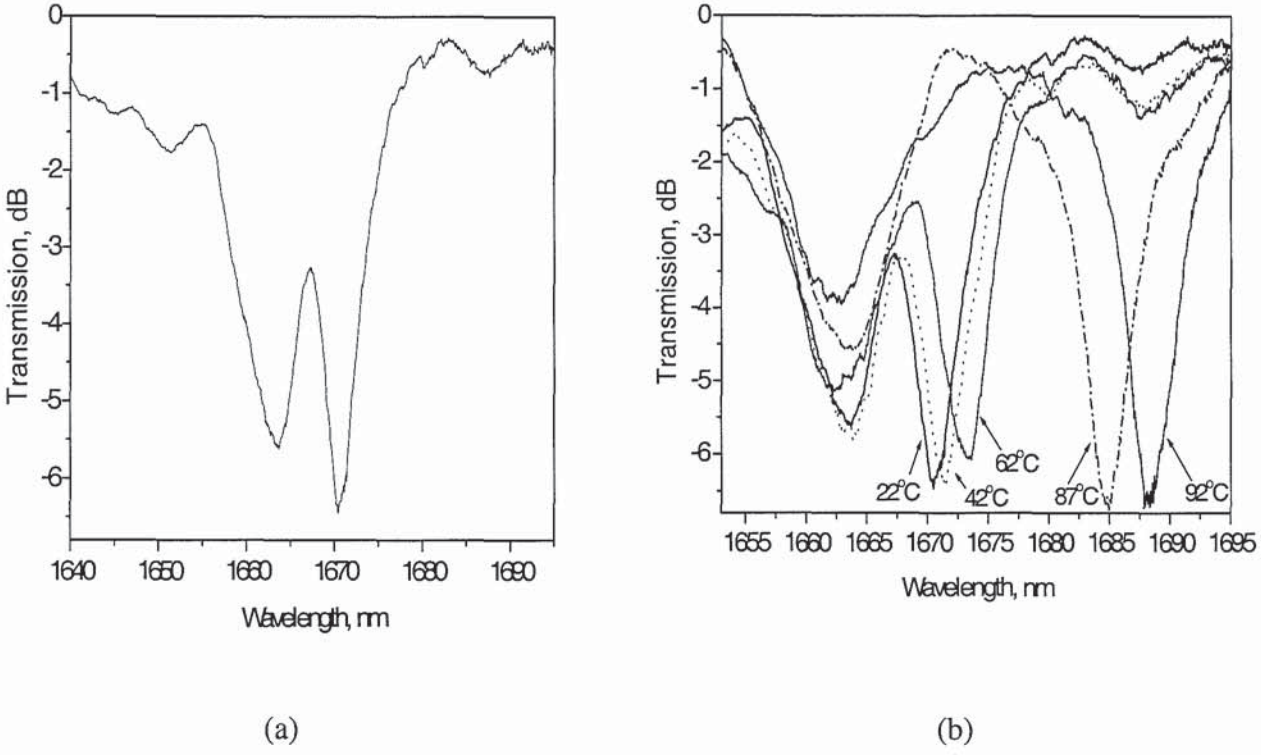

(a) (b)

Fig. 5.41: The spectral response of 60 μm-pitch LPG fabricated in SMM900 double-cladding fibre (a) at 22°C (b) at different temperature values.

For the set 'B', however, a series of peaks that have shown no measurable responsivity to SRI were observed, consistently. These peaks have shown considerable responsivity to temperature, with higher order cladding modes, in this case, exhibiting more responsivity to temperature than those of the lower order. The series of peaks can be seen in Fig. 5.42 which shows the spectral responses of four LPGs from the set B with periods 96, 98, 100, and 105 μm in the spectral range 910 to ~1580nm.

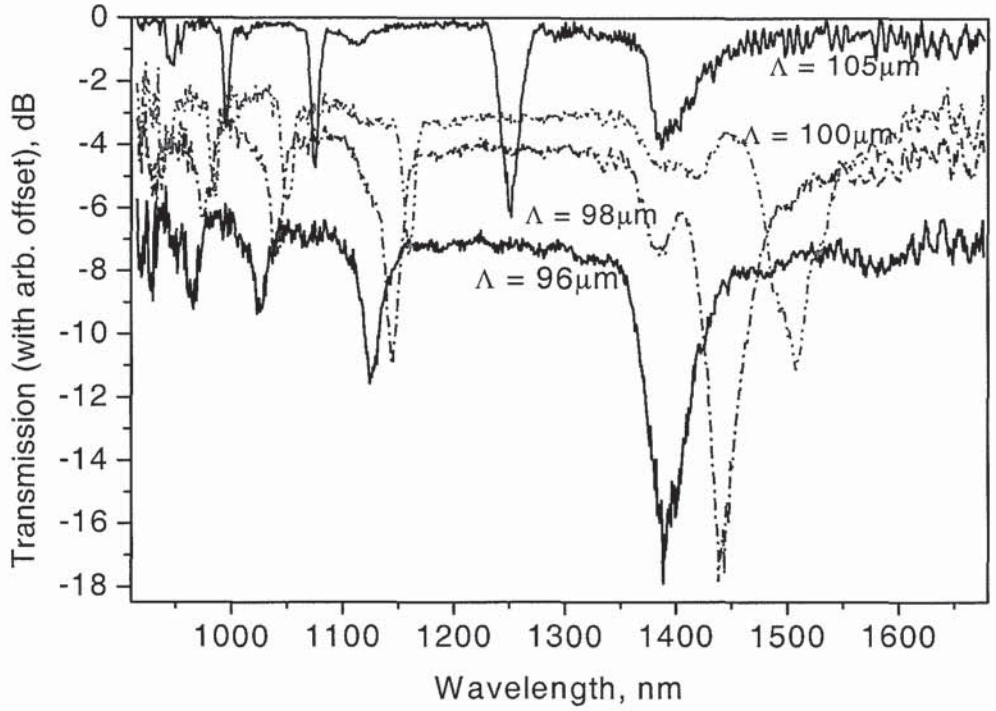

Fig. 5.42: The spectral responses of ~1.9cm long LPGs with 96, 98, 100, and 105 μm pitches showing series of index-insensitive cladding modes with one broad peak in the Erbium-doped fibre amplifier (EDFA) wavelength region.

Peak 'f' of LPG100 shown in Fig. 5.40 is broad and more responsive to temperature in comparison with peaks 'a-e' in view of its proximity to the highly sensitive dispersion turning point region [73]. The peak has been selected for the measurements in order to exploit the benefits of the high temperature responsivity. The peak 'f' was designed to appear close to peak 'g' of LPG62 so that the advantages of using a single light source for interrogation can be exploited. Although peak 'f' is much more responsive to temperature, its intrinsic width can reduce sensing resolution depending on the interrogation technique employed. Further investigations needs to be carried out to produce an LPG in this fibre with an SRI-sensitive higher-order cladding-mode that can appear in the 1200 to1300nm region without much compromise to SRI responsivity.

It has also been observed that the double-cladding fibre is highly responsive to bending which results in some rather noisy losses in the spectral region 1500 to 1700nm. To reduce such bending loss effects, the fibre needs to be maintained as straight as possible during the measurements.

5.3.2.2 SRI and temperature sensing performance

To measure the SRI, the in-fibre cascaded LPG device was used in the way described in Subsection 4.6.3. A typical result of SRI measurement using the cascaded LPG device is shown in Fig. 5.43: the inset is the enlarged 1450 to 1700nm wavelength-region. It is clear from Fig. 5.43 that peaks 'a-f' belonging to LPG100 are insensitive to SRI (such peaks overlap almost perfectly for the SRI of 1.00 and 1.33) but the peak 'g' belonging to LPG62 did not overlap, rather, it uniquely shifts to the shorter wavelength by over 25nm with SRI increase from 1.00 to 1.33 –indicating that SRI can be measured using only peak 'g' of the device.

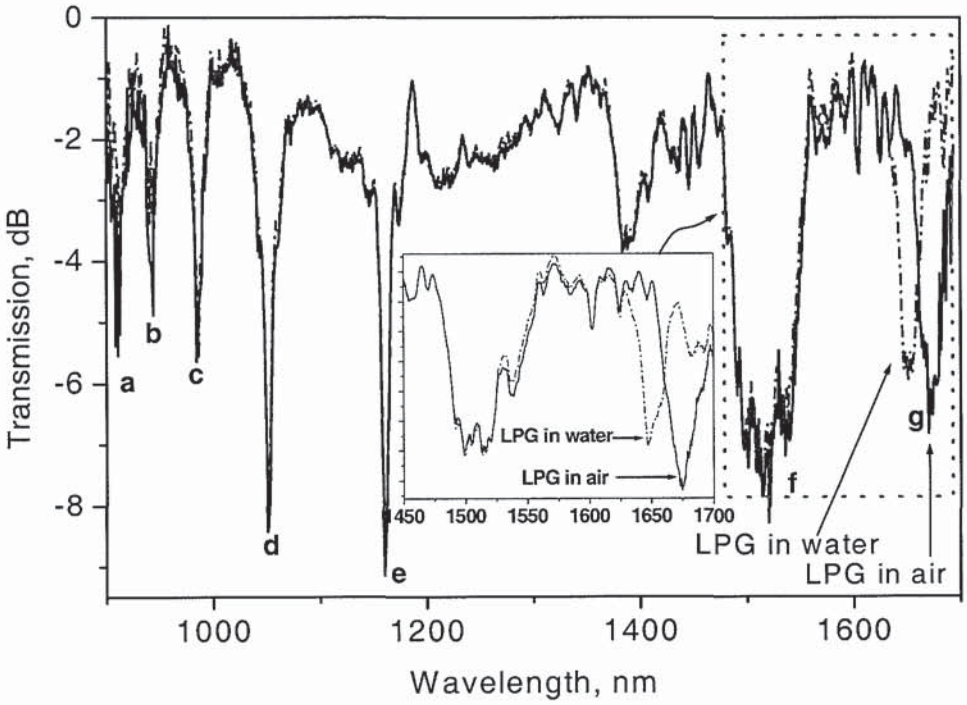

Fig. 5.43: The spectral responses of the cascaded LPG device in air (solid) and water (dotted): the inset shows the enlarged 1450 -1700nm region

To further confirm the lack of index responsivity of the peaks belonging to LPG100 (with 100 μm pitch), oils of refractive indices ranging from 1.33 to 1.70 have been tested on the device: no shift of the loss peaks 'a-f' was discernible with the HP70004A OSA that has a resolution of ~0.1 nm. Furthermore, for an LPG of 108 μm pitch, as can be seen in Fig. 5.44, no shift was observed for the cladding modes when the LPG was immersed in materials of

refractive indices 1.33, 1.42, and 1.70 During the index measurement the temperature surrounding the device was fixed.

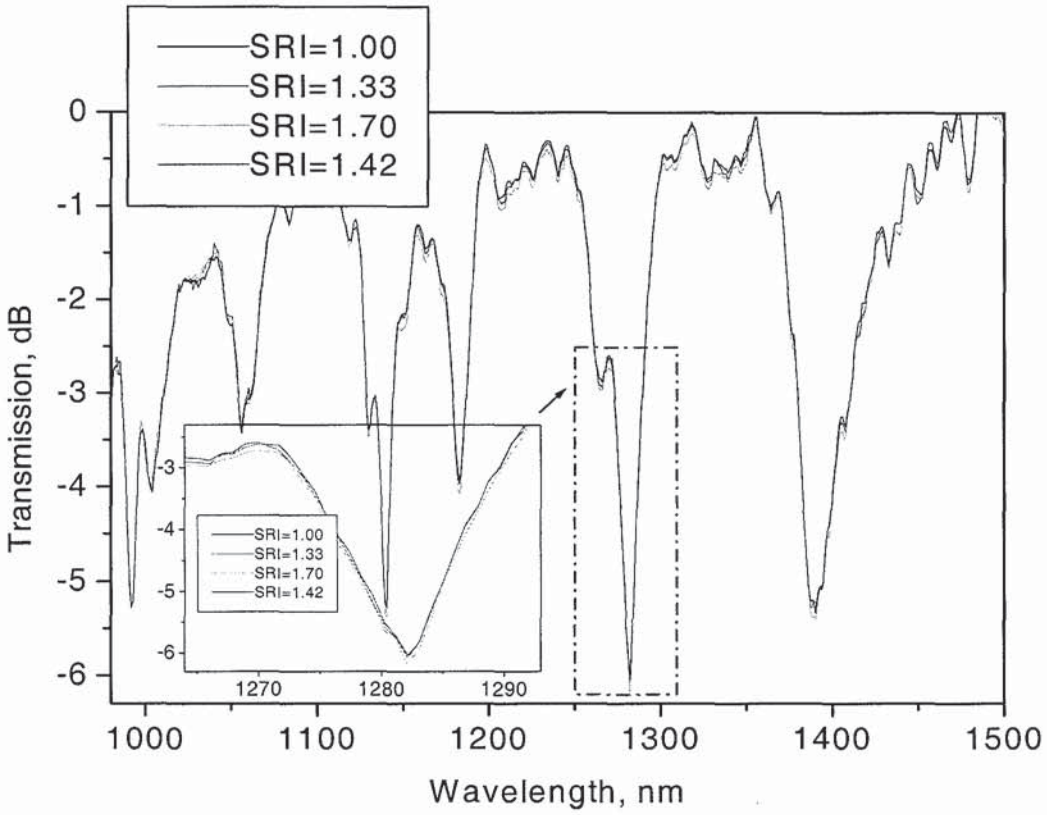

Fig. 5.44: The spectral responses of 108 μm pitch LPG in the SMM900 double-cladding fibre under SRI of 1.00, 1.33, 1.42 and 1.70: the inset is the enlarged 1264-1293nm region.

To measure temperature, the cascaded LPG device was used in the way described earlier in Subsection 4.6.2. Temperature around the device was varied from 22 to 102°C and the corresponding spectral changes were recorded using the HP70004A OSA. SRI in this case is 1.00 since no oil has been applied during the temperature change.

When the cascaded-LPG device was tested against temperature, behaviour different from that shown in Fig. 5.43 emerged, with peaks 'f' and 'g' of the cascaded LPG device shifting to the longer wavelength with increasing temperature. Typically, peak 'f' of LPG100 shifts ~19.4nm whilst peak 'g' of LPG62 shifts ~5nm for a temperature rise from 22 to 100°C, as shown in Fig. 5.45: the inset shows a typical temperature response of an SFBG that performs similar

function[32]. The temperature cross-sensitivity that could affect the SRI measurement using LPG62 (peak 'g'), therefore, can be compensated using the information extracted from LPG100 (e.g. peak 'f'). The temperature responsivity of peak 'f' of the index-insensitive LPG100 of the cascaded device have been evaluated, the value obtained is $\Delta\lambda_{LPG\ 100} / \Delta T = 194\ pm / ^\circ C$.

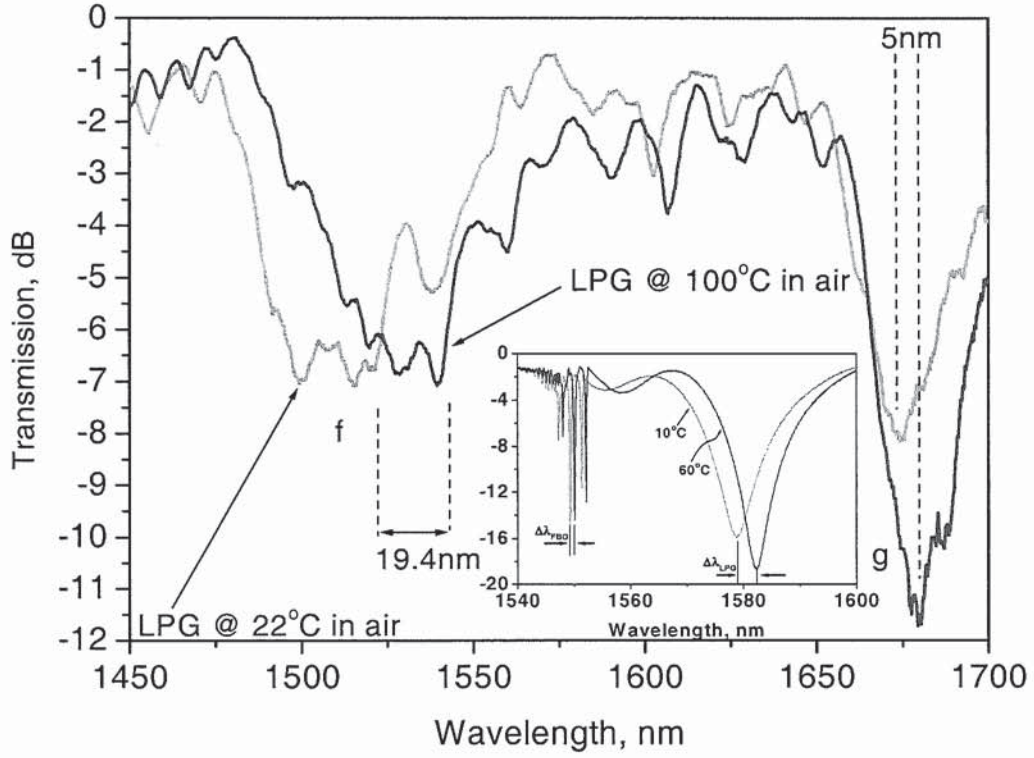

Fig. 5.45: **The temperature responses of the LPG-cascaded device in the wavelength region 1450-1700nm: the inset shows a typical temperature response of an SFBG that performs similar function. The SFBG was fabricated in a standard fibre using the point-by-point UV-scan on the fibre, through a phase-mask, with a period of 400 μm .**

For these types of sensing applications, the insensitivity of LPG mode such as 'g' (of Fig. 5.40) can allow them to be used in conjunction with the index sensitive modes for the measurement of index and temperature.

In summary, a simple and cost effective fabrication technique has been used to produce a cascaded long period grating (LPG) sensor in SMM900 double-cladding fibre and the capability of the LPG-sensor to measure the SRI and temperature simultaneously has been

[32] The use of SFBG and its response to SRI is described in detail in subsection 5.4.1.

successfully demonstrated. The scheme consists of two long period gratings (LPGs) of different periods inscribed side-by-side in a single piece of SMM900 double-cladding fibre. One of the LPGs exhibits a shift in its resonance wavelength with changes in both the SRI and temperature. The other LPG is SRI-insensitive but show spectral wavelength shift with temperature changes. The index insensitive LPG used to make up the device has temperature responsivity that is 16 times more than that of Bragg peaks of SFBG used for similar application.

5.4 Sampled Fibre Bragg Grating (SFBG) sensors

In-fibre gratings, including FBGs and LPGs, have attracted considerable attention for applications as optical sensors to measure various physical parameters such as temperature and strain [193]. The LPGs offer the additional capability of refractive index sensing [178,194]. However, because LPGs are also responsive to temperature, there is a potential temperature cross-sensitivity problem when they are used in refractive index, strain or curvature sensing.

5.4.1 SFBG sensor for simultaneous measurement of refractive index and temperature

Patrick *et al* [164] have suggested that simultaneous measurement of temperature and refractive index may be achieved by employing an additional FBG-sensor as temperature monitor co-operating with LPG index sensor. This apart, little experimental or theoretical work on this topic has been reported. In this section, a simple scheme for simultaneous temperature and refractive index measurement using a single SFBG is discussed.

In Section 4.2, it was shown that SFBGs posses both LPG and FBG spectral components. The spectral response of the FBG components is defined by $\lambda_{FBG} = 2n_{co}^{eff}\Lambda_{FBG}$ and in FBGs the LP_{01} core mode is well bounded in the core region, and is dependent on the effective index of the fibre core and the changes to the grating period. Since this mode is core-bounded it is therefore insensitive to the properties of the surrounding medium. In contrast, the LPG response, defined by eqn (5.4) i.e. $\lambda_{LPG} = (n_{co}^{eff} - n_{cl,m}^{eff})\Lambda_{LPG}$, shows a clear dependence on the

effective index of the fibre cladding, $n_{cl,m}^{eff}$, which in-turn is strongly influenced by the SRI. Thus, the LPG is clearly responsive to SRI.

The fact that both the FBG and LPG spectral responses are temperature dependent, the combined structure allows the temperature to be measured from its FBG response and the SRI information to be extracted from the total response of the LPG with the temperature effect being easily compensated.

The SFBG used in this work was UV-written in a hydrogen-loaded standard SMF using a 50-mm-long uniform-period phase mask and a CW frequency-doubled argon laser with an output power of 100mW. The inscription was implemented by scanning the UV beam on the fibre lengthwise through the mask and sampling was induced in an on-off fashion with a 50% duty-cycle using a computer-controlled UV-light shutter. The SFBG contains 125 samples with 400 μm pitch. After the inscription, the SFBG was annealed at 110°C for 24 hours in an oven. The spectral response of the SFBG was measured using a broadband LED light source and an HP70004A OSA with a resolution of 0.1nm.

To measure the temperature varied from 10 to 60°C, the SFBG device was employed in line with the description of Subsection 4.6.2. Fig. 5.46 shows its transmission spectrum measured

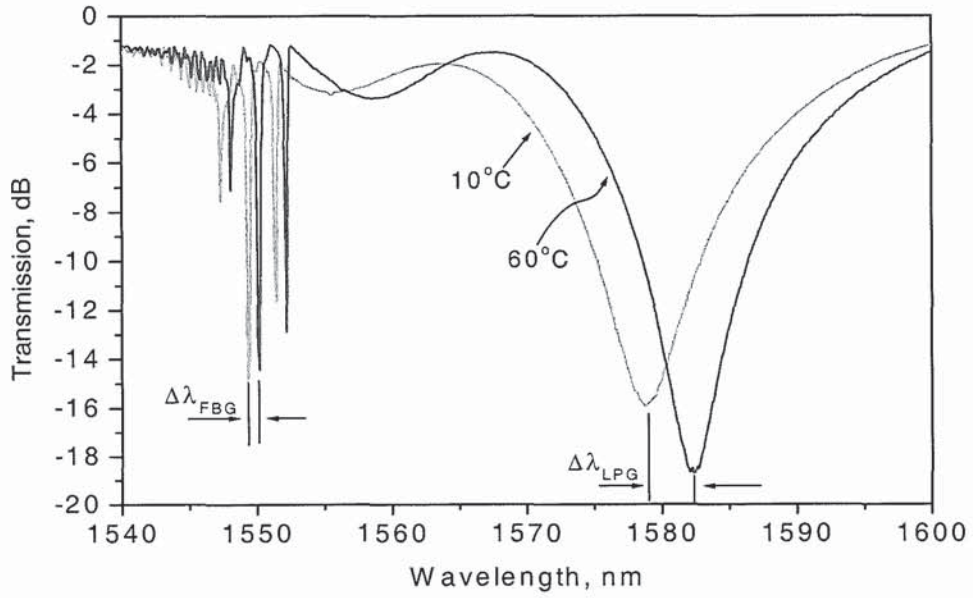

Fig. 5.46: Transmission spectra of the SFBG measured at 10 ℃ and 60 ℃.

at 10°C in air, in the wavelength range 1540-1600nm, displaying three FBG harmonic resonances around 1550nm and a broad loss band around 1580nm corresponding to one of the LPG coupled cladding modes.

When heat was applied, both the FBG and LPG resonances were found to shift towards longer wavelengths when the temperature was increased from 10 to 60°C. The dependence of the wavelength shift on temperature for both FBG and LPG are plotted in Fig. 5.47. The thermal responses of both showed linear characteristics and the temperature responsivity of the FBG is much less than that of the LPG as clearly evident in the figure. Using a linear regression fitting technique, the FBG and LPG temperature coefficients were found to be $\Delta\lambda_{FBG}/\Delta T = 12.2 \pm 0.26 pm/^{\circ}C$ and $\Delta\lambda_{LPG}/\Delta T = 80.78 \pm 0.93 pm/^{\circ}C$, respectively. The linearity of the thermal responses allows for good correlation so that the temperature induced resonant wavelength shift of the LPG cladding mode can be compensated during the SRI measurement.

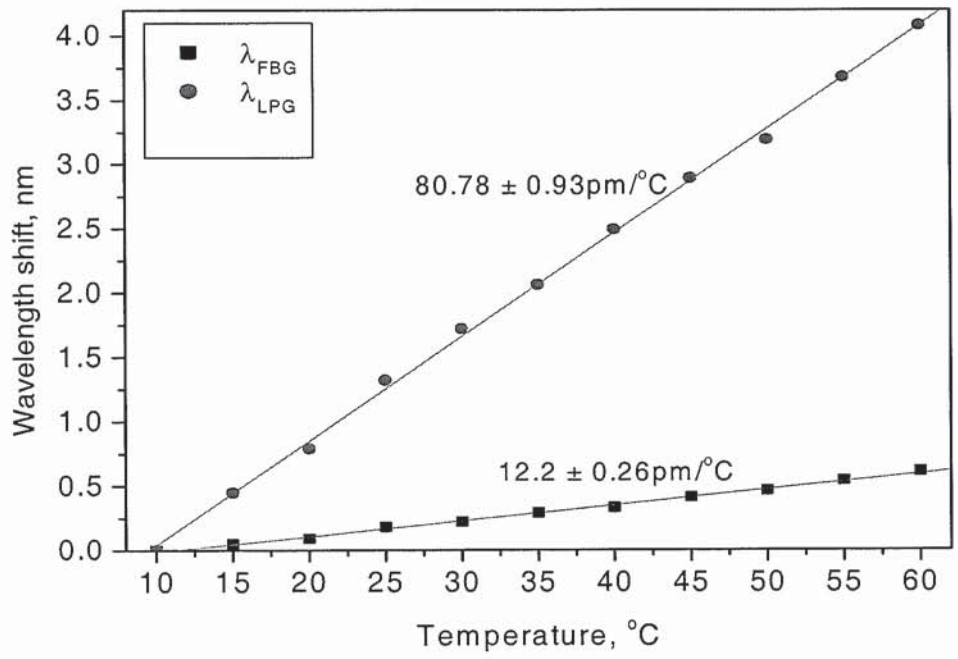

Fig. 5.47: Dependence of the wavelength shift on temperature for both the FBG resonance and LPG resonance of the SFBG.

To measure the SRI, the in-fibre SFBG device was used in the way described in Subsection 4.6.3. A typical result of SRI measurement using the SFBG device is shown in Fig. 5.48. It is evident that the FBG response was not affected by changes in the surroundings since its

resonance wavelengths are unchanged. In contrast, the LPG resonance shifted towards shorter wavelengths as the SRI increased. Note that the LPG resonance completely disappeared when an oil of refractive index of 1.46 was applied, whereas the FBG resonances remained intact showing a total immunity to the SRI. Hence, the temperature can be measured solely from the FBG response and then be used to compensate for the thermal contribution in the LPG response, leaving the net effect due to the SRI.

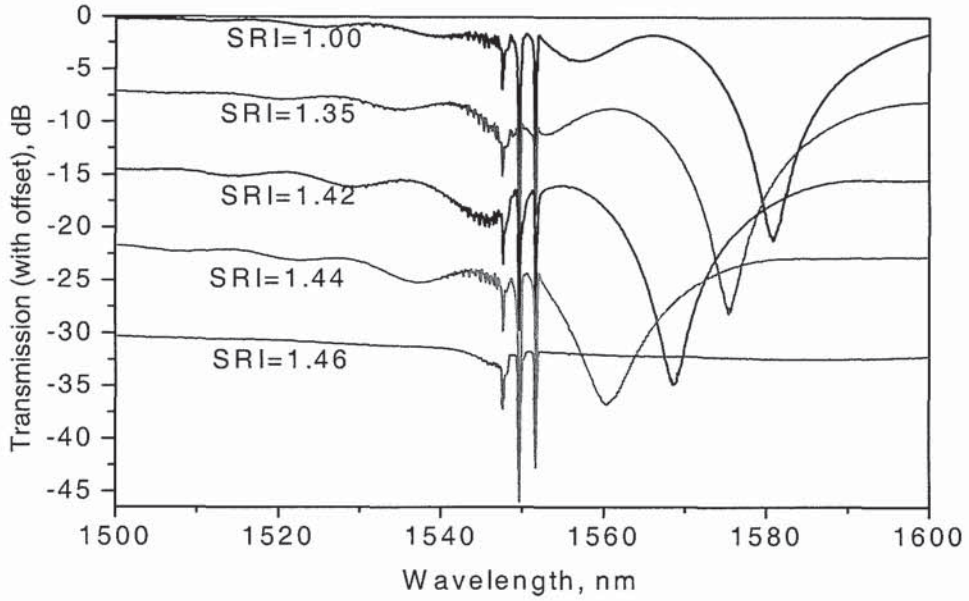

Fig. 5.48: Transmission spectra of the SFBG measured at various SRI. Offset introduced for clarity.

It is noted that in applications where back reflection is a major concern the cascaded LPG device can provide an alternative solution when compared with SFBG approach. Table 5.9 compares the temperature coefficients obtained for the LPG in 3-layer fibre with that of the SFBG experiment. It can be seen that the temperature insensitive component of the LPG in the SMM900 fibre is 16 times more responsive to temperature in comparison to FBG components of SFBG.

	Index insensitive gratings	Index and temperature sensitive gratings
SFBG	$\Delta\lambda_{FBG} / \Delta T = 12.2 pm/^\circ C$	$\Delta\lambda_{LPG62} / \Delta T = 80.78 pm/^\circ C$
LPG pair	$\Delta\lambda_{LPG100} / \Delta T = 194 pm/^\circ C$	$\Delta\lambda_{LPG62} / \Delta T = 50.08 pm/^\circ C$
Comparison	16 times more responsive	0.62 times as responsive

Table 5.9: A typical comparison of the temperature coefficients for SFBG and LPG-cascade sensors.

In summary, a scheme for the simultaneous refractive index and temperature measurement using a single SFBG has been successfully demonstrated. The dual-parameter sensing functionality of a SFBG originates from its unique configuration combining the FBG and LPG structures. The advantages of simple fabrication, easy interrogation and, more importantly, inherent temperature referencing of SFBG structures offer the prospect of the development of practical sensors for temperature compensated chemical/biochemical sensing applications.

5.4.2 SFBG for co-measurement of strain, temperature and curvature.

Optical fibre based monitoring techniques for strain, temperature, and for curvature, for applications in smart structures has generated a significant interest over the years [195,196, 197]. To date, however, there has been no report of any single device that offers measurement of strain and curvature or the three parameters simultaneously, despite the frequent occurrence of this requirement. In-fibre grating techniques, employing either UV-inscribed FBGs or LPGs, offer a range of approaches for strain and temperature sensing (see, for example, [168]). For curvature measurement, FBGs have also shown considerable promise, particularly when the gratings are incorporated in special fibre types, including eccentric and multiple core types [198], and D-type [199]. There have been a number of reports describing the use of LPGs in curvature sensors, based on measurement of either an induced wavelength shift [200], or resonant mode splitting [34,201], with the latter technique exhibiting a very high responsivity.

As discussed in Section 4.2 and Subsection 5.4.1 an SFBG is formed by superimposing a periodic, low spatial frequency amplitude variation on the high spatial frequency refractive index modulation of an inscribed FBG [202] and, thus, offers elements of both the FBG and LPG responses [168]. A series of recent experiments has demonstrated that the properties of the SFBG may be exploited, in various ways, to provide a number of simultaneous, dual-parameter sensor schemes [168].

In this section, it is shown that certain of these principles can be adapted and extended to provide simultaneous measurement of strain, temperature, and curvature using a single

SFBG. It is shown that the curvature may be effectively determined from the LPG-like resonant mode splitting, whilst the axial strain and temperature may be evaluated from the wavelength shift of the FBG harmonics of the structure and the corresponding shift of the midpoint of the separation between the split bands of the LPG-like mode. The mode splitting has insignificant cross sensitivity to either strain or temperature; thus, the curvature measurement depends only on the spectral gap between the split bands. For the mode used in the experiments discussed herein, the temperature responsivity of the midpoint of the separation between split bands is an order of magnitude higher than that of the FBG resonance peak, whereas the strain responsivity is almost the same, therefore, temperature and strain can, as described herein, be evaluated from a well conditioned matrix of strain and temperature coefficients.

The SFBGs used in this work were UV-written in both non-hydrogenated and the hydrogenated B/Ge fibre using a uniform-period phase-mask and a CW frequency-doubled argon laser with a power of 100mW. The inscription was implemented by scanning the UV beam on the fibre lengthwise through the mask and sampling was induced in an on-off fashion with a 50% duty-cycle using a computer-controlled UV-light shutter. Three 50mm long SFBGs, first containing 125 samples with 400 μm pitch (SFBG1), second containing 140 samples with 357 μm pitch (SFBG2), and the third contains 128 samples with 390 μm pitch (SFBG3), were fabricated for the experiments. After the inscription, the gratings were annealed at 90°C for 48 hours in an oven.

(A) Measurement of Large and small curvature at constant temperature:

Simultaneous measurement of curvature and temperature was implemented using two different curvature inducement schemes. Scheme I employed a 4-point bending jig shown in Fig. 5.49. This scheme allowed for inducing and measurement of both very small and fairly large curvatures (from 0 m^{-1} to 8.44 m^{-1}).

The 4-point bending jig was employed to induce different values of curvature (in the range 0m^{-1} to 8.44m^{-1}) on the SFBGs, and also facilitate the application of axial strain using the

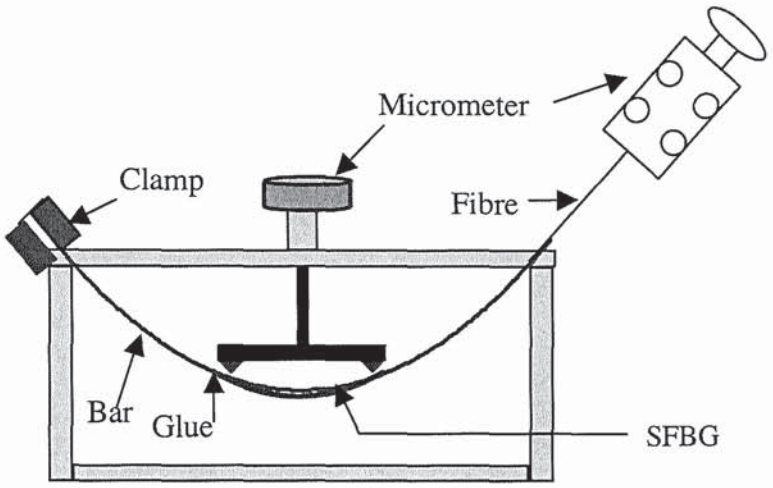

Fig. 5.49: ***The configuration of the four-point bending-jig used in Scheme I.***

micrometer. In each experiment using this jig, the fibre containing the SFBG was attached to a 0.5mm thick spring-metal bar of 20mm width and 150mm length. One end of a 10cm central section of the SFBG-containing fibre was fixed firmly to the bar, whilst the other end was attached to a micrometer-drive by which axial strain could be applied. Curvature was induced by depressing the centre of the spring metal bar with a second micrometer-drive, and the resulting displacement, h, of the bar, as indicated in Fig. 5.49 was converted to curvature using Dr Liu's model earlier described Subsection 5.3.1.3(C) [34]. In all of the experiments discussed in this section, the spectral responses of the SFBGs were measured using a broadband LED light source and an HP70004A OSA with a resolution of 0.1nm.

Scheme II was designed specifically for measuring large curvatures and for application of heat and strain to the SFBG-sensors. The test fixture used in this scheme was a metal plate containing one straight V-groove and a set of curved V-grooves of precise curvatures ranging from 8.13 m^{-1} to 11.03 m^{-1} as shown in Fig. 5.50. The plate having dimension 75mm X 56mm was mounted on a thermoelectric-cooler to facilitate temperature control allowing the strain to be applied by fixing one end of the fibre while the other end was driven axially via a micrometer drive, following the example of Scheme I. The dash lines indicate the fit-in socket underneath the plate into which the thermo-electric cooler is fitted.

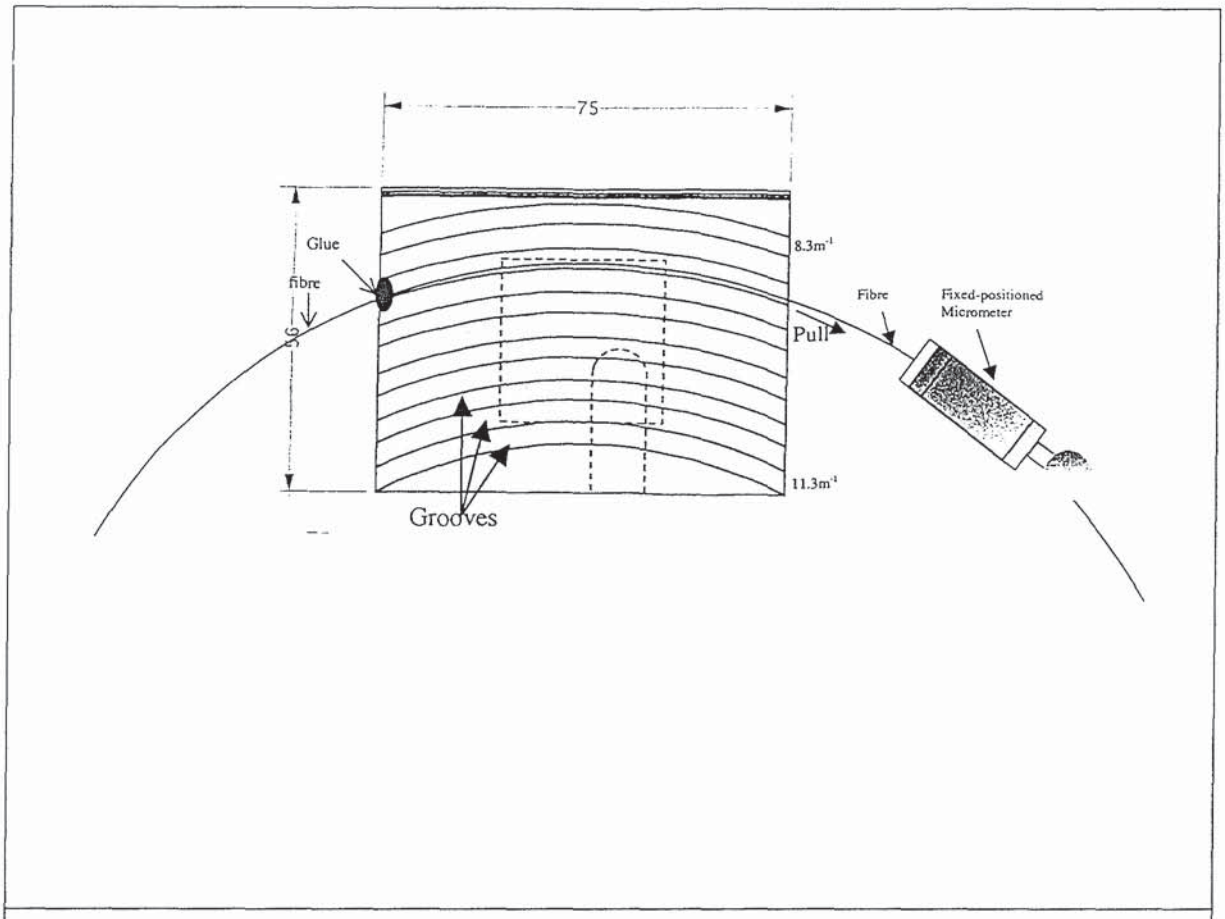

Fig. 5.50: ***The configuration of the curvature inducing metal plate.***

The curvature response of each SFBG was first investigated with arbitrary axial strain applied. Curvature-induced mode-splitting was observed for each of six coupled cladding modes (LP_{01} to LP_{06}) in all the three SFBGs in the spectral range 1200 – 1586nm. Fig. 5.51 shows the spectral evolution with changing curvature for SFBG1 in two wavelength regions. Fig. 5.51(a) shows the 1460 – 1586nm region with curvature increased from zero to $5.94m^{-1}$, and Fig. 5.51(b) shows the 1238 – 1328nm region, with curvature increased from zero to $3.13m^{-1}$ respectively. These curvatures were induced using the jig shown in Fig. 5.49.

It should be mentioned that there is a potential for stiction of the grating at the bent region, in respect of both bending schemes, and when dealing with FBGs stiction could result in the broadening of the spectral response in view of the uneven distribution of strain within the grating. But, in the case of SFBG, the fact that short period regions are sampled rather than continuous, and the grating response results from beating of sub-gratings that are separated by large spatial periods, the effect of stiction is not significant. This explanation is supported

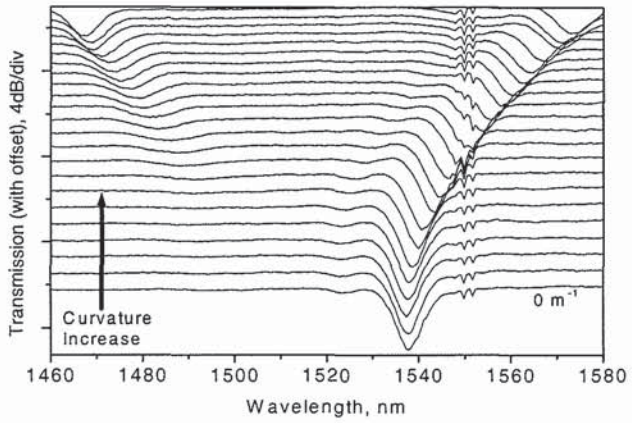

(a)

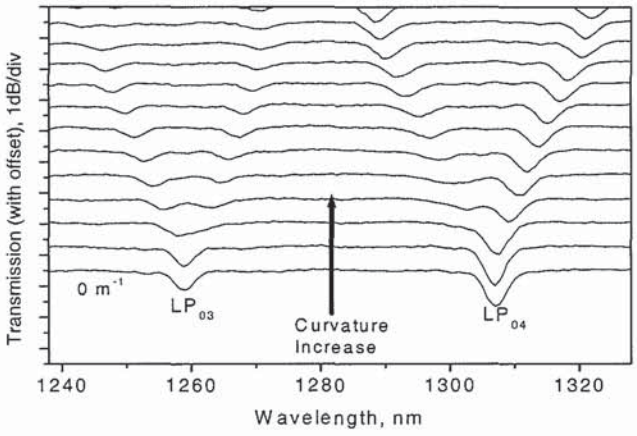

(b)

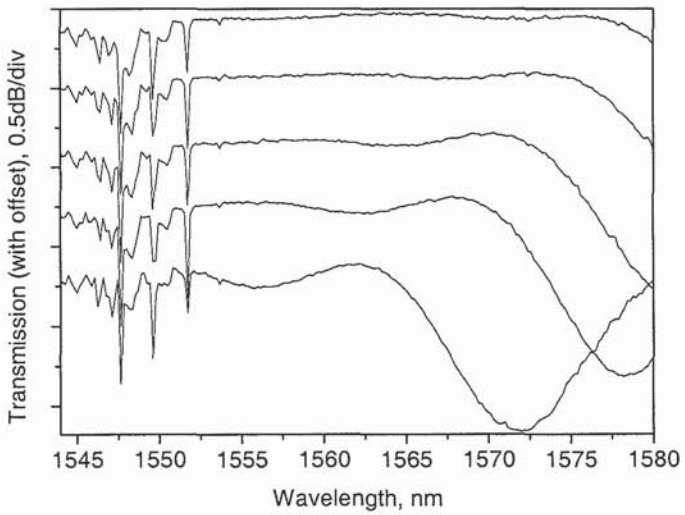

(c)

Fig. 5.50: ***(a) Spectral responses of SFBG1 at 0 $\mu\varepsilon$ at different curvatures showing the LP_{06} and FBG components. (b) Spectral responses of SFBG1 at 0 $\mu\varepsilon$ under different curvatures showing modes LP_{03} and LP_{04}. (c) Spectral responses of SFBG1 at 0 $\mu\varepsilon$ under different curvatures showing modes FBG resonance peaks.***

by the appearance of un-distorted narrow FBGs responses of the SFBG, as will be seen in the inset to Figs. 5.55(a), 5.56 and 5.58(a). Furthermore, stiction-induced spectral distortion is unlikely to affect LPG components.

It is clear from Fig. 5.51(a) that, prior to bending, there are two narrow FBG harmonic peaks located at ~1551nm and a broad LPG loss band centred on ~1538nm, corresponding to the LP_{06} cladding mode. Fig. 5.51(b) displays two LPG loss bands corresponding to the LP_{03} and LP_{04} modes, located at ~1258nm and ~1307nm, respectively, prior to bending. It is also clear that as the SFBG is subjected to curvature, each of the broad loss bands bifurcates with one sub-band shifting to longer wavelengths (LP_{06}-red) and the other to shorter wavelengths (LP_{06}-blue) with increased curvature. The FBG peaks, on the other hand, remain un-shifted.

The apparent insensitivity of the FBG components to curvature was corroborated by examining the response at higher resolution in the spectral range 1551±2.5 nm under the same curvature condition; no wavelength shift was discernible. The response of the FBG peaks under some applied curvatures can be seen in Fig. 5.51 (c). It is however believed that cross sensitivity between curvature and strain cannot be totally ruled out, but looking at the FBG peaks in Figs. 5.51 (a) and (c) that have been recorded at a resolution of 0.1nm, it can be concluded that such cross sensitivity introduced negligible effect to the measurements.

The splitting of the LP_{06} mode was not apparent at very small curvatures due to the relatively weak coupling strength of the LP_{06}-blue mode [as depicted in Fig. 5.51(a)]. To further support these results, using Scheme I, SFBG2 (357μm) was subjected to different curvatures at a constant temperature of 22.8°C and the spectral responses recorded. As expected there is clear evidence of mode splitting of LP_{06} cladding mode as seen in Fig. 5.52 (a) and such splitting becomes obvious only at slightly larger values of curvature.

Fig. 5.52 (a) shows transmission spectra of this grating displaying both FBG and LPG characteristics. Again, prior to bending, there are two FBG resonance peaks at ~ 1565nm and a broad LPG loss band at 1490nm corresponding to the LP_{06} coupled cladding mode. When the grating was subjected to bending, the single loss band split into two parts with one shifting towards the longer wavelengths (LP_{06}-red) and the other towards the shorter

wavelengths (LP_{06}-blue). It can also be seen from the figure that, because the temperature was kept constant, the spectral locations of the FBG peaks remained un-shifted, even after bending of large magnitude was applied. The relationship between the mode splitting and the curvature with respect to SFBG2 is depicted in Fig. 5.52 (b), which shows a near-linear response with a bending responsivity of 8.47 nmm^{-1} at the point where mode splitting becomes obvious.

Comparison of Figs. 5.51(a) and 5.52(a) on the one hand and Fig. 5.51(b) on the other reveals that pronounced mode-splitting occurs for the LP_{03} and LP_{04} modes at rather smaller induced curvatures than for the LP_{06} mode, though the rate of separation of the split bands increases with mode order. In earlier works [34,201], where use of mode splitting techniques was concentrated on higher order modes, the measurement of very small curvatures was not achieved since the peak that is shifting to the shorter wavelength could not be fully resolved. The spectral separation has been plotted against curvature for the modes LP_{03} to LP_{06} of SFBG1 in Fig. 5.53, showing clearly that the LP_{03} and LP_{04} are capable of measuring

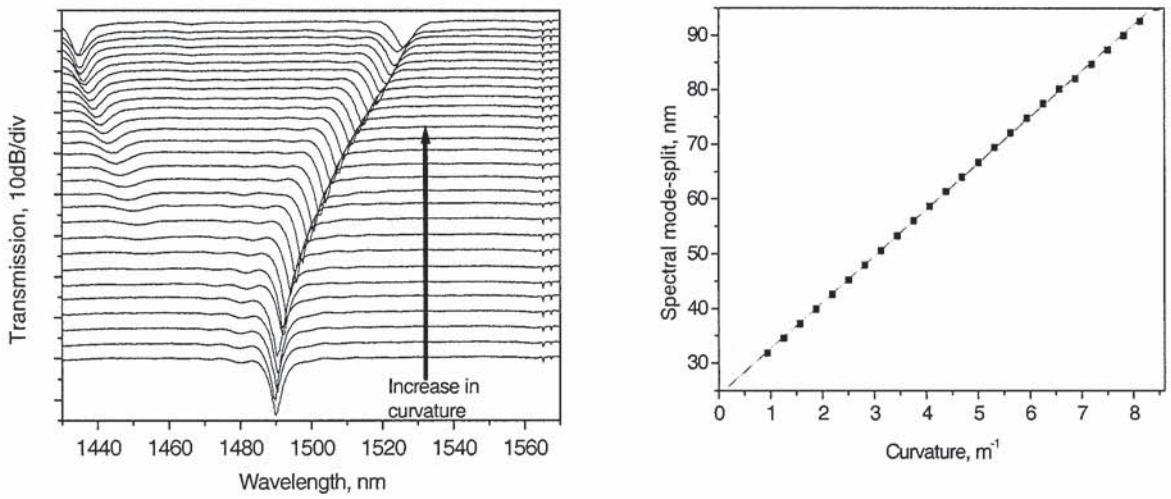

(a) (b)

*Fig. 5.52: **(a) Spectral responses of SFBG at temperature of 22.8°C under different bending curvatures. (b) Spectral splits in (a) plotted with respect to curvature***

curvatures smaller than $0.4m^{-1}$. This is significantly smaller than minimal value for which LP_{06} begins to show clear splitting and lower than any previously recorded figure.

At zero curvature, of course, there is no mode splitting, but beyond the curvature magnitudes where the splitting of the modes becomes detectable, the separations show some degree of linearity with respect to curvature. For the LP_{03}, LP_{04}, LP_{05}, and LP_{06} modes our measurements yield sensitivities of 10.03, 10.80, 10.95, and 12.05nm.m, respectively, consistent with the increasing rate of separation with mode order. Although the lower-order modes LP_{03} and LP_{04} facilitate measurement of smaller curvatures, their effectiveness diminishes at higher values due to reduced coupling strength of the split bands and the onset of secondary mode splitting. Thus, these modes have not been used to measure curvatures greater than 3.13 m^{-1}, beyond which measurements are readily carried out using the higher order modes.

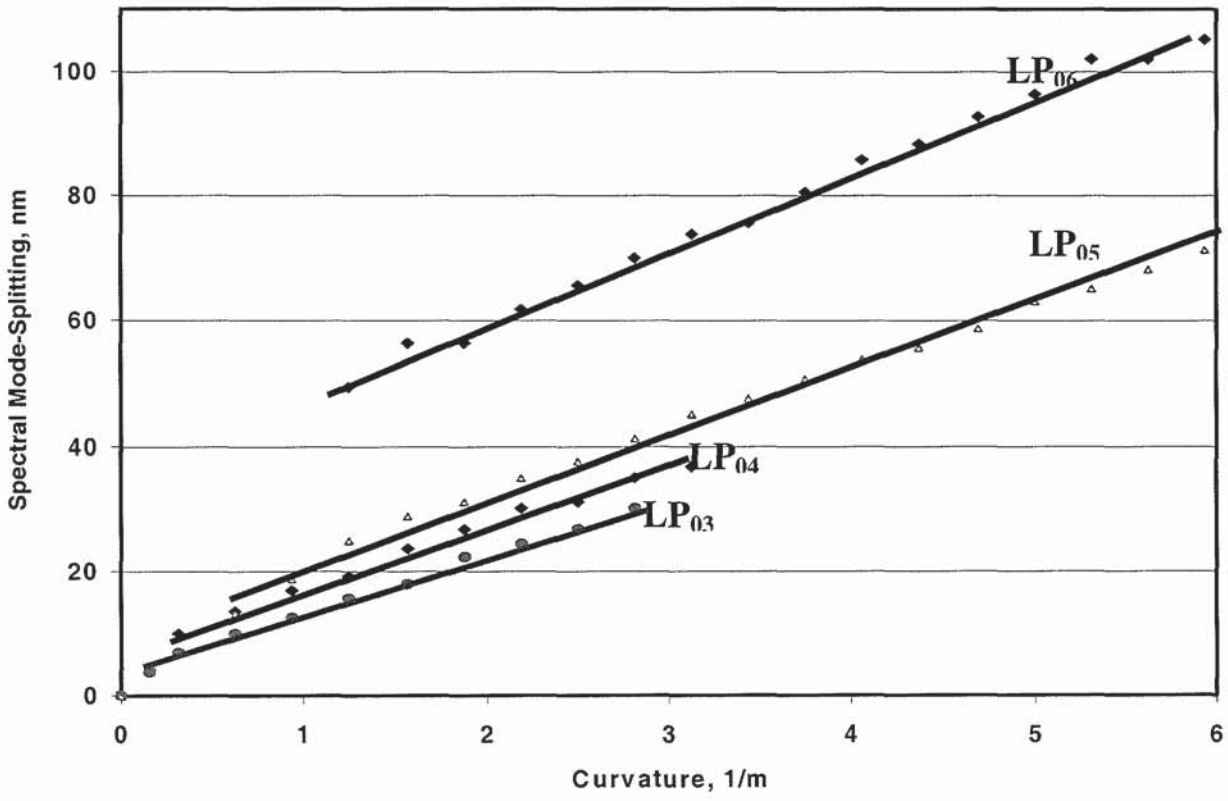

*Fig. 5.53: **Spectral splitting of the LP_{03}, LP_{04}, LP_{05} and LP_{06} modes of SFBG1 plotted against curvature.***

To investigate the measurements of large curvatures, the curvature response of each SFBG1 was first investigated with no axial strain and at a fixed temperature. Curvature-induced mode splitting was observed for each of six coupled cladding modes (LP_{01} to LP_{06}) as earlier

mentioned. Fig. 5.54 shows the spectral evolution with changing curvature for SFBG1 in the wavelength region 1457.5 – 1597.5nm with curvature increased from 8.13 to 11.03m^{-1}. These curvatures were induced using the plate with concentric V groves shown in Fig. 5.50. It can be seen from the Fig. 5.56 that there are two broad LPG sub-bands, one located at ~1467nm and the other at ~1572nm corresponding to the curvature-induced splitting of mode LP_{06} of the SFBG1. The split bands result from a single LPG loss band (at ~1530nm prior to the application of curvature) which, on application of the initial curvature of 8.13m^{-1}, bifurcates with one sub-band shifting to longer wavelengths (LP_{06}-red) and the other to shorter wavelengths (LP_{06}-blue) with increased curvature. It can also be seen from the figure that, because both the temperature and the strain were kept constant, the spectral locations of the FBG peaks remained un-shifted, even after a curvature of larger magnitude was applied. It has been shown in Fig. 5.53 that mode splitting occur and the separation between the modes varies linearly with respect to the application or changes to curvature, thus, making it easier to measure the applied curvature from the spectral separations of the split sub-bands.

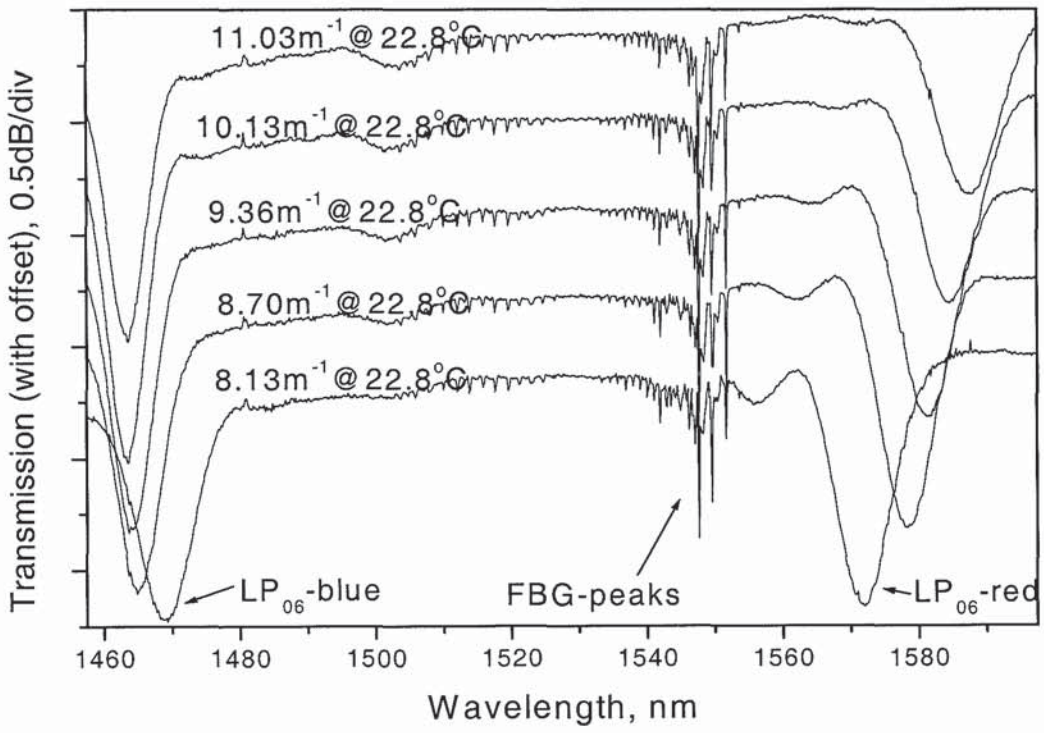

Fig. 5.54: ***Spectral responses of SFBG1 at 0 $\mu\varepsilon$ & 22.8°C at different curvatures showing the LP_{06} and the FBG components.***

(B) Constant curvature Vs Variable temperature:

In a subsequent experiment, the curvature applied on SFBG1 was maintained at a constant value of 8.13 m^{-1} and the temperature varied from 62.8°C to 12.8°C. The corresponding spectra recorded are shown in Fig. 5.55(a). It may be seen from this figure that both bands, LP_{06}-blue and LP_{06}-red, shifted laterally to the longer wavelengths with the falling temperature while their spectral separations remained virtually constant. The peak wavelengths of the two split bands are plotted against temperature in Fig. 5.55(b): the two fitted lines are parallel indicating clearly that the grating was subject to a constant curvature. Analysis of the peak wavelengths of the two split bands suggest that both of the bands shifted linearly with temperature: the two bands exhibit almost equal temperature coefficients of ~-0.317nm/°C. In this experiment, however, the FBG peaks shifted to shorter wavelengths with decreasing temperature, as clearly shown in the inset to Fig. 5.55(a). It is clear that the mode splitting of the LPG component of the SFBG provides a measure of the curvature whilst the wavelength shift of the FBG transmission peaks can be used independently to determine the temperature, bearing in mind that the applied strain was kept constant in this case. A Bragg

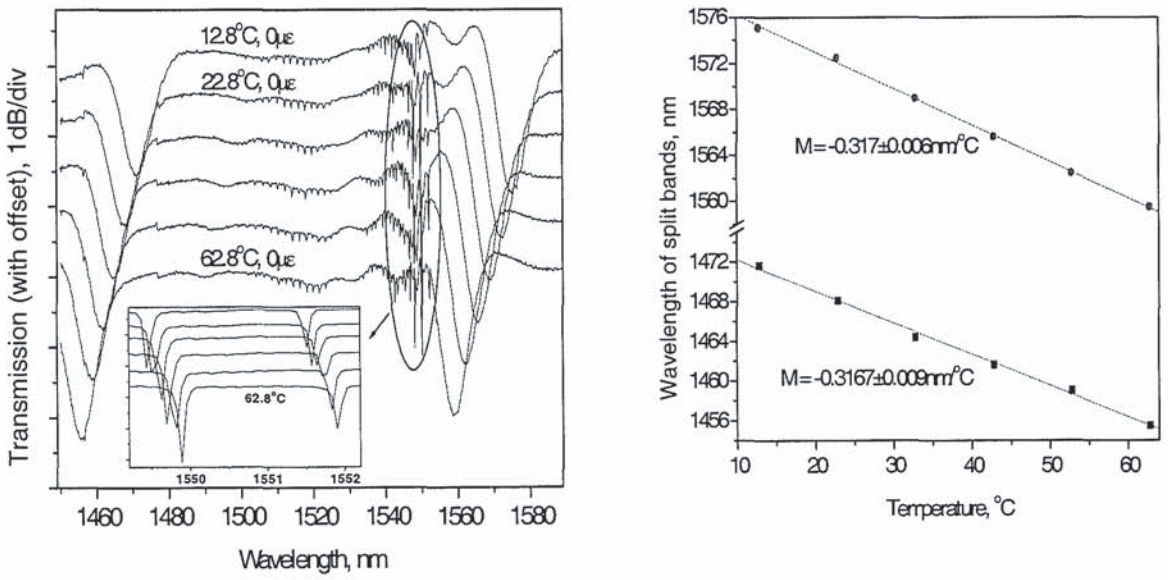

(a) (b)

*Fig. 5.55: **(a) Spectral responses of SFBG1 at a curvature of 8.13 m^{-1} at various temperatures; the inset is a magnified spectral plot of the FBG components, (b) Spectral response of peaks of the split mode plotted against temperature.***

wavelength shift of 0.52nm was observed when the temperature fell from 62.8°C to 12.8°C indicating a Bragg temperature coefficient of ~10.4pm/ °C. It is also noted that since the two split LPG bands posses the same temperature coefficients, the midpoint between their spectral positions will have almost the same temperature coefficient of ~-0.317nm/ °C.

(C) Arbitrary curvature Vs temperature:

Simultaneous measurements of arbitrary combinations of the curvature and temperature were also performed at an axial strain of 0 $\mu\varepsilon$ for temperatures in the range 52.8° C to 12.8° C and curvature in the range 8.13 m^{-1} to 11.03 m^{-1} as shown in Fig. 5.56. In keeping with the earlier results, it was possible to measure all applied curvatures and temperatures independently from the LPG mode splitting and the shifting of the FBG resonance peaks, respectively.

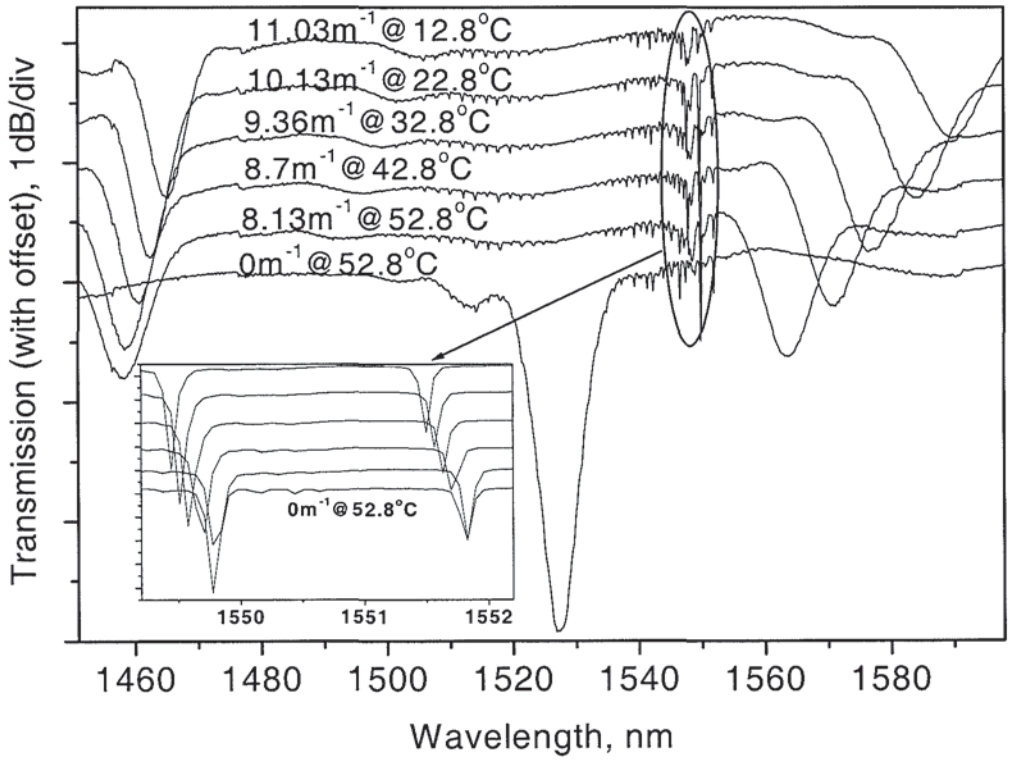

Fig. 5.56: Spectral responses of SFBG1 at different curvatures and various temperatures; the inset is a magnified spectral plot of the FBG components.

(D) Constant curvature Vs variable strain:

Following the curvature and temperature measurements at constant strain, the spectral response of SFBG3 to axial-strain was subsequently investigated at constant curvature and temperature. In order to compare the results, axial strain was first measured using the technique presented in Subsection 4.6.1. The spectra obtained are shown in Fig. 5.57 and yield a similar strain responsivity of 9 x 10^{-4} nm / $\mu\varepsilon$ for both the LPG and the FBG spectra as clearly suggested by the parallel nature of the plotted positions of the spectral peaks shown in Fig. 5.57(b).

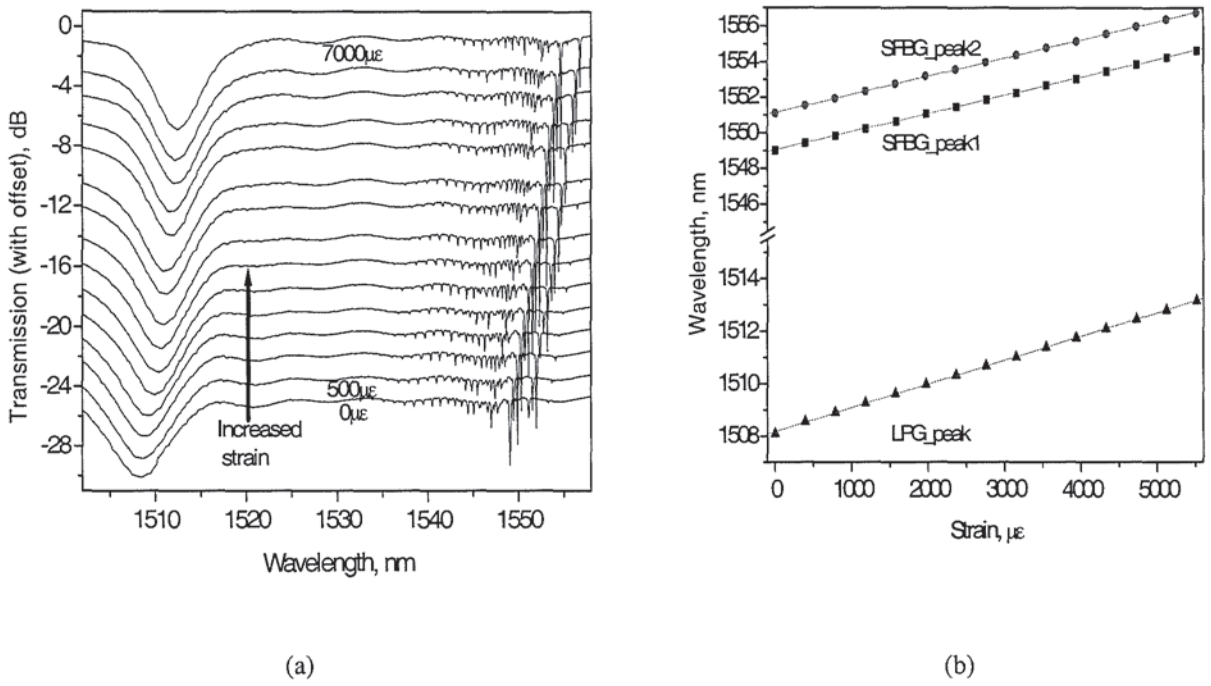

Fig. 5.57: ***Spectral responses of SFBG3 at zero curvature under different applied axial strains from 0 to 7 x 10^3 $\mu\varepsilon$ showing mode LP_{06} and FBG components (b) Spectral locations of the Peaks of the SFBG plotted against strain.***

Following the measurement of strain at zero curvature the grating was maintained at a fixed curvature of 8.13m^{-1} and a temperature of 22.8°C whilst the magnitude of axial strain was varied: resulting spectra are displayed in Fig. 5.58(a). It is noted from the figure that the FBG harmonics were superimposed on the LP_{06}-red mode. Over a large wavelength monitoring range of >100nm, changes in the LPG and FBG responses in relation to the strain are not immediately obvious from the successively recorded spectra, as may be seen from figure. At higher resolution, however, it is clear that both the LPG and FBG resonance are shifted linearly towards longer wavelengths with increasing strain yielding a similar responsivity of

~9 x 10^{-4} nm / $\mu\varepsilon$. But as shown in the inset to Fig. 5.58(a), the narrow spectral widths of the FBG peaks facilitate measurement of the shift with rather greater precision. In the inset, the FBG spectra show the responses for strains ranging from 0 to 2400 $\mu\varepsilon$.

Fig. 5.58(b) provides plots of the wavelength shifts against applied axial strain for the LP_{06}-blue and LP_{06}-red modes of the SFBG3. Both modes shifted with increasing strain showing a strain coefficient of ~9 x 10^{-4} $nm/\mu\varepsilon$. The separation between them, however, clearly remained constant, showing that the curvature response was unaffected by the applied axial strain. On the other hand, the two FBG harmonics responded to the axial strain only. Since both the split LPG bands and the FBG peaks posses the same strain coefficients, it implies that the midpoint between the split bands will also have the same strain coefficient of ~9 x 10^{-4} nm / $\mu\varepsilon$.

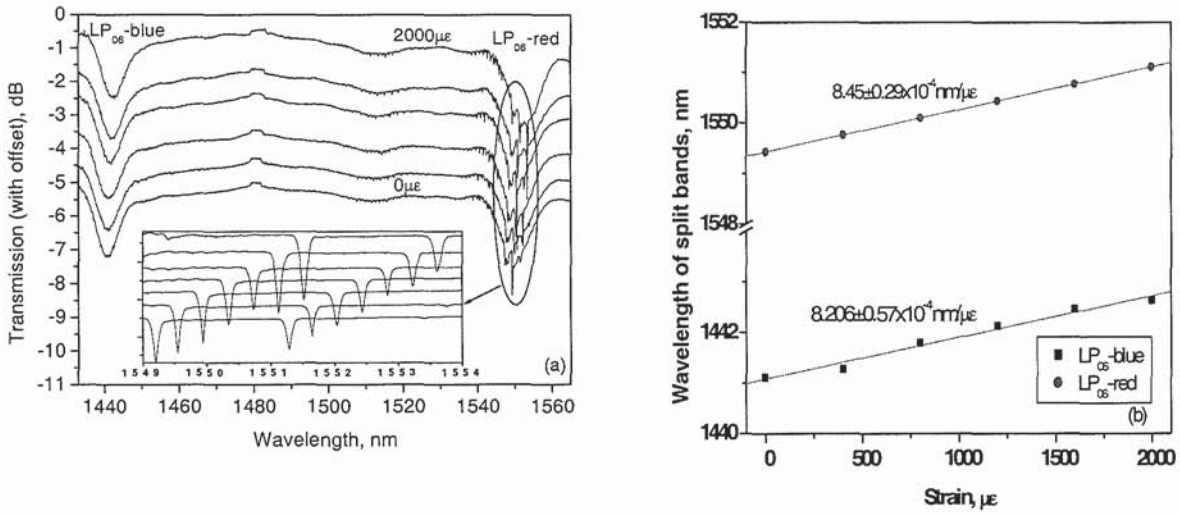

(a) (b)

*Fig. 5.58: **(a) Spectral responses of SFBG3 at a curvature of 8.13m^{-1} under different applied axial strains, showing the split mode LP_{06} and FBG components; the inset is a magnified spectral plot of the FBG components, (b) Peak wavelengths of the split mode LP_{06} plotted against strain.***

(E) Simultaneous triple parameter evaluation:

It has been seen that in the first set of experiments (see Figs. 5.49 through 5.56) the strain was kept constant while the temperature coefficients of an FBG peak and that of the midpoint between the LPG split bands were established, in the second set of experiments (Figs. 5.57 to 5.58) the temperature was kept constant while the strain coefficients were determined.

The coefficients of strain and temperature obtained are shown in Table 5.10 below.

Grating	Parameter	Midpoint of LPG mode-split	FBGpeak
SFBG	Strain, K_ε	~9 x 10^{-4} nm / $\mu\varepsilon$	~9 x 10^{-4} nm / $\mu\varepsilon$
	Temperature[33] K_T	~-0.316nm/°C	~10.4pm/°C

Table 5.10: **Temperature and strain coefficients for midpoint of split bands, and that of a Bragg peak.**

The contribution to wavelength shifts from strain and temperature can be calculated simultaneously using the matrix equation

$$\begin{pmatrix} \Delta\lambda_{LPG\_mid} \\ \Delta\lambda_{FBGpeak} \end{pmatrix} = \begin{pmatrix} K_{\varepsilon_{LPG\_mid}} & K_{T_{LPG-mid}} \\ K_{\varepsilon_{FBGpeak}} & K_{T_{FBGpeak}} \end{pmatrix} \begin{pmatrix} \Delta\varepsilon \\ \Delta T \end{pmatrix} \quad \ldots\ldots\ldots \quad (5.18)$$

Where $K_{\varepsilon_{LPG\_mid}}$, $K_{\varepsilon_{FBGpeak}}$ and $K_{T_{LPGmid}}$, $K_{T_{FBGpeak}}$ are the respective strain and temperature coefficients of midpoint of the separation between the LPG bands, and that of an FBG resonance peak. $\Delta\lambda_{LPG\_mid}$ and $\Delta\lambda_{FBGPeak}$ are the respective wavelength shifts of the spectral midpoint between the LPG split bands, and that of an FBG resonance peak, while $\Delta\varepsilon$ and ΔT are the applied strain and temperature changes.

The coefficients in Table 5.10 indicate that $K_{\varepsilon_{LPG\_mid}} = K_{\varepsilon_{FBGpeak}}$ and $K_{T_{LPGmid}} \neq K_{T_{FBGpeak}}$ thus the determinant of the matrix of coefficients is not zero ($|K| \neq 0$). In other words, the inverse of the matrix K is defined. Solving eqn. (5.18) above can clearly yield values for strain and temperature simultaneously and in this case, the condition number evaluated is 340.

In summary, the triple parameter measurement activity follows the following steps:

1. Calculating the strain- and temperature-coefficients of the midpoint between the LPG split bands by:
    a. measuring the wavelength shifts of the midpoint between the LPG split bands with respect to induced-strain, and evaluating the strain coefficient,

[33] Note that the temperature coefficient of mode LP_{06} of SFBG1 is assumed to be similar in magnitude to that of mode LP_{06} of SFBG3 in view of the fact that they were made in the same type of fibre and spectral locations are quite similar.

b. measuring the wavelength shifts of the midpoint between the LPG split bands with respect to changes in temperature, and calculating the temperature coefficient,

As seen from Fig. 5.55, the respective strain- and temperature-coefficients of the LPG split bands are very similar, which implies that, the strain and temperature coefficients of the midpoint are similar to that of the corresponding LPG modes.

2. Calculating the strain- and temperature-coefficients of one of the FBG resonance peaks through:
   a. recording of the wavelength shifts of the FBG resonance peak with respect to induced-strain, and calculating the strain coefficient,
   b. recording of the wavelength shifts of the FBG resonance peak with respect to changes in temperature, and calculating the temperature coefficient,

3. Calculating the matrix of coefficients recorded in steps 1 and 2. For example, suppose LP_{06} mode of the SFBG3 is selected together with one of the FBG peaks; it has already been noted, in this work, that the strain coefficients of LP_{06} of SFBG3 and the FBG peaks are similarly equal to ~9 x 10^{-4} $nm / \mu\varepsilon$ (see Fig. 5.57). The temperature coefficients, on the other hand, are expected to be an order of magnitude different (as suggested by Figs. 5.55 and 5.58). Thus, the determinant of the matrix of coefficients will have a defined value, and therefore, the temperature and strain contributions to the wavelength shifts can be determined in addition to the curvature values that can be measured from the splitting.

These experiments clearly demonstrate the capability of the single SFBG structure to perform simultaneous measurements of strain, temperature, and curvature. Whilst it is anticipated that there would be significant use of the three-parameter sensor in smart structural applications, it is noted also that for embedded sensor development, correlated measurements of strain and curvature may yield valuable information on slippage between the fibre and the host material. Indeed, silicon wafer strain measurements can be enhanced if curvature can be evaluated at the same time.

There is a potential for reducing the signal processing by evaluating the three parameters simultaneously using a single 3 X 3 matrix. Care must however be taken when implementing such matrix in view of the difficulty of measuring the splitting of high resonance order modes at very small values of curvature ($< 0.4 m^{-1}$). It must also be stressed that the splitting at these curvature values could well be non-linear. So far, to the authors knowledge, no one has reported a successful modelling of the splitting behaviour of the high order modes, thus, the author is not in a position to recommend the use of the 3 x 3 matrix in all cases.

A typical 3 x 3 matrix can be generated by extending Table 5.10 to include curvature coefficients. The curvature coefficients can be obtained using Fig. 5.54 for which strain and temperature were kept constant, and curvature-induced mode splitting was measured along with the curvature-induced shift of the mid-point between the split modes.

The coefficients of strain, temperature and curvature are now listed in Table 5.11 below.

Grating	**Parameter**	**Midpoint of LPG mode-split**	**FBGpeak**	**Split gap**
SFBG	Strain, K_ε	~9 x 10^{-4} $nm / \mu\varepsilon$	~9 x 10^{-4} $nm/\mu\varepsilon$	~0 $nm/\mu\varepsilon$
	Temperature K_T	~-0.316nm/ °C	~10.4pm/ °C	~0nm/ °C
	Curvature, K_C	1.689 nm/m^{-1}	~ 0 nm/m^{-1}	11.24 nm/m^{-1}

Table 5.11: **Temperature, strain, and curvature of a SFBG.**

The contribution to wavelength shifts from strain, temperature can be calculated simultaneously using the matrix equation

$$\begin{pmatrix} \Delta\lambda_{LPG\_mid} \\ \Delta\lambda_{FBGpeak} \\ \Delta\lambda_{Split-gap} \end{pmatrix} = \begin{pmatrix} K_{\varepsilon_{LPG\_mid}} & K_{T_{LPG-mid}} & K_{C_{LPG-mid}} \\ K_{\varepsilon_{FBGpeak}} & K_{T_{FBG\_peak}} & K_{C_{FBG-Peak}} \\ K_{\varepsilon_{Split-gap}} & K_{T_{Split-gap}} & K_{C_{Split-gap}} \end{pmatrix} \begin{pmatrix} \Delta\varepsilon \\ \Delta T \\ \Delta C \end{pmatrix} \quad \ldots\ldots\ldots \quad (5.19)$$

Substituting the coefficients, in eqn. 5.19 leads to

$$\begin{pmatrix} \Delta\lambda_{LPG\_mid} \\ \Delta\lambda_{FBGpeak} \\ \Delta\lambda_{Split-gap} \end{pmatrix} = \begin{pmatrix} 0.0009 & -0.316 & 1.689 \\ 0.0009 & 0.0104 & 0.0 \\ 0.0 & 0.0 & 11.24 \end{pmatrix} \begin{pmatrix} \Delta\varepsilon \\ \Delta T \\ \Delta Cur \end{pmatrix} \quad \ldots\ldots\ldots \quad (5.20)$$

The three parameters can then be evaluated as

$$\begin{pmatrix} \Delta\varepsilon \\ \Delta T \\ \Delta Cur \end{pmatrix} = \begin{pmatrix} 0.0009 & -0.316 & 1.689 \\ 0.0009 & 0.0104 & 0.0 \\ 0.0 & 0.0 & 11.24 \end{pmatrix}^{-1} \begin{pmatrix} \Delta\lambda_{LPG\_mid} \\ \Delta\lambda_{FBGpeak} \\ \Delta\lambda_{Split\text{-}gap} \end{pmatrix} \quad \ldots\ldots\ldots \quad (5.21)$$

The Determinant of the matrix of the coefficients has non-zero values[34]. Using Matlab, the condition number has been evaluated to be 1.23×10^4.

In summary, it has been shown in this subsection that a single SFBG can be used to provide simultaneous measurements of strain, temperature, and curvature. The spectral splitting of the SFBG loss bands facilitated the measurement of the curvature, whilst the wavelength shift of the FBG harmonics and that of the midpoint between the split bands provides for determination of the axial strain and temperature. Both large and small curvatures have been successfully measured. The mode spectral splitting recorded (~126nm) is the largest value so far demonstrated using either SFBG or LPG giving a bend responsivity of 11.43nm.m. The capability of the SFBG-sensor to measure very small curvature values has also been demonstrated. The values of the curvature measured ($<0.4 m^{-1}$) are the smallest so far measured directly using fibre gratings.

5.5 Conclusion

This chapter focused mainly on the applications of the three main types of fibre gratings to sensing. The gratings are FBGs, LPGs and SFBGs. In FBG-based sensing work, two related applications have been presented. First is the compact-FBG-array structure, which allows for quasi-distributed strain sensing of high-spatial-resolution. A simple interrogation method was employed to demonstrate the sensing capability of the device. Two configurations involving five and ten FBGs in an array have been considered and successfully used to implement a linearly quasi-distributed strain sensing system. In comparison with other reported sensor structures and techniques, the compact-grating-array approach may offer a simple and practical solution for real applications as the WDM FBG sensing interrogation method can be

[34] But, the value is close to zero (i.e. 0.004).

directly applied. In addition, this structure permits independent design for spectral sweeping range and spatial resolution.

The weakness of the quasi-distributed strain sensor stems from its inability to compensate for temperature-induced effects. One of the solutions to this problem is the simultaneous measurement of strain and temperature whereby temperature effects are detracted from strain measurement results. Thus, many FBG-based sensors that can measure strain and have inherent element that permit temperature compensation, have been successfully demonstrated in this chapter. The dual-parameter sensing functionality of the designed sensors originates from their unique configuration of having two Bragg reflection peaks that exhibit the same strain- but different temperature-responses. Temperature sensitivities ranging from 7.5 to 12.24pm/°C have been achieved for the sensors written in B/Ge co-doped fibre with different UV exposure durations. This clearly indicates that the responsivity of the grating peaks can be tailored. These FBG-based sensors offer the advantages of simple fabrication, tolerance of large strain effects and more importantly, the use of a single light source for interrogation, which provide the prospects of the development of practical temperature independent strain sensor.

Following the FBG sensing work, some interesting properties of LPG sensors were studied. Discussion focused on investigation into the responsivity characteristics of LPGs in conventional B/Ge co-doped and standard SMF. The LPGs fabricated in both fibres exhibit a set of harmonic cladding modes at shorter wavelength than those of the fundamental modes. A second diffraction order cladding mode of an LPG in B/Ge fibre ($^2LP_{07}$) have been successfully used along with a fundamental mode of lower resonance order ($^1LP_{02}$) to measure the values of strain and temperature simultaneously. Here, the spectral proximity of the two cladding modes can permit the use of a single light source for sensing interrogation.

One of the LPGs in B/Ge co-doped fibre exhibited a cladding mode whose characteristics have not been, to the author's knowledge, reported previously. This mode appears within the set of fundamental modes, and its responsivity characteristics are opposite to those observed for the lower resonance order fundamental modes. This mode has opened-up new sensing possibilities that permit the use of single light source for interrogation, as well as, reduced signal processing.

On the other hand, the LPGs fabricated in standard SMF also exhibited an additional previously un-reported 'broad-peak' ($^1LP_{02L}$) located between the two sets of cladding modes. A rigorous identification process for the mode $^1LP_{02L}$ was successfully pursued, and the sensing properties of the peak have been studied. The peak has been successfully utilized in conjunction with the harmonic modes to demonstrate the capability of an LPG sensor for simultaneous measurement of temperature and other parameters such as curvature, axial strain, and SRI.

Following the LPG sensing work in the conventional step index fibres, a simple and cost effective fabrication technique was adopted to produce a cascaded LPG sensor in SMM900 double-cladding fibre. The capability of the LPG-sensor to measure the SRI and temperature simultaneously has been successfully demonstrated. The scheme consists of two long period gratings (LPGs) of different periods inscribed side-by-side in a single piece of SMM900 double-cladding fibre. One of the LPGs exhibits a shift in its resonance wavelength with changes in both the SRI and temperature. The other LPG is SRI-insensitive but show spectral wavelength shift with temperature changes. In this work, the high temperature responsivity of LPGs was successfully exploited to demonstrate that a high resolution of the measurements is achievable.

After the successful sensing work on separate FBGs and LPGs, focus shifted to the exploitation of the sensing capabilities of SFBGs. To this end, a sensing scheme for the simultaneous refractive index and temperature measurement using a single SFBG was successfully demonstrated. The dual-parameter sensing functionality of an SFBG originates from its unique configuration combining the FBG and LPG structures: the FBG components provide temperature reference so that when measuring SRI, the temperature induce wavelength shift of the LPG can be compensated.

Furthermore, simultaneous measurements of strain, temperature, and curvature has also been demonstrated using the SFBG, where the spectral splitting of the SFBG loss bands facilitated the measurement of the curvature, whilst the wavelength shift of the FBG harmonics and that of the midpoint between the split bands provides for determination of the axial strain and temperature. Both large and small curvatures have been successfully measured. The mode spectral splitting recorded (~126nm) is the largest value so far demonstrated using either SFBG or LPG, giving a bend responsivity of 11.43nm.m. The capability of the SFBG-sensor

to measure very small curvature values has also been demonstrated. The values of the curvature measured ($<0.4m^{-1}$) are the smallest so far measured directly using fibre gratings.

5.6 References:

146. E.J. Friebele, "Fibre Bragg grating strain sensors: present and future applications in smart structures," *Optics and Photonics News*, pp. 33-38, Aug 1998.
147. R.M. Measures, "Fibre optic sensing for composite smart structures," *Compos. Eng.*, vol. 3, no. 7-8, pp. 715, 1993.
148. Y.J. Rao, "In-fibre Bragg grating sensors," *Meas. Sci. Technol.*, vol. 8, 1997, pp. 355-375.
149. S.M. Melle, K.X. Liu, and R.M. Measures, "Practical fibreoptic Bragg grating strain-gauge system," *Appl. Optics*, vol. 32, no. 19, pp. 3601-3609, July 1993.
150. E. Bocherens, S. Bourasseau, V. Dewynter-Marty, S. Py, M. Dupont, P. Ferdinand, and H. Berenger, "Damage detection in a radome sandwich material with embedded fibre optic sensors," *Smart Mat. & Struc.*, vol. 9, no. 3, pp. 310-315, Jun 2000.
151. G. Zhou, and L.M. Sim, "Damage detection and assessment in fibre-reinforced composite structures with embedded fibre optic sensors – review," *Smart Mat. Structures*, vol. 11, no. 6, pp. 925-939, Dec 2002.
152. J.D.C. Jones, "Review of fibre sensor techniques for temperature and strain discrimination," in Proc. 12th OFS, *ofs*97, Williamsburg, VA, pp.36-39, 1997.
153. T.A. Berkoff, and A.D. Kersey, "Fibre Bragg grating array sensor system using a bandpass wavelength division multiplexer and interferometric detection," *IEEE Photon. Technol. Lett.*, vol. 8, no. 11, pp. 1522-1524, Nov 1996.
154. M. Froggatt, and J. Moore, "Distributed measurement of static strain in an optical fibre with multiple Bragg gratings at nominally equal wavelengths," *Appl. Opt.*, vol. 37, no. 10, pp. 1741-1746, 1998.
155. M.A. Davis, A.D. Kersey, J. Sirkis, and E.J. Friebele, "Shape and vibration mode sensing using a fibre optic Bragg grating array," *Smart Mater. Struct.*, vol. 5, no. 6, pp. 759-765, Dec 1996.
156. I. McKenzie, R. Jones, I.H. Marshall, and S. Galea, "Optical fibre sensors for health monitoring of bonded repair systems," *Comp. Struct.*, vol. 50, no. 4, pp. 405-416, Dec 2000.
157. M. Volanthen, H. Geiger, M.J. Cole, and J.P. Dakin, "Measurement of arbitrary strain profiles within fibre gratings," *Electron. Lett.*, vol. 32, pp. 1028-1029, 1996.
158. M. LeBlanc, S. Huang, M. Ohn, R.M. Measures, A. Guemes, and A. Othonos, "Distributed strain measurement based on a fibre Bragg grating and its reflection spectrum analysis," *Opt. Lett.*, vol. 21, pp. 1405-1407, 1996.
159. M. LeBlanc, and A.D. Kersey, "Distributed, intra grating sensing by Fabry-Perot wavelength tuned low-coherence interferometry," *Proceeding of 12th International Conference on Optical Fibre Sensors*," pp. 52-55, 1997.
160. K.E. Chisholm, "Progress in the fabrication and applications of short and novel structures In-fibre Bragg gratings," *PhD Thesis*, Aston University, UK, pp. 127-162 Jan 2000.
161. R.J. Campbell, and R. Kashyap, "Spectral profile and multiplexing of Bragg gratings in Photosensitive fibre," *Electron. Letts.*, vol. 16. no. 12, pp. 898-900, Jun 1991.
162. C.I. Merzbacher, A.D. Kersey, and E.J. Friebele, "Fibre Optic sensors in concrete structures: A review," *Smart Mater. Struct.*, vol. 5, no. 2, pp. 196-208, Apr 1996.

163. S. Kabashima, and T. Ozaki, "Strain and temperature monitoring in composite sandwich panels in space environment," *Proc. 14th Intl. Conf. on Optical Fibre Sensors*, Venice, Italy, pp. 126-129, Oct 2000.
164. H.J. Patrick, G.M. Williams, A.D. Kersey, J.R. Pedrazzani, and A.M. Vengsarkar, "Hybrid fibre Bragg grating/long period fibre grating sensor for strain/temperature discrimination," *IEEE Photonics Techn. Lett.*, vol. 8, no. 9, pp. 1223-1225, Sept 1996.
165. Y.J. Rao, P.J. Henderson, D.A. Jackson, L. Zhang, and I. Bennion, "Simultaneous strain, temperature and vibration measurement using a multiplexed in-fibre-Bragg-grating/fibre-Fabry-Perot sensor system," *Electron. Lett.,* vol. 33, no. 24, pp. 2063-2064, Nov 1997.
166. M.G. Xu, J.L. Archambault, L. Reekie, and J.P. Dakin, "Discrimination between strain and temperature effects using dual-wavelength fibre grating sensors," *Electron. Lett.,* vol. 30, no. 13, pp. 1085-1087, Jun 1994.
167. S.W. James, M.L. Dockney, and R.P. Tatam, "Simultaneous and independent temperature and strain measurement using In-fibre Bragg grating sensors," *Electron. Lett.*, vol. 32, no. 12, pp. 1133-1134, Jun 1996.
168. B.O. Guan, H.W. Yaw, X. Tao, and X. Dong, "Simultaneous strain and temperature measurement using a superstructured fibre Bragg grating," *IEEE Photon. Technol. Lett.*, vol. 6, no. 12, pp. 675–677, Jun 2000.
169. J. Jung, H. Nam, J.H. Lee, N. Park, and B. Lee, "Simultaneous measurement of strain and temperature by use of a single-fibre Bragg grating and an erbium-doped fibre amplifier," *Appl. Opt.*, vol. 38, no. 13, pp. 2749-2751, 1999.
170. W.C. Du, X.M. Tao, and H.Y. Tam, "Fibre Bragg grating cavity sensor for simultaneous measurement of strain and temperature," *IEEE Photon. Technol. Lett.*, vol. 11, no. 1, pp. 105–107, 1999.
171. S.E. Kanellopoulos, V.A. Handerek, and A.J. Rogers, "Simultaneous strain and temperature sensing with photogenerated In-fibre gratings," *Opt. Lett.*, vol. 20, no. 3, pp. 333-335, Feb 1995.
172. B.O. Guan, H.W. Yaw, S.L. Ho, W.H. Chung, and X.Y. Dong, "Simultaneous strain and temperature measurement using a single fibre Bragg grating," *Electron. Lett.*, vol. 36, no. 12, pp. 1018–1019, Jun 2000.
173. I. Raint, and F. Haller, "Study of photosensitivity at 193nm and comparison with photosensitivity at 240nm influence of fibre tention- TypeIIa aging: Fibre gratings, Photosensitivity, and poling," *Jn. lightwave Technol.*, vol. 15, no. 8, pp. 1464–1469, 1997.
174. T. Poulsen, M.O. Berendt, A. Bjarklev, L. Gruner-Nielsen, and C.E. Soccolich, "Bragg grating induced cladding mode coupling caused by ultra-violet light absorption," *Electron. Lett.*, vol. 34, no. 10, pp. 1007-1009, May 1998.
175. J.P. Dakin, and M. Volanthen, "Distributed and multiplex fibre grating sensors, including discussion of the problem areas," *IEICE Trans. Electron.* Vol. E83-C, no.3, pp. 391-399, 2000.
176. A.M. Vengsarkar, P.J. Lemaire, J.B. Judkins, V. Bhatia, T. Erdogan, and J.E. Sipe, "Long-period fibre gratings as band-rejection filters," *Jn. Lightwave Technol.*, vol. 14, no. 1, pp. 58-64, 1996.
177. V. Bhatia and A.M. Vengsarkar, "Optical fibre long-period grating sensors," *Opt. Lett.*, vol. 21, no. 9, pp. 692-694, 1996.
178. H.J. Patrick, A.D. Kersey, and F. Bucholtz, "Analysis of the response of Long-period fibre gratings to the external index of refraction," *Jn. Lightwave Technol.*, vol. 16, no. 9, pp. 1606-1612, 1998.

179. A.A. Abramov, A. Hale, R.S. Windeler, and T.A. Strasser, "Widely tuneable long-period fibre gratings," *Electron. Lett.*, vol. 35, no. 1, pp. 81-82, 1999.
180. A.A. Abramov, B.J. Eggleton, J.A. Rogers, R.P. Espindola, A. Hale, R.S. Windeler, and T.A. Strasser, "Electrically tuneable efficient broad-band fibre filter," *IEEE Photon. Technol. Lett.*, vol. 11, no. 4, pp. 445-447, 1999.
181. V. Bhatia, D. Campbell, R.O. Claus, and A.M. Vengsarkar, "Simultaneous strain and temperature measurement with long-period gratings," *Opt. Letts.*, vol. 22, no. 9, pp. 648-650, May 1997.
182. T.W. MacDougall, S. Pilevar, C.W. Haggans, and M.A. Jackson, "Generalized expression for the growth of long period gratings," *IEEE Photon. Technol. Lett.*, vol.10, no. 10, pp. 1449-1451, 1998.
183. V. Grubsky, A. Skorucak, D.S. Starodubov, and J. Feinberg, "Fabrication of long-period fibre gratings with no harmonics," *IEEE Photon. Technol. Lett.*, vol. 11, no. 1, pp. 87-89, 1999.
184. T.B. Lee, and J. Nishii, "Cladding-surrounding interface insensitive long-period grating," *Electron. Lett.*, vol. 34, no. 11, pp. 1129-1130, 1998.
185. S.A. Vasiliev, E.M. Dianov, D. Varelas, H.G. Limberger, and R.P. Salathe, "Postfabrication resonance peak positioning of long-period cladding-mode-coupled gratings", *Opt. Letts.*, vol. 21 no. 22, pp. 1830-1832, Nov 1996.
186. K.M. Zhou, H.T. Liu, and X.W. Hu, "Tuning the resonant wavelength of long period fibre gratings by etching the fibre's cladding," *Opt. Comms*, vol. 197, no. 4-6, pp. 295-299, Oct 2001.
187. M.J. Adams, "An introduction to optical waveguides," Wiley, New York, 1981.
188. G. Meltz, W.M. Morey, W.H. Glenn, "Formation of Bragg gratings in optical fibres by a transverse holographic method," *Opt. Lett.*, vol. 14, no. 15, pp.823-825, 1989.
189. S. Yin, K-W. Chung, and X. Zhu, "A highly sensitive long period grating based tuneable filter using a unique double-cladding layer structure," *Optics Comms.*, vol. 188, no. 5-6, pp. 301-305, 2001.
190. Y-G. Han, B.H. Lee, W-T. Han, U-C Paek, and Y. Chung, "Fibre-optic sensing applications of a pair of long-period fibre gratings," *Meas. Sci. Technol.*, vol. 12 , no. 7, pp. 778-781, 2001.
191. Z. Zhang, and J.S. Sirkis, "Temperature compensated long period grating chemical sensor," *Proc. 12th Int. Conf. on Optical Fibre Sensors*, pp. 294, 1997.
192. X.W. Shu, and D.X. Huang, "Highly sensitive chemical sensor based on the measurement of the separation of dual resonant peaks in a 100-mu m-period fibre grating," *Optics Comms*, vol. 171, no. 1-3, pp. 65-69. Nov 1999.
193. A.D. Kersey, M.A. Davis, H.J. Patrick, M. LeBlanc, K.P. Koo, C.G. Askins, M.A. Putnam, and E.J. Friebele, "Fibre grating sensors," *Jn. Lightwave Technol.*, vol. 15, no. 8, pp. 1442-1463, 1997.
194. X. Shu, X. Zhu, S. Jiang, W. Shi, and D. Huang, "High sensitivity of dual resonant peaks of long-period fibre grating to surrounding refractive index changes," *Electon. Lett.*, vol. 35, no. 18, pp. 1580-1581, Sept 1999.
195. K.T. Lau, L.M. Zhou, P.C. Tse, and L.B. Yuan, "Applications of composites, optical fibre sensors and smart composites for concrete rehabilitation: An overview," *Appl. Composite Materials*, vol. 9, no. 4, pp. 221-247, Jul 2002.
196. K.T. Lau, "Fibre-optic sensors and smart composites for concrete applications," *Magazine of Concrete Research*, vol. 55, no. 1, pp. 19-34, Feb 2003.
197. B. Culshaw, C. Michie, P. Gardiner, and A. McGown, "Smart structures and applications in civil engineering," *Proc. IEEE*, vol. 84, no. 1, pp. 78-86, Jan 1996.

198. M.J. Gander, W.N. MacPherson, R. McBride, J.D.C. Jones, L. Zhang, I. Bennion, P.M. Blanchard, J.G. Burnett, and A.H. Greenaway, "Bend measurement using Bragg gratings in multicore fibre," *Electron Lett*, vol. 36, no. 2, pp 120-121, Jan 2000.
199. L.A. Ferreira, F.M. Araujo, and J.L. Santos, "Temperature and strain insensitive bend measurements with D-type fibre Bragg gratings," *Proc. 14th Intl. Conf. on Optical Fibre Sensors*, Venice, Italy, pp. 5-8, Oct 2000.
200. H.J. Patrick, C.C. Chang, and S.T. Vohra, "Long period fibre grating for structural bend sensing," *Electron. Letts.*, vol. 34, no. 18, pp. 1773-1775, Sept 1998.
201. C.C. Ye, S.W. James, and R.P. Tatam, "Simulataneous temperature and bend sensing with long-period fibre gratings," *Opt. Lett.*, vol. 25, no. 14, pp. 1007-1009, July 2000.
202. B.J. Eggleton, P.A. Krug, L. Poladian, and F. Ouellette, "Long periodic superstructure Bragg gratings in optical fibres," *Electron. Lett.*, vol. 30, no. 19, pp.1620-1622, Sept. 1994.

6 Gratings-based devices for telecom applications

6.1 Introduction

In the last two decades telecommunication has been the main driving force for the development of fibre grating technology. Some of the attractive features of fibre gratings are their potential for use in the different areas of telecommunications. In this chapter three types of fibre gratings are demonstrated to achieve various types of practical filter for use in telecommunications. These filters are:

1. Fibre Bragg Gratings (FBG)-based filters: Two types of FBG-based filters are demonstrated herein. These include those achieved by suppressing cladding mode-coupling loss, and by suppressing FBG sidelobes using apodisation technique.
2. Long Period Grating (LPG)-based filters: Filters demonstrated here are based on the use of LPGs, that have high temperature responsivity, to achieve tuneable loss filters in the two main telecommunication windows (i.e. 1300 and 1500nm).
3. Superstructured Fibre Bragg Gratings (SSFBG)-based filters: Here the filters are based on the use of SSFBGs to achieve two types of microwave sub-carrier filters, and also an optical DWDM filter.

6.2 FBG Filters

The improvements in the loss characteristics of optical fibres coupled with the development of EDFA has revolutionised the use of optical fibres in long-haul high capacity telecommunications signal transmission. It has been shown in Section 2.1 that at 1500nm region standard telecom fibre exhibits the lowest attenuation.

However, unlike in the 1300nm region at which the fibre dispersion is zero, at 1500nm the dispersion can limit the bandwidth at which signal is transmitted through the fibre without inter-symbol interference. Thus, there is the need to develop systems or devices that can compensate for the effects of the dispersion.

In view of their intrinsic nature, Chirped Bragg gratings are now commonly used to compensate for the effects of fibre dispersion and dispersion-slope. In addition, Bragg gratings have found many other applications in telecommunications. Some of these applications include filtering, in both optical and microwave domains, where gratings are used to provide band-pass and tuneable characteristics. The FBGs used as band rejection elements possess very steep spectral slope and are easy to fabricate making them suitable for other applications, such as channel add-and-drop, gain flattening filters, multiplexer-demultiplexers, and band splitters. Indeed, FBGs have also been employed in WDM systems and such applications have attracted much attention over the recent years due to their overwhelming advantages for high capacity optical transmission.

In Section 4.5.1, the apodisation technique used to suppress the FBG sidelobes during fabrication for the minimization of inter-symbol interference (ISI) has been discussed. Other techniques of reducing ISI, such as the suppression of cladding mode-coupling loss, are examined and presented in this section.

6.2.1 Suppression of cladding-mode coupling loss

An FBG with high reflectivity inscribed in a standard SMF induces a significant amount of loss at the shorter wavelength side of the Bragg peak. The loss is cause by the coupling of light from the forward propagating guided LP_{01} mode within the core to the backward propagating modes within the cladding, and to the radiation modes. The cladding-modes manifest themselves in the form of a series of discrete transmission dips in the spectrum at wavelengths that are shorter than the Bragg reflection wavelength. These losses can be quite severe in strong gratings and incur insertion loss in the neighbouring WDM channels, which restricts the use of such grating filters in DWDM systems. It has been observed that this unwanted coupling arises from the non-uniform refractive index modulation over the cross-section of the fibre-core [203].

Various techniques have been proposed to reduce the cladding-mode coupling loss, including the use of photosensitive inner-cladding fibre structures [203, 204], high Numerical Aperture (NA) fibre [205,206], and depressed cladding fibre [207, 208, 209]. All these methods rely on the use of specialty fibres, at a cost, and eventually lead to increase splicing loss, which is not

desired in optical fibre communication systems. In this section a novel and flexible technique for suppressing cladding-mode coupling loss in the fabrication of UV-induced FBGs is discussed. Suppression of cladding-mode coupling loss down to ~0.2 dB in a Bragg grating of 18dB reflectivity has been achieved in hydrogen-loaded standard SMF. The method employed is based on the use of UV pre-exposure onto the fibre to raise the refractive index of the core before an FBG is finally inscribed. The key advantages of this method are that no special fibre is required, and the refractive index of the fibre core is changed only within the section into which the FBG is written thereby introducing no extra loss. In addition, whilst the work in ref. [205] reported an observation of a shift on the onset of cladding mode coupling loss peaks, the work did not go further to report the key observation of the mode suppression effect that accompany such a shift. The work reported in this section attempts to close such a gap and simulation results clearly support the experimental observation.

6.2.1.1 Suppression of FBG cladding-mode coupling loss

The scanning phase mask fabrication technique was used in this work to inscribe 8mm long Bragg gratings in standard telecom single mode fibre (SMF). The mask period is 1083nm. Before grating inscription, the SMF was loaded with hydrogen (H_2) at 150bars for 48 hours at a temperature of 80°C so as to increase the photosensitivity. The UV laser used for the fabrication operates at 244nm, with an output power of 100mW. An 8mm long Bragg grating was first fabricated in the H_2-loaded standard SMF that was not pre-exposed to UV: the spectral response of the resulting grating showing pronounced cladding-modes is shown in Fig. 6.1, with a Bragg peak of ~22.5dB located at ~1566.4nm. The appearance of cladding-mode coupling loss with the largest dip at ~1565nm can be seen on this grating.

Pieces of H_2-loaded standard SMF were pre-exposed to the scanning UV beam without using a phase mask. The fibre length pre-exposed to the UV beam in each case was 15mm. Scanning speed was set at different values leading to different UV pre-exposure times of 60, 100 and 120 minutes per 10mm of the fibre. Thereafter, all the pre-exposed fibre pieces were re-hydrogenated under the same conditions, and subsequently the FBGs were inscribed in the section of the re-hydrogenated pieces of fibre that were pre-exposed with UV. The transmission responses of the gratings obtained are shown in Fig. 6.1: the grating with a pre-exposure time of 60 minutes shows rejection strength of ~25.6dB while the cladding-mode

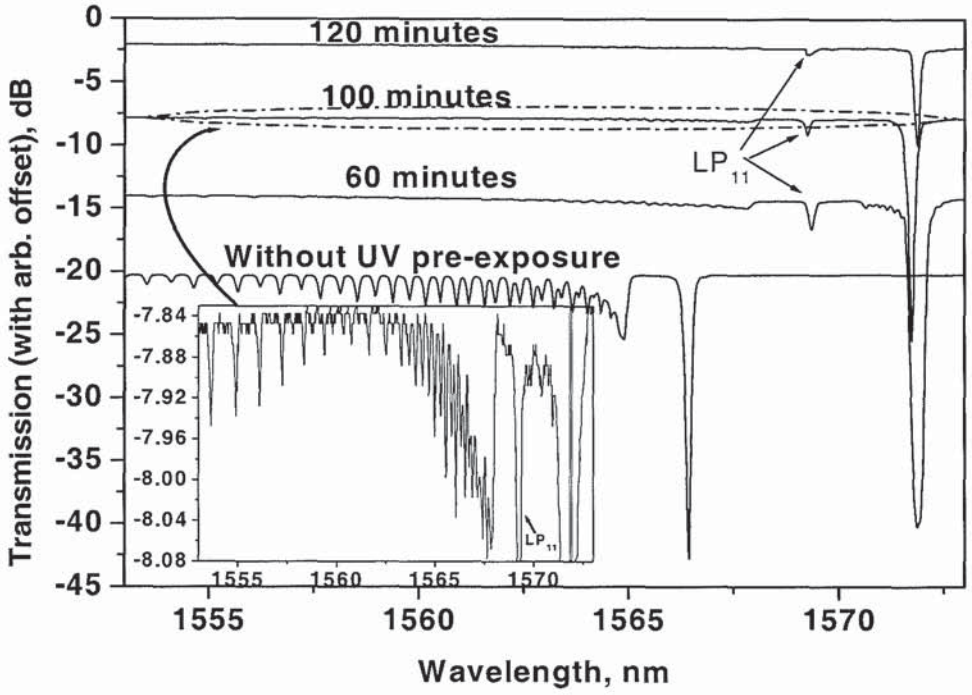

Fig.6.1: The experimentally obtained transmission spectra of fibre gratings (traces offset for clarity): with and without UV pre-exposure, the inset is the response of the FBG pre-exposed with UV for 100 minutes/cm

coupling loss has a level of 0.5dB, which clearly is much smaller in comparison to that of the FBG in the non-pre-exposed fibre. It should be pointed out that the small transmission dip close to the Bragg wavelength is the LP_{11} mode [210], the negative effect of which, as demonstrated herein, can be eliminated by ensuring a zero blazed angle.

The central wavelength of the FBGs in the pre-exposed fibre is ~6nm greater than that of the FBG obtained with non-pre-exposed fibre, clearly showing a positively induced index change that resulted from the pre-exposure. By increasing the pre-exposure time the cladding-mode coupling loss can be further reduced. Typically, with a pre-exposure time of 100 minutes the grating obtained shows reduction in the cladding-mode coupling loss to ~0.2dB, but at a reduced strength of the Bragg peak to ~18dB. The inset to Fig.6.1 is the enlarged spectral response of this grating. The pre-exposure of 120 minutes led to 0.09dB level of cladding-mode coupling, but at an increased penalty to the strength of the main FBG peak, in view of the reduced photosensitivity of the fibre section, induced through UV pre-exposure over a longer period. The reduction of photosensitivity is the result of gradual approach to exposure

saturation, which reduces the available index-change necessary for writing strong gratings. Beyond saturation level a damaged or Type II grating could result. This indicates that an optimum level of pre-exposure needs to be established depending on the application.

The cladding mode suppression is attributed to the increase of the OH-induced [211] core refractive index. The difference in the pre-exposure time represents a difference in the OH ions created within the sections, thus, leading to the difference in refractive indices of the fibre core. Longer UV pre-exposure has, in this technique, led to larger increase of the core refractive index, which raises the index difference between fibre core and cladding consequently resulting in reduced cladding-mode coupling loss.

It should be stressed that a single small (<5dB) loss dip appearing between cladding-modes and the Bragg resonance at around 1569.4nm in Fig. 6.1 is the LP_{11}, the so-called "ghost-mode" in fibre gratings. This LP_{11} ghost-mode, that is only visible in transmission rather than reflection, appears because of a very small blazed angle [210] during grating inscription, and as mentioned earlier such angle is difficult to eliminate in practice. However, if the value of the normalized propagation frequency[35] of the fibre supports more than a single mode, there is a greater tendency for the emergence of the ghost mode LP_{11}, which indicates the presence of a blazed angle.

For the FBGs reported herein the mode LP_{11} cannot be seen in reflection, as only a small part of the fibre (15mm) has the increased core refractive index that supports it. If the mode exists it can always be seen in transmission, therefore can have an impact on the adjacent WDM channels. High core/cladding index difference does increase the tendency of generating this mode. However, it can be minimised by carefully controlling the pre-exposure time and UV inscription procedure. The effectiveness of this method has also been demonstrated by using B/Ge co-doped fibre that permits larger increase to the NA of the fibre. In Fig. 6.2 the transmission spectrum of a 7mm long FBG obtained with pre-exposure shows that the emergence of LP_{11} mode was optimally controlled for a Bragg grating of 12dB resonance strength. This indicates the increasing potential of this method for producing high quality Bragg gratings.

[35] Normalized propagation frequency referred here has been defined by eqn. 3.12.

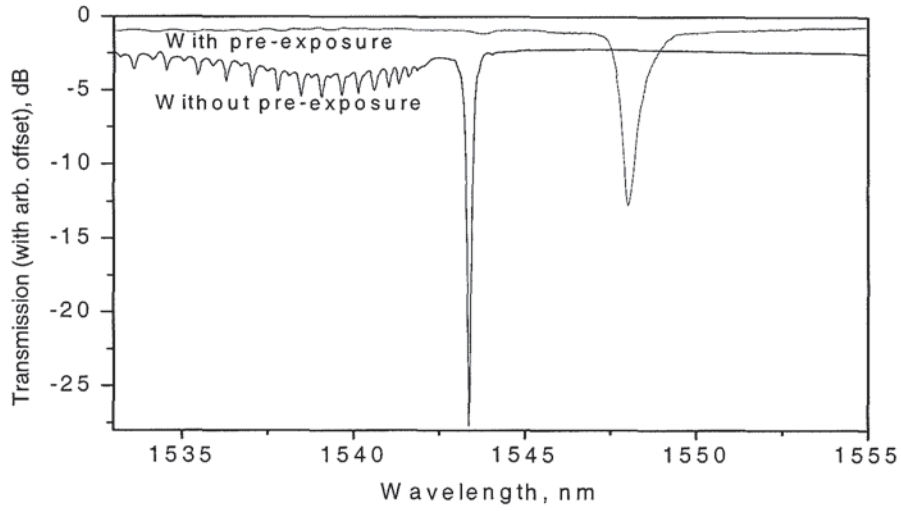

Fig. 6.2: The experimentally obtained transmission spectra of fibre gratings (traces offset for clarity): with limited and without UV pre-exposure

Using the increase in refractive index estimated from Fig. 6.1, and some parameters shown in Table 6.1, simulations of the suppression effect were carried out using commercial Optiwave™ IFO software. The results obtained, as shown in Fig. 6.3, indicate the effectiveness of this method of UV-induced index increase, the cladding modes have been clearly suppressed from ~1dB (see traces 'a-b') to ~0.2dB (see traces 'c-d') by increasing the core refractive index from 1.4488 to 1.4560: the inset is the enlarged 1561 to 1573nm region.

Fig.	FBG label	Core radius (μm)	Fibre diameter (μm)	Cladding index	Core index	Blazed angle (deg)	Rejection level (dB)		
							LP_{11}	LP_{02}	Other modes
6.3	a	4.15	125	1.444	1.4488	0			~1
6.3	b	4.15	125	1.444	1.4488	0.65			~1
6.3	c	4.15	125	1.444	1.4560	0.65	1.35	≤0.2	≤0.2
6.3	d	4.15	125	1.444	1.4560	0	0	≤0.2	≤0.2
6.4	e	6.50	125	1.444	1.4488	0.4	1.58	<0.65	0.65
6.4	f	6.50	125	1.444	1.4560	0.4	1.4	0.38	0.06
6.4	g	6.50	125	1.444	1.4560	0.1	0.1	0.30	0.06
6.4	h	6.50	125	1.444	1.4560	0	0	0.30	0.06

Table 6.1: Simulation parameters for the 8mm long FBGs in standard SMF.

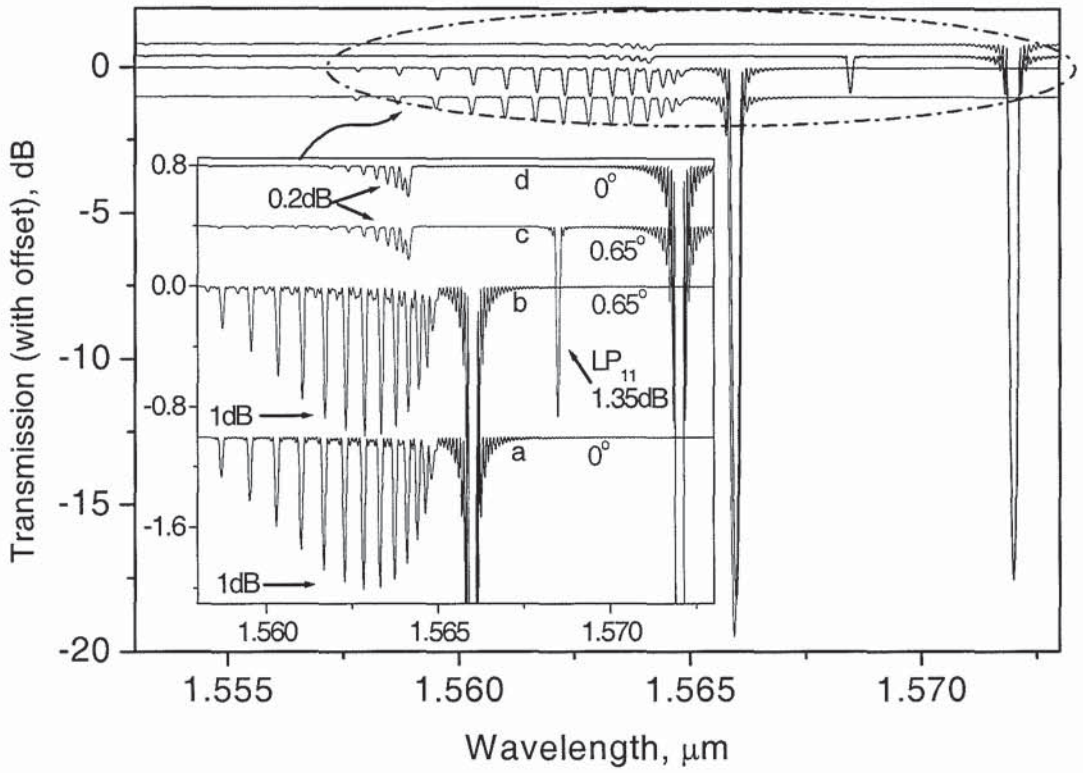

Fig. 6.3: Simulated spectra demonstrating cladding mode suppression, and the control of the effect of blazed angle.

By comparing trace 'a' simulated with no blazed angle and 'b' simulated with a blazed angle of 0.65°, it can be seen that there is no clear difference between the traces, which indicates that even if there is a very small blazed angle, for normal fibre conditions the effect of the resulting LP_{11} mode will be insignificant. However, as the refractive index of the fibre core increases, for example, as can be seen in trace 'c' the significance of the small blazed angle begins to manifest in the form of a growing ghost mode LP_{11}. In trace 'd' where the core index is the same as that of trace 'c' it can be seen that by removing the blazed angle, even for high core refractive index the ghost mode LP_{11} can be eliminated. There is however a limit to which cladding modes can be suppressed by raising fibre core index; whilst the ghost mode LP_{11} can be removed by zero blazed angle, simulation suggest that a further increase in core refractive index by 0.015 (≡16.3nm shift to the longer wavelength) will incur a slightly strong (~0.4dB) ghost mode LP_{02}. So far it has not been possible to increase the refractive index of standard fibre by such an amount using UV exposure for up to 4 hours.

It is however noted that if a different fibre of larger core radius (for example 6.5μm) is used, at high values of core refractive indices an increase in the strength of ghost mode LP_{02} will result during FBG inscription. Unfortunately, similar to what happens in depressed cladding fibre [209], this ghost mode LP_{02} cannot be eliminated by ensuring a zero blazed angle. In standard SMF there is little chance of producing an FBG with a strong LP_{02} ghost mode using UV pre-exposure. The method of UV pre-exposure is therefore quite promising in addressing the problem of cladding-mode coupling loss in FBGs. In retrospect however, it would have been useful to measure the experimental value of insertion loss in this type of filters.

In Fig. 6.4 the effect of the ghost mode LP_{02} in relation to that of mode LP_{11} is demonstrated where a fibre having core radius of 6.5μm is considered. It is shown here that whilst mode LP_{11} can be reduced or eliminated by changing the blazed angle, the ghost mode LP_{02} cannot be removed using the same technique. It can be seen on trace 'e' (representing a grating with no increase in core index) that for a grating of 0.4° blazed angle, the LP_{11} mode is well pronounced with strength of 1.58dB due to the large core radius, but, the mode LP_{02} remains insignificant and weaker than the other cladding modes.

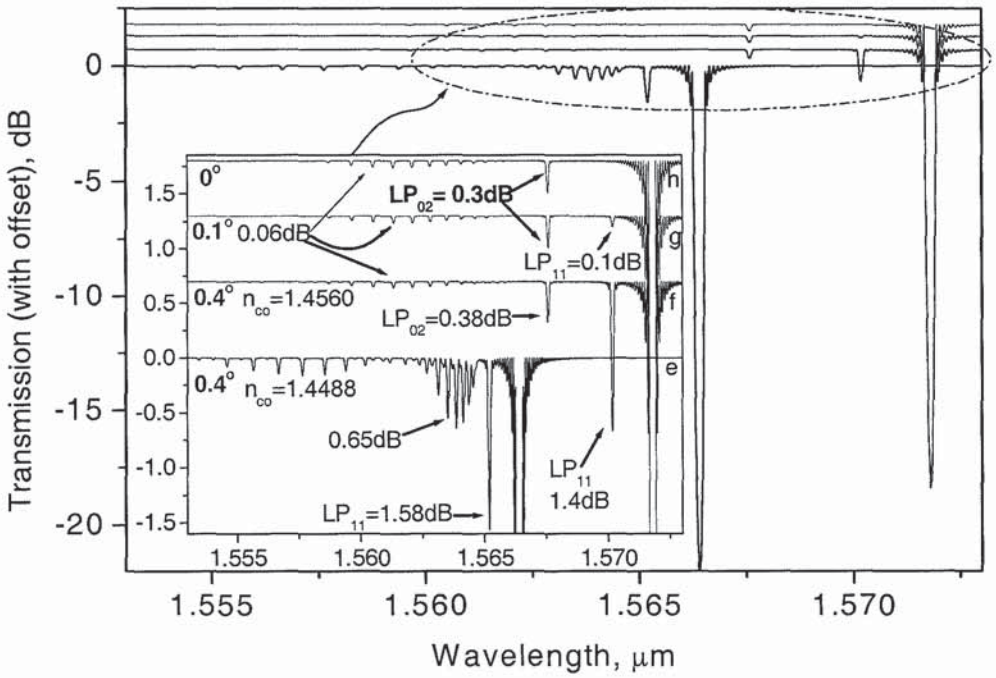

Fig. 6.4: Simulated spectra demonstrating cladding mode suppression and the effect of large LP_{02} mode

As the index of the fibre is increased from 1.4488 (trace 'e') to 1.456 (trace 'f-h'), it can be seen on trace 'f', for example, that the mode LP_{11} becomes slightly weaker (~1.4dB) and the other cladding modes are clearly suppressed from ~0.65dB to ~0.06dB. On the contrary, with this increase in the core refractive index the ghost mode LP_{02} attains a level of, in this case, ~0.38dB. When the blazed angle was reduced from 0.4^{o} to 0.1^{o} whilst the mode LP_{11} reduces to ~0.1dB, as seen on trace 'g', there is no significant reduction in the level of the ghost mode LP_{02} which remains at ~0.3dB. As the blazed angle is removed, it can be seen in trace 'h' that the mode LP_{11} is completely eliminated leaving mode LP_{02} unchanged, clearly showing that the mode LP_{02} cannot be removed by ensuring zero blazed angle.

6.2.1.2 Effects of different fibre dimensions

In this Sub-section, simulation result for the suppression of cladding mode coupling, generated using Optiwave™ IFO, will be discussed. Starting from the study of the effect of large cladding radius, next is the investigation into the impact having different core sizes, and finally the effect of reduction in the cladding radius are investigated.

(a) Simulation to demonstrate the effects of large cladding radius

The last subsection discussed the variation of the strength of the cladding-mode coupling loss caused by changing the refractive index of the fibre-core. In this subsection, the changes in the strength of the cladding mode coupling loss in FBGs within a fibre with an un-usually large size of cladding radius ($129.05\ \mu m$) were also studied. For this fibre a slightly different behaviour emerged with the increase in the fibre core refractive index: it can be seen in Fig. 6.5 that the strength of the cladding mode coupling loss was not significantly affected even for a large increase in the core refractive index from 1.4488 to 1.463592. However, a shift in the cladding modes to the shorter wavelength was observed, in agreement with the result demonstrated in [205]. In addition, there is also a very large increase in the depth and width of the main Bragg peak of the grating when the index of the core increased, as clearly shown in the figure.

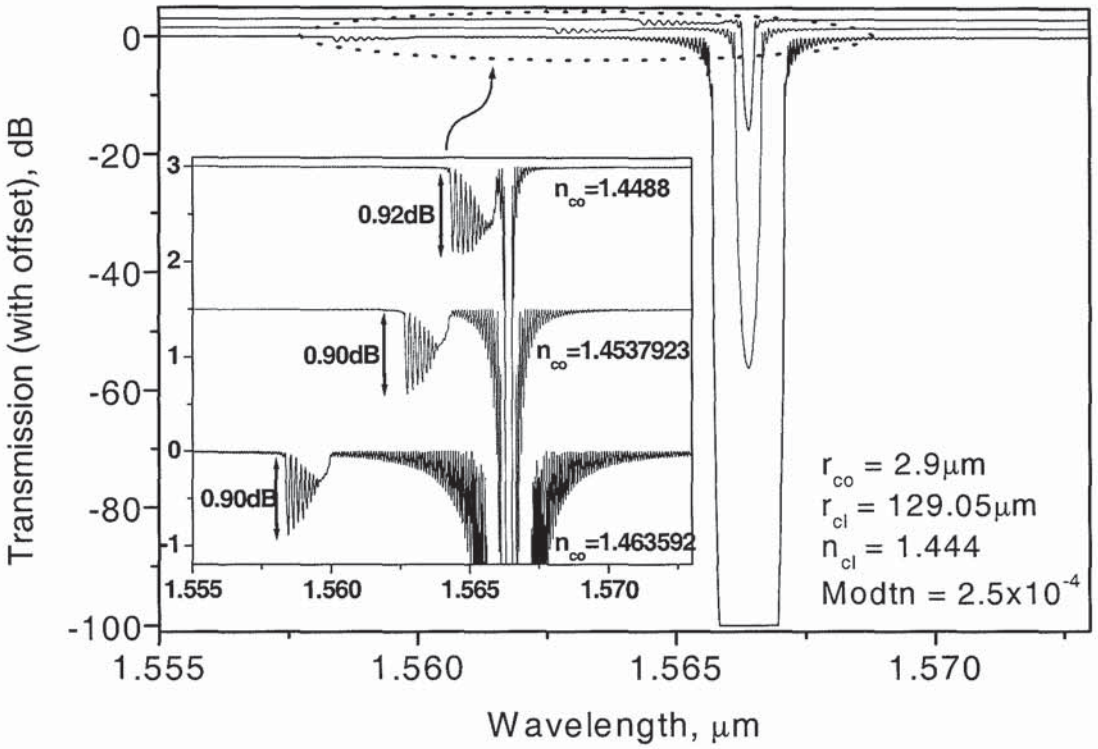

Fig. 6.5: Simulation results for the effect of increase in core index in a fibre of large cladding radius (n_{co} and n_{cl} are the respective core and cladding material indices. r_{co} and r_{cl} are the respective core and cladding radii, index modulation is 2.5x10^{-4}, the some spectra were arbitrarily offset above 0dB to enable comparison.

The increase in the grating coupling strength is caused by the rise in the value of the overlap constant C_{01}^{co} as a result of a boost in the induced core index, which in turn leads to proportionate increase in the value of the grating reflectivity $|r(\lambda_0)|$.

(b) Simulation to demonstrate the effect of changes in core radius

To demonstrate the effects of changing core radius on the level of cladding mode coupling loses, in Fig. 6.6(a) a series of simulated FBGs' spectral responses are shown. Here, the radius of the fibre core has been changed by 7 μm from 2.9 μm to 9.9 μm with a step change of 1μm while keeping UV-induced index modulation and all other grating parameters constant. It is clear from the figure that reduction in the cladding mode coupling loss has been

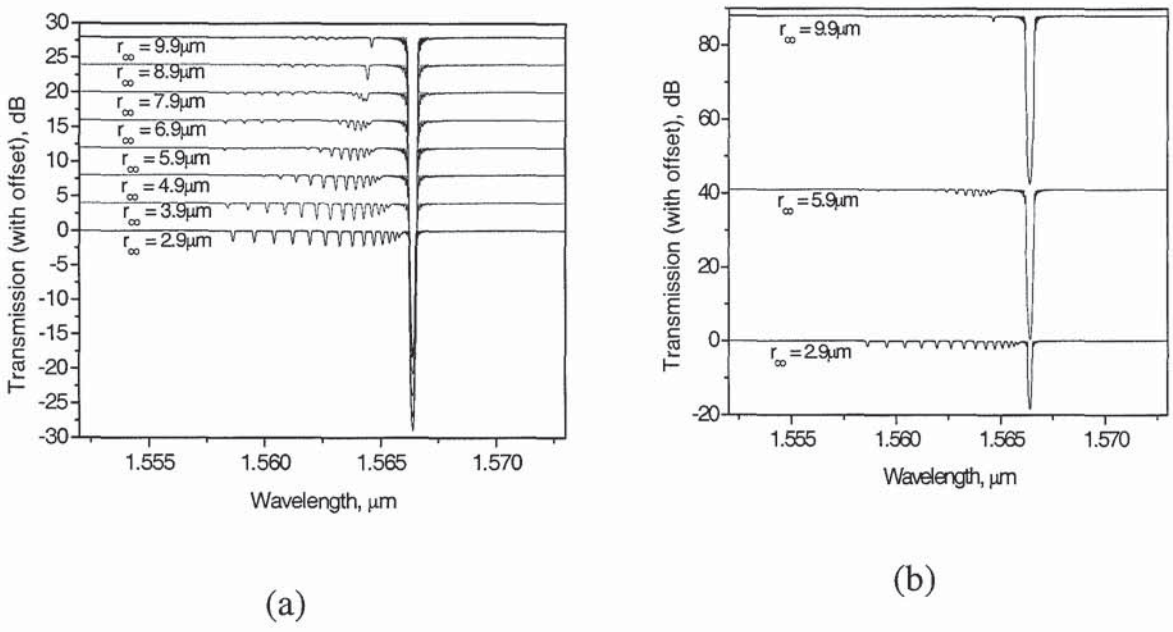

Fig. 6.6: Simulation results for the effect of increase in the core radius (r_{co} is the core radius, index modulation is 3 X 10^{-4}), n_{co} =1.4488, n_{cl} =1.444.

achieved with 9.9μm radius. In Fig. 6.6(b) some of the FBGs shown in Fig. 6.6(a) are re-plotted with more significant offset on the y-axis for improved clarity. As the other cladding modes become smaller with increase in the core radius -the core mode LP_{02}^{co} on the other hand becomes more pronounced indicating a departure from the single mode condition (i.e. V > 2.401). It was also observed that with every increase in the core radius, the transmission depth of the main peak also increases, as clearly seen in Fig. 6.6(b). This can be explained by using the power reflectance at resonance wavelength, that is

$$\left|r(\lambda_0)\right|^2 = \tanh^2\left(C_{01}^{co}\pi\Delta nL/\lambda_0\right) \tag{6.1}$$

Where Δn is half of the index modulation depth, λ_0 is the grating resonance wavelength, L is the grating length and C_{01}^{co} is core modes overlapping factor. The mode overlap factor is given by

$$C_{01}^{co} \approx 1 - \frac{1}{\left(V^{co}\right)^2} \tag{6.2}$$

where V^{co} is the normalised frequency of the fibre core and is given by

$$V^{co} = \frac{2\pi r_{co}}{\lambda}\sqrt{{n_{co}}^2 - {n_{cl}}^2} = \frac{2\pi r_{co}}{\lambda} \cdot NA \tag{6.3}$$

n_{co} and n_{cl} are the respective core and cladding material indices. r_{co} is the radius of the fibre core. Clearly, the value of C_{01}^{co} (and hence the grating reflectivity $|r(\lambda_0)|$) can be changed by altering either the *core radius* or the *index depth* between the core and cladding materials.

(c) Simulation to demonstrate the effects of reduction in cladding radius

Fig. 6.7 shows the simulated spectral responses of FBGs with a strength of 18dB in fibre sections having core radius of 2.9μm each with different sizes of cladding radius, but with all other parameters relating to the FBGs, such as grating length, index modulation, core and cladding indices etc kept constant. It can be seen clearly from the figure that with the increase in cladding radius from 19.05 to 119.05μm the level of the coupling loss has been reduced dramatically from ~6dB down to ~2dB, at the same time, the resulting weaker cladding modes are shifted towards the longer wavelengths and closer to the main Bragg peak of the FBG. This is more obviously seen in the FBG for the fibre of 119.05μm cladding radius. In addition, it can be seen that since the FBGs have the same index modulation the grating transmission depth is maintained.

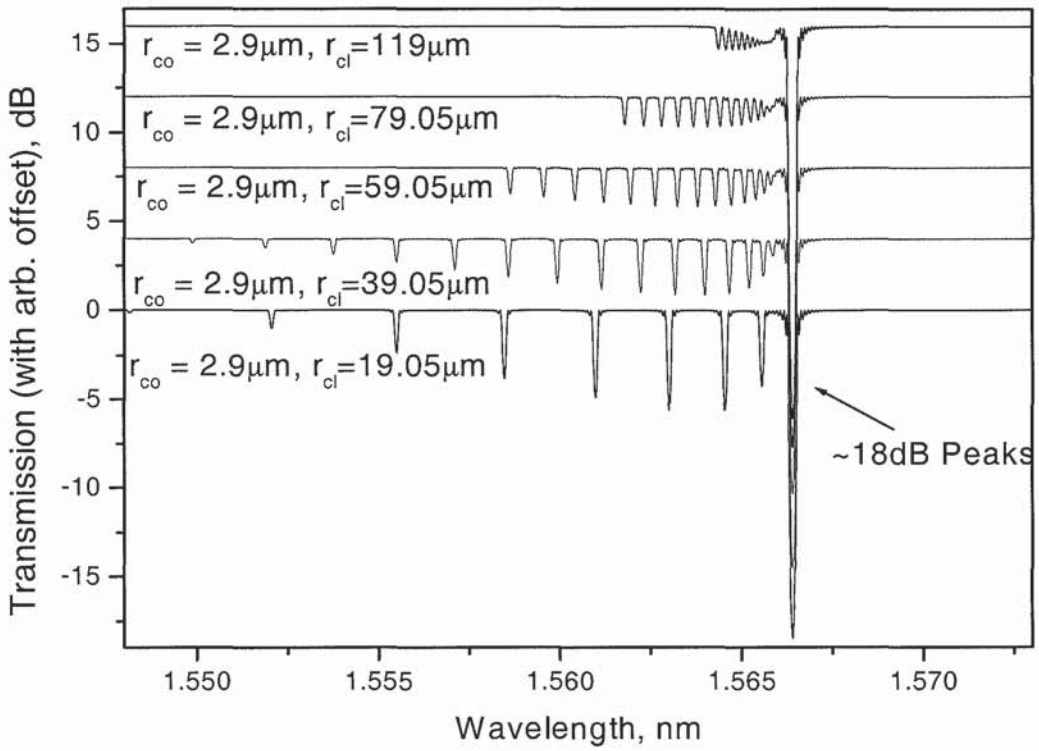

Fig. 6.7: Simulated results for the increase in the cladding radius (r_{cl} is the core radius, index modulation is $3x10^{-4}$)

In conclusion, simple and effective methods for suppressing of cladding-mode coupling loss have been demonstrated by simulation and experiment. For the experimental analysis, a standard SMF has been used so as to reduce fabrication costs. Another attractive advantage of the method is that it allows for reducing the splice- and insertion-losses in view of the fact the NA was increased only at the fibre section into which the FBG was inscribed.

Simulations were also carried out to establish the necessary parameters that need to be altered in order to suppress the cladding mode coupling loss. The simulations are useful for designing fibre type that may be relevant for achieving gratings with low cladding mode coupling loss. The proposed technique offers the prospects of the development of practical DWDM devices. In retrospect, it would have been useful to measure the exact value of the insertion loss for each device, which should help in assessing the practical applications of the devices.

6.3 LPG Filters

Recently there has been increasing interest in the application of loss filters that are based on LPGs within optical fibre systems. Such filters have the advantages of easy fabrication, low insertion loss, low level of back-reflection and compactness, and are ideal for gain equalising/flattening of EDFAs [212]. The ability to tune the wavelength of the grating loss peak allows for adaptive equalization of EDFAs. The principle of operation of this type of filter lies in its capability to route-out the unwanted signal from the fibre core into the cladding. Thus, the uneven EDFA peak can be levelled using these grating filters.

6.3.1 LPG-based tuneable loss filters

The tuning of LPG loss filters can offer a form of dynamic spectral control [213,214], enhancing the performance of gain equalising/flattening filters. However, the resonance of a typical fundamental mode of an LPG written in the standard SMF can only shift by 3-10nm for 100°C change in temperature [212]. This thermal tuning efficiency may not be sufficient for some applications. In this section, it will be shown that a second diffraction order[36] mode of an LPG offers the same order of tuneability as its corresponding resonance order fundamental mode. It is also shown that there is the possibility of generating efficient tuneable filters that can operate in each of the three main optical communications windows (i.e. 1.5, 1.3 and 0.8 μm).

In view of the work reported in refs. [214,215] where it was reported that the temperature responsivity of LPG could be enhanced significantly by recoating or partially cladding the fibre with special polymers to achieved highly tuneable loss filters, in this section, comparable tuneable LPG loss filters are demonstrated in the B/Ge co-doped fibre: a thermal induced spectral shift as large as 48nm has been achieved for a mode located in the 1500nm wavelength region using a relatively small temperature tuning range from 10°C to 40°C, demonstrating a super-high thermal tuning efficiency for LPG structures. In addition, it is

[36] For N = 2 in the phase-matching condition, eqn. 5.4, the modes generated are of the second harmonic order. In similarity with fundamental modes (i.e with N = 1), the high resonance order modes are more responsive to external perturbations in comparison to lower resonance order modes of any diffraction order, because they are positioned closer to the fibre surface.

also demonstrated that up to 9.4nm wavelength shift can be obtained in the 1300nm region for a temperature change of 35°C.

To demonstrate the spectral shifts of gratings inscribed in two different types of fibre with their spectral peaks moving in opposite direction under the influence of the same external perturbation, a set of LPGs with a periods of 240, 204 and 421μm were UV inscribed in a conventional B/Ge co-doped fibre without H_2-loading. Another grating with a period of 390μm was fabricated in the standard SMF, and after the UV exposure, the gratings were all annealed at 110°C for 48 hours to stabilise their optical properties. The measurement of the varying transmission profile of the grating was carried out using a broadband LED and an HP70004A OSA with a resolution of 0.1nm.

6.3.1.1 Tuneable loss filter in the 1500nm wavelength region.

The thermal tuning experiment from 10 to 80°C was implemented by using each of the LPGs in the way described in Subsection 4.6.2 and the corresponding spectral changes were recorded using the HP70004A OSA. It was noted that the resonant loss peaks shifted towards shorter wavelength as temperature increased, (see, for example, Fig. 6.8).

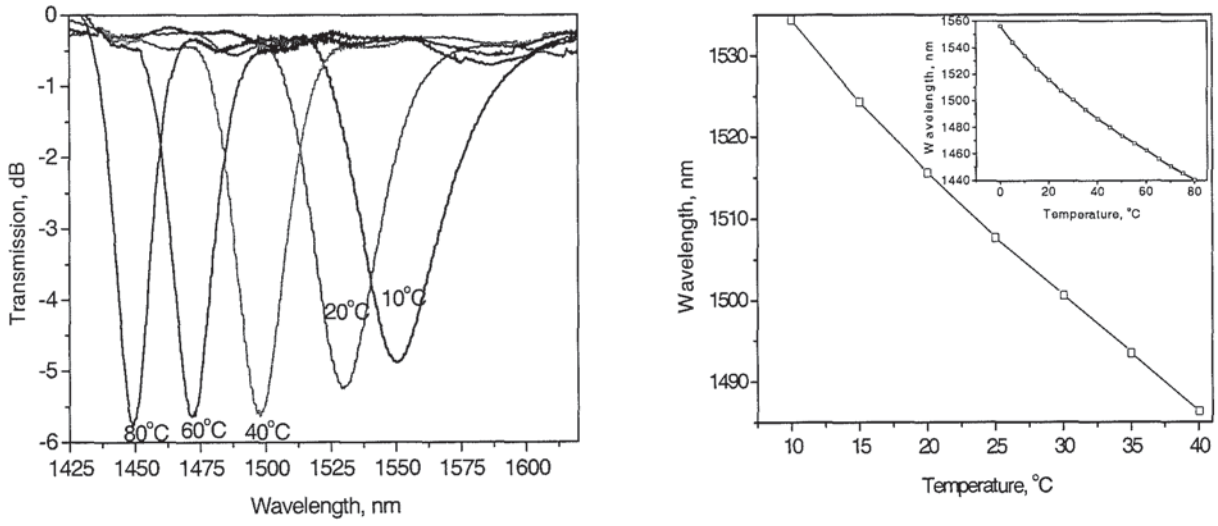

(a) (b)

Fig. 6.8: Variation of the resonance wavelength of transmission spectra of the tuneable filter at temperature between 0 ℃ and 80 ℃ (a) The spectral variation caused by the change in temperature, (b) plot of the spectral shift against temperature from 10 ℃ to 40 ℃. The inset is for temperature varying from 0 ℃ to 80 ℃

It can be seen in Fig. 6.8(a) that the resonant loss peak narrowed and deepened with temperature increase and –48.1nm resonant wavelength shift was obtained for only 30°C change in temperature, corresponding to a thermal tuning efficiency of 1.6nm/°C, which is fifteen times higher than that of the LPGs fabricated in the standard SMF [212], and twice that of the LPG recoated by the special polymer [214,215].

The wavelength shifts are plotted against temperatures in Fig. 6.8(b), showing a near-linear thermal response from 10°C to 40°C. However, when the grating was further heated up to 80°C thermal responsivity over the temperature range was slightly reduced and the overall response exhibited a slightly non-linear characteristic, as shown in the inset to Fig. 6.8(b).

6.3.1.2 Tuneable loss filter in the 1300nm wavelength region

Consider Fig. 6.9, which shows the temperature responses of the second diffraction order mode LP_{07} (i.e. $^2LP_{07}$) of LPG inscribed in B/Ge co-doped fibre with a period of 421μm. It can be seen that a large responsivity is demonstrated by the harmonic modes of the LPGs located in the 1300 nm region. In particular, this second diffraction order mode of the LPG shows responsivity to temperature of -269.11pm/°C, which is over 4 times that observed for the most responsive second diffraction order mode obtained in the LPG inscribed in a standard SMF. To corroborate this result, shown in Figs. 6.9(a) and (b), a grating with a period of 204 μm was tested. Figs. 6.9(c) and (d) demonstrate the results obtained with a grating having temperature responsivity of – 383pm/°C.

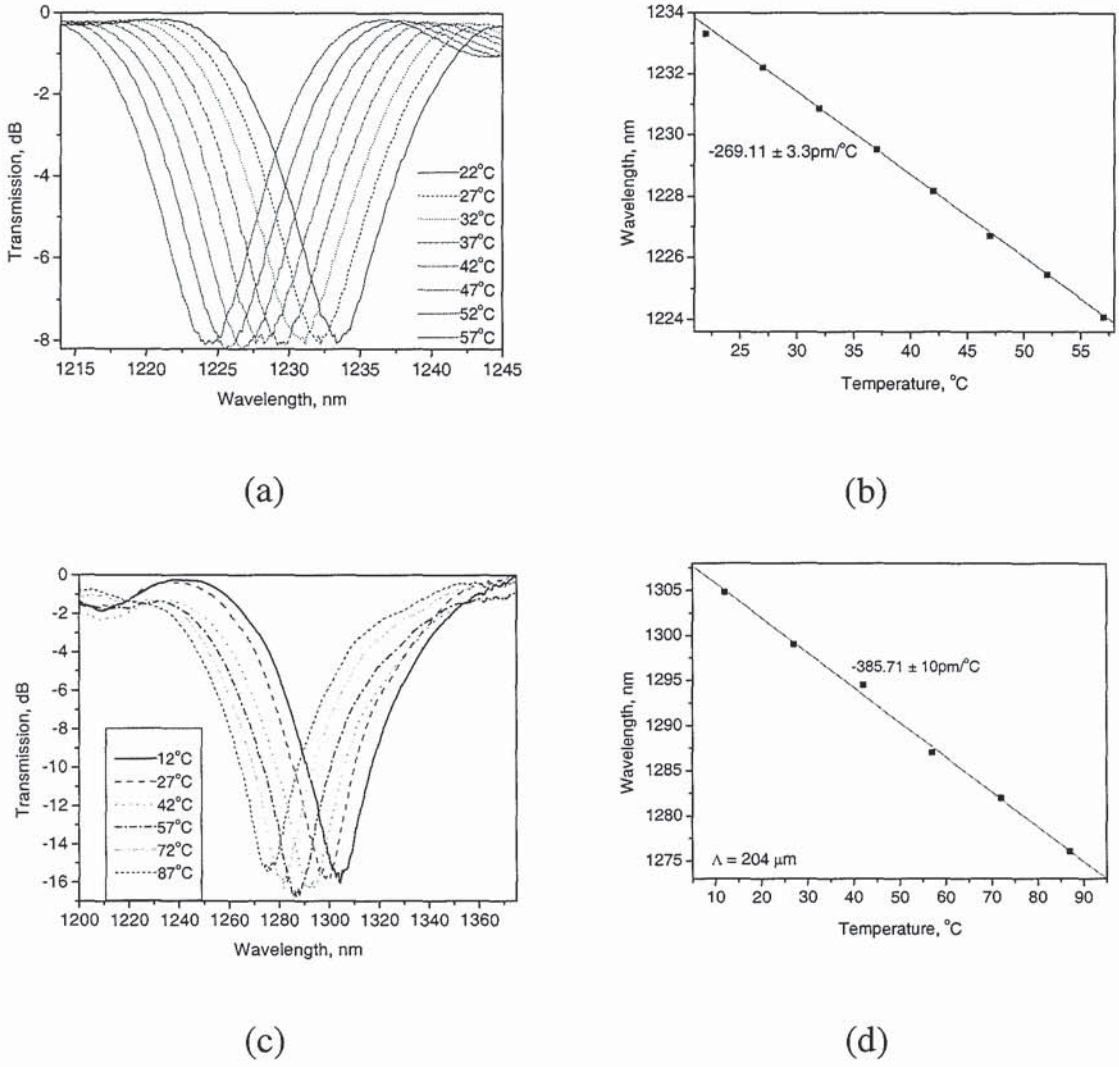

***Fig. 6.9:** (a) and (b) showing the temperature responses of the second diffraction order mode $^2LP_{07}$ of an LPG inscribed in B/Ge co-doped fibre with a period of 421 μm. (c) and (d) show the temperature responses of the fundamental mode $^1LP_{06}$ of an LPG inscribed in B/Ge co-doped fibre with a period of 204 μm.*

Clearly, the high thermal tuneability (~33.6GHz/°C) of mode $^2LP_{07}$ in B/Ge fibre (see Fig. 6.9(a)) indicates that a tuneable loss filter for use in the 1300nm wavelength region can be implemented. Indeed, for the right fibre dispersion properties, such second diffraction order modes can be obtained, in principle, at half the wavelength of the fundamental modes, thus, allowing a tuneable loss filter to be implemented in the visible wavelength region.

6.3.1.3 Positive slope in LPGs responsivity

It has been seen earlier in Subsections 6.2.1.1 and 6.3.1.2 that the slope of LPG-sensitivity to temperature that emerged was negative. In this subsection, it will be shown that such negative

slope is not always the case. It is demonstrated that whilst the low resonance order modes of LPGs made in B/Ge co-doped fibre shift to shorter wavelength with temperature increase, the corresponding modes of LPG in a standard SMF on the other hand shift to longer wavelengths.

To demonstrate the opposing trends in the shifts between LPGs inscribed in the standard SMF and those produced in B/Ge fibre, a standard SMF-based LPG with a period of 390 μm was produced. Figs. 6.10(a) and (b) show the responses of this LPG. Fig. 6.10(a) shows the spectral responses of the second diffraction order modes of the LPG to temperature in the wavelength range 960 to 1030nm for temperature changes from 22 to 57°C. The temperature

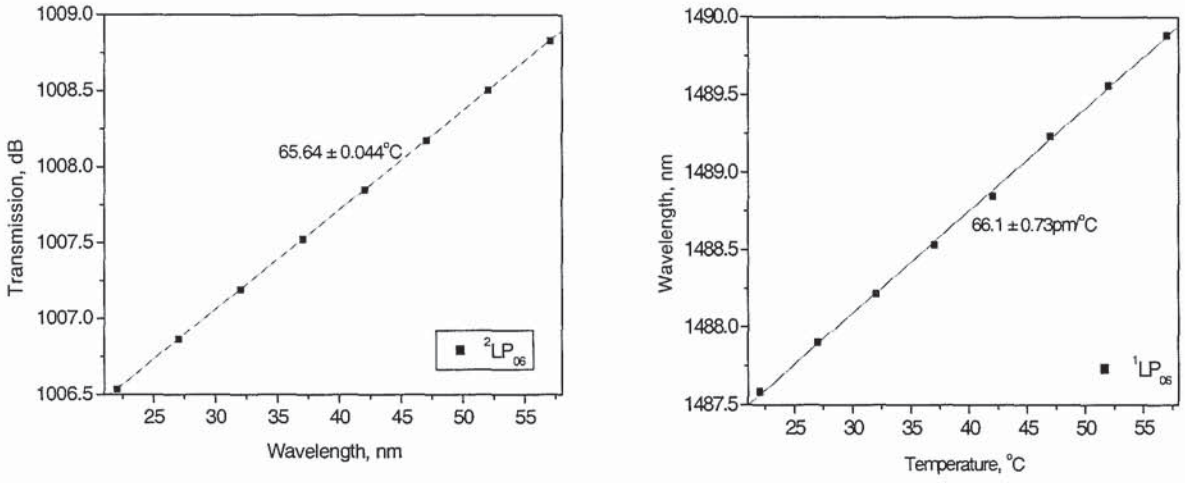

(a) **(b)**

Fig. 6.10: Temperature response of 2 modes of the LPG produced in standard SMF: (a) the plot of the wavelength shifts against temperature for the second diffraction order mode $^2LP_{06}$ in the wavelength region 960 to 1030nm, (b) for the fundamental mode $^1LP_{06}$

coefficient of the second diffraction order mode $^2LP_{06}$ of this LPG is evaluated to be 59pm/°C. Fig. 6.10(b) shows the response of the fundamental mode $^1LP_{06}$ of the same grating, which has a responsivity value of 61.6pm/°C. Clearly, the responsivity of these modes is of the same order. Also, both modes indicate a shift to the longer wavelength with temperature increase. Indeed, the results shown in Fig. 6.10 suggest that the slopes are positive for LPGs produced in the standard SMF. This is in line with earlier discussion given in Section 5.3 (using gamma plots of Fig. 5.17) where it was explained that because the temperature-induced shifts of LPG modes depends the sign of the product $\gamma \cdot \Gamma$. For standard

fibre, the product is positive up to the 9th mode where the sign reverses. The reversal of the sign indicates a wavelength shift in the opposite direction. Similarly for B/Ge fibre the product $\gamma \cdot \Gamma$ is negative up till the 10th mode, at which point, the sign reverses. It is therefore clear that for the same order of cladding modes in the B/Ge and standard fibre, the temperature induced shifting characteristic is opposite.

6.3.2 Effects of H_2 and OH loss-peaks

In Subsection 6.3.1, LPG-based loss filters have been discussed. In the study, a wide tuning range permitted by the HP70004A OSA was considered; it spans from 700 to 1700 nm. During the analysis two loss peaks were observed which have the potential to limit the performance of a tuneable loss filter. The peaks are located at 1245 and 1400nm wavelength regions. These peaks can distort the spectral response of LPGs that possess a coupled cladding mode that is located in the two regions or the fibre itself [216]. Therefore, it is of vital importance to study their properties with a view to avoid or eliminate them. To this end, the properties of both standard SMF and B/Ge co-doped fibres have been investigated to establish the loss contributions of both hydrogen and the UV-induced hydroxyl (OH) ions [217,218]. The loss is found to be more severe in B\Ge fibre as compared with standard SMF.

Contrary to the general belief that the loss peak at ~1400nm is always present in optical fibres, it has been noted that such a peak appears mainly in a long length of fibre [9] or short pieces of hydrogen-loaded fibres that are exposed to UV.

6.3.2.1 Effects of hydrogen loading in a standard SMF

Fig. 6.11 shows the spectral response of a standard fibre under different levels of H_2 and UV exposures. It can be seen that the loss peak at the wavelength of ~1245nm is clearly present in only pieces of fibre that are hydrogen-loaded and un-annealed [219]. When these pieces of fibre were annealed in an oven at 115°C for over 24hrs, however, this loss peak clearly disappeared –consistent with the established knowledge that annealing can remove residual H_2 in the fibre. The disappearance of this loss peak at 1245nm after annealing clearly suggests that this loss peak is hydrogen induced. It has also been found that for fibres that were stored in H_2-loading tube for 5 days, the strength of this loss peak is less than that of the

peak obtained in the fibre that received 10 days of H_2-loading in the same tube under the same conditions. Clearly this loss peak can be use to estimate the level of hydrogen remaining in a given piece of fibre. Indeed, since it is also known that presence of H_2 in a given piece of fibre can cause serious splicing loss, this loss peak at 1245nm can help to indicate whether or not a given piece of fibre is suitable or ready for fusion splicing.

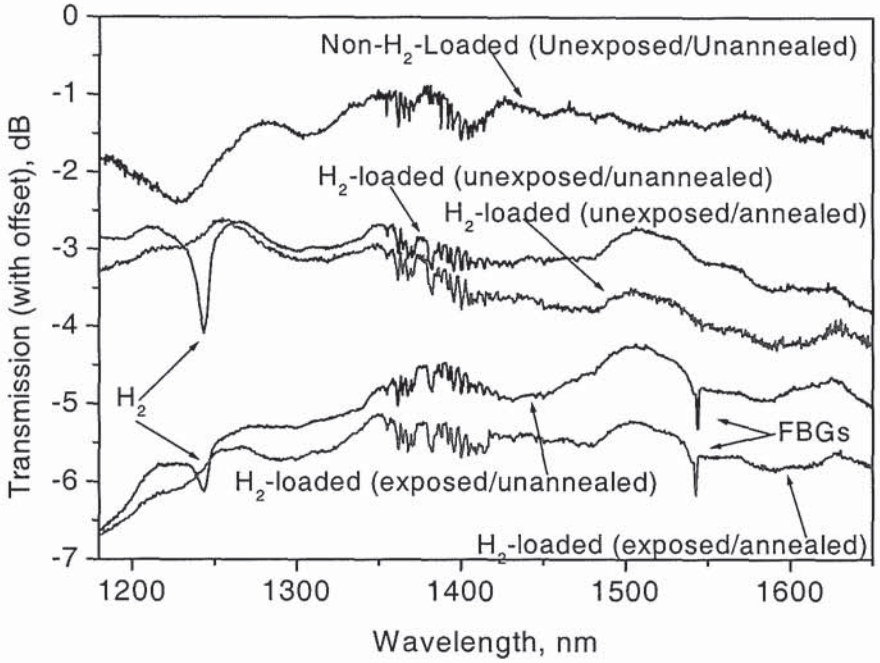

Fig. 6.11: The spectral response of a standard fibre under various conditions

It can be seen in Fig. 6.11 that a standard SMF, whether hydrogen-loaded or not, exhibits a rather weak loss peak at the wavelength of ~1400nm. The same condition also applies whether these fibres are UV exposed or not. The losses at this wavelength are such that they do not inhibit the use of standard SMF-based LPG devices.

6.3.2.2 Effects of hydrogen loading in B/Ge co-doped fibre

In Subsection 6.3.2.1, the effects of hydrogen loading in standard SMF fibre were studied. In a subsequent experiment, a B/Ge co-doped fibre was used to replicate the standard SMF-based experiment; the spectral response obtained for the fibre at different conditions are shown in Fig. 6.12: the response labelled (a) if for Non-H_2-loaded (unexposed/un-annealed)-, (b) for Non-H_2-loaded (unexposed/annealed)-, (c) for H_2-loaded (unexposed/un-annealed)-,

(d) for H_2-loaded (unexposed/annealed)-, (e) for H_2-loaded (exposed 25mm/un-annealed)-, (f) for H_2-loaded (exposed 25mm/annealed)-, (g) for H_2-loaded (exposed 45mm/annealed)-, and (h) for H_2-loaded (exposed 45mm/un-annealed)- fibres.

It can be seen that, in addition to the presence of hydrogen-related peak at the wavelength of ~1245nm there is another broad loss-peak at the wavelength of ~1400nm exhibited by all hydrogen-loaded fibres that are exposed to UV light[37]. This broad loss peak at 1400nm is generally attributed (but not limited) to the effect of hydroxyl ions (OH) formed during the UV exposure. Such broad loss-peak was observed to remain even after a prolonged annealing process (48hrs at 110°C) was carried out to remove residual hydrogen. Clearly, any LPG cladding mode that appear at this wavelength will be spectrally distorted and hence will not provide an efficient tuneable loss filter.

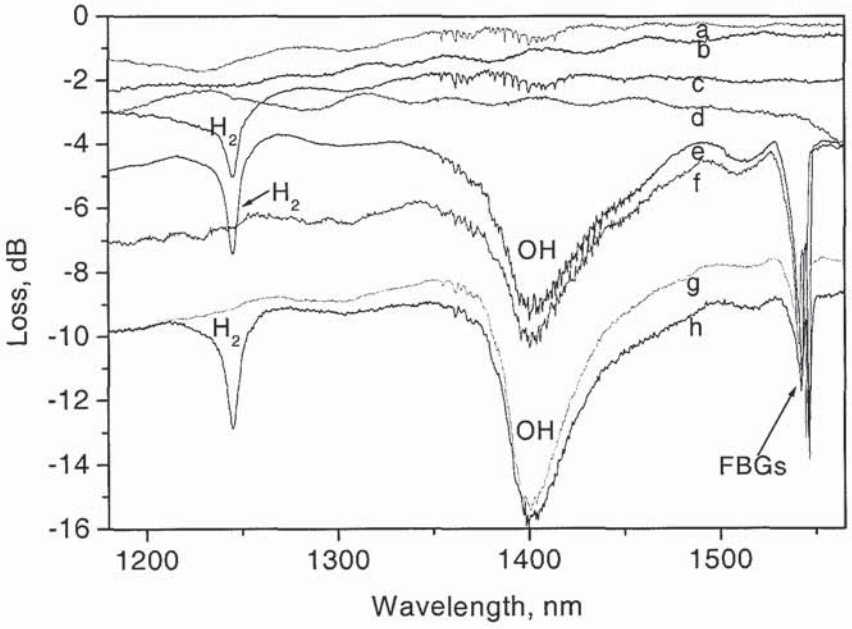

Fig. 6.12: (a) Non-H_2-loaded (unexposed/un-annealed), (b) Non-H_2-loaded (unexposed/annealed), (c) H_2-loaded (unexposed/un-annealed), (d) H_2-loaded (unexposed/annealed), (e) H_2-loaded (exposed 25mm/un-annealed), (f) H_2-loaded (exposed 25mm/annealed), (g) H_2-loaded (exposed 45mm/annealed), and (h) H_2-loaded (exposed 45mm/un-annealed).

[37] Those pieces that were not H_2-loaded did not exhibit such a strong peak both before and after UV exposure. The UV exposure was carried out by inducing an FBG with a central wavelength of ~ 1567nm in the given piece of fibre.

In line with what obtains in standard fibre, it has also been observed that the loss peak at the wavelength of ~1245nm exhibited by B/Ge fibre clearly disappears after annealing - indicating the near-total removal of the hydrogen.

To observe the smoothing effect of annealing, traces 'a' and 'b', shown in Fig. 6.12, can be compared. In addition, comparing traces 'c' with 'd', or 'e' with 'f', or 'g' with 'h' can reveal that the peak at 1245nm is H_2-induced; such a peak disappeared after the annealing process. To demonstrate that the loss peak at 1400nm is obtainable only in H_2-loaded fibres that are exposed to UV traces 'c-d' can be compared with 'e-h'. To support this analysis, Fig. 6.13 shows the comparison of the spectral responses of non-H_2 loaded B/Ge co-doped fibre that is unexposed/un-annealed (solid) with the exposed/un-annealed (dash). It can be seen clearly that even with UV exposure the broad loss peak at 1400nm was not observed in the short piece of fibre that is not H_2-loaded. This clearly suggest that even though H_2-loading can improve photosensitivity, if LPG is being produced for the purpose of tuneable loss filter, H_2-loading particularly in B/Ge fibre is not desirable.

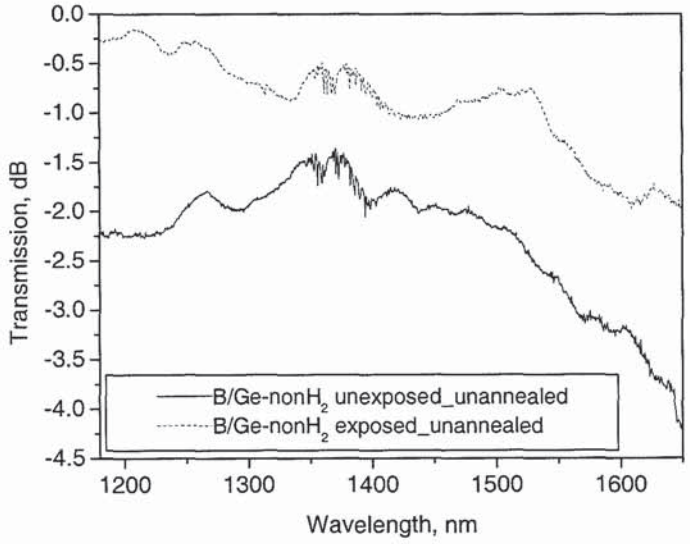

Fig. 6.13: (a) Non-H_2-loaded (unexposed/un-annealed) (b) Non-H_2-loaded (exposed/unannealed).

Traces 'f' and 'g' in Fig. 6.12 were obtained by making UV-induced FBGs of 25mm and 45mm length respectively using the same UV power. It can be seen by comparing these traces that exposure duration can also influence the strength of the broad loss peak at 1400nm; the longer the exposure the stronger the loss.

In view of the fact that the loss peak at 1400nm in standard fibre is not as strong as that obtained in the B/Ge fibre, it may be argued that this peak is not only related to OH but also to other ions emerging from UV-induced breaking of chemical bonds within the fibre. This phenomenon is yet to be clearly understood but it might be linked to the interaction of hydroxyl ions with Boron, Silicon and Germanium.

Using the results from these investigations it is clearly possible to use the same technique to verify whether or not a given piece of fibre contains hydrogen, and also to confirm the level of hydrogen present within the fibre. This should lead to efficient use of fibre for grating production (reducing guess work), and to the minimization of the overuse of hydrogen loading equipment. In addition, it can also permit the hydrogen loading equipment to be characterised. Furthermore, it should also minimise the damaged that may otherwise be caused to the grating containing fibre because of the unnecessarily long annealing process.

In summary, the behaviours of standard SMF and B\Ge co-doped fibres have been investigated to establish the contributions of both hydrogen and the UV-induced hydroxide (OH) ions to the emergence of loss peaks at 1245 and 1400nm. The loss, which manifest in the form of a transmission peak at the wavelength of 1400nm, is found to be more severe in B\Ge co-doped fibre than in a standard SMF, due to the formation of hydroxyl ions associated with both silica and boron. The loss peaks limit the use of UV-induced LPG for the implementation of tuneable loss filter. Techniques to avoid this spectral distortion effect have been clearly demonstrated.

6.4 SSFBG Filters

The generation and transmission of microwave/millimetre-wave sub-carrier signals using optical devices is highly desirable in applications such as multipoint video distribution systems, remote antenna links, millimetre-wave radio LANs, radio-on-fibre systems, and mobile communications [220]. To fully exploit the advantages of the fibre-optic microwave sub-carrier system signal processing needs to be performed while the signal is still in the optical modulated form. The optical microwave sub-carrier signal processing commonly is based on the principles of optical delay lines. In an intensity-modulation system using direct modulation or an external optical modulator, when two or more optical signals carrying

microwave sub-carrier modulated information meet incoherently at the photodetector, the resultant microwave sub-carrier response will be characterised by the delay between those optical signals and weighting between the adjacent optical signals. A number of different optical fibre delay line filters have been proposed and demonstrated using different optical fibre components [221,222,223,224]. More recently the development of FBGs has led to a new family of optical delay line filters for microwave sub-carrier signal processing [225,226,227,228,229,230,231,232,233,234]. The ability to control intensity and group delay characteristics of complex in-fibre Bragg grating devices make them ideal candidates for performing passive microwave sub-carrier signal processing in the optical domain.

In this section, the microwave sub-carrier related applications of SSFBGs in both transmission and reflection modes are considered. In particular, the work in this section was carried out principally to implement microwave sub-carrier filtering that does not suffer from coherence noise. Subsection 6.4.1 involves SSFBG operating in reflection mode to give transversal filter, and in Subsection 6.4.2, a compact bandpass filter that operate in transmission mode of the SSFBG is discussed.

6.4.1 Microwave sub-carrier transversal filter using SSFBG in reflection mode

Fibre grating techniques allow the fabrication of compact complex structures with precise position and amplitude profile control. It therefore offers a useful technique to produce optical delay line filters. In general, more optical taps in the delay line could generate bandpass response with a higher rejection level and Q factor[38] [232,235]. With these devices, positioning all the delay lines precisely to obtain a desired unit time delay is critical to the performance of the filter [235, 236]. In Yu et al's work [231] a bandpass filter was proposed using up to 29 fibre grating taps with a Kaiser window profiling, to give a 35dB out-of-band rejection. However, the achieved rejection level is far lower than theoretical prediction, as errors in the optical time delays between the adjacent taps generally reduce the achievable rejection level. Increasing the number of gratings increases the difficulty of this problem.

[38] Q-factor provides a measure of how selective the filter is, and in this case is dictated by the ratio of the width of the passband to the Free Spectral Range (FSR).

In this section, an investigation on a novel microwave sub-carrier on optical-wave transversal filter using a SSFBG in reflection mode is discussed. Microwave sub-carrier filtering is achieved using an SSFBG. The time delay of the optical taps is precisely controlled by the grating characteristics and fibre dispersion. A bandpass response with an electrical rejection level of >45dB is achieved, which, to the author's knowledge, is the highest rejection level achieved so far in passive optical delay line filter. The transversal filter in Subsection 6.4.1 relies on intensity addition, thus it is optically incoherent. In addition, the filter also relies on the use of low-coherent light source, the broadband source. Indeed most fibre-based microwave sub-carrier transversal filters are optically incoherent. On the other hand, all microwave sub-carrier filters whether optically coherent or otherwise need to be sub-carrier coherent for them to be able to produce sub-carrier responses.

6.4.1.1 The principle of delay line filters

In an intensity-modulated system using direct modulation or external optical modulator, optical delay line filtering is realised by incoherently summing of N optical signals with an optical path increment. A delay line filter is typically represented by the flow chart shown in Fig. 6.14. Z-transform is the standard tool for characterizing a delay-line.

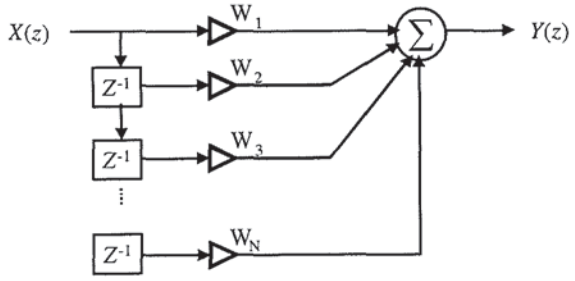

Fig. 6.14: The flow-chart of Transversal filter

For a filter with N optical fibre delay lines, the transfer function can be expressed with the z-transform as [237]:

$$H(z) = \frac{Y(z)}{X(z)} = \frac{1}{N}\sum_{k=1}^{N} w_k z^{-(k-1)} \tag{6.4}$$

where w_k is the weight and z^{-1} represent a unit delay associated with the length increment between adjacent delay lines ($z = e^{jw\tau_k}$). τ_k is the unit time delay in respect of the length increment, L_0, between delay lines, and it is defined by $\tau_k = \frac{nL_0}{c}$, where n is the refractive index of the fibre core, and c the light velocity in vacuum. A bandpass filtering is realised at the microwave sub-carrier frequencies defined by,

$$f_i = i\frac{c}{nL_0} \quad i = 0,1,2,... \tag{6.5}$$

where f_i is the modulation frequency. The microwave sub-carrier signals constructively add at these frequencies, thus a bandpass response can be achieved using N optical fibre delay lines. By setting the weight of the delay lines to different apodisation profiles sidelobe suppression can be realised.

6.4.1.2 SSFBG-based transversal filter

The SSFBG used for the transversal filter was fabricated by using a phase mask technique. During fabrication UV exposure was periodically sampled 25 times, onto the fibre through a phase mask in an on-off fashion with a 7.5% duty ratio, so a periodic refractive index change was induced over a fibre length of 50mm to form the SSFBG. After inscription the fibre containing the SSFBG was annealed at 105°C for 48 hours in an oven. The reflection spectrum of this experimentally obtained SSFBG is shown in Fig. 6.15.

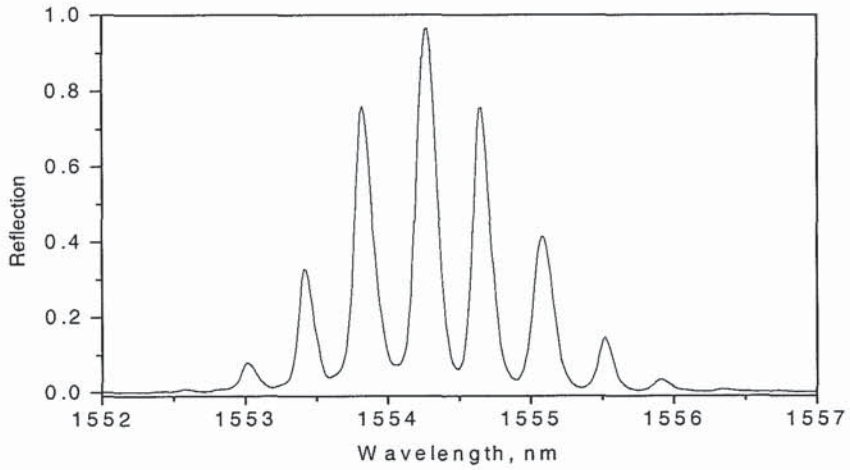

Fig. 6.15: experimental reflection spectrum of an SSFBG with an intrinsic-Gaussian-shaped envelope

If a reflected signal is launched into dispersive medium such as a chirp-Bragg grating or dispersive fibre, these peaks will experience differential time delays [238]. Such a device can thus generate a series of optical taps with a unit time delay determined by the product of the wavelength spacing $\Delta\lambda$ [239] and the dispersion introduced by the medium. All the taps will be precisely set without positioning error.

6.4.1.3 Experimental implementation of transversal filter

An experimental arrangement for measuring the microwave sub-carrier frequency response is shown in Fig. 6.16. A broadband light source (BBS) model 1550A from AFC-technologies was used to launch a beam through an optical fibre circulator onto the SSFBG as shown in the figure [235,236,240,241]. The reflected optical signal then is with an intensity profile as depicted in Fig. 6.15, where the wavelength spacing between the adjacent peaks is ~0.41nm. Coupled into an electro-optic modulator by which microwave sub-carrier signal is imposed onto the optical beam, the optical signal further travels through a 25km-long single mode fibre, and is detected and analysed using a Lightwave Components Analyser (LCA), giving the microwave sub-carrier response of the device. An EDFA is used to compensate for the insertion loss from the modulator and the fibre.

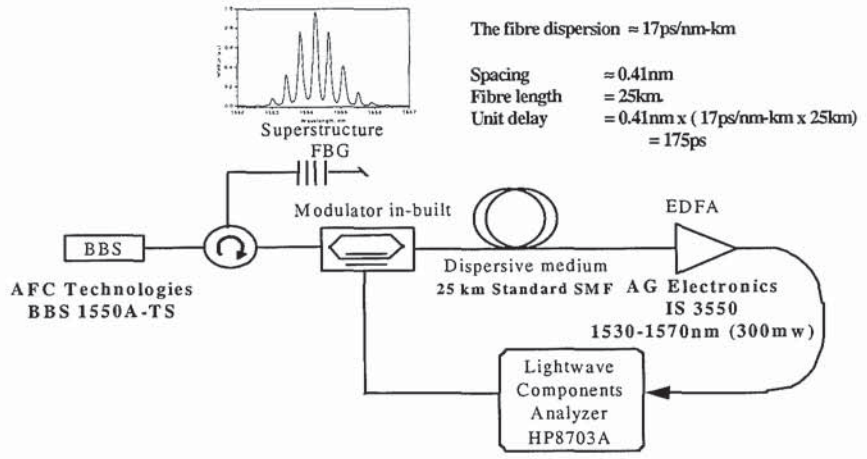

Fig. 6.16: Experimental arrangement for filter implementation

An experimentally measured microwave sub-carrier response is shown as solid trace 'iii' in Fig. 6.17. It gives a bandpass response with free spectral range (FSR[39]) of around 5.8GHz,

[39] In filters a large value of FSR improves selectivity and reduces the chances of inter-symbol interference (cross-talk).

corresponding to a unit time delay of τ_k=175ps, which is exactly the product[40] of the wavelength spacing between the Bragg peaks of the SSFBG and the fibre dispersion at around 1550nm. The available noise rejection level is greater than 45dB, which was the highest rejection level reported in passive optical delay line filter. The measured rejection level is very close to the theoretical prediction shown as a solid trace 'i' in Fig. 6.17: this agreement is attributed to the precise tap positioning achieved using an SSFBG and a dispersive fibre. It is however noted that, as with all filters having positive coefficients, the range of transfer function is limited; in this case, square shaped microwave sub-carrier passbands with flat top are not achievable because there are no SSFBGs with sinc-profiles on the overall optical envelope (i.e. giving negative weights) [242,243].

Since the grating length is limited and no apodisation profile is imposed on the low frequency index modulation, the spectral reflectivity profile of the SSFBG therefore shows a Gaussian rather than a flat-top (sinc-sampled) profile [244]. There is therefore an intrinsic apodisation effect to the weights of the optical taps. The intrinsic apodisation of the reflectivity profile greatly reduces the sidelobe level in the bandpass filter and thus increases the rejection level [232,233]. A simulated bandpass response of a filter with 11 optical taps of equal weights is shown as the dotted trace 'iv' in Fig. 6.17, which indicates a sidelobe rejection level less than 13dB. Meanwhile the simulated bandpass filter of 11 taps with Gaussian weighting profile as shown by the solid trace 'i' in the figure produces a rejection level of 50dB which is the equivalent of 25dB in optical domain.

[40] The fibre dispersion = 17ps/nm-km, $\Delta\lambda \approx 0.41$nm, and Fibre length = 25km. Therefore τ_k = 0.41nm x (17ps/nm-km x 25km) = 175ps

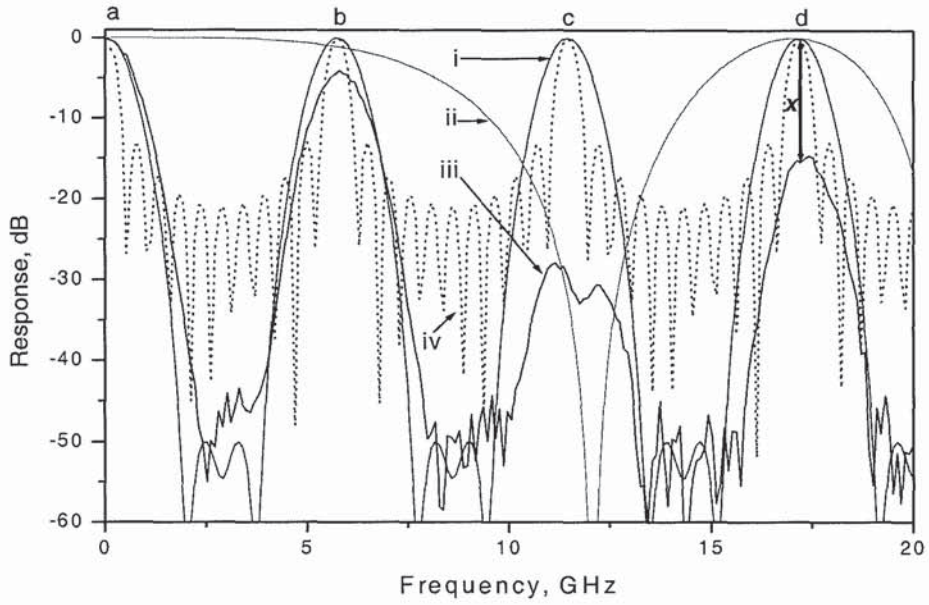

Fig. 6.17: Simulated and measured microwave sub-carrier responses of an SSFBG-based transversal filter, and a singlemode fibre: 'i' and 'iv' (dotted) are the simulated responses of SSFBG-based filter of 11 taps with gaussian, and flat-top (equal weights) profile respectively, 'iii' is the response measured experimentally for a filter of 11 taps based on SSFBG with the profile shown in Fig. 6.15, 'ii' is the response of a 25-km long singlemode fibre.

By comparing traces 'i' and 'iii', it can be seen that in the experimental result (trace 'iii') the maximum noise rejection level is slightly lower than that obtained by simulation (trace 'i'). This is because the amplitudes of reflected peaks from the SSFBG are not symmetrically distributed around the centre of the Gaussian-shaped reflectivity envelope as earlier shown in Fig. 6.15. This, however, can be improved through the grating fabrication process.

6.4.1.4 The effect of dispersive element

The implementation of microwave sub-carrier filter using "spectral splicing" method relies on using a dispersive element to provide the basic time delay between each spectral splice (tap). In delay-line filters, signals experiencing different time delays are usually added together at the photo-detector. One of the basic methods to achieve delay effect on signals is by interfacing a dispersive element such as standard SMF at 1500nm or a chirp-FBG on the signals' path. If a Chirp-FBG or a length of dispersive fibre is used to introduce time delay along a path of intensity modulated light beam, the magnitude of the light signal associated with dispersion is expressed as [245]

$$i_1 \propto \cos^2(\phi_d)\exp[j(\omega t + \phi_1)] \tag{6.6}$$

Where ω represents the modulating angular frequency, ϕ_1 is the phase shifts associated with the travelled optical length. ϕ_d is the phase characterizing the chirped grating- or standard SMF- induced dispersion, given by [245]

$$\phi_d = \pi c D (\frac{\omega}{\omega_0})^2 \tag{6.7}$$

Where, c is the speed of light in a vacuum, D the dispersion of the grating or the fibre, and ω_o the light frequency. Then the resultant optical power at the modulating frequency has a form [245]

$$P_\omega \propto \left|\cos^2(\phi_d)\{\exp(-j\phi_1) + \exp(-j\phi_2) + \ldots\ldots + \exp(-j\phi_n)\}\right| \tag{6.8}$$

Where ϕ_n is the phase shifts associated with the nth optical path length. Here the magnitude of the resultant signal depends not only on the time-delay between the optical taps, but also on the induced dispersion.

Fig. 6.18 shows simulated responses of intensity-modulated signals passing through two pieces of different fibres having a dispersion of 17 and 15 ps/nm-km. The length of each piece is 100km. A series of notches can be seen at different frequencies. These notches are related to dispersion introduced by the medium. Clearly, by changing the length of the fibre (which is similar to changing the amount of dispersion or time-delay experienced by the signal within the fibre) the positions of the dispersion notches can be altered. This dispersion effect causes power degradation at certain frequencies when a fixed length of fibre link is used, alternatively a similar effect can be generated using a fixed operating frequency but different lengths of fibre.

The negative-effect of the dispersive element can be seen in the proposed transversal filter in Fig. 6.17. It is noted that some of the experimentally measured passband levels clearly are lower than expected (see, for e.g., bands 'b', 'c', and 'd' of trace 'iii' in Fig. 6.17). The degradation is mainly caused by the fibre dispersion effect as described above and that the fibre or chirped grating dispersion does introduce power degradation to optical fibre microwave sub-carrier link [238,246]. The optical signals in the proposed filter suffer this

degradation as seen on passband 'b' and more severely on passband 'c'. A simulated response of a 25km fibre link is shown as the solid trace 'ii' in Fig.6.17, from which it can be

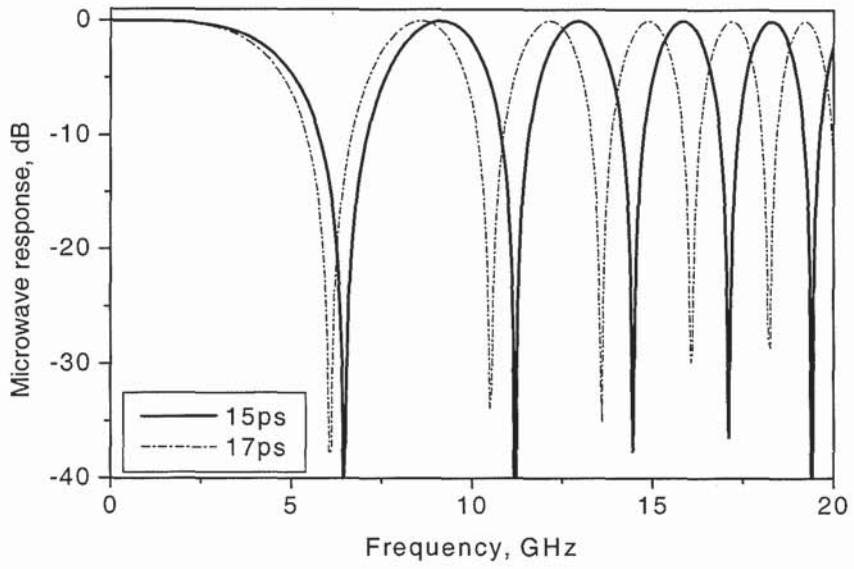

Fig. 6.18: Dispersion notches obtained by simulation in 100km length of dispersive fibre; the solid trace is for the fibre with a dispersion of 15ps/nm-km, the dashed trace is for the type with 17ps/nm-km.

seen that the fibre dispersion is the main effect responsible for the degradation of the experimentally obtained passband 'c' of Fig. 6.17 centred at 11.6GHz. A number of techniques are suggested to mitigate the effects [247,248]. The degradation level of the last passband 'd', which is seen in the experimental result marked as 'x' is mainly caused by the source spectral bandwidth noise effect, which introduces additional power degradation in optical fibre link that supports microwave sub-carrier [249]. It has been established that narrow bandwidth or less noise on grating reflection peaks generally leads to smaller amount of distortion.

In summary, a novel microwave sub-carrier transversal filter using an SSFBG is proposed and has been demonstrated in this section. Electrical rejection level larger than 45dB has been achieved due to the error-free positioning of optical taps in the filter. Since the weighting profile is determined by grating reflection profile, higher rejection level can be expected by achieving proper weighting function through grating fabrication.

6.4.2 Microwave sub-carrier band-pass filter using SBFG in transmission mode

In the last subsection the use of SSFBG in reflection mode to achieve a microwave sub-carrier filter has been discussed. In this subsection the use of such type of grating in transmission mode to achieve another form of microwave sub-carrier filter is considered. In microwave sub-carrier system, optical signal is often double-sideband modulated with microwave/millimetre wave sub-carrier basebands.

If the carrier wavelength of the optical signal locates within a spectral reflection peak or between spectral transmission peaks of a multiple-peak SSFBG, then passing through the grating will affect not only the optical carrier, but also the two sidebands, which are associated with the microwave sub-carrier modulation. Therefore, a certain microwave sub-carrier filtering function can be applied to the double sideband modulated optical signal by the grating.

Fibre grating fabrication techniques allow the compact structure of complex devices to be produced on a short piece of fibre, therefore, the controllable and stable True Time Delays (TTDs) are applicable in such configurations. In this section a second microwave sub-carrier filtering response of an SSFBG is investigated. Bandpass response is achieved while grating operates, this time, in transmission mode. Compact microwave sub-carrier filter with large FSR and immunity to optical coherence noise is realised.

6.4.2.1 The design of SSFBG used for microwave sub-carrier filter

The design of grating with the required spectral profile was carried out by simulation. Different spectral responses can be obtained with a defined shape of spectral profile and spacing between Bragg peaks. For a good microwave sub-carrier response the design should also aim to provide SSFBG peaks with reasonably smooth tops.

Fig. 6.19(a) shows the simulated reflection spectrum of a dense-channel SSFBG made with rectangular index modulation having a length of 5cm, four UV samples, and sample duty ratio of 7.5%. Fig. 6.19(b) shows the experimental version of the SSFBG of Fig. 6.19(a),

which was fabricated using 244nm UV-laser scanned on a fibre through a phase mask. It is clear from the two figures that there is a very good match between the theoretical prediction and the experimental implementation. Clearly, the fabrication technique allows for flexible realization of the desired grating spectral response.

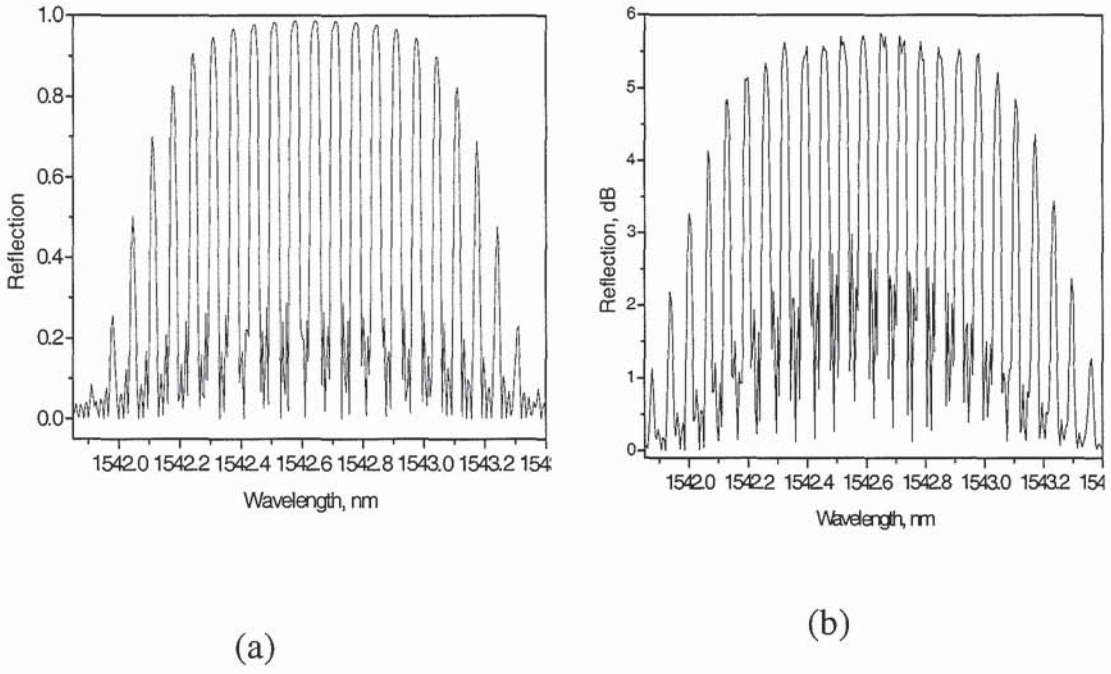

(a) (b)

Fig. 6.19: The spectral response of a dense-channel 50mm long SSFBG made with 4 samples and 7.5% duty ratio of the slow index modulation (a) simulation, (b) experiment

6.4.2.2 Experimental implementation and results

In the experiments, two SSFBGs were investigated, first individually, and then connected in series. Both of the SSFBGs have the same parameters but different strengths. This gives rise to two gratings with the same passband spacing but different stop-band levels as seen in Figs. 6.20 (a) and (b). The optical transmission spectra of SSFBG1 and SSFBG2 are shown in Figs. 6.20(a) and (b) respectively, each with passband spacing, $\Delta\lambda$, of about 0.066nm.

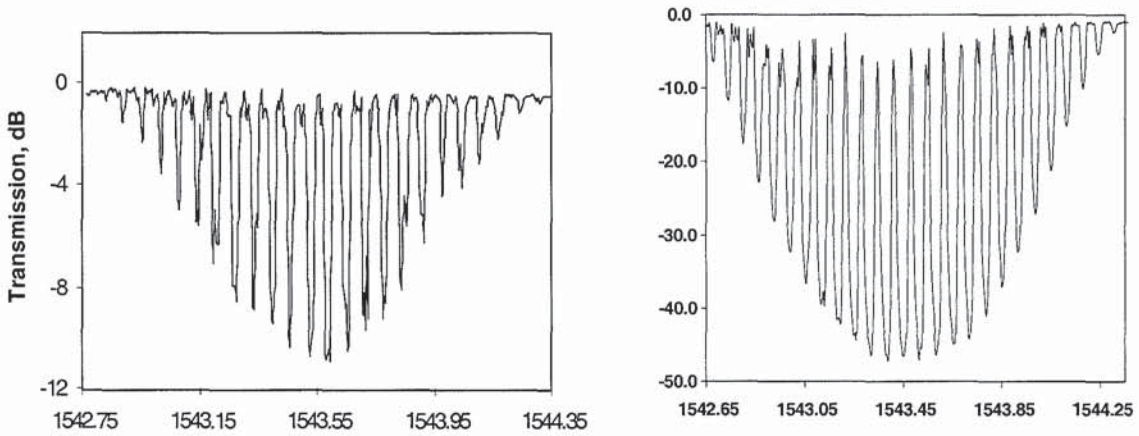

Fig. 6.20: Optical experimental transmission spectra of two SSFBG with one exhibiting ~11dB and the other ~48dB

The experimental arrangement for measuring the microwave sub-carrier frequency response of these SSFBGs is shown in Figs. 6.21(a) and (b). The microwave sub-carrier response of SSFBG1 was first investigated. A tuneable laser was used to launch a beam into an electro-optic modulator by which a microwave sub-carrier signal is imposed onto the optical beam. Then, the modulated optical signal was coupled into the grating. The carrier signal was positioned in the centrally located passband, ensuring the sidebands are positioned in the adjacent passbands on both left and the right hand side of the central passband. High frequency components are then positioned in the remaining passbands. If there is a carrier then the double sidebands will beat with the carrier to produce a sub-carrier response. The sidebands will also beat with other sidebands to produce sub-carrier response of higher frequency[41]. The cascaded SSFBG passbands are align so that the transmission strength will add-up to produce larger out of band rejection. The Isolator between the SSFBGs prevents beating of the optical signal that may lead to Fabry-Perot effect.

The output from the gratings is detected and analysed using a Lightwave Components Analyser (LCA), giving the microwave sub-carrier responses of the gratings. Fig. 6.21 (a) shows the experimental set-up used to investigate the response of the SSFBGs individually

[41] Sub-carrier response of resulting from the beating of the sidebands is beyond the scope of this discussion.

and Fig. 6.21(b) illustrates the experimental set-up used to measure the response of the two SSFBGs connected in series.

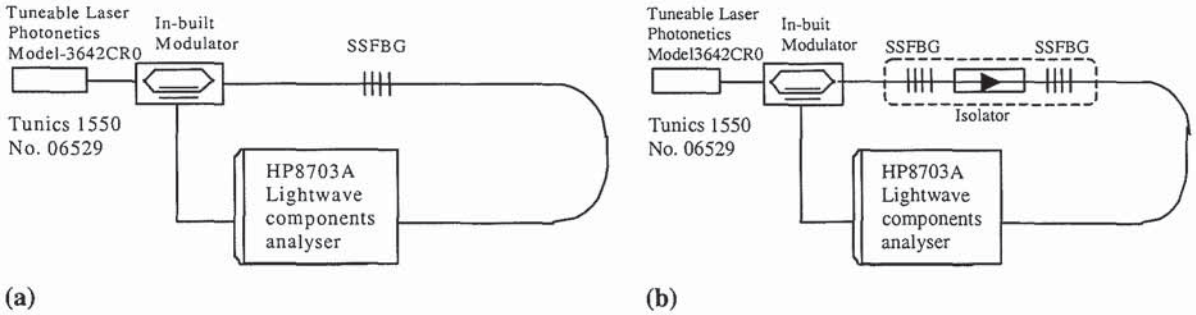

Fig. 6.21: Experimental set-up for measuring the microwave sub-carrier response of: (a) individual SSFBGs, (b) serially connected SSFBGs

The measured frequency response of SSFBG1 is shown as trace 1 in Fig. 6.22. As indicated by the optical spectrum, a bandpass frequency response is obtained from the transmission of the superstructure and an FSR of 8.3GHz is achieved. The frequency response of SSFBG2 when measured individually is also shown as trace 2 in the figure. Clearly, both gratings show a bandpass response with the same FSR.

For SSFBG1, a flat top response is obtained and the stopband rejection level is ~ –10dB. For SSFBG2, a much higher rejection level (~ -30dB) is achieved, and steep rising and falling edges of the passband is obtained. However, the top of the passband is noisy. This arises from the periodic refractive index modulation of the grating, which produces high order harmonics, and deteriorates the passband performance of the grating. Larger index change results in the larger harmonic components. For a practical bandpass filter, flat passband top, steep rising and falling edges and high rejection level are desired. To achieve this the high order harmonics must be suppressed. This can be improved by using appropriate apodisation technique.

After the study of the microwave sub-carrier responses of the two SSFBGs individually, a cascaded configuration was investigated in which the two gratings were connected in series, as shown in Fig. 6.21(b). A fibre isolator was placed between the two gratings to remove the effect of reflections. In view of the slightly different spectral positions of the grating peaks

for the two SSFBGs, strain was used to align the spectra such that the spectral location of each of the passbands of one SSFBG overlap that of the other.

A frequency response for the series arrangement is obtained and is shown as trace 3 in Fig. 6.22. Comparing trace 3 with trace 2, it can be seen that the benefits from the individual spectra of the SSFBGs are combined in trace 3 which shows improvement in the flatness of the top of the passband, while keeping the rejection level still around –30dB.

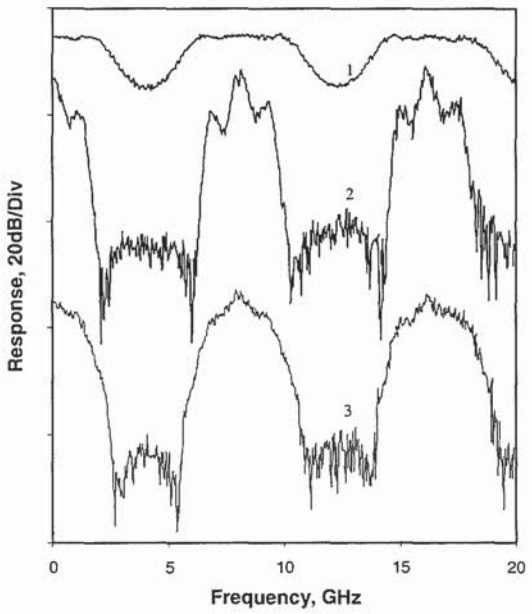

Fig. 6.22: Experimentally measured microwave sub-carrier frequency responses

To summarise, Section 6.4.2 investigated the microwave sub-carrier filtering responses of SSFBGs arranged in transmission mode and the results obtained were discussed. Positioning of the optical carrier in the middle of the passband is critical to this filtering method. However, in view of the noisy nature of the grating peaks, as seen in Fig. 6.20, the positioning of the carrier in the passband becomes particularly difficult. It is, however, anticipated that by using a sinc-sampled FBG [244] the difficulty can be mitigated and an improved performance of the filter can be expected.

It should be pointed out that the microwave sub-carrier bandpass filter demonstrated in Subsection 6.4.2 operates by exploiting optical coherence. The main feature that differentiates it from most microwave sub-carrier filters is that it relies on the addition of

fields rather than intensity, and because it works on the basis of optical coherence it is thus wavelength dependent. The operating wavelength must be located in the centre of one of the passbands due to the characteristics of dual sideband modulation of optical signal. In obtaining the result shown in Fig. 6.22 the line-width of the tuneable laser used was ~100kHz, which suggests a high optical coherence. However, large FSRs have been realised without suffering coherent noise due to its compact structure and direct filtering. It is also easy to cover the frequency range up to terahertz for microwave sub-carrier system as the corresponding SSFBG bandwidth can be readily obtained. Another attractive advantage is that the filter discussed requires no fibre couplers or circulators. Thus it is viewed as a cost-effective filter configuration.

6.4.3 DWDM optical filter

Over the last few years, optical devices that can increase transmission capacity of optical communication links have attracted so much attention with much research focusing on production of Arrayed Waveguide Gratings (AWGs) for use in DWDM systems [250,251,252]. DWDM systems allow for assigning optical signal to specific frequencies within a given frequency band. AWG-based devices have been shown to offer a more than 1000 optical WDM channels [252,253]. In FBG technology, however, up to 16 channels have been experimentally demonstrated in a single sinc-sampled FBG with flat-top characteristics [244]. In this section, it is shown that >16 channels with reasonably flat reflection peaks can be experimentally obtained from a single sinc-sampled FBG.

6.4.3.1 DWDM filter: Simulation results

A typical spectrum of a sinc-sampled FBG obtained by simulation is shown in Fig. 6.23. In this grating, all reflection peaks are of equal strength, have near flat-top and are of equal wavelength spacing, indicating the potential of the device to offer a compact DWDM filter. By changing the index modulation parameters in eqn. (4.11) different spectral profiles can be obtained.

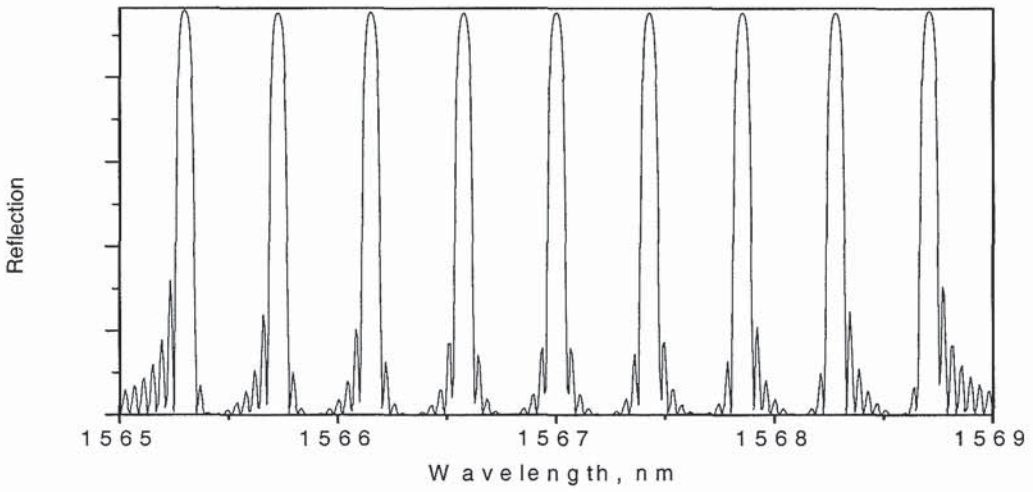

Fig. 6.23: Simulated optical reflection spectrum of a 9 channel sinc-sampled FBG

6.4.3.2 DWDM filter: Experimental results

The author has successfully designed and fabricated a number of sinc-sampled FBG with reasonably flat-top envelope. A typical 5 cm long sinc-sampled FBG fabricated with dense channels is shown in Fig. 6.24. The spectral response of this grating suggests that there is increased potential for FBGs to be used in DWDM systems.

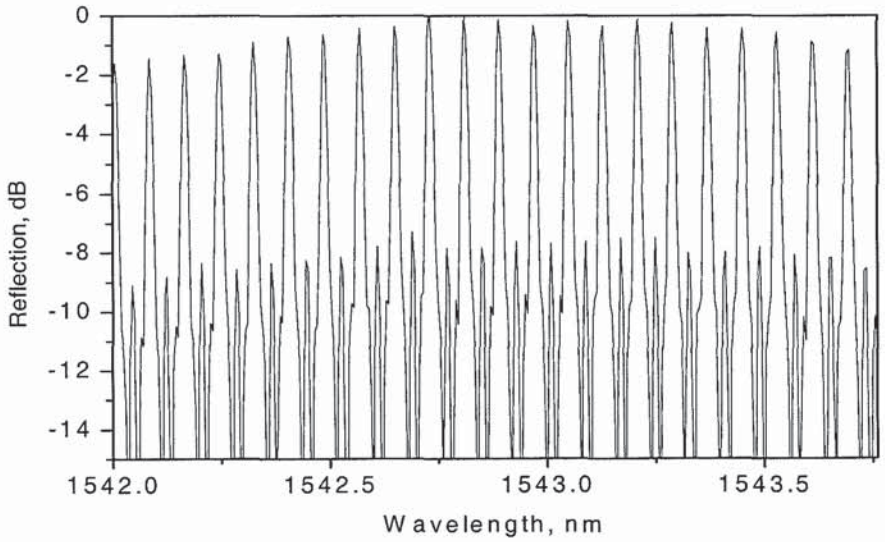

Fig. 6.24: Reflection spectrum of an experimentally obtained dense channel sinc-sampled FBG

Different FSRs, corresponding to different wavelength spacing, can be obtained, also, by changing the number of the UV samples. The width of the passband is determined by the sample duty ratio and sinc-sampled FBG period. Further work needs to focus on (a) improving the spectral characteristics and the rejection levels of the sinc-sampled FBG from ~8dB to ≥ 25dB to make it practically attractive, as well as (b) investigation on the use of the filter for multiple channel dispersion compensation. Clearly, this work has demonstrated an additional potential of fibre grating technology that can be exploited for use in high-capacity telecommunication systems. However, in comparison to AWGs, the performance of this SSFBG-based filter is far less attractive: the number of channels achieved so far are fewer and the out of band rejection is significantly lower than that of current AWGs (≥ 15dB difference). Nevertheless this work has demonstrated further improvement to the SSFBG technology.

In conclusion, three SSFBG filter arrangements that have numerous advantages have been proposed in this section and are implemented with attractive results. The first filter, which is a transversal filter, was implemented by using an SSFBG in reflection mode. The second arrangement focused on the use of a single as well as a cascade of two SSFBGs in transmission mode to achieve a bandpass filter. Significantly high microwave sub-carrier rejection levels of >45dB was obtained for the transversal filter and ~30dB was achieved for the bandpass transmission arrangement. The third filter demonstrated allows for multiplexing optical signals into 22 different channels. This indicates the attractive potentials of fibre grating technology for use in advanced DWDM systems. However in comparison to AWGs

For the transversal filter, further work can focus on improving the apodisation profiles of the SSFBGs. For the bandpass filter operating in transmission mode and the DWDM filter, it is necessary to investigate further into the ways by which smooth tops of pass bands can be obtained in the sinc-sampled FBGs.

6.5 Conclusion

In this chapter, fibre grating-based devices and systems for use in the area of telecommunications have been discussed. In particular, the application of filters based on FBGs, LPGs and SSFBG in optical and microwave domains has been demonstrated.

FBG filters achieved by the suppression of cladding-mode coupling loss have been shown to suppress the loss down to 0.2dB in an 18dB FBG. In addition, the simulation results suggest that there are a number of ways through which cladding modes can be minimised.

Using LPG, efficient loss filters have been demonstrated in both 1300nm and 1500nm regions. In the 1300 and 1500nm regions, respective tuning efficiencies of up to ~0.4 and ~1.6nm/°C has been demonstrated in LPGs fabricated in B/Ge co-doped fibre. In view of the limitations imposed by the interfering OH-induced perturbation-independent loss peaks at 1245nm and 1400nm on this type of filter, a technique has been demonstrated to mitigate such effects.

The use of SSFBG has been demonstrated to achieve two types of microwave sub-carrier filter. The first filter which is a bandpass transversal type provides a rejection level > 45 dB and the second filter, a bandpass transmission-based type, provides a rejection level >30 dB.

Finally, SSFBG has also been demonstrated to achieve >22 channels for use in DWDM applications with potential use for multiple-channel dispersion compensation. Many ways to advance the work presented in this chapter have been highlighted.

6.6 References:

203. T. Taru, S. Ishikawa, and A. Inoue, "Suppression of Cladding-Mode Coupling Loss in Fibre Bragg Grating by Precise Control of Photosensitive Profiles in an Optical Fibre," *Proc. Optical Amplifiers and their Applications and Bragg Gratings, Photosensitivity, and Poling in Glass Waveguides*, Stressa, Italy, Paper BThC11, 4-6th July 2001.

204. J.M. Kim, K. Oh, T.S. Park, C.S. Kim, and K. Jeong, "Suppression of Cladding-Mode Coupling Loss in Fibre Bragg Gratings by Independent Control of Refractive Index and Photosensitive Profiles in a Single-Mode Optical Fibre," *IEEE Photon. Technol.* Lett., vol. 12, no. 11, pp. 1504-1506, Nov 2000.

205. T. Komukai, and M. Nakazawa, "Efficient Fibre Gratings Formed on High NA Dispersion-shifted Fibres," *Proc. ECOC'95*, Brussels, vol. 1, pp. 31-34, Sept 1995

206. M.O. Berendt, A. Bjarklev, L. Gruner-Nielsen, C.E. Soccolich, "Reduction of Bragg grating-induced coupling to cladding modes," *Fibre and Integrated Optics*, vol. 18, no. 4, pp. 255-272, 1999.

207. L. Dong, L. Reekie, J.L. Cruz, J.E. Caplen, J.P. de Sandro, and D.N. Payne, "Optical Fibres with Depressed Claddings for Suppression of Coupling into Cladding Modes in Fibre Bragg Gratings," *IEEE Photon. Technol. Lett.*, vol. 9, no. 1, pp. 64-66, Jan 1997

208. L. Dong, G.Q.M. Marro, V. Bhatia, L.L. Hepburn, M. Swan, A. Collier, and D.L. Weidman, "Suppression of coupling loss in fibre Bragg gratings," *Jn. Lightwave Technol.,* vol. 18, no. 11, pp. 1583-1590, 2000.

209. T. Poulsen, M.O. Berendt, A. Bjarklev, L. Grüner-Nielsen, and C.E. Soccolich, "Bragg grating induced cladding mode coupling caused by ultra-violet light absorption," *Electron. Lett.*, vol. 34, no. 10, pp. 1007-1009, May 1998.

210. W.W. Morey, G. Meltz, J.D. Love, and S.J. Hewlett, "Mode-coupling characteristics of UV-written Bragg gratings in depressed-cladding fibre," *Electron. Lett.*, vol. 30, no. 9, pp. 731-732, April 1994.

211. J. Canning, M. Aslund, and P-F. Hu, "Ultraviolet-induced absorption losses in hydrogen-loaded optical fibres and in presensitized optical fibres," *Opt. Lett.*, vol. 25, no. 22, pp. 1621-1623, Nov. 2000.

212 . A.M. Vengsarkar, P.J. Lemaire, J.B. Judkins, V. Bhatia, T. Erdogan, and J.E. Sipe, "Long-period fibre gratings as band-rejection filters," *Jn. Lightwave Technol.*, vol. 14 no. 1, pp. 58-64, 1996.

213. D.M. Costantini, C.A.P. Muller, S.A. Vasiliev, H.G. Limberger, and R.P. Salthe, "Tuneable loss filter based on metal-coated long-period fibre grating," *IEEE Photon. Technol. Lett.*, 1999, vol. 11, no. 11, pp. 1458-1460.

214. A.A. Abramov, A. Hale, R.S. Windeler, and T.A. Strasser, "Widely tuneable long-period fibre gratings," *Electron. Lett.*, 1999, vol. 35, no. 1, pp. 81-82.

215. C.G. Atherton, A.L. Steele, and J.E. Hoad, "Resonance conditions of long-period gratings in temperature sensitive polymer ring optical fibre," *IEEE Photon. Technol. Lett.*, vol. 12, no. 1, pp. 65-67, 2000.

216 . P.J. Lemaire, "Reliability of optical fibers exposed to hydrogen - prediction of long-term loss increases," *Optical Eng.*, vol. 30, no. 6, pp. 780-789, Jun 1991.

217 . Y. Koyano, M. Kakui, T. Kashiwada, M. Onishi, M. Shigematsu, H. Kanamori, M. Nishimura, "Long-term reliability of Er-doped fibers in hydrogen environments," *Elec & Comms in JPN Part II-Electronics*, vol. 79, no. 1, pp. 33-42, Jan 1996.

218 . V.B. Neustruev, "Color-centers in germanosilicate glass and optical fibers," *Jn. Physics-condensed matter,* vol. 6, no. 35, pp. 6901-6936, Aug 1994.

219 . P.J.Lemaire, R.M.atkins, V.Mizrahi, and W.A.Reed, "High pressure H_2 loading as a technique for achieving ultrahigh UV photosensitivity and thermal sensitivity in GeO_2 doped optical fibres", *Electron. Lett.*, **29**,1191-1193, 1993.

220 . S. Komaki, K. Tsukamoto, and M. Okada, "Requirements for the radio-wave photonic devices from the view point of future mobile radio system," *IEEE Trans. Microwave Theory Tech.*, vol. 43, pp. 2222-2228, 1995.

221 . J.E. Bowers, S.A. Newton, and H.J. Shaw, "Fibre-optic variable delay lines," *Electron. Lett.* vol. 18, pp. 999-1000, 1982.

222 . K.P. Jackson, S.A. Newton, B. Moslehi, M. Tur, C.C. Cutler, J.W. Goodman, and H. J. Shaw, "Optical fibre delay-line signal processing," *IEEE Microwave Theory & Tech.*, MTT-33, no. 3, pp. 193-210, 1985.

223 . B. Moslehi, J.W. Goodman, M. Tur, and H.J. Shaw, "Fibre-optic lattice signal processing," Proc. IEE, vol. 72, pp. 909-930, 1984.

224. D. Norton, S. Johns, C. Keefer, and R. Soref, "Tuneable microwave filtering using high dispersion fibre time delay," *IEEE Photonics Technol. Lett.*, vol. 6, no. 7, pp. 831-832, 1994.

225. D. B. Hunter, R.A. Minasian, and P. A. Krug, "Tuneable optical delay line filter based on chirped gratings," *Electron. Lett.* vol. 31, pp. 2205-2207, 1995

226. W. Zhang, J.A.R. Williams, and I. Bennion, "Recirculating fibre-optic notch filter employing fibre gratings," *IEEE Photon. Technol. Lett.*, vol. 11, no.7, pp. 836-838, 1999.
227. D. B. Hunter, and R.A. Minasian, "Microwave optical filters using in-fibre Bragg grating arrays," *IEEE Microwave and Guided wave Lett.*, vol. 6, no. 2, pp. 103-105, Feb 1996.
228. J. Capmany, D. Pastor, and B. Ortega, "Experimental demonstration of tunability and transfer function reconfiguration in fibre-optic microwave filters composed of linearly chirped fibre grating fed by laser array," *Electron. Lett.*, vol. 34, no. 23, pp. 2262-2264, 1998.
229. J. Marti, F. Ramos, and R.I. Laming, "Photonic microwave filter employing multimode optical sources and wideband chirped fibre gratings," *Electron. Lett.*, 1998, vol. 34, pp. 1760-1761.
230. W. Zhang, J.A.R. Williams and I. Bennion, "Fibre-optic Bandpass Transversal Filter Employing Fibre Grating Arrays," *Electron. Lett.* vol. 35, no. 12, pp. 1010-1011, 1999.
231. G. Yu, W. Zhang, and J.A.R. Williams, "High performance microwave transversal filter using Fibre Bragg grating Arrays," *IEEE Photon. Technol. Lett.* vol. 12, no. 9, pp. 1183-1185, 2000.
232. W. Zhang, G. Yu, and J.A.R. Williams, "Tap multiplexed optical transversal filter by using fibre gratings," *Electron. Lett.*, vol. 36, no. 20, pp. 1708-1710, 2000
233. J. Capmany, D. Pastor, and B. Ortega, "Efficient sidelobe suppression by source power apodisation in fibre optic microwave filters composed of linearly chirped fibre grating by laser array," *Electron. Lett.*, vol. 35, no. 8, pp. 640-642, April 1999.
234. J. Capmany, D. Pastor, and B. Ortega, "New and flexible fibre-optic delay line filters using chirped Bragg gratings and laser arrays," *IEEE Trans. Microwave Theory Tech.*, vol. 47, no. 8, pp. 1321-1327, 1999.
235. J. Capmany, D. Pastor, and B. Ortega, "Fibre-optic microwave and millimetre-wave filter with high density filtering and very high sidelobe suppression using sub-nanometre optical spectrum splicing," *Electron. Lett.*, vol. 35, no. 6, pp. 494-496, 1999.
236. W. Zhang, J.A.R. Williams, L. Zhang, and I. Bennion, "Optical microwave signal processing by using fibre grating based Fabri-Perot cavity," *Cleo2000*, San Francisco, USA, pp. 330-331, May 2000.
237. E. C. Ifeachor, and B.W. Jervis, "Digital Signal Processing," Addison-Wesley, pp. 50-93,134-144, 1993.
238. W. Zhang, and J.A.R. Williams, "The frequency response of a tuneable fibre-optic notch filter using a dispersive device," *Microwave & Optical Techno. Lett.*, vol. 22, no. 1, pp. 4 –7, 1999.
239. B.J. Eggleton, P.A. Krug, L. Poladian, and F. Ouellette, "Long periodic superstructure Bragg gratings in optical fibres," *Electron. Lett.*, vol. 30, no.19, pp. 1620-1622, 1994,.
240. A.P. Foord, P.A. Davies, and P.A. Greenhalgh, "Synthesis of microwave and millimetre-wave filters using optical spectrum-splicing," *Electron. Lett.*, vol. 32, no. 4, pp. 390-391, Feb 1996.
241. D. Pastor, B. Ortega, J. Capmany, S. Sales, A. Martinez, and P. Munoz, "Flexible and tuneable microwave filters based on arrayed Waveguide gratings," no. P2-5, WP2002 *International Topical Meeting on Microwave Photonics*, Awaji, Japan, pp. 189-192, Nov 2002.

242. S. Sales, J. Capmany, J. Marti, and D. Pastor, "Experimental demonstration of fibre-optic delay line filters with negative coefficients," *Electron. Lett.*, vol. 31, no. 13, pp. 1095-1096, Jun 1995.
243. L. Nguyen, B. Aazhang, and J.F. Young, "All-optical CDMA with bipolar codes," Electron. Letts., vol. 31, no. 6, pp. 469-470, Mar 1995.
244. M. Ibsen, M.K. Durkin, M.J. Cole, and R.I. Laming, "Sinc-sampled fibre Bragg gratings for identical multiple wavelength operation," *IEEE Photon. Technol. Lett.*, vol. 10, no. 6, pp. 842-844, 1998.
245. H. Schmuck, "Comparison of optical millimetre wave system concepts with regard to chromatic dispersion," *Electron. Lett.*, vol. 31, no. 21, pp. 1848-1849, 1995.
246 C. Peucheret, F. Liu, and R.J.S Pedersen, "Measurement of small dispersion values in optical components," *Electron. Lett.*, vol. 35, no. 5., pp. 409-411, Mar 1999.
247. J.M. Fuster, J.Marti, J.L. Corral, V. Polo, and F. Ramos, "Generalized study of dispersion-induced power penalty mitigation techniques in millimetre-wave fibre-optic links", *IEEE Jn. Lightwave Technol.*, vol. 18, no. 7, pp. 933-940, July 2000.
248. G.H. Smith, D. Novak, and Z. Ahmed, "Techniques for optical SSB generation to overcome fibre dispersion penalties in fibre-radio systems," *Electron. Lett.*, vol. 33, no. 1, pp. 74-75, Jan 1997.
249. W. Zhang, and J.A.R. Williams, "Effect of source spectral bandwidth on frequency response of fibre-optic microwave system," Submitted to *Electron Lett.*, 2002.
250. X.F. Chen, Y. Luo, C.C. Fan, T. Wu, and S.Z. Xie, "Analytical expression of sampled Bragg gratings with chirp in the sampling period and its application in dispersion management design in a WDM system," *IEEE Photon. Technol. Lett.*, vol. 18, no. 8, pp. 1013-1015, Aug 2000.
251. Y. Hida, Y. Hibino, T. Kitoh, Y. Inoue, M. Itoh, M. Shibata, A. Sugita, and A. Himeno, "400-channel arrayed-waveguide grating with 25 GHz spacing using $1.5\% - \Delta$ waveguides on 6-inch Si wafer," *Electron. Lett.*, vol. 37, no. 9, pp. 576-577, 2001.
252. K. Takada, M. Abe, T. Shibata, and K. Okamoto, "A 25-Ghz-spaced 1080-channel tandem multi/demultiplexer covering the S-, C-, and L-Bands using an arrayed-waveguide grating with gaussian passbands as a primary filter," *IEEE Photon. Technol. Lett.*, vol. 14, no.5, pp. 648-650, May 2002
253. M. Abe, Y. Hibino, T. Tanaka, A. Itoh, A. Himeno, and Y. Ohmori, "Mach-Zehnder interferometer and arrayed-waveguide-grating integrated multi/demultiplexer with photosensitive wavelength tuning," *Electron. Lett.*, vol. 37, no.6, pp.376-377, Mar 2001.

7 Conclusion

7.1 Introduction

This thesis has presented research work on the design and fabrication of different types of fibre grating and grating-based devices for applications to sensing and telecommunication. Three main types of grating –the FBGs, the LPGs, and the SFBGs- have been studied extensively. Their respective theories, characteristics, and fabrication methods have been systematically investigated, while their novel applications to sensing and telecommunication have been successfully demonstrated.

In Section 7.2, an itemised summary of the main achievements recorded during this research is given. Subsection 7.2.1 provides a list of achievements in the area of sensing for the three main types of grating. Subsection 7.2.2, on the other hand, presents a list of the major successes recorded in the development and application of gratings to produce some devices that can be used in telecommunications.

Section 7.3 focuses on the detailed conclusions giving more specific information on the key results from the research. Section 7.4 finally suggests different directions in which further work may be carried out.

7.2 Summary of research achievements

All the three main types of grating can be used in sensing and telecommunications. This section provides a list of achievements relating to both areas of application.

7.2.1 Key achievements related to sensing

The sensing related achievements are grouped into three categories to correspond with the types of grating used.

For FBG-based sensing:

(I) Compact-arrays with 2.5mm spatial resolutions have been successfully produced

and demonstrated for arbitrarily quasi-distributed strain measurement.

(II) Four FBG-based novel sensors for simultaneous strain and temperature measurement have been successfully demonstrated.

For LPG-based sensing:

(I) A single LPG has been successfully demonstrated for simultaneous measurement of strain and temperature using its fundamental and harmonic modes.

(II) A special LPG with a pronounced index-insensitive peak called LP_{02L} has been fabricated in a standard SMF. It allows for the simultaneous measurement of

(i) SRI and temperature,

(ii) Curvature and temperature, and also

(iii) Strain and temperature.

(III) Another special LPG inscribed in a B/Ge co-doped fibre, which has revealed opposite trends in the shifts of its cladding modes with temperature and also with the changes in the value of SRI has been demonstrated.

(IV) In an SMM900 double-cladding fibre an LPG with index-insensitive peaks has been successfully demonstrated for simultaneous SRI and temperature measurement.

For SFBG-based sensing, it has been shown that a single SFBG can be used for the measurement of:

(I) SRI and temperature.

(II) Arbitrary values of curvature and temperature.

(III) Strain and curvature.

(IV) A combination of strain, curvature and temperature.

(V) Very small values of curvature.

(VI) Very large curvatures.

7.2.2 Key achievements related to telecommunications

For the research work in respect of applications of fibre gratings in devices used for telecommunications, again, each of the three main types of grating produced has been used successfully, particularly in filter implementations. The lists of achievements have been categorised into FBG, LPG and SFBG related.

For FBG-based devices:

Whilst many gratings of different types have been produced the most important contributions described in the thesis are:

(II) The production of repeatable apodised gratings, which can be used in many areas of telecommunications.

(III) The demonstration of suppression of cladding mode-coupling loss using a low-cost approach, which has offered new possibilities in the wide range of applications where inter-symbol interference needs to be minimised.

For LPG-based devices:

(I) Efficient tuneable loss filters have been demonstrated in the two main telecommunication windows, i.e., the 1500nm and the 1300nm.

(II) A method that has been successfully demonstrated to minimise the negative effects of H_2 and UV-induced OH ions, and improve the efficiency of grating production.

Finally, for SSFBG devices:

(I) A microwave sub-carrier transversal filter based on the use of SSFBG in reflection has been successfully demonstrated.

(II) Another microwave sub-carrier filter based on the use of SSFBG in transmission has also been successfully produced.

(III) A sinc-SSFBG with > 22 channels has been fabricated –offering the potential for DWDM filtering.

7.3 Conclusions

The thesis has been structured into review, fabrication work, and application to sensing and telecommunication devices. Whilst the literature survey offered an insight into the current state of research in fibre grating technology, the theoretical review and analysis led to a number of simulations and thus helped in the interpretation of the observed grating characteristics. In addition, the simulation work also led to improved efficiency in grating fabrication to achieve specific profiles for novel applications. Many grating profiles have been achieved and shown in the thesis.

The novel applications started with the fabrication of two configurations of five- and ten-compact-grating-arrays, which have been used to implement quasi-distributed and arbitrarily applied strain measurements. The maximum measurand ranges estimated are ±4539με and

±2182με, and spatial resolutions are 5mm and 2.5mm for the two structures, respectively. In comparison with other reported sensors and techniques, the compact arrays provide a simple and practicable solution for real applications as the WDM FBG-sensing interrogation method can be directly applied. Despite the success of this compact structure, it was noted that with the measurement of strain there is a potential for temperature cross-sensitivity which needs to be compensated. Thus, four novel FBG strain sensors with the capability to compensate for temperature-induced wavelength shifts have been proposed and demonstrated. The dual-parameter sensing functionality of the sensors originates from their unique configuration of having two Bragg reflection peaks that exhibit the same strain- but different temperature-responses. Temperature sensitivities ranging from 7.5 to 12.24pm/°C have been shown for the FBG-sensors written in the same piece of B/Ge fibre with different UV exposure times. This clearly indicates that the temperature responsivity of the gratings can be tailored. The advantages of simple fabrication, tolerance of large strain effects and, more importantly, the use of a single light source for interrogation offer the prospects of the development of practical temperature independent arbitrary strain sensing system.

In the experiments involving the use of LPGs for sensing, a single LPG that can use a single light source for interrogation has been demonstrated for simultaneous measurement of strain and temperature. The measurements rely on the use of a fundamental and harmonic modes that are located ~50nm apart. The costs of producing this LPG offer the prospects of a practical sensor device.

Some special LPGs fabricated in both conventional B/Ge co-doped fibre and standard SMFs are shown to exhibit a set of harmonic cladding modes at shorter wavelengths than those of the fundamental modes. In addition, those gratings fabricated in standard SMF exhibited an additional 'broad-peak' (referred to as $^{1}LP_{02L}$) located between the harmonic and the fundamental cladding modes. A rigorous identification process for the mode $^{1}LP_{02L}$ has been successfully pursued through LPG simulation. Also, the sensing properties of the mode have been extensively studied whilst the mode has been used in conjunction with the harmonic modes to demonstrate the capability of the single LPG for simultaneous measurement of temperature and other parameters, such as curvature, axial strain, and SRI. The peak $^{1}LP_{02L}$ is neither responsive to curvature nor to SRI but only to temperature, making it possible to deduct temperature-induced wavelength shift from the other modes using correlation from

such a peak. As for strain and temperature, the usual matrix method has been applied, and strain and temperature values have been successfully evaluated.

Another special LPG made within a piece of B/Ge co-doped fibre has been shown to exhibit a cladding mode whose characteristics have not been, to the author's knowledge, demonstrated previously. This mode appears within the set of fundamental modes, and its responsivity characteristics are opposite to those observed for the lower resonance order fundamental modes. This mode has opened-up new sensing possibilities, and permits the use of single light source for interrogation, thereby reducing the cost of signal processing[42].

Additional sensing work relates to a compact scheme that has been successfully developed for simultaneous measurements of temperature and the SRI using two LPGs of different periods inscribed side-by-side in a single piece of a double-cladding fibre. One of the LPGs is responsive to both SRI and temperature changes whilst the other is SRI-insensitive but show spectral shift with temperature changes. In addition, it has also been shown that a resonance peak of the SRI-insensitive LPG can be designed to appear in the EDFA wavelength region with potential use for gain flattening applications.

The sensing work relating to SFBGs started with a novel scheme successfully developed for simultaneous refractive index and temperature measurement using a single SFBG. The intrinsic nature of an SFBG possessing both the FBG and LPG spectral responses permits the temperature effect to be measured solely from the former while the refractive index information is extracted from the latter. Furthermore, a single SFBG for simultaneous measurement of arbitrary values of bending curvature and temperature has also been successfully demonstrated. In comparison with the previously reported LPG method, the single SFBG approach provides a simple technique to independently measure the two parameters from a single device.

It has also been demonstrated that a single SFBG can be used to provide simultaneous measurements of strain, temperature and curvature. The spectral splitting of the SFBG loss bands facilitates measurement of the curvature, whilst the wavelength shift of the FBG harmonics, in conjunction with the shift in the mid-point between the split LPG bands,

provides for determination of the axial strain and temperature. Moreover, an investigation of the cladding mode splitting for several orders of the LPG structure revealed that small values of curvature ($<0.4m^{-1}$) that could not be measured previously, can now be detected using the lower resonance order cladding modes. However, highest resolution at large curvature values is obtained using a higher resonance order mode. For example, using a high resonance order mode, a bending curvature of 11.03 m^{-1} was recorded corresponding to a spectral mode splitting of 126nm which is the highest value ever reported. Thus, it is readily possible that a single sensor employing both lower- and higher -resonance order modes be constructed to combine high resolution with high responsivity.

The telecommunication related work involving the three main types of grating was begun by the work on apodisation of FBGs, which has been examined through both simulation and experiment. In particular, FBGs with different lengths were apodised by using Gaussian and Blackman profiles –the results suggest that over 50dB rejection is theoretically achievable. Experimentally, however, over ~19dB sidelobe suppression has been successfully demonstrated in a grating with ~19dB transmission and reflection. It is difficult to achieve the theoretical rejection levels through experiment because of error resulting from vibration, laser beam quality, Phase-mask qualify and other militating experimental conditions.

Further research on FBG application into telecommunication devices included the successful development of a simple and effective method for the suppression of cladding-mode coupling loss by raising the NA of a fibre through repeated or prolonged UV exposure. Standard SMF was used so as to reduce fabrication costs. Suppression of cladding-modes down to 0.2 dB in a Bragg grating of 18dB reflectivity has been achieved in hydrogen-loaded standard SMF. Another attractive advantage of the method is that it allows for reducing the splice- and insertion-loss as the NA was increased only at the fibre section into which the FBG was inscribed. The proposed technique offers the prospects of the development of practical DWDM devices.

In a nutshell, the effective suppression of- (a) cladding mode coupling loss through the prolonged UV-exposure, and (b) FBG sidelobes using apodisation has paved the way for the

---

[42] . It should be noted that with all LPGs the broad nature of the modes lead to reduce accuracy of the interrogation results in comparison to FBGs, which are very narrow.

use of such types of FBGs in tuneable optical filters and lasers, and indeed can also improve the transmission capacity of high bit-rate systems.

An investigation of thermal properties of an LPG of 240μm period fabricated in B/Ge co-doped fibre has been carried out revealing that the temperature responsivity of the LPG produced in the B/Ge fibre is much higher than that obtained in a standard SMF. A spectral shift of 27.5nm was achieved for temperature change of only 10°C using a peak in the 1500nm telecommunications window, demonstrating the highest reported responsivity of 2.75nm/°C. In the 1300nm wavelength region, LPG tuneability of 383pm/°C has been achieved using a mode $^{2}LP_{07}$ of an LPG produced in B/Ge co-doped fibre, which indicates that a tuneable loss filter for this window can be implemented using the LPG harmonics. Indeed, for the right fibre dispersion properties, such second diffraction order modes can be obtained, in principle, at half the wavelength of the fundamental modes, thus allowing a tuneable loss filter to be implemented in the visible wavelength region.

An important observation during LPG fabrication is that two perturbation-independent loss peaks appeared at 1245 and 1400nm wavelength regions, which are, related to hydrogen and UV-induced hydroxyl (OH) ions, respectively. The loss at 1400nm was found to be more severe in B\Ge co-doped fibre than in standard SMF due to the formation of hydroxyl ions associated with both silica and boron. The loss peaks limit the tuning range of the loss filters. Techniques to avoid this spectral distortion effect have been clearly demonstrated in the thesis.

The use of SSFBG in telecommunication devices has focused on two main areas: the microwave sub-carrier and the DWDM filters. To this end, a simple and cost-effective fabrication method has been adopted to produce an SSFBG with intrinsic and controllable apodisation. It has been shown that the SSFBG may be used either with a 25km long piece of fibre or a CFBG to realise a microwave sub-carrier transversal filter. The fabrication of the SSFBG allows for precise control of unit time delay and FSR, -giving a flexible and low cost filtering with response of large (>45dB) rejection level. This offers a potential for more complex signal processing and improves the prospect of achieving practical radio on fibre systems.

In addition, another microwave sub-carrier filter has been successfully implemented using a single-, and cascaded configuration of SSFBG. A single SSFBG was first employed to produce a compact bandpass microwave sub-carrier filter that offered 10dB rejection level. The cascading of the SSFBG devices led to an improvement in performance to 30dB microwave sub-carrier rejection level. This filter relies on locating the operating wavelength in the centre of one of the passbands, which permits dual sideband modulation of the optical signal. One of the main advantages of these microwave sub-carrier filters is that they require no optical coherence to operate.

7.4 Further work

On FBG array, further work would be desirable in improving the spatial resolution and maximum measurand range to a sub-millimetre level ($\leq$ 1mm) and up to $\pm$7200$\mu\varepsilon$, respectively. Also, further work may focus on the in-depth analysis of strain within flat metal beams and correlating the result with the measured data to evaluate slippage effects, etc. In addition, the use of grating array embedded in composite material to evaluate directional information in respect of applied stress could also be further investigated; grating arrays have already been embedded using different mesh-arrangements. The experiment could well be completed in the future.

Gain flattening potentials of the index insensitive LPGs produced in both the double-cladding fibre and the standard SMF need to be further evaluated. Further work would be necessary in evaluating the light emission from the surface of LPGs: preliminary results have been obtained showing promising potential for the implementation of LPG-based couplers and filters, but further evaluation could be necessary. It might also be necessary to collaborate with theoreticians to establish the reason for secondary mode splitting during the application of curvature or indeed the exact reason for the poor resolution at lower values of applied curvature when a high resonance order fundamental mode is considered for measuring the splitting. Unfortunately, there are still a very small number of reports on the theoretical interpretation of LPG characteristics when subjected to bending curvature.

Future work on SFBG sensing should include the simultaneous measurement of temperature, SRI and curvature or possibly strain, SRI and curvature or indeed load and temperature.

For the microwave sub-carrier transversal filters, further work may focus on improving the apodisation profiles of the SSFBGs. For the bandpass microwave sub-carrier filter that is operating in transmission mode, it is necessary to investigate further into the ways by which smooth tops of optical passbands can be obtained in the gratings. It has been shown that different spacing between optical taps can be obtained during SSFBG fabrication, which can lead to different microwave sub-carrier passband spacing. For example, a tap spacing of about 0.066nm led to the measured frequency response giving an FSR of ~8.3GHz. With different passband spacing it is possible in principle to cover a frequency range up to terahertz. In addition, a tuneable FSR could be realized by using a series of isolated SSFBGs with well-separated central wavelengths and different tap spacing.

Further work on dense-channel sinc-SSFBG may focus on improving the spectral characteristics, the number of flat-top channels and the rejection levels of the grating, and possibly explore the possibility of dense channel dispersion compensation. Also, the use of this type of dense-channel SSFBG for WDM-based interrogation of FBG-array could be exploited.

In reality, there are many ways to advance some of the work reported here. It is almost impossible to list all possible future directions in view of the fact that grating design and applications to both sensing and telecommunications are still very actively researched areas.

Appendix1: Publications during this research period

[1] B A L Gwandu, W Zhang and J A R Williams, "Implementation of microwave photonic filtering using a profiled superstructured fibre Bragg grating and dispersive fibre", *MWP2002 International Topical Meeting on Microwave Photonics*, Awaji, Japan (nov 2002)

[2] B A L Gwandu, W Zhang, J A R Williams, L Zhang and I Bennion, "Microwave photonic filtering using a Gaussian-profiled superstructured fibre Bragg grating and dispersive fibre", *Electron. Lett.* **38** (22), pp. 1328-1330 (oct 2002)

[3] B A L Gwandu, W Zhang, X Shu, L Zhang, D J Webb and I Bennion, "Suppression of cladding-mode coupling loss in Bragg grating using standard single-mode fibre ", *15th IEEE Lasers and Electro-Optics Society Annual Meeting*, 2, Glasgow, UK, pp. 815-816 (nov 2002)

[4] B A L Gwandu, W Zhang, X Shu, D J Webb, L Zhang and I Bennion, "Fabrication of Index-insensitive Long Period Fibre Gratings", op2.p2 *Proc. of The IoP International conference on Optoelectronics, (Photon 02)*, op2.p2, Cardiff (aug 2002)

[5] B A L Gwandu, W Zhang, X Shu, D J Webb, L Zhang and I Bennion, "Simultaneous measurements of temperature and axial strain using the fundamental cladding mode 1LP02 and a high resonance order second harmonic cladding of an LPG", op2.p1 *Proc. of The IoP International conference on Optoelectronics, (Photon 02)*, op2.p1, Cardiff (aug 2002)

[6] X Shu, D Zhao, Y Liu, B A L, Gwandu, F Floreani, L Zhang, and I Bennion, "Effectively simultaneous temperature and strain measurement utilising a dual-grating sensor formed by Type IA and Type IIA FBGs", *Proc 1st IEEE International Conference on Sensors*, **2**, Kissimmee, Florida, USA, pp. 1740-1745 (jun 2002)

[7] B A L Gwandu, X Shu, Y Liu, W Zhang, L Zhang and I Bennion, "Simultaneous measurement of Strain and Curvature Using Superstructure Fibre Bragg Gratings", *Sensors and Actuators A* **96** (2-3), pp. 133-139 (feb 2002)

[8] B A L Gwandu, X Shu, T D P Allsop, W Zhang, D J Webb, L Zhang and I Bennion, "Simultaneous refractive index and temperature measurement using cascaded long-period grating in a double-cladding fibre", *Electron. Lett.* **38** (14), pp. 695-696 (jul 2002)

[9] X Shu, B A L Gwandu, L Zhang and I Bennion, "Fabrication and characterisation ultra-long-period fibre gratings", *Opt. Commun.* **203** (3-6), pp. 277-281 (mar 2002)

[10] X Shu, Y Liu, D Zhao, B A L Gwandu, F Floreani, L Zhang and I Bennion, "Dependence of temperature and strain coefficients on fibre grating type and application to simultaneous temperature and strain measurement", *Opt. Lett.* **27** (9), pp. 701-703 (may 2002)

[11] X Shu, B A L Gwandu, L Zhang and I Bennion, "Super-High Temperature Sensitivity of Long-Period Gratings in B/Ge Co-doped Fibre", *Photonics West 2002*, San Jose, California, USA (jan 2002)

*[12] B A L Gwandu, X Shu, T Allsop, W Zhang, D J Webb, L Zhang and I Bennion, "Simultaneous refractive index and temperature measurement using a cascaded long-period grating device", *Proc 1st IEEE International Conference on Sensors*, **2**, Kissimmee, Florida, USA, pp. 1032-1035 (jun 2002)

[13] X Shu, Y Liu, D Zhao, B A L Gwandu, F Floreani, L Zhang and I Bennion, "Fibre grating type dependence of temperature and strain coefficients and application to simultaneous temperature and strain measurement", *15th Conference on Optical Fibre Sensors (OFS 2002)*, **TuB4**, Portland, Oregon, USA, pp. 83-86 (may 2002)

[14] B A L Gwandu, L Zhang, K Chisholm, Y Liu and I Bennion, "High-spatial-resolution-Distributed Sensing Using Compact FBG Grating Array Structures", *Proc. IoP, Appl. Opt. & Opto-electronics*, Loughborough, UK, pp. 16-17 (sep 2000)

[15] B A L Gwandu, X Shu, Y Liu, W Zhang, L Zhang and I Bennion, "Simultaneous and independent sensing of arbitrary temperature and bending using sampled fibre Bragg grating", *Electron. Lett.* **37** (15), pp. 946-948 (jul 2001)

[16] B A L Gwandu, X Shu, Y Liu, W Zhang, L Zhang and I Bennion , "Simultaneous measurement of Strain, temperature, and Curvature Using a Sampled Fibre Bragg Grating", *15th Conference on Optical Fibre Sensors (OFS 2002)*, **TuB3**, Portland, Oregon , pp. 79-82 (may 2002)

[17] B A L Gwandu, W Zhang, J A R Williams, X Shu, L Zhang and I Bennion, "Microwave photonic response of superstructured fibre Bragg grating", *Photonex2001 In-Fibre Bragg Gratings and Special Fibres Meeting*, **11**, NAC Stoneleigh Park, Coventry, UK, pp. 17-18 (oct 2001)

[18] X Shu, B A L Gwandu, L Zhang and I Bennion, "Ultra -long-period fibre gratings", *27th European conference on Optical Communications*, Amsterdam, Netherlands , pp. 386-387 (sep 2001)

[19] B A L Gwandu, L Zhang, K Chisholm, Y Liu, X Shu and I Bennion, "Compact FBG array structure for high spatial resolution distributed strain sensing", *Meas. Sci. Tech.* **12** (7), pp. 918-921 (2001)

[20] X Shu, T Allsop, B Gwandu, L Zhang and I Bennion, "High Temperature Sensitivity of Long-Period Gratings in B/Ge Co-doped Fibre", *IEEE Photon. Technol. Lett.* **13** (8) , pp. 818-820 (aug 2001)

[21] X Shu and B A L Gwandu and Y Liu and L Zhang and I Bennion, "Sampled Fibre Bragg Grating for Simultaneous Refractive Index and Temperature Measurement", *Opt. Lett.* **26** (11), pp. 774-776 (jun 2001)

[22] X Shu, T Allsop, B Gwandu, L Zhang and I Bennion, "Room Temperature Operation of Widely Tuneable loss Filter", *Electron. Lett.* **37** (4), pp. 216-218 (2001)

[23] X Shu, T Allsop, B Gwandu, L Zhang and I Bennion, "Thermally tuneable optical fibre loss filter with wide tuning range", *Lasers and Electro-Optics (CLEO 2001)*, APS/IEEE/OSA, San Francisco, CA, USA, pp. 126-127 (may 2001)

[24] B A L Gwandu, L Zhang, K Chisholm, Y Liu and I Bennion, "Compact FBG grating array structure for high spatial resolution distributed strain sensing", *15th International Conference on Optical Fibre Sensors (OFS'2000), Technical Digest*, **4185**, Venice, Italy, pp. 756-759 (oct 2000)

[25] B A L Gwandu, X Shu, W Zhang, D J Webb, L Zhang and I Bennion, " Long period grating exhibiting a broad LP_{02} cladding mode and harmonics: their use for multiple parameter measurement, gain flattening, and tuneable loss-filter applications", Submitted to *Jn. Lightwave Technol.*, (nov 2002)

* Nominated for the overall-best conference paper award

UK and US Patents

[1] X Shu, D Zhao, Y Liu, B A L, Gwandu, F Floreani, L Zhang, and I Bennion, "Dual-parameter optical wave-guide grating sensing device and sensor", *US Patent Application* (2003)

[2] X Shu, D Zhao, Y Liu, B A L Gwandu, F Floreani, L Zhang, and I Bennion, " Dual-parameter optical wave-guide grating sensing device and sensor", *European Patent Application no. 01309335.6EP* (Nov. 2001)

Appendix2: Matlab program for LPG curves

```
%************************************************************ *%
% This Program is use to evaluate the phase relationships for the first 53   *%
% Cladding modes                                                             *%
% ************************************************************%

clear all
close all
% general constants are;

pi=3.1415926535897;
namb=1.0;
lam=[0.2:0.01:2.4];

% for the core the coeffs. are;

% 3.1 m/o GeO2, 96.9 m/o SiO2 (Adams pp. 244); %spec. for standard fibre%
A1=0.7028554;
A2=0.41463070;
A3=0.89745400;
lama1=0.072;
lama2=0.114;
lama3=9.841;

% 4.03 m/o GeO2, 9.7 m/o B2O3, 86.27 m/o SiO2 (Adams pp. 244); % spec. for B/Ge
fibre%
%A1=0.70420420;
%A2=0.41289413;
%A3=0.95238253;
%lama1=0.067974973;
%lama2=0.12147738;
%lama3=9.6436219;


%for Cladding the coeff. are;

b1=0.6961663;
b2=0.4079426;
b3=0.897479;
lamb1=0.0684043;
lamb2=0.1162414;
lamb3=9.896161;

File_lam=fopen('D:\data\File_lam.dat','w+'); %" - means APPEND to file;
File_nco=fopen('D:\data\File_nco.dat','w+');
File_ncl=fopen('D:\data\File_ncl.dat','w+');
```

```
file1=fopen('D:\data\mode1.dat','w+'); %" - means APPEND to file;
file2=fopen('D:\data\mode2.dat','w+');
file3=fopen('D:\data\mode3.dat','w+');
file4=fopen('D:\data\mode4.dat','w+');
file5=fopen('D:\data\mode5.dat','w+');
file6=fopen('D:\data\mode6.dat','w+');
file7=fopen('D:\data\mode7.dat','w+');
file8=fopen('D:\data\mode8.dat','w+');
file9=fopen('D:\data\mode9.dat','w+');
file10=fopen('D:\data\mode10.dat','w+');
file11=fopen('D:\data\mode11.dat','w+');
file12=fopen('D:\data\mode12.dat','w+');
file13=fopen('D:\data\mode13.dat','w+');
file14=fopen('D:\data\mode14.dat','w+');
file15=fopen('D:\data\mode15.dat','w+');
file16=fopen('D:\data\mode16.dat','w+');
file17=fopen('D:\data\mode17.dat','w+');
file18=fopen('D:\data\mode18.dat','w+');
file19=fopen('D:\data\mode19.dat','w+');
file20=fopen('D:\data\mode20.dat','w+');
file21=fopen('D:\data\mode21.dat','w+');
file22=fopen('D:\data\mode22.dat','w+');
file23=fopen('D:\data\mode23.dat','w+');
file24=fopen('D:\data\mode24.dat','w+');
file25=fopen('D:\data\mode25.dat','w+');
file26=fopen('D:\data\mode26.dat','w+');
file27=fopen('D:\data\mode27.dat','w+');
file28=fopen('D:\data\mode28.dat','w+');
file29=fopen('D:\data\mode29.dat','w+');
file30=fopen('D:\data\mode30.dat','w+');
file53=fopen('D:\data\mode53.dat','w+');


% fibre specs;

rco=4.5;
rcl=62.5;

% material index calculations using sellmier eqns [see IFO book];

nco=sqrt(1+(((A1.*lam.^2)./(lam.^2-lama1^2))+((A2.*lam.^2)./(lam.^2-
lama2^2))+((A3.*lam.^2)./(lam.^2-lama3^2))));

ncl=sqrt(1+(((b1.*lam.^2)./(lam.^2-lamb1^2))+((b2.*lam.^2)./(lam.^2-
lamb2^2))+((b3.*lam.^2)./(lam.^2-lamb3^2))));

% V calculations, eqn. 3.12;

vco=((2*pi*rco./lam).*sqrt(nco.^2-ncl.^2));
vcl=((2*pi*rcl./lam).*sqrt(ncl.^2-namb.^2));
```

```
figure(1)
hold on;
plot(lam,ncl,lam,nco)
xlabel('Material Index');
ylabel('Wavelength, nm');
grid

figure(2)
plot(lam,vco)
xlabel('Wavelength, nm');
ylabel('Normalised Freq. (Core)');

figure(3)
plot(lam,vcl)
xlabel('Wavelength, nm');
ylabel('Normalised Freq. (Clad)');


N=length(nco)

for i=1:N
u01co=fzero('fatima',[0.1,vco(i)],0.00001,0,vco(i),0,1);    %for the fundamental core mode
eqn. 3.17%

ulp(i)=u01co;

%u02co=fzero('fatima',[0.1,vco(i)],0.00001,0,vco(i),0,2);    %for the second core mode%
%ulp(i)=u02co;                                               %see lines 231,321,364-9%

end;

D=length(ncl)
for j=1:D
u01cl=fzero('fatima1',[0.1,vcl(j)],0.00001,0,vcl(j),0,1);
ulp1(j)=u01cl;

u02cl=fzero('fatima1',[0.1,vcl(j)],0.00001,0,vcl(j),0,2);
ulp2(j)=u02cl;

u03cl=fzero('fatima1',[0.1,vcl(j)],0.00001,0,vcl(j),0,3);
ulp3(j)=u03cl;

u04cl=fzero('fatima1',[0.1,vcl(j)],0.00001,0,vcl(j),0,4);
ulp4(j)=u04cl;

u05cl=fzero('fatima1',[0.1,vcl(j)],0.00001,0,vcl(j),0,5);
ulp5(j)=u05cl;

u06cl=fzero('fatima1',[0.1,vcl(j)],0.00001,0,vcl(j),0,6);
```

```
ulp6(j)=u06cl;

u07cl=fzero('fatima1',[0.1,vcl(j)],0.00001,0,vcl(j),0,7);
ulp7(j)=u07cl;

u08cl=fzero('fatima1',[0.1,vcl(j)],0.00001,0,vcl(j),0,8);
ulp8(j)=u08cl;

u09cl=fzero('fatima1',[0.1,vcl(j)],0.00001,0,vcl(j),0,9);
ulp9(j)=u09cl;

u010cl=fzero('fatima1',[0.1,vcl(j)],0.00001,0,vcl(j),0,10);
ulp10(j)=u010cl;


%----------;
u011cl=fzero('fatima1',[0.1,vcl(j)],0.00001,0,vcl(j),0,11);
ulp11(j)=u011cl;

u012cl=fzero('fatima1',[0.1,vcl(j)],0.00001,0,vcl(j),0,12);
ulp12(j)=u02cl;

u013cl=fzero('fatima1',[0.1,vcl(j)],0.00001,0,vcl(j),0,13);
ulp13(j)=u013cl;

u014cl=fzero('fatima1',[0.1,vcl(j)],0.00001,0,vcl(j),0,14);
ulp14(j)=u014cl;

u015cl=fzero('fatima1',[0.1,vcl(j)],0.00001,0,vcl(j),0,15);
ulp15(j)=u015cl;

u016cl=fzero('fatima1',[0.1,vcl(j)],0.00001,0,vcl(j),0,16);
ulp16(j)=u016cl;

u017cl=fzero('fatima1',[0.1,vcl(j)],0.00001,0,vcl(j),0,17);
ulp7(j)=u07cl;

u018cl=fzero('fatima1',[0.1,vcl(j)],0.00001,0,vcl(j),0,18);
ulp18(j)=u018cl;

u019cl=fzero('fatima1',[0.1,vcl(j)],0.00001,0,vcl(j),0,19);
ulp19(j)=u019cl;

%----------;

u020cl=fzero('fatima1',[0.1,vcl(j)],0.00001,0,vcl(j),0,20);
ulp30(j)=u020cl;

u021cl=fzero('fatima1',[0.1,vcl(j)],0.00001,0,vcl(j),0,21);
ulp21(j)=u021cl;
```

```
u022cl=fzero('fatima1',[0.1,vcl(j)],0.00001,0,vcl(j),0,22);
ulp22(j)=u022cl;

u023cl=fzero('fatima1',[0.1,vcl(j)],0.00001,0,vcl(j),0,23);
ulp23(j)=u023cl;

u024cl=fzero('fatima1',[0.1,vcl(j)],0.00001,0,vcl(j),0,24);
ulp24(j)=u024cl;

u025cl=fzero('fatima1',[0.1,vcl(j)],0.00001,0,vcl(j),0,25);
ulp25(j)=u025cl;

u026cl=fzero('fatima1',[0.1,vcl(j)],0.00001,0,vcl(j),0,26);
ulp26(j)=u026cl;

u027cl=fzero('fatima1',[0.1,vcl(j)],0.00001,0,vcl(j),0,27);
ulp27(j)=u027cl;

u028cl=fzero('fatima1',[0.1,vcl(j)],0.00001,0,vcl(j),0,28);
ulp28(j)=u028cl;

u029cl=fzero('fatima1',[0.1,vcl(j)],0.00001,0,vcl(j),0,29);
ulp29(j)=u029cl;

u030cl=fzero('fatima1',[0.1,vcl(j)],0.00001,0,vcl(j),0,30);
ulp30(j)=u030cl;

u050cl=fzero('fatima1',[0.1,vcl(j)],0.00001,0,vcl(j),0,50);
ulp50(j)=u050cl;

u053cl=fzero('fatima1',[0.1,vcl(j)],0.00001,0,vcl(j),0,53);
ulp53(j)=u053cl;
%----------;
end;

%==================================;

nco01=((nco.^2)-(((u01co.*lam)./(2*pi*rco)).^2));          %for the fundamental core
mode%

%nco02=((nco.^2)-(((u02co.*lam)./(2*pi*rco)).^2));         %for the second core mode%
%==================================;

ncl01=((ncl.^2)-(((u01cl.*lam)./(2*pi*rcl)).^2));          % see eqn. 3.19%
ncl02=((ncl.^2)-(((u02cl.*lam)./(2*pi*rcl)).^2));
ncl03=((ncl.^2)-(((u03cl.*lam)./(2*pi*rcl)).^2));
ncl04=((ncl.^2)-(((u04cl.*lam)./(2*pi*rcl)).^2));
ncl05=((ncl.^2)-(((u05cl.*lam)./(2*pi*rcl)).^2));
ncl06=((ncl.^2)-(((u06cl.*lam)./(2*pi*rcl)).^2));
```

```
ncl07=((ncl.^2)-(((u07cl.*lam)./(2*pi*rcl)).^2));
ncl08=((ncl.^2)-(((u08cl.*lam)./(2*pi*rcl)).^2));
ncl09=((ncl.^2)-(((u09cl.*lam)./(2*pi*rcl)).^2));
ncl010=((ncl.^2)-(((u010cl.*lam)./(2*pi*rcl)).^2));

% for cl-mode 11 to 19----------;
ncl011=((ncl.^2)-(((u011cl.*lam)./(2*pi*rcl)).^2));
ncl012=((ncl.^2)-(((u012cl.*lam)./(2*pi*rcl)).^2));
ncl013=((ncl.^2)-(((u013cl.*lam)./(2*pi*rcl)).^2));
ncl014=((ncl.^2)-(((u014cl.*lam)./(2*pi*rcl)).^2));
ncl015=((ncl.^2)-(((u015cl.*lam)./(2*pi*rcl)).^2));
ncl016=((ncl.^2)-(((u016cl.*lam)./(2*pi*rcl)).^2));
ncl017=((ncl.^2)-(((u017cl.*lam)./(2*pi*rcl)).^2));
ncl018=((ncl.^2)-(((u018cl.*lam)./(2*pi*rcl)).^2));
ncl019=((ncl.^2)-(((u019cl.*lam)./(2*pi*rcl)).^2));

%------------------modes 20 to 30------;
ncl020=((ncl.^2)-(((u020cl.*lam)./(2*pi*rcl)).^2));

ncl021=((ncl.^2)-(((u021cl.*lam)./(2*pi*rcl)).^2));
ncl022=((ncl.^2)-(((u022cl.*lam)./(2*pi*rcl)).^2));
ncl023=((ncl.^2)-(((u023cl.*lam)./(2*pi*rcl)).^2));
ncl024=((ncl.^2)-(((u024cl.*lam)./(2*pi*rcl)).^2));
ncl025=((ncl.^2)-(((u025cl.*lam)./(2*pi*rcl)).^2));
ncl026=((ncl.^2)-(((u026cl.*lam)./(2*pi*rcl)).^2));
ncl027=((ncl.^2)-(((u027cl.*lam)./(2*pi*rcl)).^2));
ncl028=((ncl.^2)-(((u028cl.*lam)./(2*pi*rcl)).^2));
ncl029=((ncl.^2)-(((u029cl.*lam)./(2*pi*rcl)).^2));

ncl030=((ncl.^2)-(((u030cl.*lam)./(2*pi*rcl)).^2));


%------------------modes 50 to 53------;

ncl050=((ncl.^2)-(((u050cl.*lam)./(2*pi*rcl)).^2));
ncl053=((ncl.^2)-(((u053cl.*lam)./(2*pi*rcl)).^2));
%------------------------;
prd_err=2.9;
%------------------------;

period1=lam./(nco01-ncl01)*prd_err;
period2=lam./(nco01-ncl02)*prd_err;
period3=lam./(nco01-ncl03)*prd_err;
period4=lam./(nco01-ncl04)*prd_err;
period5=lam./(nco01-ncl05)*prd_err;
period6=lam./(nco01-ncl06)*prd_err;
period7=lam./(nco01-ncl07)*prd_err;
period8=lam./(nco01-ncl08)*prd_err;
period9=lam./(nco01-ncl09)*prd_err;
period10=lam./(nco01-ncl010)*prd_err;
```

```
% for cl-mode 11 to 19----------;
period11=lam./(nco01-ncl011)*prd_err;
period12=lam./(nco01-ncl012)*prd_err;
period13=lam./(nco01-ncl013)*prd_err;
period14=lam./(nco01-ncl014)*prd_err;
period15=lam./(nco01-ncl015)*prd_err;
period16=lam./(nco01-ncl016)*prd_err;
period17=lam./(nco01-ncl017)*prd_err;
period18=lam./(nco01-ncl018)*prd_err;
period19=lam./(nco01-ncl019)*prd_err;

%----------for modes 20 to 30--------;

period20=lam./(nco01-ncl020)*prd_err;

period21=lam./(nco01-ncl021)*prd_err;
period22=lam./(nco01-ncl022)*prd_err;
period23=lam./(nco01-ncl023)*prd_err;
period24=lam./(nco01-ncl024)*prd_err;
period25=lam./(nco01-ncl025)*prd_err;
period26=lam./(nco01-ncl026)*prd_err;
period27=lam./(nco01-ncl027)*prd_err;
period28=lam./(nco01-ncl028)*prd_err;
period29=lam./(nco01-ncl029)*prd_err;

period30=lam./(nco01-ncl030)*prd_err;


%----------modes 50 to 53------;

period50=lam./(nco01-ncl050)*prd_err;
period53=lam./(nco01-ncl053)*prd_err;

%----------;

%for the second core mode%
%period1b=lam./(nco01-nco02)*prd_err;

%=====mode 1-30========%
figure(4)
hold on;
plot(period1,lam,period2,lam,period3,lam,period4,lam,period5,lam,period6,lam,period7,lam,
period8,lam,period9,lam,period10,lam,period11,lam,period12,lam,period13,lam,period14,la
m,period15,lam,period16,lam,period17,lam,period18,lam,period19,lam,period20,lam,period3
0,lam)
xlabel('Period, um');
ylabel('Wavelength, nm');
grid
```

```
%===== coupling from core mode LP01 to cladding mode 1-9========%
figure(5)
hold on;

plot(period1,lam,period2,lam,period3,lam,period4,lam,period5,lam,period6,lam,period7,lam,
period8,lam,period9,lam);

axis([60 500 0.1 2]);
xlabel('Period, um');
ylabel('Wavelength, nm');
grid

figure(6)
hold on;
plot(period10,lam,period11,lam,period12,lam,period13,lam,period14,lam,period15,lam,perio
d16,lam,period17,lam,period18,lam,period19,lam)
axis([30 200 0.1 2.4]);
xlabel('Period, um');
ylabel('Wavelength, nm');
grid

figure(7)
hold on;
plot(period20,lam,period21,lam,period22,lam,period23,lam,period24,lam,period25,lam,perio
d26,lam,period27,lam,period28,lam,period29,lam,period30,lam)
axis([20 85 0.1 2.4]);
xlabel('Period, um');
ylabel('Wavelength, nm');
grid

figure(8)
hold on;
plot(period5,lam,period8,lam,period12,lam,period15,lam,period20,lam,period25,lam,period3
0,lam,period53,lam)
axis([0 500 0.1 2.4]);
xlabel('Period, um');
ylabel('Wavelength, nm');
grid

%figure(9)
%hold on;
%plot(period1b,lam)
%xlabel('Period, um');
%ylabel('Wavelength, nm');
%grid

fprintf(File_lam,'%-12.5e \n', lam); %,Collect values of x and y;
fprintf(File_nco,'%-12.5e \n', nco);
fprintf(File_ncl,'%-12.5e \n', ncl);
```

```
fprintf(file1,'%-12.5e \n', period1); %,Collect values of x and y;
fprintf(file2,'%-12.5e \n', period2);
fprintf(file3,'%-12.5e \n', period3);
fprintf(file4,'%-12.5e \n', period4);
fprintf(file5,'%-12.5e \n', period5);
fprintf(file6,'%-12.5e \n', period6);
fprintf(file7,'%-12.5e \n', period7);
fprintf(file8,'%-12.5e \n', period8);
fprintf(file9,'%-12.5e \n', period9);
fprintf(file10,'%-12.5e \n', period10);
fprintf(file11,'%-12.5e \n', period11);
fprintf(file12,'%-12.5e \n',  period12);
fprintf(file13,'%-12.5e \n',  period13);
fprintf(file14,'%-12.5e \n',  period14);
fprintf(file15,'%-12.5e \n',  period15);
fprintf(file16,'%-12.5e \n',  period16);
fprintf(file17,'%-12.5e \n',  period17);
fprintf(file18,'%-12.5e \n',  period18);
fprintf(file19,'%-12.5e \n',  period19);

fprintf(file20,'%-12.5e \n', period20);
fprintf(file21,'%-12.5e \n', period21);
fprintf(file22,'%-12.5e \n',  period22);
fprintf(file23,'%-12.5e \n',  period23);
fprintf(file24,'%-12.5e \n',  period24);
fprintf(file25,'%-12.5e \n',  period25);
fprintf(file26,'%-12.5e \n',  period26);
fprintf(file27,'%-12.5e \n',  period27);
fprintf(file28,'%-12.5e \n',  period28);
fprintf(file29,'%-12.5e \n',  period29);
fprintf(file30,'%-12.5e \n',  period30);

fprintf(file53,'%-12.5e \n',  period53); %,Collect values of x and y;



fclose(File_lam);
fclose(File_nco);
fclose(File_ncl);

fclose(file1);
fclose(file2);
fclose(file3);
fclose(file4);
fclose(file5);
fclose(file6);
fclose(file7);
fclose(file8);
fclose(file9);
fclose(file10);
```

```
fclose(file11);
fclose(file12);
fclose(file13);
fclose(file14);
fclose(file15);
fclose(file16);
fclose(file17);
fclose(file18);
fclose(file19);

fclose(file20);
fclose(file21);
fclose(file22);
fclose(file23);
fclose(file24);
fclose(file25);
fclose(file26);
fclose(file27);
fclose(file28);
fclose(file29);
fclose(file30);

fclose(file53);
```

Appendix3: Matlab program for FBG simulation

```
%************************************************************ *%
%                    CFBG_bas.m                                *%
%This Program is for calculating spectral response of FBGs     *%
%                                                              *%
% ************************************************************%

function fun=CFBG(chirp,w0,kL,L,span,sample,div,M,N)
%
% Main Function
%
%  chirp: (nm)
%  w0: Bragg resonance wavelength (um);
%  kL: Full grating coupling strength;
%  L: the overall grating length (mm);
%  span: the spectral region (nm)
%  sample: the number of spectral data
%  div: the sections of the grating
%
% CFBG_bas(chirp,w0,kL,L,span,sample,div,M,N)
%
% CFBG_bas(0,1.55,10,20,4,400,200,10,2)

disp('CFBG_bas(chirp,w0,kL,L,span,sample,div,M,N)')
disp('CFBG_bas(0,1.55,10,20,4,400,200,10,2)')
close all;
nm=10^(-9);
um=10^(-6);
mm=10^(-3);

neff=1.446;

if nargin==0
  chirp=0;
  w0=1.567;
  kL=20;
  L=20;
  span=chirp+4;
  sample=500;
  div=1000;
  M=10;
  N=4;
end;

w0=w0*um; L=L*mm; span=span*nm; chirp=chirp*nm;

%int=kL/L*quad8('profile',-L/2,L/2,10^(-3),[],Fun,L,order,A) %Average coupling strength;
```

```
for i=1:div
  z=-L/2+L/div*(i-1/2);          %position of sub-grating Gi;       %% eqn. 3.30%%
  Z(i)=z;
  prof(i)=prof_bas(z,L,M,N);      %Normalized index modulation profile;
end;

plot(Z/mm,prof);
xlabel('Grating length (mm)');
ylabel('Strength profile');

%finding zero crossings of the profile in fig. 1 which will give the number of phase shifts%

p1=prof; p1(length(p1))=[];
p1=[p1(1),p1];
phase_pi=sign(p1.*prof);
NumberOfPhaseshifts=sum((phase_pi<0))


q=1;
for w=(w0-span/2):span/sample:(w0+span/2)
 M=1;
 for i=1:div
   wc=w0-chirp/2+chirp*(i-0.5)/div;
   kLi=kL*abs(prof(i))/div;

   deltaLi=2*pi*neff*L*(1/w-1/wc)/div;      %% eqn. 3.33%%
   SLi=sqrt(kLi^2-deltaLi^2);

   [ri,ti]=FBG_bas(deltaLi,SLi,kLi);

   Phase(1,1)=phase_pi(i); Phase(1,2)=0;
   Phase(2,1)=0;          Phase(2,2)=1;

   Mi(1,1)=1/conj(ti);    Mi(1,2)=ri/ti;          %% eqn. 3.27%%
   Mi(2,1)=-ri/ti;        Mi(2,2)=1/ti;
   M=Phase*Mi*M;                        %multiplying all sub-gratings%
 end;

 r(q)=-M(2,1)/M(2,2);                          %% eqn. 3.32%%
 t(q)=M(1,1)+r(q)*M(1,2);

 R(q)=abs(r(q))^2;
 T(q)=abs(t(q))^2;

 W(q)=w;
 q=q+1;
end;


R=1-T; W=W/nm;
```

```
logR=10*log10(R);                %linear scale%

for i=1:length(R);
 if logR(i)<-100
   logR(i)=-100;
 end;
end;



figure(2)
 plot(W,R,'b');
 xlabel('Wavelength (nm)');
 ylabel('Reflection (dB)')
 %axis([W(1) W(length(W)) -70 0])

figure(3)
 plot(W, 10*log10(T),'r');          %linear scale%
 xlabel('wavelegnth (nm)')
 ylabel('Transmission (dB)');

%figure(4)
%  plot(W, T,'b');
%  ylabel('Transmission')
%  xlabel('Wavelength (nm)')

[linewidth,w0,peak]=FWHM_tr(W,T,0.5,'tr');
fprintf('\nFWHM=%g (nm)',1*linewidth)
fprintf('\npeak_loss=%g (dB)\n\n',10*log10(min(T)))

fid=fopen('C:\Temp\mubin1t.txt','w');
fprintf(fid,'%f  %f\n',[W;10*log10(T)]);
fclose(fid);

fid1=fopen('C:\Temp\mubin2r.txt','w');
fprintf(fid1,'%f          %f\n',[W;R]);
fclose(fid1);

fid2=fopen('C:\Temp\mubin3ind.txt','w');
fprintf(fid2,'%f          %f\n',[Z/mm;prof]);
fclose(fid2);
figure(4)
disp('CFBG2(chirp,w0,kL,L,span,sample,div,Fun,order,A)')
disp('CFBG2(0,1.55,10,30,4,400,200,5,6,inf)   sinc profile')
fun={[W;T;R],[Z/mm,prof]}


%%%%%%%%%%%%%%%%%%%%%%%%%%%%%%%%%%%%%%%%%%%%%%%%%%%%%%%%%%%%
%See Ians JQE review-paper or first year report Topic 4, the 3rd page%
%%%%%%%%%%%%%%%%%%%%%%%%%%%%%%%%%%%%%%%%%%%%%%%%%%%%%%%%%%%%
```

```
function [r,t]=FBG_bas(deltaL,SL,kL) %% see eqn 3.28%%
%
% [r,t]=FBG_rt(deltaL,SL,KL)
 r=j*kL*sinh(SL)./(SL.*cosh(SL)-j*deltaL.*sinh(SL));
 t=SL./(SL.*cosh(SL)-j*deltaL.*sinh(SL));
%%%%%%%%%%%%%%%%%%%%%%%%%%%%%%%%%%%%%%%%


%%%%%%%%%%%%%%%%%%%%%%%%%%%%%%%%%%%%%%%%
%Index modulation
%%%%%%%%%%%%%%%%%%%%%%%%%%%%%%%%%%%%%%%%
function f=prof_bas(z,L,M,N)
y=0;
for i=1:N
y=y+cos(2*pi*i/L*M*z);
end;
f=(0.5+y)/(N+0.5);
%%%%%%%%%%%%%%%%%%%%%%%%%%%%%%%%%%%%%%%%
```

```
%********************************************************** *%
%                  Fatima1.m                                  *%
%This Program is called upon by the phase relationships program to   *%
% calculate eigen-value equation                              *%
% **********************************************************%

function f=fatima1(u,v,l,p)
%
%  f=fatima1(u,v,l,p)
%  geometric optics based eigen value eqn (see adams book);
% b: Normalised propagation constant;
% v: Normalised frequency;
% p: the radial number for modes;
% l: the azimuthal or angular number for modes;

u=u+(u==0)*eps;

f=sqrt(u.*u-l*l)-l*acos(l/u)-acos(sqrt(u.*u-l*l)./v)-(p-0.75)*pi;
```

```
%************************************************************ *%
%                    Fatima.m                                  *%
%This Program is called upon by the phase relationships program to  *%
% calculate eigen-value equation                               *%
% ************************************************************%


function f=fatima(u,v,l,p)
%
%  f=fatima(u,v,l,p)
%  geometric optics based eigen value eqn (eqn 3.33 in liu's thesis);
% b: Normalised propagation constant;
% v: Normalised frequency;
% p: the radial number for modes;
% l: the azimuthal or angular number for modes;

u=u+(u==0)*eps;

f=sqrt(u.*u-l*l)-l*acos(l/u)-acos(sqrt(u.*u-l*l)./v)-(p-0.75)*pi;
```

FWHM_tr.m

```
function [linewidth,w0,Y0]=FWHM_tr(W,Y,r,T_R)
%
%[linewidth,X0,Y0]=FWHM_TR(W,Y,r,T_R)
%
%Return Linewidth,
%       peak-wavelength w123(2),
%       and the region of the linewidth w123(1) w123(3),
%
%       T_R='re' reflection spectrum;
%       T_R='tr' transmission spectrum;
%       r   is reflection to set linewidth, r=0.5 for default;
%

[a,b]=max(abs(Y));

if Y(b)>=0&(prod(T_R=='re')==1)
  R=Y;                          %Linear reflection spectrum;
elseif (Y(b)<0)&(prod(T_R=='re')==1)
  R=10.^(Y/10);                 %dB reflection spectrum;
elseif (Y(b)>=0)&(prod(T_R=='tr')==1)
  R=1-Y;                        %Linear transmission spectrum;
elseif (Y(b)<0)&(prod(T_R=='tr')==1)
  R=1-10.^(Y/10.0);             %dB transmission spectrum;
end;
```

```
[Rmax,x0]=max(R);
w0=W(x0);
Y0=Y(x0);

q=(R>=r*Rmax);
wh=W(q);
w123=[wh(1),w0,wh(length(wh))];

linewidth=wh(length(wh))-wh(1);
```